

An Airbag-Based Impact Attenuation System for the Orion Crew Exploration Vehicle

Sydney Do, Olivier L. de Weck

February 2011

SSL # 1-11

An Airbag-Based Crew Impact Attenuation System for the Orion Crew Exploration Vehicle

Sydney Do, Olivier L. de Weck

February 2011

SSL # 1-11

This work is based on the unaltered text of the thesis by Sydney Do submitted to the Department of Aeronautics and Astronautics in partial fulfillment of the requirements for the degree of Master of Science at the Massachusetts Institute of Technology.

An Airbag-Based Crew Impact Attenuation System for the Orion Crew Exploration Vehicle

by

Sydney Do

Submitted to the Department of Aeronautics and Astronautics
on January 27, 2011 in partial fulfillment of the requirements for the degree of
Master of Science in Aeronautics and Astronautics

Abstract

It is a well known fact that every capsule-shaped reentry vehicle developed by NASA was initially conceived to land on land, but was ultimately designed to land in water. In all cases, the primary factor contributing to this fundamental shift was related to difficulties with keeping the vehicle to within its mass allocation. In recognizing the recurrence of this scenario during the development of the Orion Crew Exploration Vehicle (CEV), the concept of airbag-based crew impact attenuation was identified as being a potential means for providing a low mass, reconfigurable alternative to the currently baselined pallet-strut design. This thesis presents the development effort undertaken to determine the feasibility of this concept in terms of protecting an astronaut from the impact loads incurred during the nominal 7.62m/s Orion CEV landing on land.

Through the complete development and testing of an analog airbag system and an intermediate technology demonstrator, practical means for system implementation have been developed, and insights into the influence of the system configuration on its overall impact attenuation performance obtained. These findings have culminated in the design and implementation of a full-scale multi airbag system, which has been experimentally shown to be capable of maintaining the risk of injury to the occupant during a 7.85m/s, 0° impact angle land-landing to within the NASA specified limit of 0.5%. In accomplishing this, the airbag-based impact attenuation concept has been proven to be feasible.

Moreover, the obtained test results suggest that by implementing anti-bottoming airbags to prevent direct contact between the system and the landing surface, the system performance during landings with 0° impact angles can be further improved, by at least a factor of two. Additionally, a series of drop tests from the nominal Orion impact angle of 30° indicated that severe injury risk levels would be sustained beyond impact velocities of 5m/s. This is due to the differential stroking of the airbags within the system causing a shearing effect between the occupant seat structure and the spacecraft floor, removing significant stroke from the airbags.

These results combined indicate that with further detailed design in the context of the currently fixed Orion crew cabin design, and the enforcement of a flat impact angle during landing, airbag-based impact attenuation may prove to be the key to finally achieving the elusive goal of capsule-shaped vehicle reentry and land-landing.

Thesis Supervisor: Olivier L. de Weck

Title: Associate Professor of Aeronautics and Astronautics and Engineering Systems

Acknowledgments

This work was performed under prime award number NCC3989 and subaward number Z634013 with the NASA Engineering and Safety Center as part of the Constellation University Institutes Project. The author gratefully thanks the sponsors for their generous support that enabled this research.

Contents

1. Introduction	23
1.1 Background and Motivation.....	23
1.2 Objective and Approach.....	28
1.3 Thesis Outline	30
2. Literature Review	33
2.1 Terrestrial Airbag Systems.....	33
2.1.1 Garment-Based Airbag Systems.....	33
2.1.2 Seat-Based Airbag Systems.....	37
2.1.3 Cabin-Based Airbag Systems	40
2.1.4 Summary of Relevant Terrestrial Airbag System Concepts.....	43
2.2 Spacecraft Airbag Systems	45
2.2.1 Project Mercury	45
2.2.2 Luna 9 and 13	46
2.2.3 Mars Pathfinder and Mars Exploration Rover.....	47
2.2.4 Orion Crew Exploration Vehicle	49
2.2.5 ExoMars.....	50
2.2.6 Summary of Relevant Spacecraft Airbag System Concepts.....	51
2.3 Human Spaceflight Impact Attenuation Systems	52
2.3.1 Vostok.....	52
2.3.2 Project Mercury	54
2.3.3 Voskhod and Soyuz	55
2.3.4 Project Gemini	56
2.3.5 Apollo	58

2.3.6	Summary of Relevant Features of Past Human Spacecraft Impact Attenuation Systems	60
2.4	Chapter Summary	62
3.	The Impact Attenuation Problem	65
3.1	Airbag Impact Dynamics Modeling	65
3.1.1	Thermodynamic Analysis	66
3.1.2	The Single Airbag Impact Model Framework	73
3.1.3	The Integrated Single Airbag Impact Model	83
3.2	Human Injury-Risk Modeling	88
3.2.1	The Brinkley Direct Response Index	88
3.2.2	Injury-Risk Mitigation	91
3.3	Photogrammetric Methods for Impact Analysis	94
3.4	Chapter Summary	97
4.	Analog-Airbag System Development	99
4.1	Analog-Airbag System Design	99
4.1.1	System Configuration	100
4.1.2	Airbag Sizing	101
4.1.3	Test Hardware and Infrastructure Design	104
4.1.4	Airbags to Beanbags	107
4.1.5	Analog-Airbag System Manufacture	108
4.2	Analog-Airbag System Drop Test Plan	111
4.3	Analog-Airbag System Test Results & Analysis	112
4.3.1	Considerations Regarding Measurement Uncertainty	115
4.3.2	Typical Results	116
4.3.3	Trends with Varying Drop Height	121
4.3.4	Summary of Analog-Airbag Test Campaign Findings	125
4.4	Chapter Summary	126
5.	Single Airbag Impact Dynamics Investigation	127
5.1	Single Airbag System Development	127
5.1.1	System Configuration	128

5.1.2	Design of Experiments	131
5.1.3	Valve Development	137
5.1.4	Airbag Material Testing and Leakproofing	148
5.1.5	Pressure Relief Valve Vented Airbag Optimization.....	155
5.1.6	Single Airbag Drop Test Article Manufacture	159
5.2	Single Airbag System Drop Test Plan	161
5.3	Single Airbag System Test Results & Analysis	163
5.3.1	Test Session 1 Results Analysis	164
5.3.2	Test Session 2 Results Analysis	166
5.4	Single Airbag Impact Model Refinement	172
5.5	Design Space Exploration	179
5.5.1	Single Objective Optimization	180
5.5.2	Multi-Objective Optimization	192
5.6	Chapter Summary	194
6.	Multi-Airbag System Development	195
6.1	Multi-Airbag System Modeling	195
6.2	Multi-Airbag System Development	202
6.2.1	Airbag Configuration Design and Sizing	202
6.2.2	Seat Support System Development	216
6.2.3	Generation 3.1 Flapper Valve.....	218
6.2.4	Airbag Manufacture.....	220
6.2.5	Multi-Airbag System Integration.....	222
6.3	Multi-Airbag System Drop Test Plan	224
6.4	Multi-Airbag System Test Results & Analysis	227
6.4.1	Pressure Relief Valve Performance	229
6.4.2	Test Session 1 Results Analysis	231
6.4.3	Test Session 2 Results Analysis	239
6.5	Chapter Summary	246
7.	Conclusions	249
7.1	Summary of Findings.....	250

7.1.1	Findings from Preliminary Modeling of the Airbag-Based Impact Attenuation Problem.....	250
7.1.2	Findings from the Development of the Analog-Airbag System.....	250
7.1.3	Findings from the Single Airbag Impact Dynamics Investigation	251
7.1.4	Findings from the Development of the Multi-Airbag System.....	251
7.2	Recommendations for Future Work	252
Appendix A. Project Team Members		255
Appendix B. Model Newton Iteration Function Derivation		257
Appendix C. Mass Comparison between Crew Impact Attenuation Systems		261
References		263

List of Figures

1-1	The Orion Crew Exploration Vehicle.....	24
1-2	Comparison of Impact Attenuation Systems	26
1-3	Original Sketches from NESC Academy Design Course	27
1-4	Initial System Concept of Operations.....	28
1-5	Three Level Spiral Model used for this Development Effort	29
2-1	Xenith X1™ Football Helmet.....	34
2-2	Marco Simonelli falls off his motorcycle during the 2007 Valencia Grand Prix	35
2-3	Mugen Denko Hit-Air Shock Buffering System	35
2-4	The Itsumo Safety Life Jacket	36
2-5	Suit-Based Airbag Systems marketed by the NIIS and Prop Company	37
2-6	Inflatable Seat Concept.....	38
2-7	Inflatable Seat Cushions	38
2-8	Amsafe Commerical Aviation Seatbelt Airbag	39
2-9	Inflatabelt Concepts developed by BAE Systems	40
2-10	Airbag system in a 2007 Model Honda Accord	41
2-11	Airbag Applications in Terrestrial Vehicles	41
2-12	F-111 Crew Escape Module Airbags.....	42
2-13	Helicopter Out-of-Cabin Airbag Systems.....	43
2-14	Mercury Landing Airbag System	46
2-15	Luna 9 and 13 Landing Sequence.....	47
2-16	Mars Pathfinder Mission.....	48
2-17	Mars Exploration Rover Mission.....	48
2-18	Orion CEV Nominal Landing Sequence with External Airbags	49

2-19	Orion External Airbag System.....	50
2-20	ExoMars Landing Sequence	51
2-21	Drop testing of a prototype of the ExoMars airbag system	51
2-22	Vostok Mission.....	53
2-23	A technician works on the Mercury couch	54
2-24	Soviet Shock Absorbing Seats.....	55
2-25	Gemini Descent and Landing	57
2-26	Ejection Seats used in the Gemini spacecraft	57
2-27	Apollo Couch Impact Attenuation System Configuration.....	58
2-28	Detail of Apollo Crew Couch	59
3-1	Initial Condition for Thermodynamic Analysis.....	66
3-2	System State Transition	69
3-3	System during the Venting Phase	71
3-4	Overview of Developed Single Airbag Impact Model	73
3-5	Single Airbag Impact Model Initial Condition	74
3-6	Shape Function used in Single Airbag Impact Model	75
3-7	Upstream and Downstream Pressure as used by the Single Airbag Impact Model.....	79
3-8	Data used to Model the Discharge Coefficient.....	83
3-9	Single Airbag Impact Model Functional Flow Block Diagram.....	84
3-10	Brinkley Reference Frame.....	89
3-11	Magnification Effects of the Dynamic Amplification Function	93
3-12	Dot Detection Algorithm Functional Flow Block Diagram	95
3-13	Line Detection Algorithm Functional Flow Block Diagram	96
3-14	Summary of Photogrammetric Analysis Process.....	97
4-1	Baseline Airbag Configuration	100
4-2	Predicted Performance for the First Generation Personal Airbag System.....	104
4-3	Test Article and Infrastructure Design Features	105
4-4	Detail of Seat Frame Design.....	105
4-5	Drop Test Infrastructure.....	106
4-6	Anthropomorphic Test Device used during all Drop Test Campaigns	107
4-7	High Strength Polyester Tensile Strength Testing.....	109
4-8	Exploded View of Beanbag Fill Valve Design.....	110
4-9	System Components	110

4-10	Integrated First Generation System	111
4-11	First Generation System Test Setup.....	112
4-12	Typical Dynamic Response Seen During Testing	113
4-13	Test Failure from a 5 foot Drop Height	114
4-14	Photogrammetrically Obtained Test Results for a 3 foot Drop	117
4-15	Dynamic Breakdown of Accelerometer Data obtained from a 3 foot Drop Test	118
4-16	Resimulated System Dynamics for a 3 foot Test Drop	119
4-17	Injury-Risk Responses for a 3 foot Test Drop	120
4-18	X-Direction Acceleration for all Generation 1 System Drop Tests	122
4-19	X-Direction Brinkley Index for all Generation 1 System Drop Tests	123
4-20	Low Injury-Risk β -Number for all Generation 1 System Drop Tests	123
4-21	Impact Velocity for all Generation 1 System Drop Tests.....	124
5-1	Generation 2 Personal Airbag System Configuration.....	128
5-2	Generation 2 Individual Airbag Configuration.....	129
5-3	Tilting of the First Generation System after a 3ft Drop.....	130
5-4	Brinkley Response with fixed x_0 and Varying Inflation Pressure	132
5-5	Brinkley Response with fixed x_0 and Varying Orifice Diameter	133
5-6	Brinkley Response with fixed x_0 and Burst Acceleration.....	133
5-7	Brinkley Response with fixed x_1 and Varying Inflation Pressure	134
5-8	Brinkley Response with fixed x_1 and Burst Acceleration.....	135
5-9	Brinkley Response with fixed x^* and Varying Orifice Diameter.....	136
5-10	Comparison between ValveTech flapper valve and valve developed in-house	140
5-11	Flapper Valve Leakage Testing Setup	141
5-12	Close up views of leakage of First Generation Flapper Valve	141
5-13	Second Generation Flapper Valve	144
5-14	Third Generation Flapper Valve	145
5-15	Third Generation Flapper Valve Characterization Test Setup.....	146
5-16	Third Generation Flapper Valve Characterization Testing Results	146
5-17	Idealized Valve Torsional Spring Model.....	147
5-18	Flapper Valve Mounting Concept.....	148
5-19	Vectran Tensile Test Samples.....	150
5-20	Vectran Tensile Strength Test Results.....	151
5-21	High Strength Polyester Leakage Testing	152

5-22	Liquid Latex Coating Test Setup	153
5-23	Leakage Test Result.....	154
5-24	Silicone Paint Applied to Fabric Seam	154
5-25	Pressure Relief Valve Vented Airbag Design Space	156
5-26	Predicted Brinkley Response for the Single Airbag Test Article	157
5-27	Predicted Vertical Displacement Response for the Single Airbag Test Article	158
5-28	Final Integrated Single Airbag Drop Test Article Design	159
5-29	Single Airbag Drop Test Article.....	160
5-30	Single Airbag Drop Test Article.....	161
5-31	Single Airbag Drop Test Setup.....	162
5-32	Typical Dynamic Observed During all Single Airbag System Drop Tests	163
5-33	Single Airbag Drop Test Article Failure at 6 foot Drop Height	164
5-34	Single Airbag Drop Test Session 1 Accelerometer Data.....	165
5-35	Single Airbag Drop Test Session 1 Pressure Transducer Data.....	165
5-36	Single Airbag Drop Test Session 1 Pressure Transducer Data.....	166
5-37	Photogrammetric Analysis of High Speed Camera 1 Footage	167
5-38	Dynamics Data Extracted from Photogrammetry.....	167
5-39	Accelerometer Data for a 4foot Drop	168
5-40	Pressure Transducer Data for a 4foot Drop	169
5-41	X-Direction Acceleration for all Single Airbag System Drop Tests	170
5-42	X-Direction Brinkley Index for all Single Airbag System Drop Tests.....	171
5-43	Airbag Pressure for all Single Airbag System Drop Tests	171
5-44	Comparison between Original Predictions and Experimental Data for a 4 foot Drop	173
5-45	Comparison between Refined Predictions and Experimental Data for a 4 foot Drop	174
5-46	Acceleration Response over Varying Payload Mass	175
5-47	Brinkley DRI Response over Varying Payload Mass.....	176
5-48	Acceleration Response over Varying Impact Velocity.....	177
5-49	Brinkley DRI Response over Varying Impact Velocity	178
5-50	Unscaled SQP Iteration History and Solution	184
5-51	Scaled SQP Iteration History and Solution.....	186
5-52	Simulated Annealing Iteration History and Solution.....	188
5-53	Comparison of Orifice Opening Area under Different Airbag Geometries	189
5-54	Brinkley DRI Space Plotted at Coarse and Fine Resolution	190

5-55	Full Factorial Expansion of the Objective Space.....	193
6-1	Baseline Two Degree of Freedom Multi-Airbag Model	196
6-2	Multi-Airbag Impact Model Functional Flow Block Diagram.....	201
6-3	Baseline Airbag Configuration for the Multi-Airbag System Design Iteration 1	204
6-4	High Resolution Full Factorial Expansion for the first Multi-Airbag Iteration.....	206
6-5	Baseline Airbag Configuration for the Multi-Airbag System Design Iteration 2.....	207
6-6	High Resolution Full Factorial Expansion for the Second Multi-Airbag Iteration	209
6-7	Second Multi-Airbag System Iteration Objective Space Filtered by Airbag Length .	210
6-8	Baseline Airbag Configuration for the Multi-Airbag System Design Iteration 3.....	211
6-9	High Resolution Full Factorial Expansion for the Third Multi-Airbag Iteration	211
6-10	Third Multi-Airbag System Iteration Objective Space Filtered by Airbag Length	212
6-11	Objective Space Filtered by Max Hoop Stress < 540MPa & L = 0.26m or 0.28m	213
6-12	Predicted Brinkley DRI for the Nominal 30° Impact Case	214
6-13	Predicted System Dynamic for the Nominal 30° Impact Case	215
6-14	Predicted Brinkley DRI for the Nominal 0° Impact Case	215
6-15	Predicted System Dynamic for the Nominal 0° Impact Case	215
6-16	Overarching Multi-Airbag System Concept	216
6-17	Original Seat Support System Sketches.....	217
6-18	Seat Support System Sizing.....	217
6-19	Final Manufactured Seat Support Structure.....	218
6-20	Generation 3.1 Pressure Relief Valve Design	218
6-21	Generation 3.1 Pressure Relief Valve Leakage Test Setup	219
6-22	Manufactured Generation 3.1 Pressure Relief Valve Components	220
6-23	Airbag Seam Layering Scheme	220
6-24	Airbag Crush-Up Test.....	221
6-25	Integrated Airbag	222
6-26	System Hoist Test	222
6-27	Center of Gravity Testing	223
6-28	Fully Integrated Second Generation Personal Airbag System.....	224
6-29	Drop Test Configuration	225
6-30	Multi-Airbag System Drop Test Setup	226
6-31	Multi-Airbag System Drop Test Campaign Camera Locations and Views.....	227
6-32	Airbag Failure Experienced during 7 foot Drop at 30° Impact Angle.....	228

6-33	Frame by Frame Breakdown of the 7 foot, 30° Impact Angle Drop	228
6-34	Breakdown of the Pressure Relief Valve Performance	229
6-35	Pressure Transducer Output for all Test Session 1 Drop Tests	230
6-36	Pressure Transducer Output for all Test Session 2 Drop Tests	230
6-37	Test Session 1 X-Direction Acceleration Results.....	231
6-38	Test Session 1 X-Direction Brinkley DRI Results	232
6-39	Test Session 1 Low Injury-Risk β -Number Results	232
6-40	Test 19 Acceleration Response with Anomalous Consecutive Peaks Highlighted	234
6-41	Summary of Data Time Synchronization Process	235
6-42	Session 1 Test 19 Normalized and Time Synchronized Data Set.....	236
6-43	Session 1 Test 19 - Dynamically Tagged X-Direction Acceleration Response	237
6-44	Effects of Drop Height on Bottoming-Out of Multi-Airbag System.....	238
6-45	Potential System Dynamics without Bottoming-Out.....	239
6-46	Test Session 1 X-Direction Acceleration Results.....	240
6-47	Test Session 2 X-Direction Brinkley DRI Results	240
6-48	Test Session 2 Low Injury-Risk β -Number Results	241
6-49	Session 2 Test 13 Normalized and Time Synchronized Data Set.....	242
6-50	Breakdown of Valve Performance and Obstruction during Session 2 –Test 13.....	243
6-51	Session 2 Test 13 - Dynamically Tagged X-Direction Acceleration Response	244
6-52	Frame by Frame Breakdown of the 7 foot, 30° Impact Angle Drop	246

List of Tables

2.1	Summary of Reviewed Airbag System Concepts.....	63
3.1	Values Assumed for the Thermodynamic Analysis	67
3.2	NASA HSIR specified natural frequencies and damping ratios.....	90
3.3	NASA HSIR Specified Brinkley DRI Limits	90
3.4	Brinkley Limits for Moderate and High Risks of Injury	91
4.1	Parameter Values Forming the Optimization Space for Each Airbag	102
4.2	Airbag Parameter Values for First Generation CIAS Design.....	103
4.3	Time Breakdown of Significant Dynamic Events for a 3ft Drop Test	118
4.4	Summary of Photogrammetric Analysis Results for all Drop Tests Performed	122
5.1	Baseline Design Vector for a Single Airbag with Burst Valves	137
5.2	Venting Mechanism Concepts Presented to the NESC	138
5.3	Pressure Relief Valves Offered by McMaster-Carr®.....	139
5.4	Summary of Leakage Tests Conducted during the Sealing Material Investigation....	142
5.5	Summary of Leakage Tests Conducted during the Sealing Material Investigation....	143
5.6	Vectran Tensile Strength Testing Results.....	151
5.7	Liquid Latex Coating Test Matrix	153
5.8	Final Design Vector for the Single Airbag Drop Test Article	157
5.9	Summary of Sensor and Photogrammetric Analysis Results	170
5.10	Factors and Levels for the Design of Experiments	181
5.11	Orthogonal Array Analysis Results	182
5.12	Main Effect of Design Variables determined from Orthogonal Array Analysis	182
5.13	Simulated Annealing Tuning Parameters	188
5.14	Step Length Selections for Sensitivity Analysis	191

6.1	Factors & Levels used for the first iteration of the Multi-Airbag System Design.....	205
6.2	Maximum Hoop Stress Predictions (in MPa) for Design Iteration 1.....	205
6.3	Variable Ranges used in the Multi-Airbag System Design Iteration 1.....	206
6.4	Factors & Levels used for the second iteration of the Multi-Airbag System Design.	208
6.5	Maximum Hoop Stress Predictions (in MPa) for Design Iteration 2.....	208
6.6	Final Second Generation Personal Airbag System Configuration.....	214
6.7	Multi-Airbag System Mass Properties.....	223
6.8	Summary of Multi-Airbag System Drop Test Session 1 Results	233
6.9	Summary of Multi-Airbag System Drop Test Session 1 Results	241

Nomenclature

Abbreviations

ASME	American Society of Mechanical Engineers
ATD	Anthropomorphic Test Device
BFGS	Broyden Fletcher Goldfarb Shanno Method of approximating the Hessian
CEV	Crew Exploration Vehicle
CG	Center of Gravity
CIAS	Crew Impact Attenuation System
CM	Crew Module
CUIP	Constellation University Institutes Project
CxP	Constellation Program
DAQ	Data Acquisition Unit
DOF	Degree of Freedom
DR	Direct Response
DRI	Direct Response Index
GPS	Global Positioning System
HSIR	Human-System Integration Requirements
ISS	International Space Station
LaRC	Langley Research Center
LED	Light Emitting Diode
LLO	Low Lunar Orbit
MIT	Massachusetts Institute of Technology
NASA	National Aeronautics and Space Administration
NESC	NASA Engineering and Safety Center
NPT	National Pipe Thread
PSU	Pennsylvania State University
PVC	Polyvinyl Chloride

SA	Simulated Annealing
SQP	Sequential Quadratic Programming

Roman Symbols

a	Acceleration (Earth G's)
a^*	Speed of Sound (m/s)
A	Area (m^2); Dynamic Amplification Function; Orifice Area (m^2)
B	Approximation to the Hessian
C_D	Discharge Coefficient
CV	Control Volume
d_k	Search Direction
D	Airbag Diameter (m)
E	Energy Content (kJ)
F	Force (N)
g	Gravitational Acceleration (m/s^2); Inequality Constraints
h	Height (m); Specific Enthalpy (kJ/kg); Equality Constraints
H	Transfer Function
J	Objective Function; Moment of Inertia ($kg.m^2$)
k	Spring Stiffness (N/m)
ke	Specific Kinetic Energy (kJ/kg)
K	Kinetic Energy (kJ)
KE	Kinetic Energy (kJ)
L	Length (m); Lagrangean Function
m	Mass (kg); Main Effect
M	Mach Number
N	Number of Airbags
p	Load (N)
\tilde{p}	Amplitude
P	Pressure (kPa); Probability
q	Generalized Coordinate
PE	Potential Energy (kJ)

R	Specific Gas Constant (J/kg/K); Spring Arm Length (m); Airbag Radius (m)
t	Time Coordinate (s); Thickness (mm)
T	Temperature (K); Torque (Nm)
u	Vertical Degree of Freedom
U	Internal Energy (kJ); Velocity (m/s)
v	Random Number
V	Volume (m^3); Elastic Potential Energy (kJ)
\vec{V}	Velocity (m/s)
w	Mass of Gas within Airbag (kg)
W	Work (kJ)
x	Vertical Displacement Coordinate (m)
X	General Spatial Coordinate (m)
X_D	Airbag Stroke (m)

Greek Symbols

α	Search Direction
β	Beta Number
γ	Ratio of Specific Heats
θ	Spring Preload Angle (deg); Pitch Angle Degree of Freedom (deg)
Λ	Length of Payload Mass (m)
ξ	Damping Ratio
ρ	Density (kg/m^3)
σ	Stress (Pa)
ω	Frequency (rad/s)

Subscripts

atm	Atmospheric
B	Boundary
bag	Airbag
$burst$	Burst

<i>d</i>	Downstream
<i>DIFF</i>	Differential
<i>FP</i>	Footprint
<i>GAS</i>	Airbag Gas
<i>i</i>	Iteration Number
<i>I</i>	Initial
<i>IN</i>	Into System
<i>Load</i>	Equivalent Load of Seat Structure
<i>MASS</i>	Payload Mass
<i>n</i>	Natural
<i>N</i>	Normal
<i>OUT</i>	Out of System
<i>seam</i>	Seam
<i>SYS</i>	System
<i>t</i>	Time Increment
<i>T</i>	Torsion
<i>th</i>	Orifice
<i>u</i>	Upstream
<i>x</i>	Spatial coordinate in the x-direction
<i>y</i>	Spatial coordinate in the y-direction
<i>z</i>	Spatial coordinate in the z-direction

Superscripts

\lim Limit

Chapter 1

Introduction

Since the start of its development in late 2006, the Orion Crew Exploration Vehicle has experienced several modifications to its operational and design architecture as trade studies have been completed and more knowledge about the system obtained. One prevalent aspect which has been continually revisited throughout the program is the baseline mode in which the vehicle is to land on the Earth's surface, and consequently the system concept which should be employed to facilitate this landing. This uncertainty has been linked to a combination of a strained mass budget, and difficulties in developing systems capable of protecting astronauts during all possible landing scenarios [1]. This thesis aims to provide further insight into this problem by evaluating the feasibility of implementing an alternative, lightweight, airbag-based impact attenuation system within the cabin of the Orion Crew Module. This work forms one component of a greater study conducted by the NASA Engineering and Safety Center (NESC) team tasked by the Constellation Program (CxP) Office to provide design recommendations for the Orion landing system architecture. Specifically, the results of this work will be used by the NESC to decide whether or not to further pursue the airbag-based impact attenuation system concept.

1.1 Background and Motivation

In early 2004, following the Space Shuttle Columbia accident, President George W. Bush announced the “Vision for Space Exploration” – a United States space policy aimed at returning humans to the Moon by the year 2020 in order to develop the skills, technology, and infrastructure required for sustained human exploration of Mars and other destinations in

the Solar System [2]. Emerging from this was the Constellation Program, a program within NASA aimed at developing and operating the hardware required to realize the Vision.

The first vehicle to be developed under this newly implemented program was the Orion Crew Exploration Vehicle (CEV), an all purpose human transportation system intended to operate to and from the International Space Station (ISS), Low Lunar Orbit (LLO), and eventually Martian orbit. One of the most revisited decisions in the development of this vehicle and its mission architecture was the mode in which it landed on the Earth's surface at the completion of its mission.

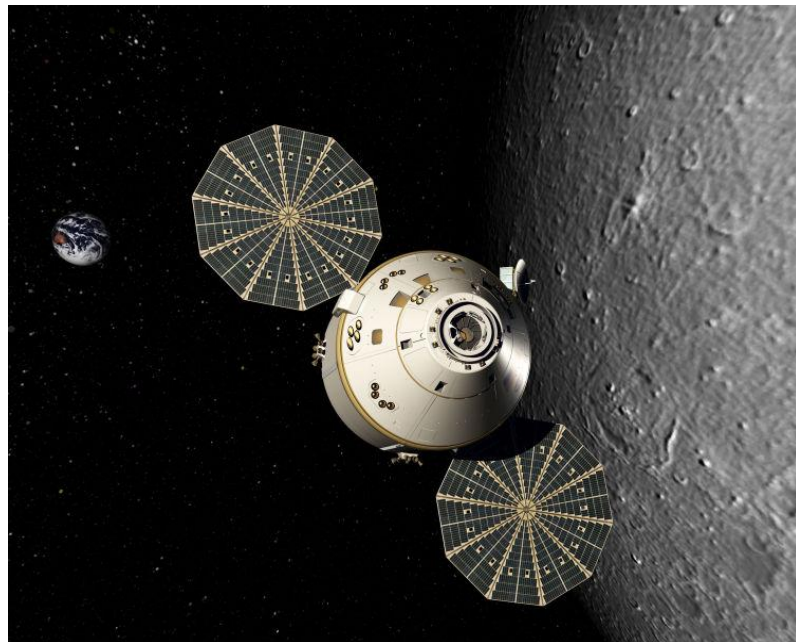


Figure 1-1: The Orion Crew Exploration Vehicle [3]

It is an interesting fact that every capsule-shaped reentry vehicle developed by NASA initially had a specific requirement to land on land. Following detailed study, and accounting for the technical and schedule risks involved, it was deemed in every case that landing on water would be less demanding. With the schedule pressures of the Cold War space race long gone and the desire to develop a sustainable, long-term space transportation program; there was an interest in revisiting the possibility of developing a land-landing capability for Orion from the outset [4, 5]. Consequently, the CxP Office commissioned the NASA Engineering and Safety Center to assess the risks and costs involved in land versus water landings for Orion [4].

In this NESC study, the key advantages of land-landings were found to be related to the recovery and refurbishment of the vehicle. Recovering a vehicle from the sea is inherently more challenging than recovering one from land. This is due to the added difficulty in gaining access to a target moving in a dynamic marine environment, as well as the need to keep the vehicle afloat to prevent it from flooding [4]. These factors combine to add a time sensitivity to water recovery operations, which can be exacerbated in the scenario where a crew member is immobile due to injury or the effects of long-term spaceflight. Contrastingly, land-landings facilitate easier egress and recovery of the vehicle, while also mitigating the risk of it sustaining water damage. This latter attribute has implications on the ease of refurbishment of the spacecraft, which in turn impacts on the life-cycle costs of the program [1]. The disadvantage of employing a land-landing mode, however, is that the increased hardness of the landing surface results in higher accelerations being imparted upon the crew during impact. This hence requires a more complex, and inevitably higher mass system required to attenuate this additional load.

It was of the NESC's view that the operational and life-cycle benefits of nominal land-landings far offset this additional complexity. This was supported by simulations which indicated that the inclusion of retro-rockets could easily maintain land-landing loads to within safe injury-risk levels, and that there was no major difference in development and post-landing recovery costs between each option [4]. Hence, based on this, the NESC recommended that the Orion CEV adopt a primary land-landing mode. To support this development, the NESC further recommended that a study be conducted to investigate various options for further injury-risk mitigation during land-landings. Here, a specific mention was made to:

"Pursue an alternate approach to the internal astronaut couch attenuation system based on difficult experience with [the] Apollo strut support system. The current CEV design of the astronaut couch and associated couch attenuation system should be revisited" [4]

Since the completion of this assessment however, the overall mass of the system has grown past its allowable mass allocation as its design has matured, prompting the initiation of a weight reduction program in late 2007. One key outcome of this activity was the decision to revert back to a nominal water-landing mode. This was based on the finding that a mass

saving of approximately 1670lb was achievable if this option was employed [1]. Coupled with this decision however, was the need for the vehicle to protect the crew during an event known as the Contingency Land Landing. This scenario occurs in the case of a launch abort or an off-nominal re-entry, where there is a risk of the vehicle being forced to land on land. This is particularly the case during the first 20 seconds of any launch from Kennedy Space Center, as the vehicle passes over the coast of Florida and is subjected to low altitude onshore winds [4].

During the Apollo era, this risk was openly accepted after several failed attempts to develop a system capable of safely protecting astronauts during land-landings. Given the lunar launch window constraints and the high wind environment at Cape Canaveral, it was widely understood that going to the Moon would not have been possible without accepting this risk [4].

With the desire to develop a more robust system and to avoid accepting such risks, the CxP Office again requested the assistance of the NESC. Specifically, the NESC was commissioned to implement its prior recommendation - to explore potential design alternatives to the baseline design of the Orion vehicle's Crew Impact Attenuation System (CIAS). Serving the same role as the Apollo's strut support system, the function of the CIAS is to attenuate all impact loads subjected to the crew throughout the mission to within tolerable levels of injury-risk. As can be seen in Figure 1-2, both baseline system designs are based on the same concept – a set of crew seats mounted to a strut-supported pallet.

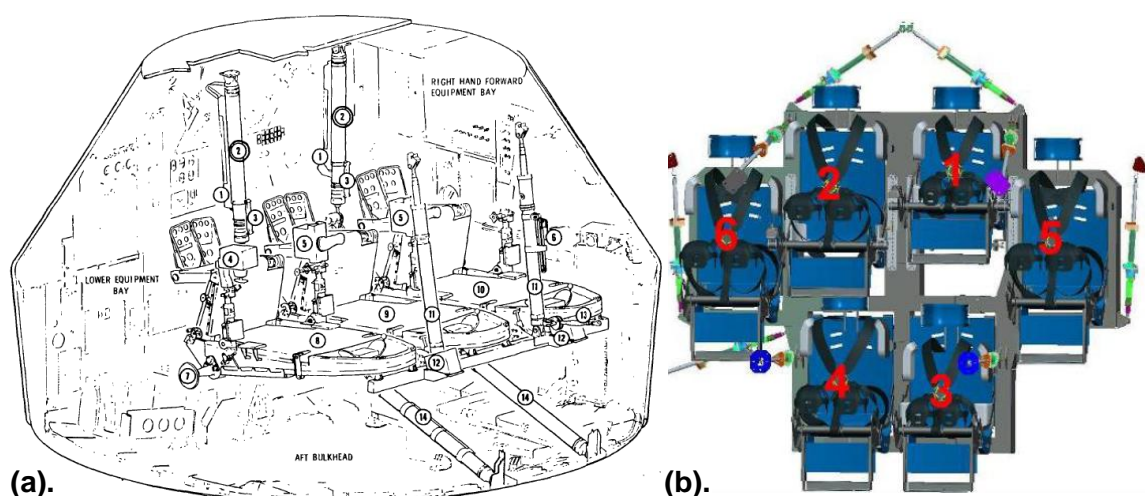


Figure 1-2: Comparison of Impact Attenuation Systems
 (a). Apollo [6] (b). Current Orion CEV Baseline [1]

During a workshop on innovative engineering conducted by the NESC in the summer of 2008, a team of academic and industry experts were tasked to develop ideas to address this issue. One such idea was the personal airbag system.

Inspired from the structure of seeds in nature, this concept involves using an inflated airbag “seat” to protect the occupant during landings of the Orion crew module. Just as seeds protect their embryos from mechanical loads by surrounding them with a layer of endosperm, this concept involves surrounding the astronaut in a personal cushion of air. When crew positioning requirements were factored, this concept evolved into the personal airbag system. This ideation process is shown in Figure 1-3.

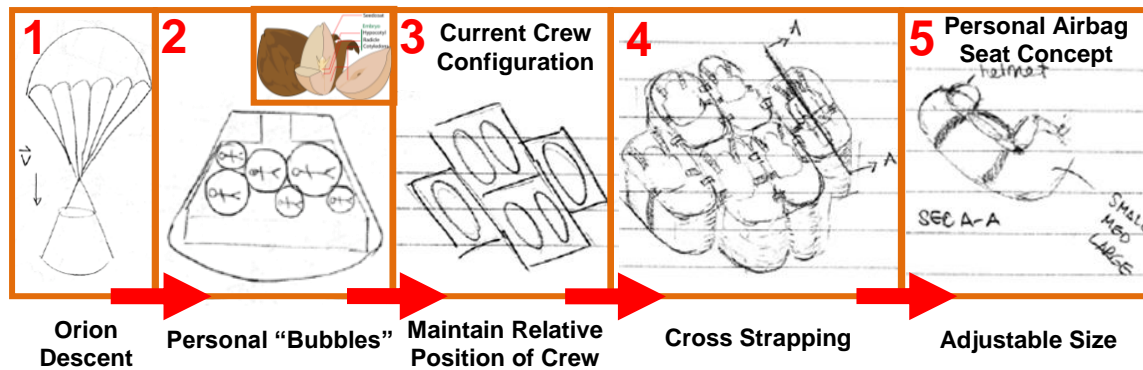


Figure 1-3: Original Sketches from NESC Academy Innovative Engineering Design Course July 28 - August 1 2008. Note that the Personal “Bubbles” concept in Cell 2 was inspired by the structure of seeds in nature

In addition to being inherently lightweight, this system has the advantage of being able to be deflated and stowed when not in use, thus providing additional in-cabin volume. Initial estimates have found that these savings equate to a potential 36% reduction in the CIAS mass without the crew, and an increase in 26% of in-orbit habitable volume [7]. From an operational point of view, this latter attribute is particularly beneficial when the spacecraft is in orbit and seats are no longer required. This is demonstrated in the initially defined system concept of operations, depicted in Figure 1-4.

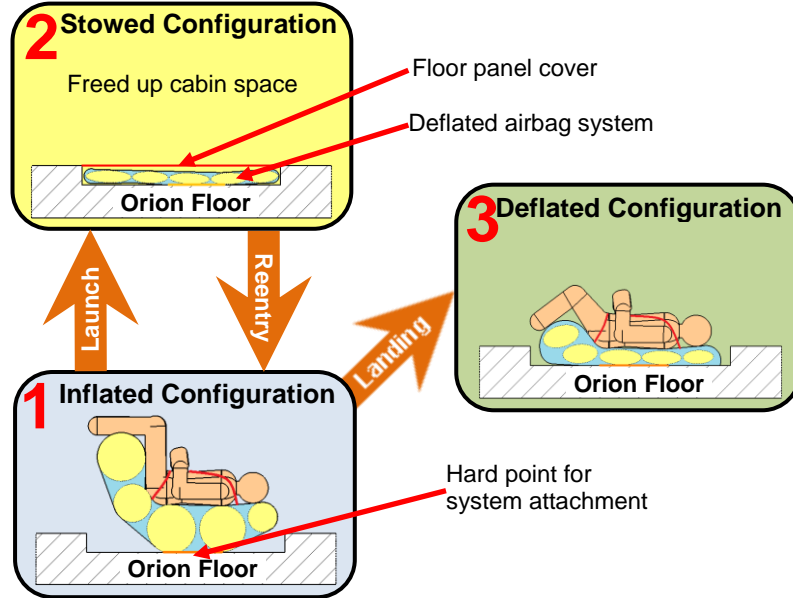


Figure 1-4: Initial System Concept of Operations consisting of the Inflated, Stowed, and Deflated Configurations. During pre-launch and launch, the system would be in the Inflated state to function as a seat to support the occupant. Once in space, the system would transition to the Stowed state to increase available cabin space. Prior to reentry, the system is then returned to its Inflated state in preparation for landing. Upon landing, the seat transitions to the Deflated state as it attenuates the impact loads subjected to the crew

Hence if this concept can be proven to protect astronauts to within a low-injury risk level during land-landings, it will not only simultaneously address both of Orion's mass and land-landing issues; but will also introduce the added benefit of increased on-orbit in-cabin volume through reconfigurability [8], thereby providing an elegant solution to a fifty year old problem. With the increasing development of commercial crew transfer vehicles, such a solution would be of significant interest as the desire for a lightweight land-landing capability continues to grow.

1.2 Objective and Approach

The objective of this thesis is:

To determine the feasibility of implementing an airbag-based crew impact attenuation system into the Orion Crew Exploration Vehicle

To meet this objective, this research aims to address the following key question derived from the requirements specified in the Constellation Program Human-System Integration Requirements (HSIR) document [9]:

Can an airbag-based system maintain an astronaut's injury-risk levels to within acceptable tolerances during a nominal land-landing?

This work addresses this question via the complete development and testing of an airbag-based crew impact attenuation system. Specifically, a three-level spiral model of system development is employed, whereby the complete development process from system conception through to its detailed design, implementation, and operation is cycled through three times; with each subsequent cycle using lessons learned from the previous to develop an improved next generation of the system.

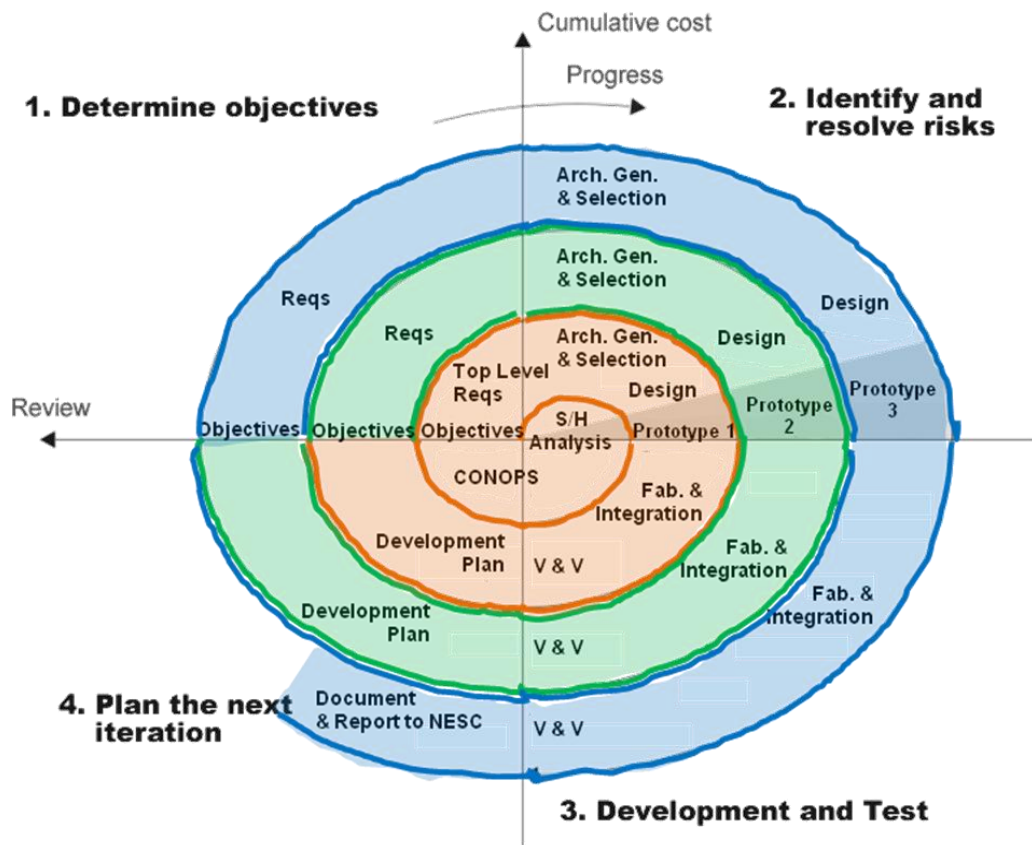


Figure 1-5: Three Level Spiral Model used for this Development Effort (Adapted from [10])

The choice of this development model is based on the revolutionary nature of this concept and the need to answer several fundamental questions prior to the commencement of any detailed design. These include:

- *How many airbags should a personal airbag system have? And what configuration should they be in?*
- *What manufacturing processes and materials are required to fabricate leak-tight, durable, and reusable airbags?*

To gain insight into these questions, each spiral of this development effort has been tailored to address a certain aspect of the problem. In particular, the first spiral focuses on developing and testing a complete analog airbag system in an attempt to gain experience in the fabrication and testing of this new concept. Here, an analog version of the system is selected as it facilitates a quick collection of experience and knowledge under relaxed design requirements. Moreover, testing is accomplished via a series of drop tests used to evaluate the impact attenuation effectiveness of the system.

The lessons learned from this initial effort are next used to develop and test a single airbag drop test article in a second development spiral. Here, the primary objective is to develop an understanding of the impact dynamics of a single airbag. Again, this is accomplished via a series of drop tests.

Using the experience and data gained from the first two development spirals, a full-scale multi-airbag impact attenuation system is then developed and subjected to a series of drop tests in the final spiral, thus allowing for the feasibility of the airbag-based crew impact attenuation system concept to be determined. Depending on this final result, the work in this thesis will act as the basis for the NESC to further develop and implement this system concept.

1.3 Thesis Outline

In order to present each of the major stages in the evolution of this work, the remainder of this thesis is organized as follows.

Chapter 2 provides a historical overview of airbag systems used in both terrestrial and space applications, as well as of previous attempts at implementing land-landing capabilities on capsule-shaped spacecraft. Through this, high level decisions on the personal airbag system architecture are made based on lessons learned from the development and operation of similar systems of the past.

Chapter 3 focuses on the modeling of the impact attenuation problem. Specifically the underlying physics governing airbag impact attenuation are first discussed, and the importance of the venting of gas from the system highlighted. Following this, an introduction to the Brinkley Index - the metric by which NASA measures injury-risk to humans during transient acceleration events, is provided. Also included in this chapter is a discussion of the techniques used to extract data from high speed camera footage of drop tests of the manufactured system. This data is subsequently used to resimulate these tests in a computational environment, thus allowing for further insight into the impact dynamics of the test article to be gained.

In Chapter 4, the development of the analog airbag system and the infrastructure required for drop testing is presented. The entire design process, from conceptual through to detailed design, is initially discussed. Subsequently, the details of the drop test campaign are presented, followed by a discussion and analysis of the test results.

Chapter 5 is focused on the development of a single airbag drop test article to investigate the dynamics of an impacting airbag. A design of experiments is first conducted in order to size the test article, as well as to gain insight into the sensitivity of the system performance to the various design variables involved. The results of this are then used as the basis for the subsequent discussion of the valve development activity, which took place as part of the implementation of this test article. Like in Chapter 4, the details of this second spiral test campaign are then presented, along with a discussion and analysis of the obtained results. Here, these results are used to validate the computational model presented in Chapter 3. This in turn allows for a subsequent detailed design space exploration to be conducted, providing valuable insight into the characteristics of the optimal airbag design.

Chapter 6 describes the final development spiral in this study. Specifically, a multi-airbag model is first presented, and used in conjunction with the insights gained in Chapter 5 to determine the final system configuration. This is accomplished via an optimization study which enables the effects of changing airbag configuration on impact attenuation capability to be quantified. With this configuration determined, the details of the final, multi-airbag

system test campaign are discussed, followed by an analysis of the obtained results. These results allow for concept feasibility to be determined by answering the key question elucidated in Section 1.2. In addition, the performance of the analog and the multi-airbag systems is also compared, revealing further insight into the physical mechanisms and key design variables governing overall system performance.

Finally, Chapter 7 concludes this work by summarizing the key findings of the previous chapters. Based on these findings, recommendations are made for the NESC's next steps in developing the airbag-based crew impact attenuation system concept.

Chapter 2

Literature Review

In this chapter, a summary of both past and present, space and terrestrial airbag system concepts is presented to provide the background required to guide high level architectural decisions on the personal airbag system. In addition, a historical overview of past attempts at implementing land-landing capabilities onboard manned capsule-shaped spacecraft is provided to gain insight into the operational context in which a personal airbag system may operate. Each of these categories of related work is discussed in the subsequent sections.

2.1 Terrestrial Airbag Systems

In general, there are three main areas in which airbag systems are implemented on terrestrial vehicles. These are:

- Within a garment worn by the occupant of a vehicle
- Within the seat in which the occupant sits; and
- Within the cabin in which the occupant operates the vehicle

The details of each of these system categories are further discussed in the following sections.

2.1.1 Garment-Based Airbag Systems

Historically, garment-based impact protection devices have been designed to provide protection to localized regions about the human body. Those incorporating airbags have found usage in a large variety of applications, ranging from protective sporting equipment, to providing a means of injury prevention for the elderly. Selected examples of such systems are presented below.

Xenith X1™ Football Helmet

First introduced to the market in the fall of 2007, the Xenith X1 football helmet incorporates eighteen hollow thermoplastic urethane shock absorbers between the inner and outer shells of the helmet [11]. As the helmet is subjected to an impact, the walls of the absorbers collapse, increasing the internal pressure, and forcing air to escape through a small hole. At the end of the impact, the shock absorbers return to their original shape due to the elasticity of the urethane material. This entire process acts to dissipate impact energy and prevent sudden motion of the head, which can lead to the onset of concussion.



Figure 2-1: Xenith X1™ Football Helmet [12]

Dainese D-Air Racing Suit

Designed to provide additional protection to the shoulder and neck regions of the body during motorcycle accidents, the Dainese D-Air Racing Suit consists of an airbag integrated within a motorcycle suit. The system makes use of a processor which senses a rider being thrown off their motorcycle via a GPS receiver and a combination of accelerometers [13]. When an impending fall is detected, the processor triggers an in-built hybrid gas generator, which inflates an airbag around the neck and shoulders of the rider. Because this entire process occurs within 40 milliseconds, the airbag system is fully inflated prior to the rider impacting the ground.



Figure 2-2: Marco Simonelli falls off his motorcycle during the 2007 Valencia Grand Prix. This was the first ever deployment of the Dainese D-Air Racing suit during competition [13]

Mugen Denko Hit-Air Shock Buffering System

Like the Dainese D-Air, the Hit-Air Shock Buffering System is a motorcycle jacket with an in-built airbag system. Rather than using a processor to actuate a gas generator, the Hit-Air utilizes a mechanical pull-pin to trigger a CO₂ gas cartridge located within the jacket. As the rider falls off their motorcycle, a cable connecting the jacket to the vehicle pulls the pull-pin, causing the gas cartridge to inflate a tubular airbag wrapped around the neck, chest, back, and hip of the rider [14]. In addition to motorcycle jackets, the Hit-Air has also been marketed for horse-riding applications, where the impact conditions experienced by the rider are similar.

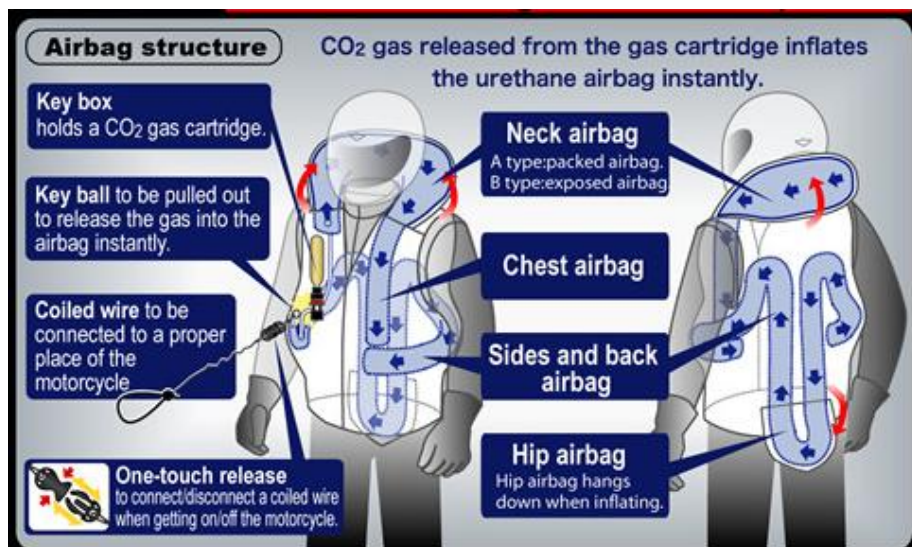


Figure 2-3: Mugen Denko marketing image explaining the functionality of the Hit-Air Shock Buffering System [14]

NIIS and Prop Co. Itsumo (Always) Safety Life Jacket

Aside from sporting applications, suit-based airbag systems have also found use in the workplace. One such application is in personal protective equipment in the construction site. To protect construction workers from the effects of falling from altitude, the NIIS and Prop Company in Japan have developed the Itsumo (Always) Safety Jacket. Contrasting to the previously discussed motorcycle jackets, the Itsumo system can be fitted within a relatively compact construction vest, due to its relaxed requirement of only protecting against back-first falls. During a fall, a series of accelerometers within the vest detects the corresponding dynamic conditions and sends a signal to trigger a CO₂ gas cartridge, also located inside the vest. This in turn inflates a tubular airbag around the neck, spine, and waist, cushioning the wearer from the impending impact.



Figure 2-4: The Itsumo Safety Life Jacket [15]

This same design concept has also formed the basis of other wearable-airbag products developed by the NIIS and Prop Company. These include the Kiruair (wearable airbag), an airbag-vest intended for use by elderly people with epilepsy who are susceptible to sudden and dangerous falls; and the Piabaggu, an airbag system designed to protect the wheelchair bound during falls. These are shown in Figure 2-5.



Figure 2-5: Suit-Based Airbag Systems marketed by the NIIS and Prop Company of Japan
 (a). Pre- and post-inflation of the Kiruair [14]
 (b). The Piabaggu system in its inflated state [15]

2.1.2 Seat-Based Airbag Systems

Seat-based airbag concepts refer to those which consist of airbags being either installed onto, or acting as a seat. Traditionally, these systems have been designed for recreational use, and hence have been optimized primarily for comfort. Even though this is the case, some guidance and inspiration for the conceptual design of a personal airbag system can still be acquired. Notable examples of such concepts are presented in the following sections.

Inflatable Seats

One of the first patents filed for an airbag seat type system was made in 1987 by Diane Hull [16]. Intended as a floatation device for use in recreational purposes, this concept consists of two stacked annular shaped airbag chambers connected to an inflatable back rest and seat cushion. In addition, each chamber is independently inflated prior to use, allowing for the entire system to remain afloat in the case that one is ruptured. This concept is shown in Figure 2-6.

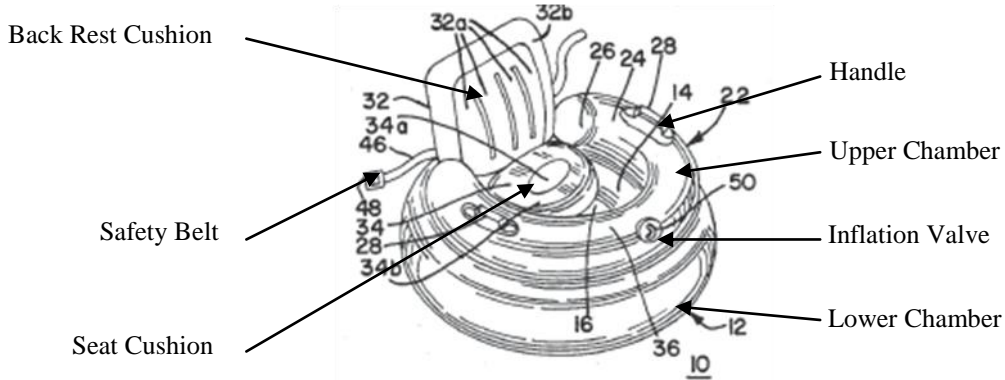


Figure 2-6: Inflatable Seat Concept [16]

Although intended for a different purpose, this multi-chamber concept is applicable to a personal airbag system in that there is a level of redundancy built into the concept. This is particularly important during the execution of the life-critical function that is the attenuation of landing loads. Furthermore, the fact that the annular shape of the airbags is designed to maintain buoyant stability is also of interest. This is because such an attribute can be related to system stability under varying impact angles, which can in turn equate to an improvement in the overall robustness of the system.

Inflatable Seat Cushions

This is a variant of the inflatable seat concept, where inflatable components are installed on a standard, rigid seat. Generally, these concepts have found use in aircraft, automobiles, and trucks, where long duration back and neck support, as well as vibration mitigation are desirable. Displayed below are two selected inflatable cushion-based concepts:

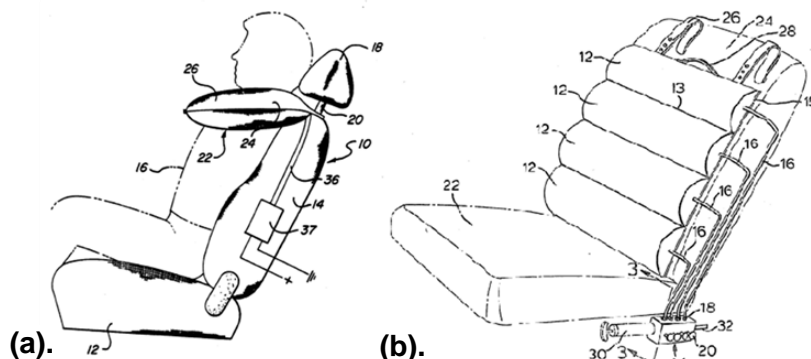


Figure 2-7: Inflatable Seat Cushions (a). Seat Integrated Inflatable Neck Support [17] (b). Inflatable Seat Cushion and Body Support Assembly [18]

Here, it can be seen that these cushion-based concepts are inherently easy to implement onto existing seating systems, hence providing potential retrofitting capabilities onto existing system designs. Additionally, the neck and head support provided by the concept depicted in Figure 2-7(a) facilitates protection against rapid head and neck movements, one of the areas in which people are most fatally susceptible to during impacts. Furthermore, the separated inflatable chambers in the concept shown in Figure 2-7(b) also allows for customized support of the occupant's back by varying the pressure distribution across the chambers. This also contributes to improving ergonomic aspects of the system, namely occupant comfort.

Seatbelt Mounted Airbags

Seatbelt mounted airbags involve the implementation of airbags within seatbelts worn by the occupant of a vehicle. They have gained popularity in recent times, especially in general and commercial aviation applications, due to a more stringent requirement for seat strength released by the Federal Aviation Administration in late 2009 [19]. Specifically, seatbelt mounted airbags provided an elegant design solution to protecting passengers sitting behind rigid bulkheads during aircraft accidents, where it was not possible to install any other form of impact attenuation device [20]. An example of this is shown below in Figure 2-8.

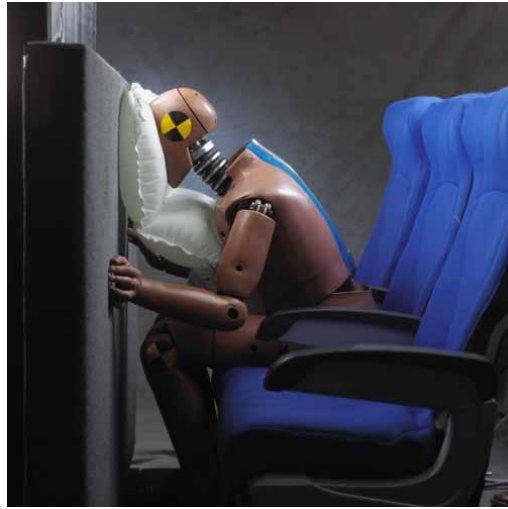


Figure 2-8: Amsafe Commercial Aviation Seatbelt Airbag [21]

Like the airbag concepts described in Section 2.1.1, seatbelt mounted airbags are triggered to inflate by a series of sensors which sense the conditions governing an

impending impact. As the airbags inflate, they fill in the space between the passenger and the aircraft bulkhead, thereby providing a means of cushioning the impact between the passenger's head and the aircraft.

In addition to aircraft, seatbelt based airbag systems have also been implemented in road vehicles. A prime example is the Inflatabelt, a product developed and marketed by BAE Systems under their Vehicle Safety Products group [22]. Instead of cushioning against impacts with a hard surface, Inflatabelts act to restrain the motion of the occupant's torso, particularly in the forward and lateral directions. Moreover, relative restraint between the torso and upper thighs is further provided to prevent straining of the lower back. Figure 2-9 displays some of the Inflatabelt concepts developed by BAE:

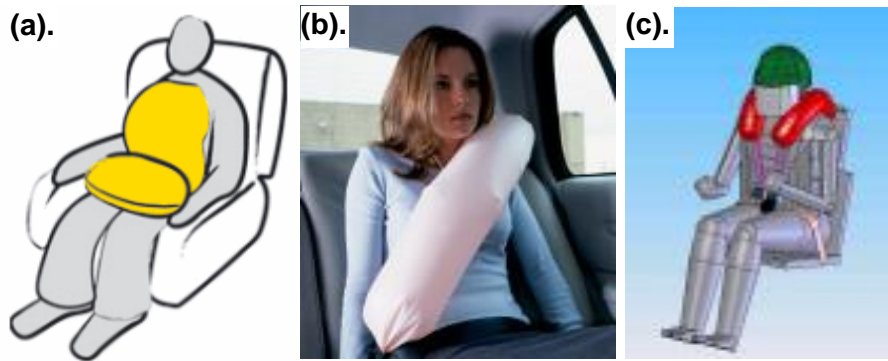


Figure 2-9: Inflatabelt Concepts developed by BAE Systems [22] (a) Original Inflatabelt Concept (b) The SMART-Belt (c). The SMART 4

2.1.3 Cabin-Based Airbag Systems

Ever since the early 1990's, when the implementation of airbags into automobiles became widespread, cabin-based airbag systems have become by far the most commonly recognized form of airbag implementation. In addition to being installed internal to a cabin, airbag systems have also been implemented to the exterior of the cabin of a vehicle. Both of these concepts will be further discussed in the following sections.

In-Cabin Airbag Systems

In the 1970s, as the driving population began to proliferate, the need for automotive safety became increasingly apparent. In response to this, car manufacturers began to first implement airbags within the steering wheel of their vehicles to protect the heads of passengers from

heavy impacts during accidents. Since then, the value of this innovation in saving lives has become increasingly recognized, inspiring its widespread use throughout other areas of the car interior. Notable examples of such regions include the side and windows, as can be seen in Figure 2-10.



Figure 2-10: Airbag system in a 2007 Model Honda Accord automobile consisting of steering wheel mounted, side, and side curtain airbags [23]

In addition to automotive applications, airbags have also gained popularity in other terrestrial vehicles, with well-known examples being within the cabin of helicopters and motorcycles.

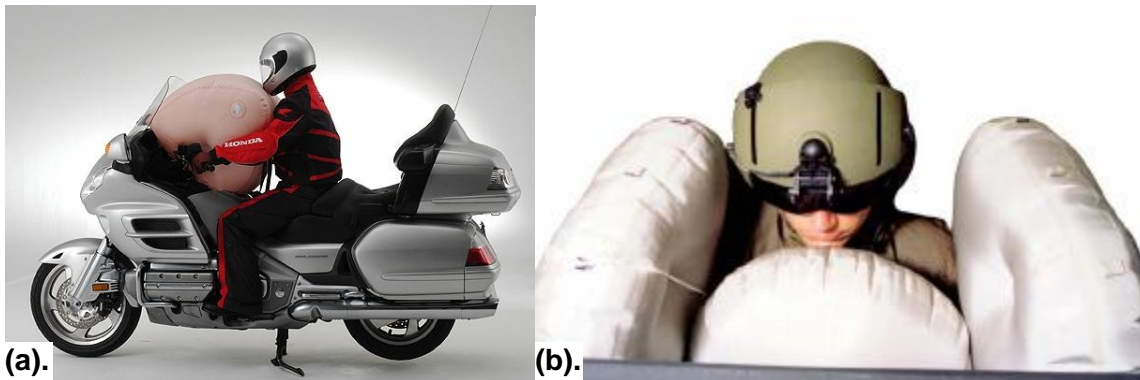


Figure 2-11: Airbag Applications in Terrestrial Vehicles (a). The Honda Gold Wing Motorcycle Airbag System [24] (b). The BAE Systems Cockpit Airbag System, now implemented on all U.S. Army UH-60A/L Black Hawk and OH-58D Kiowa Warrior helicopters [25]

In all of these applications, the underlying technologies employed have been virtually the same. As the vehicle is subjected to an impact, a network of sensors located throughout the vehicle sends data to a central control unit, which then commands a gas generator to inflate an airbag. Basic versions of this sensor suite include accelerometers, gyroscopes, and seat occupancy sensors; while more advanced automotive multi-airbag systems include impact sensors, wheel speed sensors, brake pressure sensors, and door pressure sensors. These more advanced sensor suites act to ensure that the appropriate combination of airbags is inflated, according to the location and severity of the impact [24-26].

Out-of-Cabin Airbag Systems

Contrasting to their in-cabin counterparts, out-of-cabin airbag systems have seldom seen use in terrestrial vehicles. Part of this is because scenarios in which such a system would be ideally suited to, are uncommon in terrestrial vehicles. One example of such a scenario is the cushioning of falling objects, such as aircraft crew escape capsules, from the impact loads incurred during an emergency escape or landing.

The most notable example of such an implementation is within the crew escape module of the F-111 fighter aircraft, as seen in Figure 2-12.

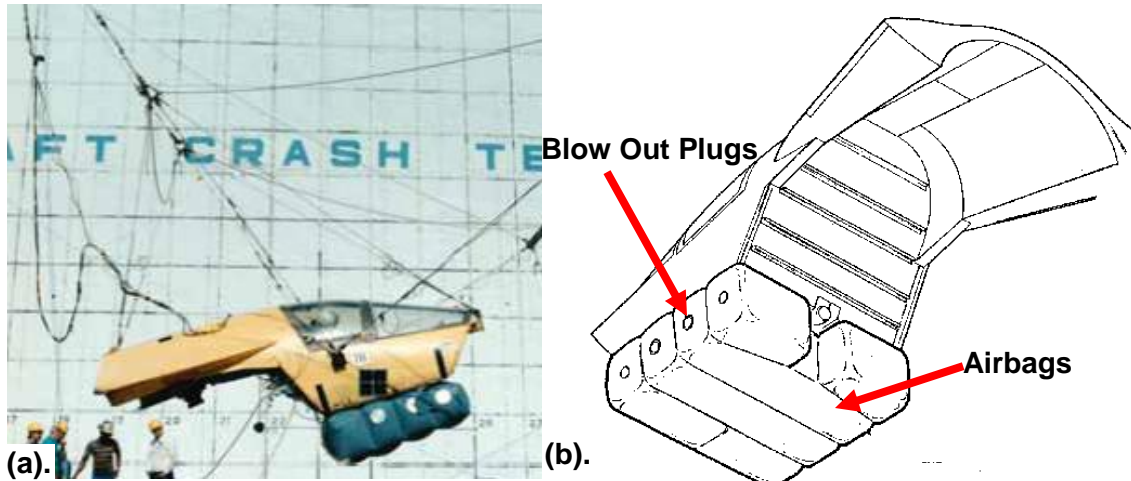


Figure 2-12: F-111 Crew Escape Module Airbags (a). Drop Testing at NASA Langley Research Center [27] (b). Detail of Airbag Configuration [28]

During an emergency ejection scenario, a series of charges is triggered around the escape module to separate it from the aircraft fuselage. Shortly after, a small rocket motor in the

compartment is activated to separate the capsule from the falling aircraft. Once the capsule is clear from the aircraft, a parachute is deployed, triggering a switch to commence the inflation of an airbag located on the underside of the capsule. Constructed of neoprene coated nylon cloth, this airbag consists of several interconnected chambers inflated by compressed nitrogen bottles stowed within the escape capsule. During impact, blowout plugs located on the side of the airbag are released, venting gas and reducing the shock loads on the module to within allowable limits.

More recently, airbags have been implemented into the undercarriage of helicopters to limit impact loads to the crew and damage to the airframe during crashes. Like those of the F-111 escape module, these airbags also release gas through vents during impact to facilitate improved load attenuation. The degree to which these vents release gas is dependent on the surface being impacted upon, as determined by the frequency content of the returning signal emitted from a proximity sensor. During water landings, the vents are commanded to remain closed, thus providing floatation for the cabin, in addition to impact attenuation [29]. Figure 2-13 shows some examples of out-of-cabin airbag systems used in helicopter applications.

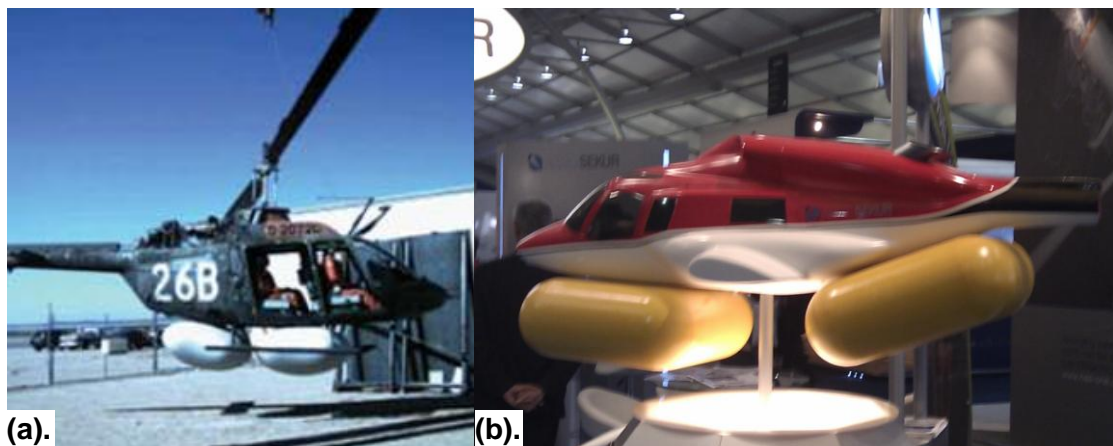


Figure 2-13: Helicopter Out-of-Cabin Airbag Systems (a). The Rafael Rotorcraft External Airbag Protection System (REAPS) undergoing a drop test [30] (b). The Aero Sekur Hard-Landing Helicopter Inflation System Concept displayed at the 2010 Farnborough Airshow [29]

2.1.4 Summary of Relevant Terrestrial Airbag System Concepts

In reviewing the various terrestrial airbag system concepts several lessons can be learned which can influence high level architectural decisions in the design of a personal airbag

system. A common concept which has appeared consistently thus far is the use of active systems. That is, those which employ sensors to trigger the rapid inflation of a set of airbags via a gas canister or a gas generator. In all of these cases, the airbags are fully inflated within 30-80 milliseconds from the moment of actuation, allowing for the system to be fully deployed prior to impact. The need for this rapid inflation arises from the uncertain nature of the impacting event, which is especially so in terrestrial settings, such as vehicular accidents and accidental falls by construction workers and the elderly. Conversely, in the spacecraft landing scenario, the time of an imminent landing is typically known beforehand. Because of this, a personal airbag system can be inflated well in advance of landing, thus negating the need for a complex inflation system.

Another observation made from this review is the importance of providing comfort and support to the occupant's back and neck. This was especially highlighted by the seat-based airbag concepts. In these systems, back support was provided by incorporating a multi-chambered airbag system which conformed to the occupant's back. In addition, neck support, as was also provided by all reviewed suit-based airbag concepts, was facilitated by a pressurized airbag situated around the neck and shoulders. The fact that this was a ubiquitous attribute highlights the importance of including a means to limit the relative motion between the head, neck, and shoulder in the design of a personal airbag system. This is especially important as this relative motion is a primary cause of fatal head and neck injuries during impact events [31].

Furthermore, upon review of the out-of-cabin airbag system concepts, explicit inclusion of venting was also observed. As will be discussed in Section 3.1.1, venting of gas from the airbag aids in improving impact attenuation performance by effectively removing energy from the system. This is particularly critical when the mass of the object is large, as is the case with the 3000lb escape module and the helicopter out-of-cabin systems presented.

Hence in summary, the following observations, relevant to the conceptual design of a personal airbag system, were made in the review of past and present terrestrial airbag systems:

- Actively actuated airbag systems are not necessary when the time of impact is known well in advance
- It is important to limit relative motion between the head, neck, and shoulders during an impact as this is a primary cause of fatal injuries

- Comfort is an important factor when designing a seat, especially when the occupant is expected to sit within it for long periods of time. One characteristic of a comfortable seat is its conformance to the occupant's back; and
- The inclusion of venting mechanisms within an airbag aids in its ability to attenuate impact loads

2.2 Spacecraft Airbag Systems

It is interesting to note that airbags have been consistently considered as viable options for landing attenuation systems in spacecraft since the start of the U.S. and Soviet space programs, when the need for safely returning a vehicle from space first became apparent. More recently, the European Space Agency has also commenced the development of airbag-based landing technique for use in its missions. This section presents the details of these spacecraft airbag systems in an attempt to gain more insight into the design of a personal airbag system.

2.2.1 Project Mercury

In response to the rapid development of Soviet technological capability in space, Project Mercury was initiated in 1959 as NASA's first human spaceflight program. A key feature of the landing system of the Mercury spacecraft was the inclusion of a passive airbag installed in a skirt between the heat shield and the capsule. As the capsule traveled through the atmosphere prior to impact, the heat shield would be separated and air would be drawn through holes in the skirt. This air would then fill the airbag, which upon impact would be forced back out through the same holes in which it entered; in a venting process similar to that discussed in Section 2.1.3 [4]. Figure 2-14 shows this airbag deployment sequence.

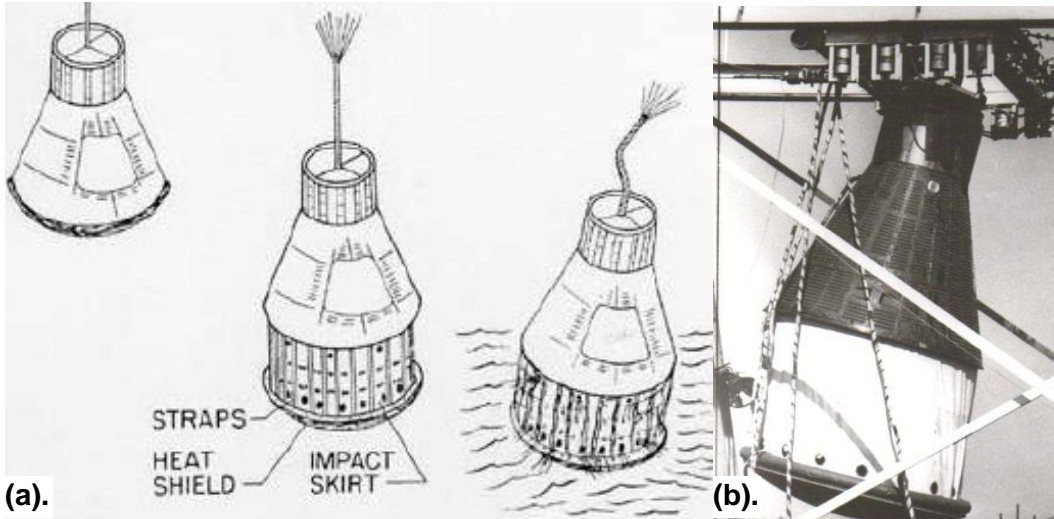


Figure 2-14: Mercury Landing Airbag System (a). Deployment Sequence [4] (b). Detail of Landing Airbag Post-Landing [32]

2.2.2 Luna 9 and 13

Airbags were also prominent in the early days of Soviet space exploration, with the Luna 9 lunar lander, in February 1966, using airbags to achieve the first ever soft landing of a human-made vehicle on an extraterrestrial planetary body. This system involved completely enveloping the spacecraft in a protective airbag layer at an altitude of 75km above the landing site, 48 seconds before impact. While the airbags were being inflated during this landing sequence, retrorockets were fired to slow the vehicle's velocity from 2.6km/s to 6.1m/s [33]. At an altitude of 5m, contact sensors were activated, commanding the descent engine to shut down and the landing capsule to be ejected. Upon initial contact with the lunar surface, the nitrogen gas inside the airbag compressed and expanded, causing the entire system to experience several bounces before finally coming to rest [34]. Figure 2-15 shows this entire landing sequence.

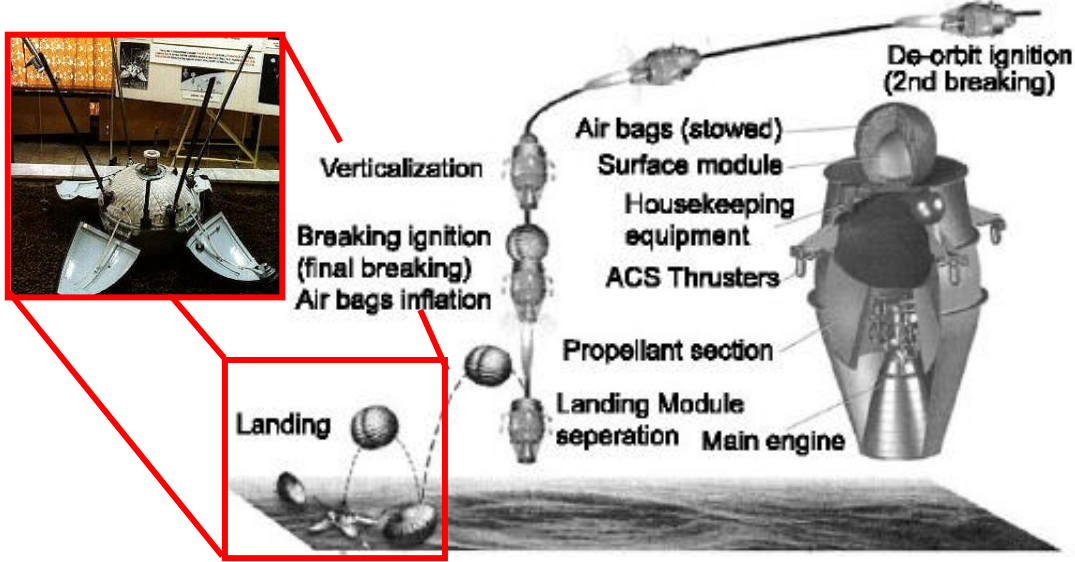


Figure 2-15: Luna 9 and 13 Landing Sequence [35] (Inset: Model of the Luna 9 lander on display at the NPO Lavochkin Museum [36])

Following the success of Luna 9, the Luna 13 follow-up mission was launched in December of the same year, carrying a larger suite of scientific instruments. Three days after launch, the vehicle also achieved a soft-landing on the lunar surface using the same landing sequence and airbag system as that of its predecessor [37].

2.2.3 Mars Pathfinder and Mars Exploration Rover

As part of NASA’s “Faster, Better, Cheaper” approach to the scientific exploration of space in the mid to late 1990s, the concept of using airbags was chosen as a low-cost alternative to previously employed techniques for landing a rover on the Martian surface [38].

Similar to the Luna spacecraft, the Mars Pathfinder used a series of airbags to protect it from the impact loads incurred during landing. Here, four interconnected multi-layered airbags surrounded the lander in a tetrahedral shape. During the landing sequence, at an altitude of 355m above the ground and at a velocity of 68m/s, the airbags were inflated via three catalytically cooled solid rocket motors [39]. Soon after, retrorockets from the overhanging aeroshell were fired such that the velocity of the lander was zero at an altitude of between 15 and 25m – a dynamic range appropriate for the airbag system to adequately protect the lander during impact. Once this dynamic state was achieved, the bridle supporting the lander from the aeroshell was severed, dropping the lander from its current altitude.

Following this, in the same manner as the Luna 9 and 13; the airbag-covered lander impacted and bounced off of the ground approximately 15 times before coming to a final rest. This landing sequence is summarized below in Figure 2-16.

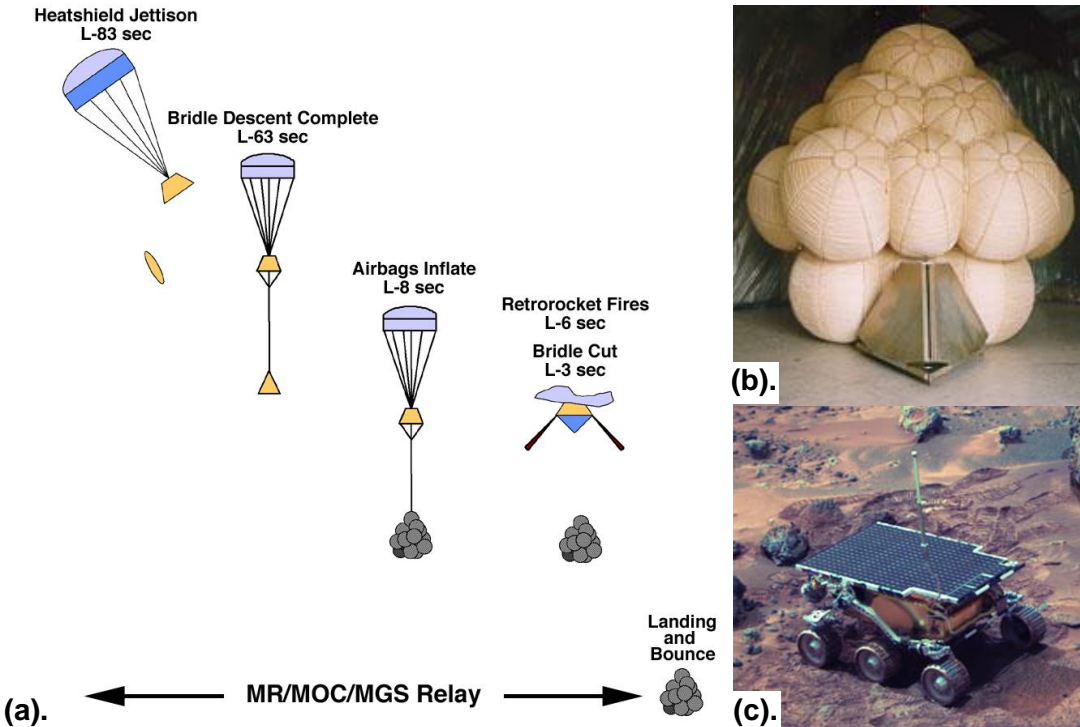


Figure 2-16: Mars Pathfinder Mission (a). Entry Descent & Landing Sequence [40] (b). Landing Airbag System Detail [41] (c). The Sojourner Rover deployed after landing [42]

Having successfully protected its payload from the loads incurred during landing, this same airbag concept was employed on the subsequent twin Mars Exploration Rovers, which both successfully landed on the Martian surface in January 2004.

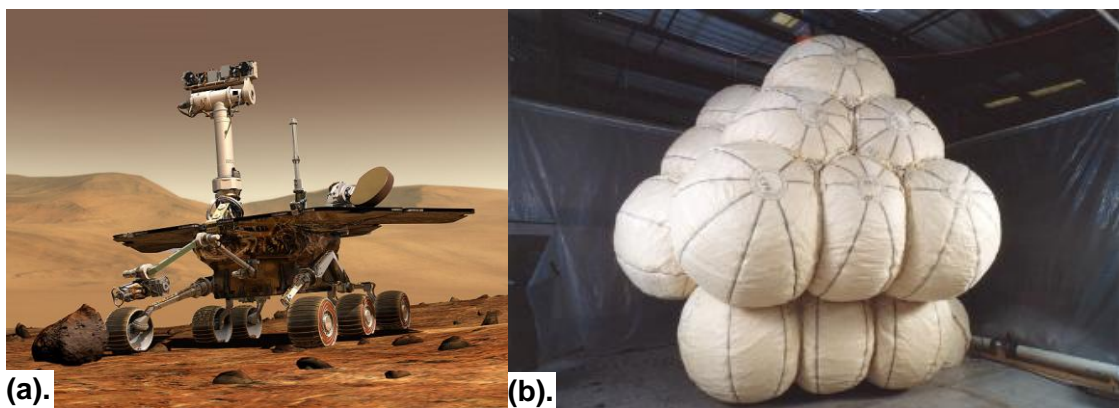


Figure 2-17: Mars Exploration Rover Mission (a). Rover [43] (b). Airbag Landing System [44]

2.2.4 Orion Crew Exploration Vehicle

It is interesting to note that following the NESC's original recommendation that the Orion CEV adopt a primary land-landing mode, external airbags were baselined for the vehicle's landing attenuation system. This system consisted of a ring of six cylindrical airbags located in a circular pattern between the base of the Orion crew module and its heatshield. Contrasting to the airbag concepts previously employed by NASA, this system employed pyrotechnically actuated vents to facilitate a "stuck" landing, where the system would come to rest shortly after impact without bouncing. An additional feature of this system is that it incorporated a "bag within a bag approach" [45], whereby an anti-bottoming bag was placed within an external vented airbag to prevent direct contact between the module and the ground. This phenomenon is typically referred to as "bottoming-out" and can result in significant increases in impact acceleration.

During a nominal landing sequence, the system was intended to be deployed after heat shield jettison, approximately 40 seconds prior to impact. Upon contact with the ground, pressure transducers would trigger pyrotechnic cutters to open the vents within the airbags, once a predefined pressure threshold was exceeded. This would enable gas to escape the airbags, thereby enabling a "stuck" landing. This sequence is summarized in Figure 2-18.

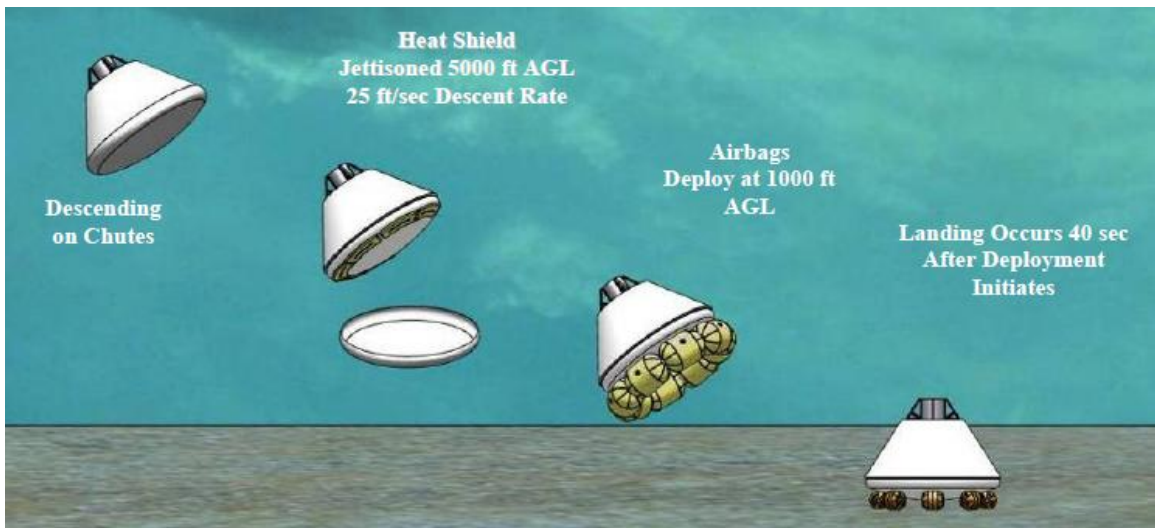


Figure 2-18: Orion CEV Nominal Landing Sequence with External Airbags [46]

To evaluate this concept, a full-scale drop test campaign was performed at NASA Langley Research Center (LaRC) in mid 2008. The results of this campaign indicated that the external airbag system was indeed capable of facilitating land landings under nominal

conditions [45]. However, by this time, the decision had already been made to revert to a nominal water landing mode due to continuing mass constraints. As a consequence external airbags were removed from the baseline Orion landing system design, in favor of lighter, crushable structures.

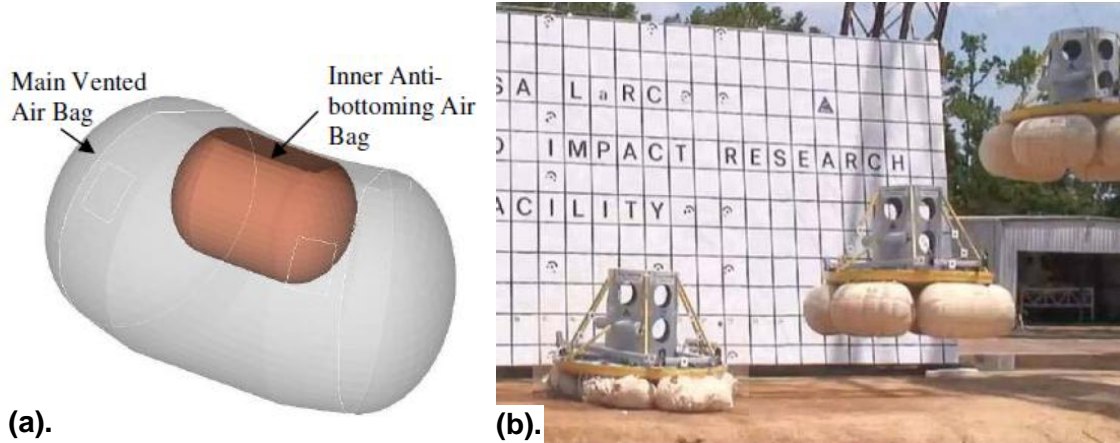


Figure 2-19: Orion External Airbag System (a). Detail of the “Bag within a bag approach” [45] (b). Drop Testing at NASA LaRC [1]

2.2.5 ExoMars

Currently under development, ExoMars is a robotic mission to Mars led by the European Space Agency, anticipated for launch between 2016 and 2018. The primary payload of this mission is the ExoMars rover, a wheeled robotic vehicle designed to perform in-situ science on the Martian surface.

Unlike the “bouncy-ball” landing technique employed by NASA’s rovers, ExoMars will use a vented airbag system to protect it in a manner similar to that of the original Orion landing system. Here, a multi-compartment toroidal shaped airbag would be inflated with nitrogen gas shortly after lander separation from the aeroshell. Upon impact, the system would use an accelerometer actuated pyrotechnic cutter system, similar to that of Orion’s original external airbags, to open vents within each of the six airbag compartments. This would in turn result in a “stuck” landing, from which the rover would unfurl and commence its ground operations. This concept of operations is depicted below, in Figure 2-20.

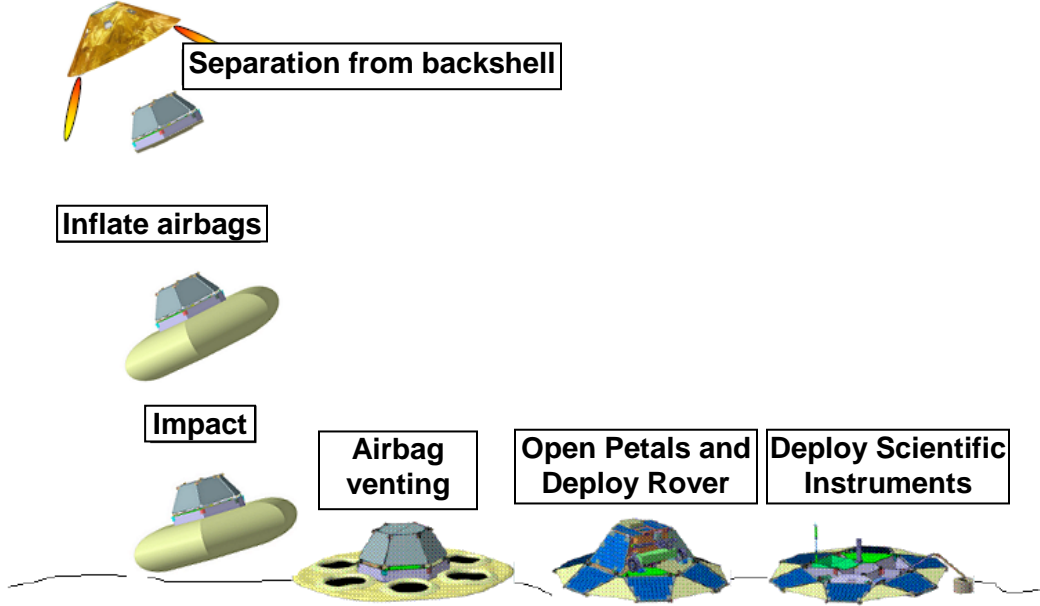


Figure 2-20: ExoMars Landing Sequence [47]

It is interesting to note that unlike the Orion external airbag system, the baseline ExoMars airbag system does not incorporate anti-bottoming bags



Figure 2-21: Drop testing of a prototype of the ExoMars airbag system [48]

2.2.6 Summary of Relevant Spacecraft Airbag System Concepts

In the review of airbag system concepts used in space applications, two overarching categories of airbag systems have been identified, being those which are vented, and those which are unvented. The choice of whether or not to implement venting directly impacts on the dynamics of the landing event, with unvented systems leading to a “bouncy ball” type

landing, while vented systems result in a “stuck” type landing. As will be seen in Section 3.1.1, this effect is due to the energy conversions taking place in each process.

Of these two categories, it is evident that vented airbag systems are more appropriate for implementation into the cabin of a spacecraft. This is emphasized by the increased risk to injury associated with additional bounces beyond the first moment of contact. Additionally, the fact that the landing attitude is controlled and known before impact, allows for airbag placement to be optimized, thus yielding an overall lighter weight system.

Furthermore, in all of the vented airbag systems reviewed thus far, only actively controlled architectures have been employed. These have typically involved using accelerometer or pressure transducer data to actuate a pyrotechnic cutter to open a vent within an airbag. While standard for implementation outside of the cabin of a vehicle, incorporating pyrotechnic devices in a personal airbag seat in which the occupant is sitting on is clearly unsafe, especially when the system is situated within a pressurized cabin.

Hence from this, it appears that one of the key challenges in developing a practical airbag-based crew impact attenuation system is determining a method to vent gas without the use of pyrotechnics. Moreover, because the impending landing event is known beforehand, it would be preferable to avoid any form of active actuation, as was mentioned earlier in Section 2.1.4. This implies that the ideal venting mechanism for the system being developed is one which is purely mechanical in nature.

2.3 Human Spaceflight Impact Attenuation Systems

With the exception of NASA’s space shuttle program, all human spaceflight programs conducted since the dawn of the space age have required a means of protecting humans from the impact loads experienced upon landing. This section reviews the techniques which have been utilized in past programs in an attempt to gain insight into the design process and operating environment, as well as inspiration for the conceptual design of an airbag-based crew impact attenuation system. Here, each program will be discussed in chronological order, based on the time at which the first launch of the vehicle occurred.

2.3.1 Vostok

In order to become the first nation to launch a person into space under the demanding pressures of the Cold War, the Soviet Union adopted a minimalist approach to their first

manned spacecraft, Vostok. A prime example of this approach was the spacecraft's landing system. Rather than returning the spacecraft to the Earth's surface with the cosmonaut still inside, the Soviets opted to eject the cosmonaut from the vehicle during the landing sequence, thereby combining the nominal and contingency landing modes into a single system [49]. Specifically, this involved the cosmonaut sitting in an emergency ejection seat throughout the entire flight. During the landing sequence, approximately 7km above the Earth's surface, a hatch would be blown off the descent module. Two seconds later, two solid-propellant rockets attached to the pilot's seat were triggered, ejecting the cosmonaut and the seat together. At an altitude of 4km, the cosmonaut separated from the seat by deploying a parachute. This parachute would then guide the cosmonaut to an approximate 5m/s land-landing in the Saratov region [50, 51]. Figure 2-22 summarizes this landing profile.

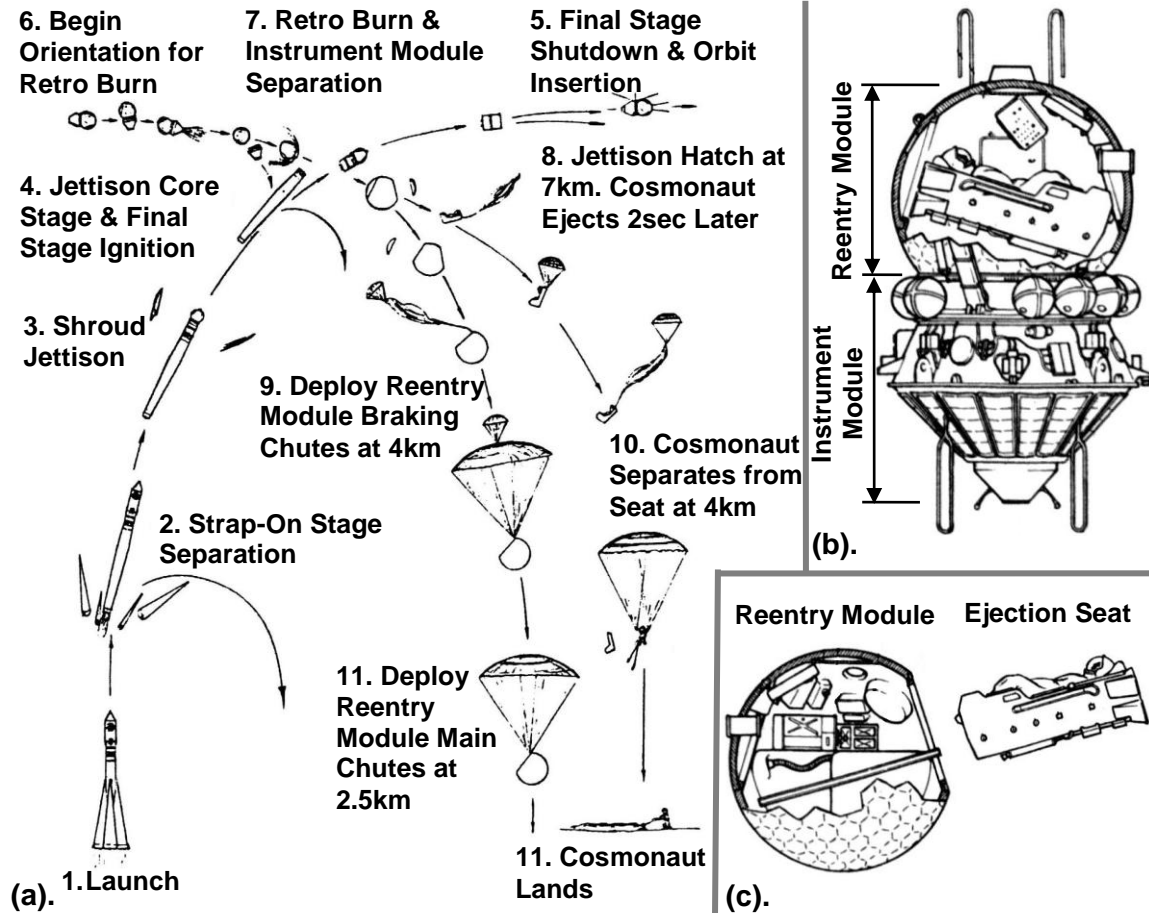


Figure 2-22: Vostok Mission (a). Mission Profile (Image adapted from [51]) (b). Detail of Vostok Vehicle [50] (c). Detail of Seat Ejection [50]

As can be seen from Figure 2-22(c), a key feature of the Vostok seat system was that it was oriented in a semi-reclined position, 65° to the horizontal [51]. This acted to minimize the acceleration loads on the cosmonaut during launch, as well as ensured the correct orientation during ejection from the descent module.

2.3.2 Project Mercury

In addition to the airbag system discussed in Section 2.2.1, a significant effort was made early in Project Mercury to develop a lightweight system which could minimize the level of sustained acceleration experienced by the astronaut during launch and reentry. This was motivated by concerns of increased strain on bodily organs during sustained acceleration events which could cause potentially fatal injuries.

To address this issue, a series of centrifuge tests were conducted in the mid to late 1950s to quantify the limits of acceleration tolerance in humans. A key finding of this was that when the occupant was positioned such that the acceleration loads were applied backward and transversely to their center of rotation, breathing became easier. Furthermore, it was found that when the occupant sat in a contoured couch subjected to the aforementioned acceleration conditions, they were able to tolerate higher levels of sustained acceleration due to the improved distribution of loads across the body. These findings led to the final Mercury couch design consisting of a fiberglass couch contoured to fit the dimensions of a particular occupant lying in a semi-supine position [52].



Figure 2-23: A technician works on the Mercury couch (Inset: An early design sketch of the couch liner with the occupant positioned in a semi-supine position) [52]

When combined with the landing airbag, the spacecraft was capable of protecting the astronaut from all transient and sustained acceleration conditions expected to occur throughout a mission.

2.3.3 Voskhod and Soyuz

In the push to continually be the first to achieve the major milestones of human spaceflight at the height of the Cold War, the Soviet Union abruptly began the Voskhod program in the spring of 1963. Primarily, Voskhod's design consisted of modifying already fabricated Vostok descent modules such that they were capable of carrying a three person crew into orbit. Because Vostok was originally designed for one occupant, significant spacing constraints were imposed on the configuration of the cabin [50].

One means to address this constraint was to omit the ejection seats and spacesuits from the vehicle's design. Instead, the three cosmonauts sat in a pressurized cabin, in shock absorbing "Elbrus" couches dressed in regular clothes. Like those of Project Mercury, these couches consisted of liners which conformed to the occupant to improve their acceleration tolerance. In addition, these couches incorporated a shock absorber system which aided in attenuating impact loads during landing [51]. Prior to landing, the shock absorber would be extended to its maximum position, thereby pivoting the couch upwards into its cocked position [53]. As the spacecraft approached impact, a 1.18m contact probe would be pressed, triggering the ignition of a solid-propellant braking rocket. This rocket acted to slow the impact velocity from between 8 and 9.75m/s, to 0.15m/s. As the vehicle impacted the ground, the seat shock absorber would compress, attenuating the force of impact and allowing for a soft land-landing [54].

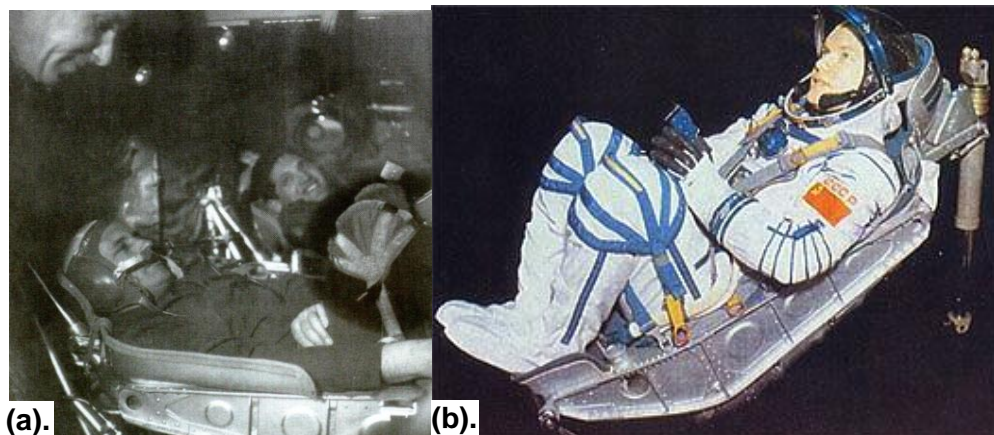


Figure 2-24: Soviet Shock Absorbing Seats (a). The backup Voskhod 1 crew training in their Elbrus couches [50] (b). A cosmonaut sitting in a Kazbek seat used in all Soyuz vehicles [54]. Note the shock absorber at the end of the seat towards the head

Having successfully facilitated soft land-landings on the two Voskhod missions, this same landing mode was employed on the later Soyuz spacecraft. Here, a modified version of the couch, named the Kazbek seat, was implemented. The design of this couch was much the same as that of the Elbrus, with the additional feature that the personalized liner could be removed and replaced, thus allowing for different people to use the spacecraft. To this very day, all expedition members onboard the International Space Station are required to have a personalized Kazbek seat liner made. This is because the Soyuz vehicle is currently the only means of emergency escape from the orbital outpost.

2.3.4 Project Gemini

Following the success of the Mercury program, Project Gemini was officially approved in December 1961 with the goal of demonstrating the capabilities necessary for a future manned lunar exploration campaign. One such capability was the ability to land on land. This would allow for efficient refurbishment of the vehicle for additional flights, thus reducing the operational costs of the program. After detailed development and testing of descent and landing concepts, a final decision was made to revert back to a nominal water-landing mode due to heavy schedule pressure. Of the investigated concepts, the furthest developed included one employing a paraglider with landing gear, and another using a parasail combined with landing rockets.

Ultimately, the Gemini spacecraft's primary form of impact attenuation came from controlling its impact attitude under a ring-sail parachute, rather than from the use of a landing airbag. This in turn resulted in a reduction in the relative mass of the spacecraft's landing system by removing the need for an additional system. Here, the parachute was configured such that the reentry module hung at a 35° angle to the horizontal, allowing the spacecraft to impact the water at the edge of its heat shield. This resulted in reduced landing loads to the crew when compared to the Mercury system, due to the reduced initial contact area between the spacecraft and the water surface [4].

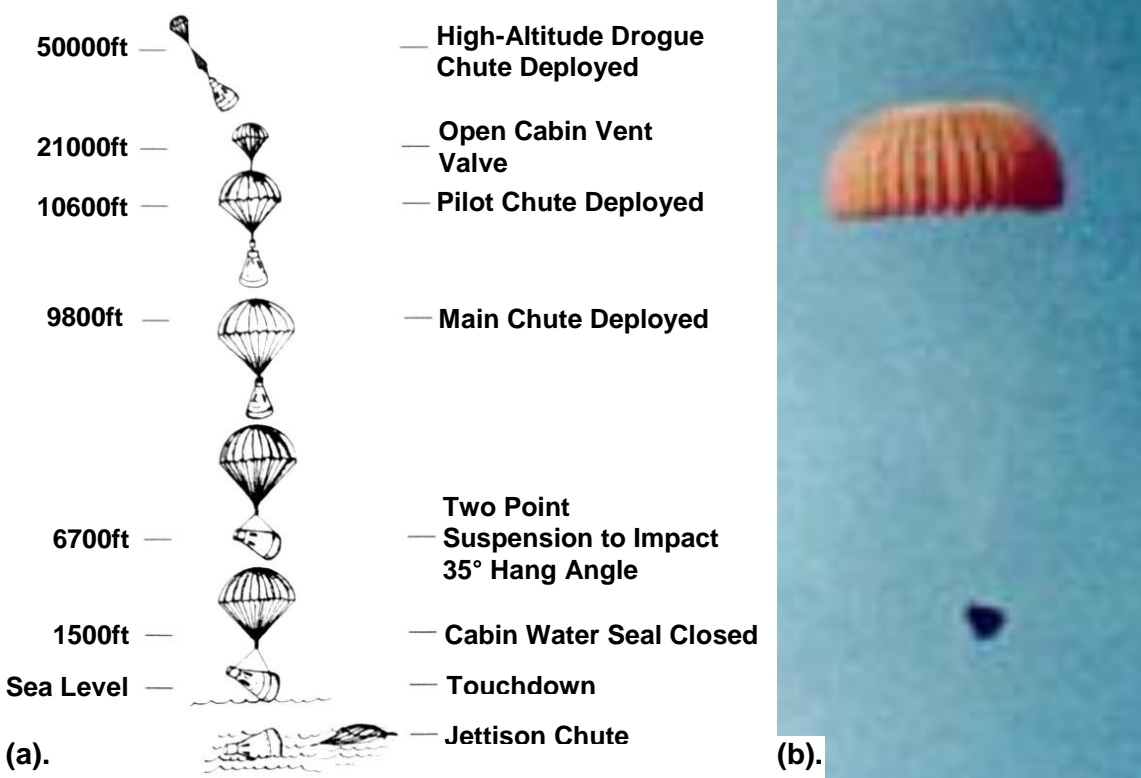


Figure 2-25: Gemini Descent and Landing (a). Landing Sequence [55] (b). Gemini 12 at 35 ° Hang Angle during Descent [56]

Additionally, Vostok style ejection seats were used as the acceleration loads imposed during launch and reentry were found to be low enough such that body-conforming couches were not required. These ejection seats also doubled as a form of escape from the spacecraft during contingency launch and landing events.

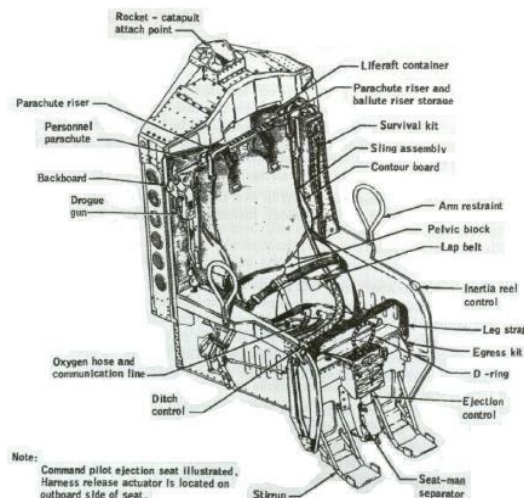


Figure 2-26: Ejection Seats used in the Gemini spacecraft [54]

2.3.5 Apollo

As was mentioned earlier in Section 1.1, the Apollo Crew Module centered its impact attenuation capability on a couch supported by shock absorbing struts. This was introduced as a result of the significant mass increase in the Apollo Crew Module compared to previously flown spacecraft, where it was recognized that the use of parachutes and a favorable hang angle alone, were not enough to prevent injury to the astronauts. This mass increase also resulted in a system which constantly struggled to meet the limits imposed by the launch vehicle – a constraint which dictated the ultimate landing mode and system configuration.

Like the Gemini program, Apollo was initially planned to employ a nominal land-landing, using a combination of parachutes and a strut-supported crew couch. After a preliminary set of drop tests however, it was found that this newly implemented couch did not have enough stroke to prevent accelerations to the crew from exceeding safe limits during landings on land. Contrastingly, when drop tests were performed on water, adequate impact attenuation was achieved, but significant water leakage into the crew module occurred, causing it to sink within minutes of impact. This prompted structural modifications to be made to the vehicle, which resulted in added mass to the system, and an additional impact attenuation requirement for this added mass. To resolve this issue, a crushable structure was implemented into the region anticipated to come into first contact with the landing surface under nominal conditions. This would provide some additional cushioning, whilst minimizing the impact on the already strained system mass budget. Figure 2-27 shows the landing system configuration used for all Apollo missions, while Figure 2-28 shows a more detailed view of the Apollo crew couch.

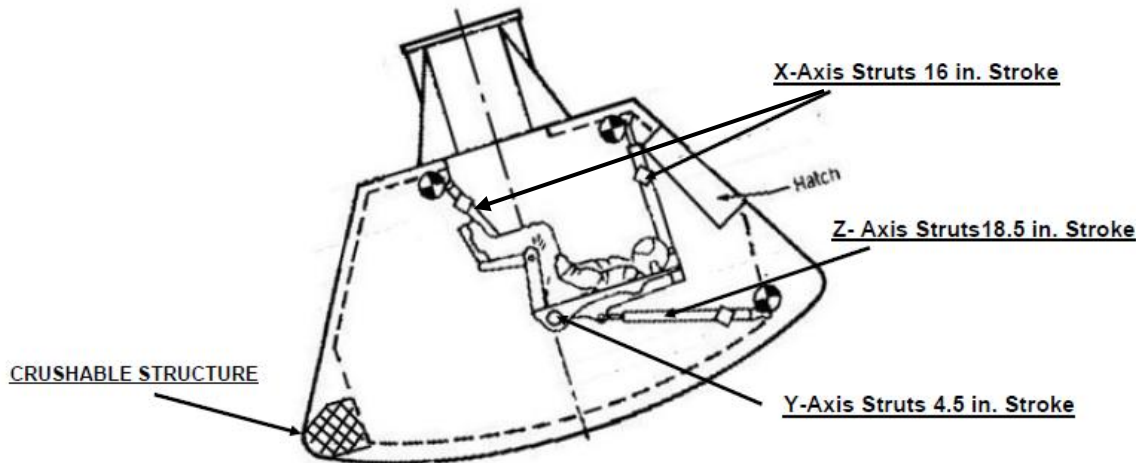


Figure 2-27: Apollo Couch Impact Attenuation System Configuration [32]

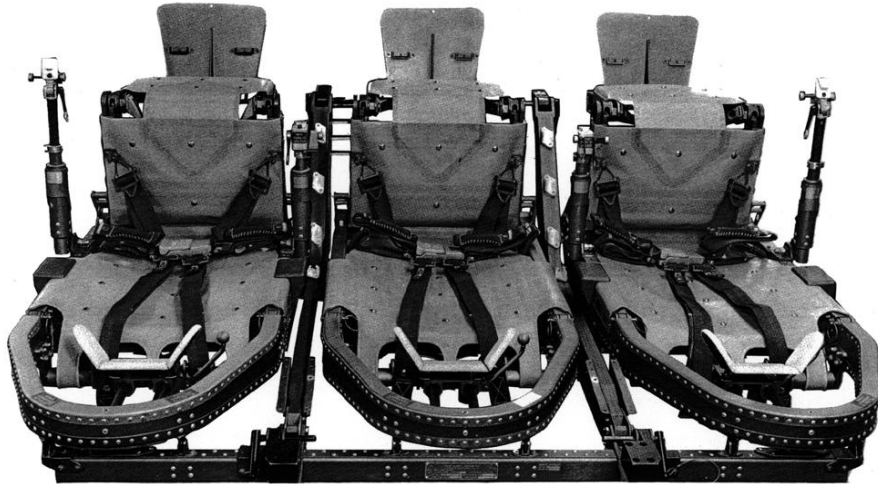


Figure 2-28: Detail of Apollo Crew Couch [57]

As can be seen in Figure 2-27, the Apollo crew couch consisted of three seats connected together by a common pallet structure, which in turn was connected to the spacecraft by eight shock-absorbing struts. A standard liner was employed across all three seats, rather than the personally molded type used onboard the Mercury spacecraft. Like Gemini, this was a result of the more benign sustained acceleration loads subjected to the crew during launch and reentry of the vehicle.

However, even with these more favorable sustained loads, and the implementation of the crew couch and crushable structure, the impact experienced during landing was still much higher than expected. In an interview, Frank Borman, Commander of Apollo 8 mentioned [58]:

“The one item that we were perhaps not expecting was the impact at touchdown... There was a severe jolt and we got water in through the cabin repress valves even though they were closed. A good deal of water came in the cabin pressure relief valve”

Similarly, when asked about landing in a separate interview, Buzz Aldrin of Apollo 11 noted [58]:

“It was a lot harder than I expected... I was standing by with my fingers quite close to the circuit breaker. The checklist fell, and the pen or pencil... dropped. It didn’t seem as though there was any way of keeping your fingers on the circuit breakers”

Moreover, during the Apollo 12 landing, the impact was so severe, that a camera mounted above Alan Bean disconnected from its bracket and hit him on the head, rendering him momentarily unconscious. Pete Conrad, commander of the mission recalls [58]:

“We really hit flatter than a pancake, and it was a tremendous impact. Much greater than anything I’d experienced in Gemini. The 16mm camera... whistled off and clanked Al on the head to the tune of six stitches... He was out to lunch for about 5 seconds...I was convinced he was dead over there in the right seat, but he wasn’t”

These high impact loads, coupled with the known fact that it was almost certain that the crew would be severely injured during a Contingency Land Landing; led to the NESC recommendation described in Section 1.1 – that a different method of impact attenuation be explored for the Orion CEV.

2.3.6 Summary of Relevant Features of Past Human Spacecraft Impact Attenuation Systems

Across all of the previously developed spacecraft, one characteristic has remained ubiquitous in the design of the landing and impact attenuation system, being the semi-supine posture in which the occupant has been positioned. As was discussed in Section 2.3.2, this posture facilitates improved tolerance to sustained acceleration environments when compared to other positions. This is due to the more even distribution of loads and blood supply across the body.

To support the occupant in this position, both customized and standard liners have been used in past spacecraft seats. The choice of this liner has been dictated by the sustained acceleration loads subjected to the crew during launch, which is dependent on the launch

vehicle and its flight path. Moreover, a four or five point harness has typically been used to support the occupant within the seat. As of late 2008, the baseline Orion seat consisted of a standard seat liner combined with a five-point harness [1].

In addition, the effect of the impact angle of the spacecraft on the acceleration loads experienced by the astronaut has also been observed. As was discussed in Section 2.3.4, an oblique impact angle facilitates a softer water landing due to the lower initial contact area. During land-landings however, analysis by the NESC has found that flatter impact angles are preferred, as this aids in the prevention of tumbling of the spacecraft, which can in turn induce further injury to the crew [4].

Finally, this review has revealed a fundamental trend in impact attenuation systems amongst all capsule-shaped spacecraft; being that as the mass of the spacecraft grows, providing impact attenuation to the crew becomes increasingly difficult. This can be seen in the difficulties in the development of the Apollo impact attenuation system when compared to that of Mercury and Gemini, as well as the fact that similar difficulties are currently being experienced in the development of the Orion CEV. From a physics standpoint, this can be explained by the fact that greater masses result in a larger amount of energy required to be attenuated upon impact.

Hence, from the aforementioned observations, it can be concluded that the personal airbag system should be designed such that it positions the astronaut in a semi-supine position. This consequently constrains the configuration and placement of the airbags about the system. In addition, a five-point harness will be used to support the occupant within the seat. This is based on the successful use of this method on several previous spacecraft designs, as well as the fact that it is currently baselined for the Orion CEV.

Furthermore, with regard to system validation, drop tests will be performed at impact angles of both 0 and 30 degrees. This arises from the NESC finding that flatter impact angles are preferable for land-landings [4] and the fact that Orion is currently planned for a nominal 30° impact angle, similar to that of the Gemini and Apollo spacecraft. Consequently, this will provide insight into the difference in performance of the personal airbag system at varying impact angles.

2.4 Chapter Summary

Throughout this chapter, a review of past and present airbag systems designed for both terrestrial and space applications has been performed, in an attempt to obtain inspiration for the baseline concept for the personal airbag system. Moreover, an overview of previously operated spacecraft impact attenuation systems was also conducted to gain insight into the basic requirements of the astronaut when operating in the spacecraft environment. From this study, the following high level architectural decisions have been made to guide the detailed design of the system:

1. The personal airbag system shall be configured such that it supports the occupant in a semi-supine posture
2. The airbags shall employ a “stuck” type landing mode using passively actuated vents
3. Either a four- or five- point harness shall be used to support the occupant in the personal airbag system
4. Provisions shall be implemented to limit the relative motion between the head, neck, and shoulders during an impact as this is a primary cause of fatal injuries
5. A liner shall be implemented to facilitate better load distribution across the body while also acting as a provision for occupant comfort; and
6. System validation shall be performed at both 0 and 30 degree impact angles

When compared to the previously reviewed airbag concepts, it can be seen that this preliminary definition results in a system which does not require high speed computational processing to perform time critical events. This was intentionally implemented into the system definition, as there was a desire to develop a system with minimal complexity. This leads to a more elegant architecture, which has improved reliability due to the reduced number of failure modes arising from the lower number of components and component interactions. This can be seen in Table 2.1, which lists the attributes of all of the airbag concepts reviewed. Here, those concepts which require real-time processing are highlighted in orange, while those which achieve the listed attribute via a mechanical means are highlighted in green. Note that this is only applicable to functions which can be time-critical, such as inflation, and venting.

Table 2.1: Summary of Reviewed Airbag System Concepts

Attribute	Terrestrial Airbag Systems				Spacecraft Airbag Systems			
	Suit-based	Seat-based ¹	In-Cabin ²	Out-of-Cabin	Project Mercury	Bouncy-Ball Landing	Stuck Landing	Personal Airbag System
Time of Inflation	Upon impact	Before impact	Upon impact	Before impact	Before impact	Before impact	Before impact	Before impact
Vented airbag?	No	No	No	Yes	Yes	No	Yes	Yes
Method of venting	N/A	N/A	N/A	Pyro-cutter	Passive flow	N/A	Pyro-cutter	Mech. valve
Body position	Semi-supine	Upright	Upright	Upright	Semi-supine	N/A	Semi-supine	Semi-supine
Head / neck / shoulder support?	Yes	No	Yes	N/A	Yes	N/A	Yes	Yes

¹Does not include seatbelt-mounted airbag systems

²Includes seatbelt-mounted airbag systems

In addition to the preliminary system definition, this principle of minimizing system complexity will also be used to guide the detailed design of the personal airbag system, as described in later chapters of this work.

Chapter 3

The Impact Attenuation Problem

In this chapter, a framework for modeling and evaluating the performance of an airbag-based impact attenuation system is established. This framework consists of two primary components which interact with each other to provide a quantitative measure of impact attenuation capability. In particular, this involves firstly executing an airbag system dynamics model, and then inputting the obtained results into the Brinkley Direct Response Index model – the NASA mandated human injury-risk model to be used on all Constellation program vehicles [9]. Each of these components, as well as a technique called photogrammetry; will be discussed in the following sections. Commonly used to analyze impact events, this latter method will form the basis for the analysis of the drop test results obtained at the end of each spiral of the system development.

3.1 Airbag Impact Dynamics Modeling

Fundamentally, airbags attenuate impact loads on objects through a series of energy conversion processes. During a “stuck” landing mode, the kinetic energy of an impacting object is transferred into the internal energy of the gas within the airbag. When predetermined conditions are met, vents within the airbag open, releasing the gas into the open environment and thereby removing this energy from the system. Although seemingly simple, detailed analysis of this elegant process involves bringing together principles from a number of disciplines, including thermodynamics, fluid mechanics, and structural dynamics. As will be seen in the following sections, analysis from the point of view of each of these fields allows for insight to be gained into the various aspects of the problem.

3.1.1 Thermodynamic Analysis

Consider a system being dropped vertically from a fixed height onto a rigid surface, consisting of a solid mass supported underneath by a gas-filled airbag with an in-built vent, as shown in Figure 3-1 below:

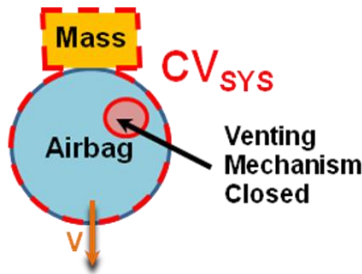


Figure 3-1: Initial Condition for Thermodynamic Analysis

Throughout the duration of this process, the system experiences three main dynamic phases, each of which having a unique thermodynamic state. These phases include:

- Freefall
- Compression of the airbag after contact with the ground surface; and
- Venting of the airbag, assumed here to commence at the moment at which the airbag has attained its maximum compression

In the following sections, a thermodynamic analysis at each of these states is performed to gain insight into the relevant design variables and their interaction with each other. It should be noted that even though the entire process is inherently transient, the state of the system at the end of each major phase will be assumed to be in quasi-equilibrium. That is, the properties of the system are uniform across the system at each of these phases. This results in a simplified analysis which highlights the key characteristics of this process.

From Freefall to First Contact of the System with the Ground Surface

During the period prior to initial contact with the ground surface, the system is closed and isolated. That is, the energy content of the system stays constant, and no work is done on the system. It should be noted here that the system is defined by the control volume indicated in Figure 3-1. The energy content (E) is a result of the combination of the kinetic (KE) and potential energy (PE) of the mass and the gas within the airbag, along with the internal energy (U) of the gas within the airbag. This can be represented mathematically as follows:

$$E_{SYS} = \underbrace{PE_{MASS} + KE_{MASS}}_{\text{Mass}} + \underbrace{PE_{GAS} + KE_{GAS} + U_{GAS}}_{\text{Gas in Airbag}} \quad (3.1)$$

Note here that the contributions to the system energy by the airbag itself are neglected here as they are insignificant to those of the mass and the gas within in the airbag. Furthermore, the internal energy of the mass is also ignored as it is negligible compared to the other energy contributions to the system.

Now, for the purpose of gauging the relative magnitude between the quantities listed in Equation 3.1, let values for the system parameters comparable to those expected for a personal airbag system be assumed. These are listed as follows, in Table 3.1.

Table 3.1: Values Assumed for the Thermodynamic Analysis

Parameter	Quantity	Rationale
Mass	77.4kg	Equivalent mass of a 50 th percentile male aviator [59]
Impact velocity	7.62m/s (25fps)	Corresponds to the nominal impact velocity of the Orion CEV [46, 60, 61]
Airbag		
Operating Medium	Atmospheric air	Most likely to be accepted as the operating medium for airbags located within the spacecraft cabin environment
Operating Temperature	20°C (293K)	Equivalent to room temperature. This is a reasonable approximation to the expected temperature within a spacecraft cabin environment
Initial pressure	130kPa	Inflation pressure of a candidate design for the original external airbag system for the Orion CEV [62]
Volume	$\approx 1\text{m}^3$	Equates to a $\phi 1.13\text{m} \times 1\text{m}$ cylinder - a reasonable first estimate for an airbag designed to support a human body
Thermodynamic Properties of Operating Medium		
Internal Energy	210.49kJ/kg	Ideal gas property of air at 295K [63]
Enthalpy	295.17kJ/kg	Ideal gas property of air at 295K [63]
Specific gas constant	0.2869kJ/kg/K	Standard value for air [63]

With these values, the energy contribution of each component of the system can now be calculated via the following standard relationships for kinetic and potential energy.

$$KE = \frac{1}{2} m \vec{V} \cdot \vec{V} \quad (3.2)$$

$$PE = mgh \quad (3.3)$$

Where m is mass of the contributing component to the system, h is the altitude of the system, \vec{V} is the vertical velocity, and g is the gravitational acceleration.

Since the operating medium is assumed here to behave as an ideal gas, the Ideal Gas Law can be used to determine the mass of air within the airbag. This is given by:

$$PV = mRT \quad (3.4)$$

Where P is the pressure, V is the volume, m is the equivalent mass of the gas, R is the specific gas constant, and T is the operating temperature.

Substituting the values listed in Table 3.1 into Equation 3.4 and solving for the mass yields a value of 1.55kg. Similarly, substituting this value with those in Table 3.1 into Equations 3.1 to 3.3 yields the following value for the system energy at the first point of contact between the system and the ground surface:

$$\begin{aligned} E_{SYS} &= \overbrace{PE_{MASS} + KE_{MASS}}^{\text{Mass}} + \overbrace{PE_{GAS} + KE_{GAS} + U_{GAS}}^{\text{Gas in Airbag}} \\ &= (77.4 \text{ kg})(7.62 \text{ m/s})^2 / 2 + (1.55 \text{ kg}) \left\{ (7.62 \text{ m/s})^2 / 2 + (210.49 \times 10^3 \text{ J/kg}) \right\} \\ &= \overbrace{2.25 \text{ kJ}}^{KE_{MASS}} + \overbrace{0.045 \text{ kJ}}^{KE_{GAS}} + \overbrace{326 \text{ kJ}}^{U_{GAS}} \\ &= 328.3 \text{ kJ} \end{aligned} \quad (3.5)$$

Here, it can be seen that the internal energy of the airbag gas has by far the most significant energy contribution to the system. This indicates that by removing this 1.55kg of gas from the system during impact, most of its energy will be attenuated. Moreover, the fact that this process only requires a small amount of mass is especially beneficial for the highly mass-constrained Orion CEV program. An additional insight gathered in this basic analysis is

the insignificant contribution of the kinetic energy of the operating medium to the overall system energy. As a consequence, it will be ignored from here on.

From Initial Contact with the Ground to Maximum Airbag Compression

Now, consider the system operating over the period between initial contact with the ground surface, and the time at which the airbag reaches its maximum compression, as shown below in Figure 3-2.

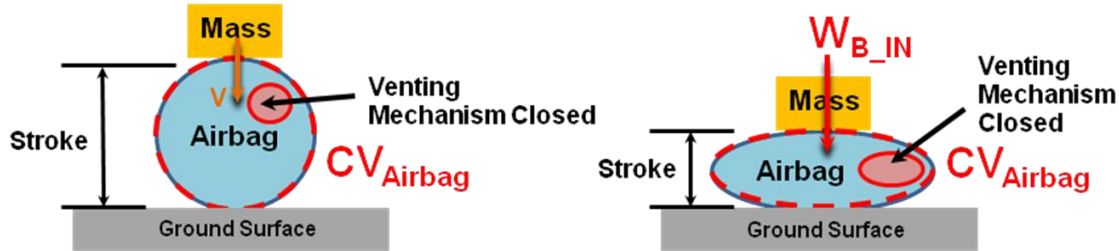


Figure 3-2: System State Transition between Initial Contact with the Ground and Maximum Airbag Compression

During this phase, the mass does boundary work on the airbag as its weight acts to compress the airbag. Consequently, only a thermodynamic analysis of the gas within the airbag is required. As can be seen by the corresponding control volume indicated in Figure 3-2, the system remains closed but is no longer isolated, due to the work being done on it. This process can be represented quantitatively using the First Law of Thermodynamics, which states that energy must be conserved. That is:

$$E_{IN} - E_{OUT} = \Delta E_{GAS} \quad (3.6)$$

For the case here, this process is assumed to be adiabatic. As a result of this, along with the fact that no work is being done by the internal gas, there is no energy leaving the control volume. That is, $E_{OUT} = 0$. Hence the energy content of the gas within the airbag can be expressed as:

$$W_B = U_2 - U_1 \quad (3.7)$$

Where W_B denotes the boundary work being done on the operating medium, and the subscripts 1 and 2 denote respectively the period of initial contact between the airbag and the ground surface, and the time at which the airbag reaches its maximum compression. The energy content of the system at this latter period can be observed by simply rearranging Equation 3.7.

$$U_2 = U_1 + W_B \quad (3.8)$$

In effect, Equation 3.8 states that during the compression phase of the airbag, the kinetic energy of the mass is being transferred into the internal energy of the operating medium via the means of boundary work. The amount of kinetic energy transferred is equal to the magnitude of the boundary work, which is defined as the integral of the system pressure (P) over its changing volume (V). That is:

$$W_B = \int_1^2 P dV \quad (3.9)$$

A dependence on pressure and volume implies that boundary work, and hence the efficiency of the energy transfer between the mass and the gas within the airbag, is directly related to the change in the geometry of the airbag as it compresses. For the case here, this will be further characterized in Section 3.1.2.

Since the geometric time history of the compressing airbag is currently unknown, it will be assumed that the energy transfer process is completely efficient for this sample calculation. That is, the boundary work at state two equals to the kinetic energy of the mass at state one. Hence, based on this, the energy content of the operating medium at the moment at which the airbag has attained its maximum compression is equal to the energy of the original combined mass and airbag system. That is:

$$\begin{aligned} U_2 &= U_1 + KE_{MASS} \\ &= 328.3kJ \end{aligned} \quad (3.10)$$

From Airbag Venting to Rest

Finally, the thermodynamic processes involved during the venting phase of the system impacting event will be considered. Here, it is assumed that the vents built into the airbag are opened immediately after it has reached its maximum compression. At this point, the system becomes one which is open, as mass is allowed to cross the boundary of the control volume. This is illustrated below in Figure 3-3.

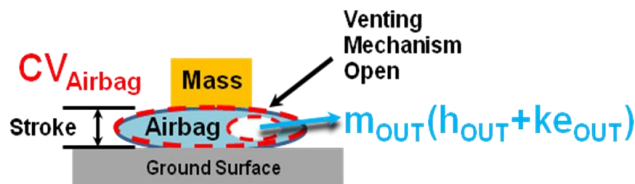


Figure 3-3: System during the Venting Phase

As was performed in the previous analysis, the energy content of the system will be determined by employing the First Law of Thermodynamics (Equation 3.6). To simplify the analysis, it will be assumed that boundary work is no longer being done on the operating medium during this phase. As a consequence, $E_{IN} = 0$, and the energy content of the system by the time it comes to rest can be represented by:

$$-m_{OUT}(h_{OUT} + ke_{OUT}) = U_3 - U_2 \quad (3.11)$$

Where h denotes the specific enthalpy, ke denotes the specific kinetic energy, and the subscript 3 denotes the state of the system being at rest. Here, the kinetic energy of the gas exiting the system is included as its velocity is likely to be comparable to the speed of sound, resulting in a considerable contribution to the energy of the outflowing gas. Again, the energy content of the system after this process can be expressed by rearranging Equation 3.11 as follows:

$$U_3 = U_2 - m_{OUT}(h_{OUT} + ke_{OUT}) \quad (3.12)$$

Here, it can be seen that the final energy of the content of the system is equal to its energy prior to venting, minus the energy content removed by the kinetic energy and enthalpy of the vented gas. Note here that the internal energy and flow work component of this outflowing gas is captured by this enthalpy term.

Ideally, this system would have zero energy at the end of the venting stage, signifying a complete attenuation of the impact energy. To obtain an estimate for the proportion of gas required to be vented to achieve this, U_3 will be set to zero and Equation 3.12 will be solved for m_{OUT} . Using the values listed in Table 3.1, and making the conservative assumption that there is zero kinetic energy contribution of this outflowing gas, the maximum amount of gas required to be vented to achieve complete energy attenuation is found to be:

$$m_{OUT} = \frac{U_2}{h_{OUT} + ke_{OUT}} = 1.1 \text{ kg} \quad (3.13)$$

This value equates to approximately 72% of the original mass of gas within the airbag prior to impact, indicating that it is possible to achieve complete energy attenuation based on only the enthalpy of the outflowing gas. In reality however, this mass value is likely to be lower due to the contribution of the kinetic energy of the outflowing gas.

Hence based on this simple analysis, the following observations can be made regarding the performance of an airbag-based impact attenuation system:

1. The efficiency of the energy transfer between the supported mass and the airbag is directly related to the geometry of the airbag as it compresses under the weight of the mass
2. The extent to which energy is attenuated from the system is directly proportional to the amount of gas vented out of the system
3. The higher the velocity of the outflowing gas, the lower the amount of gas required to be vented from the system to achieve complete energy attenuation

Here, the first observation has implications on the geometry of the airbags, and the second and third observations impact the design of the venting mechanism to be installed on the airbags. These will be further discussed in Section 3.1.2.

3.1.2 The Single Airbag Impact Model Framework

It was found in the previous section that variables such as the airbag geometry and the manner in which venting was facilitated were influential factors in the overall energy attenuation of airbag-based systems. In this section, a framework will be established to allow the explicit modeling of these variables for a single airbag impacting in the vertical direction. Based on the original dynamics model used to develop the airbag system for the Mars Pathfinder [64], this framework treats the airbag impact attenuation problem from a fluid mechanics perspective. Specifically, a time stepping scheme is employed where at each time increment, the change in airbag geometry is calculated based on the position of the supported mass. This is then used to obtain the pressure, volume, and mass of the operating medium, which is in turn used to determine conditions for venting of the airbag. Figure 3-4 presents a general overview of this model.

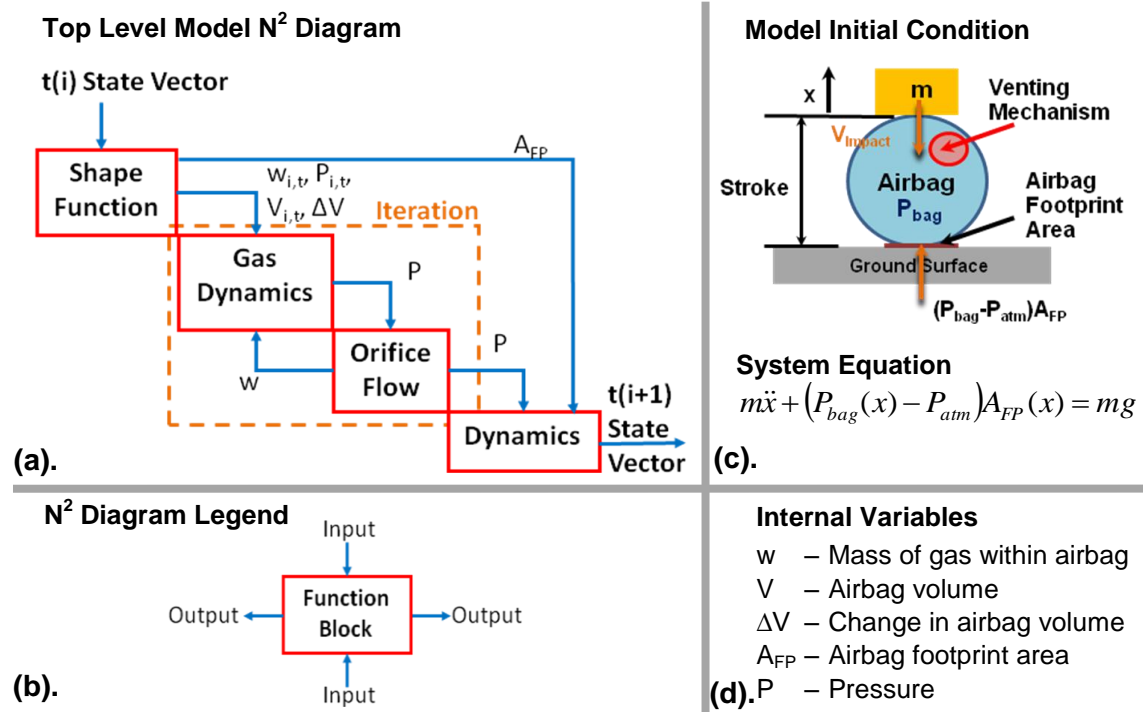


Figure 3-4: Overview of Developed Single Airbag Impact Model (a). N² Diagram (b). N² Diagram Legend (c). Model Initial Condition (d). Model Internal Variables

As can be seen in Figure 3-4(a), this model consists of four basic modules, each of which representing the fundamental physical phenomena governing airbag impact dynamics, as

identified from the first order thermodynamics analysis performed in Section 3.1.1. The details of the modules will be further expanded upon in the following sections.

System Dynamics Equation

Consider the initial condition of the model presented in Figure 3-4 and shown below again in Figure 3-5 for further clarity:

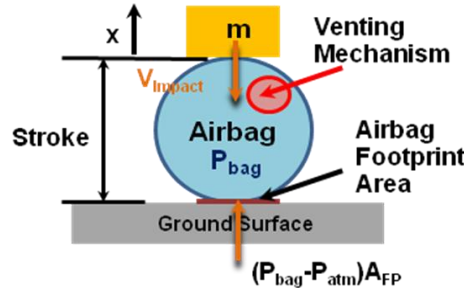


Figure 3-5: Single Airbag Impact Model Initial Condition

Here, it can be observed that the forces present in this single degree of freedom model are:

- The force resulting from the acceleration of the mass sitting atop the airbag as it impacts with the ground surface
- The weight force of the mass sitting atop the airbag; and
- The reaction force from the ground surface, which can be simplified to be equivalent to the effects of the differential pressure between the airbag operating medium and the local atmosphere on the contacting area

Performing a force equilibrium calculation with these forces in the vertical direction yields the following system dynamics equation:

$$\frac{Acceleration}{m\ddot{x}} + \frac{Reaction Force}{(P_{bag}(x) - P_{atm})A_{fp}(x)} = \frac{Weight}{mg} \quad (3.14)$$

It will be this equation which forms the basis for the determination of the system dynamic state at each timestep within the airbag impact model. In particular, the following form of Equation (3.14) will be used to represent the change in system velocity over each timestep:

$$\Delta U = \frac{A_{FP} P_{atm} \Delta t}{m} \left(\frac{P_{bag}}{P_{atm}} - 1 - \frac{mg}{A_{FP} P_{atm}} \right) \quad (3.15)$$

Where ΔU is the change in velocity, which arises from the finite difference representation of the acceleration term:

$$a = \frac{\Delta U}{\Delta t} \quad (3.16)$$

Shape Function Equations

One of the key findings of the thermodynamic analysis performed in Section 3.1.1 was that the efficiency of the energy transfer between the supported mass and the airbag is dependent on the manner in which the airbag geometry changes as it compresses. As will be explained in Section 4.1.1, cylinders were chosen as the baseline airbag geometry throughout this study for the purposes of manufacturability. Consequently, two simple shape functions have been implemented to represent the changing volume and ground contact surface of the airbag as it is compressed.

Based on those used by Esgar and Morgan [65] in an analytical study performed in 1960, these shape functions assume that the axial length of the cylindrical airbags remains constant throughout the compression process. As a result, these functions only focus on the changing cross section of the airbag from its initial circular shape, as is shown below in Figure 3-6.

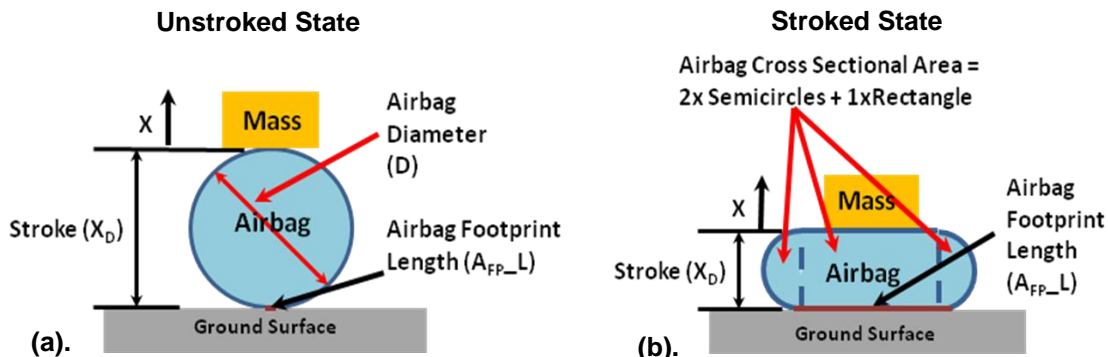


Figure 3-6: Shape Function used in Single Airbag Impact Model
(a). Unstroked State (b). Stroked State

Here, a condition is enforced such that the circumference of the airbag cross section remains constant. In effect, this is equivalent to a conservation of airbag surface area condition. Hence, in terms of the framework presented in Figure 3-6, this can be expressed as:

$$\text{Unstroked Airbag Circumference} = \text{Stroked Airbag Circumference} \quad (3.17)$$

Therefore:

$$\pi D = \overbrace{\pi X_D}^{2x\text{Semicircles}} + \overbrace{2A_{FP} - L}^{\text{Exposed Rectangular Edges}} \quad (3.18)$$

Rearranging Equation (3.18) yields a relationship for the airbag footprint length as a function of the airbag stroke:

$$A_{FP} - L = \pi(D - X_D) \quad (3.19)$$

With this, the cross sectional area of the airbag in the stroked state can be determined using the fact that it consists of a rectangle and two semi-circles, as depicted in Figure 3-6(b). Thus:

$$A_{X-Section} = \overbrace{\pi X_D^2 / 4}^{2x\text{Semicircles}} + \overbrace{X_D A_{FP} - L}^{\text{Rectangle}} \quad (3.20)$$

Now, since the axial length is assumed to remain constant throughout the compression process, the airbag volume and contact surface (or footprint) area can be obtained by multiplying Equations (3.19) and (3.20) by this fixed length. That is:

$$\text{Airbag Footprint Area} = A_{FP}(X_D) = L\pi(D - X_D) \quad (3.21)$$

And

$$\text{Airbag Volume} = V(x) = LX_D \left(\frac{\pi X_D}{4} + A_{FP} - L \right) \quad (3.22)$$

Where L is the fixed airbag axial length.

Gas Dynamics Equations

With an expression for the airbag volume now obtained, standard gas dynamics equations can be used to determine the conditions required for the airbag venting mechanisms to open. Here, a simplifying assumption is made such that the operating medium within the airbags acts as an ideal gas, and that the process is isentropic. As will be discussed in Section 4.1.1, the operating medium will be fixed to atmospheric air for this development effort. This in turn validates the ideal gas assumption, and hence the use of the Ideal Gas Law. Moreover, the isentropic process assumption is widely used to model typical engineering devices such as pumps, nozzles, and turbines, which operate in an essentially adiabatic manner [63]. Since the airbag impact attenuation process is also essentially adiabatic, and because the impact of irreversible effects is relatively small; the isentropic process assumption is appropriate. With this, the gas dynamics equations implemented within this model are listed as follows:

Ideal Gas Law:

$$PV = wR_{GAS}T \quad (3.23)$$

Where P is the pressure, V is the volume, w is the equivalent mass of the gas, R_{GAS} is the specific gas constant, and T is the operating temperature.

Isentropic Process Equation:

$$\frac{T_2}{T_1} = \left(\frac{P_2}{P_1} \right)^{\frac{1}{\gamma}} = \left(\frac{\rho_2}{\rho_1} \right)^{\frac{1}{\gamma}} \quad (3.24)$$

Where the subscripts 1 and 2 indicate the state of the system at the beginning and the end of a process respectively, ρ is the gas density, and γ is the ratio of specific heats of the operating medium.

Density Equation:

$$\rho = \frac{w}{V} \quad (3.25)$$

Given this set of equations, the pressure of the operating medium can be determined during each timestep, which subsequently allows for the opening condition of the airbag venting mechanism to be determined. This is due to the fact that typically, venting mechanisms are designed to open once a given pressure threshold is exceeded. As will be discussed in Section 4.1.4, this is indeed the case with the personal airbag system.

Orifice Flow Equations

Fundamentally, the flow of a gas can be modeled using the mass flow equation applied at the location of the orifice, as given by:

$$\frac{dw}{dt} = C_D A_{th} \rho_{th} \vec{V}_{th} \quad (3.26)$$

Where the subscript *th* indicates the state at the orifice, C_D is the discharge coefficient – a factor representing inefficiencies in the flow stream, A_{th} is the orifice area during the current timestep, and u_{th} is the flow velocity through the orifice.

Here, the mass flow rate through the orifice can be represented in terms of only the pressure and temperature of the operating medium via the use of the following equations:

Density Form of the Ideal Gas Law Applied at the Orifice:

$$\rho_{th} = \frac{P_{th}}{R_{GAS} T_{th}} \quad (3.27)$$

Velocity of Gas:

$$\vec{V}_{th} = M_{th} a_{th}^* \quad (3.28)$$

Where M_{th} is the Mach number of the gas flowing through the orifice, and a_{th}^* is the speed of sound through the operating medium, given by:

Speed of Sound through a Medium:

$$a_{th}^* = \sqrt{\gamma R_{GAS} T_{th}} \quad (3.29)$$

Combining Equations (3.27) through to (3.29) and substituting them into Equation (3.26) yields the following relationship for the mass flow rate:

$$\frac{dw}{dt} = C_D A_{th} P_{th} M_{th} \sqrt{\frac{\gamma}{R_{GAS} T_{th}}} \quad (3.30)$$

Now, since there is close to zero average flow of gas within the airbag, a standard nozzle flow equation can be used to relate the flow velocity through the orifice, to the ratio of pressure at the orifice and upstream from it. This equation is given by [66]:

$$\frac{P_{th}}{P_u} = \left(1 + \frac{(\gamma - 1) M_{th}^2}{2} \right)^{\frac{\gamma}{1-\gamma}} \quad (3.31)$$

Here, the subscript u indicates the pressure upstream from the orifice. This is effectively the same pressure as of that internal to the airbag, as shown in the figure below:

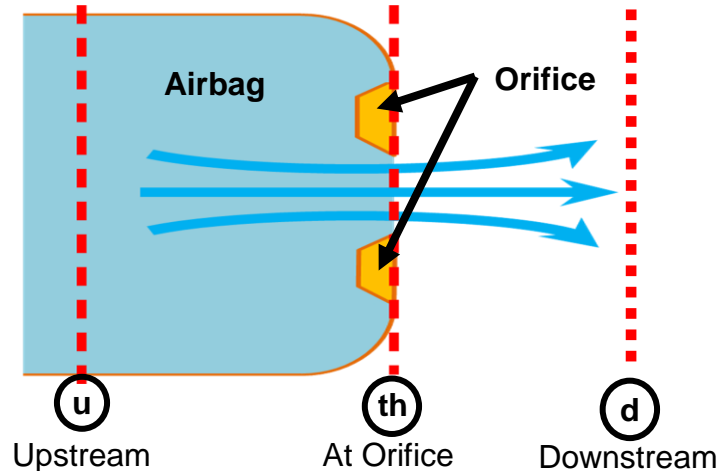


Figure 3-7: Definition of Upstream and Downstream Pressure as used by the Single Airbag Impact Model

With this, Equation (3.31) can be combined with Equation (3.30) by firstly rearranging the former such that the Mach number is the subject, That is:

$$M_{th} = \left(\frac{2}{\gamma - 1} \left(\left(\frac{P_{th}}{P_u} \right)^{\frac{1-\gamma}{\gamma}} - 1 \right) \right)^{\frac{1}{2}} \quad (3.32)$$

Substituting this result into Equation (3.30) yields:

$$\frac{dw}{dt} = C_D A_{th} P_{th} \left(\frac{2\gamma}{\gamma - 1} \left(\left(\frac{P_{th}}{P_u} \right)^{\frac{1-\gamma}{\gamma}} - 1 \right) \right)^{\frac{1}{2}} \left(\frac{1}{R_{GAS} T_{th}} \right)^{\frac{1}{2}} \quad (3.33)$$

Now, assume that the gas at the orifice experiences an isentropic process from the initial system state to the current state. Because the orifice is initially closed, the initial pressure and temperature of the gas at the orifice is the same as that of the gas within the airbag. That is:

$$\frac{1}{T_{th}} = \frac{1}{T_1} \left(\frac{P_I}{P_{th}} \right)^{\frac{\gamma-1}{\gamma}} \quad (3.34)$$

Where the subscript I indicates the initial state of the system. Thus, substituting Equation (3.34) into Equation (3.33), results in:

$$\frac{dw}{dt} = C_D A_{th} P_{th} \left(\frac{2\gamma}{\gamma - 1} \left(\left(\frac{P_{th}}{P_u} \right)^{\frac{1-\gamma}{\gamma}} - 1 \right) \right)^{\frac{1}{2}} \left(\frac{1}{R_{GAS}} \right)^{\frac{1}{2}} \left(\frac{1}{T_I} \left(\frac{P_I}{P_{th}} \right)^{\frac{\gamma-1}{\gamma}} \right)^{\frac{1}{2}} \quad (3.35)$$

Lastly, algebraically manipulating this equation and recognizing that the upstream pressure is equivalent to the airbag pressure, as well as assuming that the orifice pressure is equal to the local, downstream atmospheric pressure; the final form of this orifice flow equation can be expressed as:

$$\frac{dw}{dt} = C_D A_{th} P_{atm} \left(\frac{1}{R_{GAS} T_I} \right)^{\frac{1}{2}} \left(\frac{2\gamma}{\gamma-1} \left(\frac{P_I}{P_{atm}} \right)^{\frac{\gamma-1}{\gamma}} \right)^{\frac{1}{2}} \left(\left(\frac{P_{bag}}{P_{atm}} \right)^{\frac{\gamma-1}{\gamma}} - 1 \right)^{\frac{1}{2}} \quad (3.36)$$

Here, it can be seen that the mass flow rate through the nozzle is primarily a function of the ratio between the airbag pressure and the local atmospheric pressure. Moreover, it is important to note that this relationship is only valid for subsonic flows, as this is the velocity regime over which Equation (3.31) is valid.

When the flow through the orifice is sonic, $M_{th} = 1$, and Equation (3.31) reduces to:

$$\frac{P_{th}}{P_u} = \left(\frac{\gamma+1}{2} \right)^{\frac{\gamma}{1-\gamma}} \quad (3.37)$$

With this, the relationship for sonic flow through an orifice can be obtained by substituting Equations (3.34) and (3.37) into the original orifice flow equation given by Equation (3.30). This results in:

$$\frac{dw}{dt} = C_D A_{th} P_u \left(\frac{1}{R_{GAS} T_I} \right)^{\frac{1}{2}} \gamma^{\frac{1}{2}} \left(\frac{2}{\gamma+1} \right)^{\frac{\gamma}{\gamma-1}} \left(\left(\frac{P_I}{P_{th}} \right)^{\frac{\gamma-1}{\gamma}} \right)^{\frac{1}{2}} \quad (3.38)$$

Again, replacing the P_{th} term with the relationship given by Equation (3.37), yields:

$$\frac{dw}{dt} = C_D A_{th} P_u \left(\frac{1}{R_{GAS} T_I} \right)^{\frac{1}{2}} \gamma^{\frac{1}{2}} \left(\frac{2}{\gamma+1} \right)^{\frac{\gamma}{\gamma-1}} \left(\left(\frac{P_I}{P_u} \right)^{\frac{\gamma-1}{\gamma}} \left(\frac{\gamma+1}{2} \right) \right)^{\frac{1}{2}} \quad (3.39)$$

After some algebraic manipulation, and recognizing the pressure upstream from the orifice is equivalent to the pressure of the airbag operating medium; the final form of the equation for sonic flow through the airbag orifice is given as:

$$\frac{dw}{dt} = C_D A_{th} P_I \left(\frac{1}{R_{GAS} T_1} \right)^{\frac{1}{2}} \left(\gamma \left(\frac{2}{\gamma+1} \right)^{\frac{\gamma+1}{\gamma-1}} \right)^{\frac{1}{2}} \left(\left(\frac{P_{bag}}{P_I} \right)^{\frac{\gamma+1}{\gamma}} \right)^{\frac{1}{2}} \quad (3.40)$$

Here, it can be observed that the sonic orifice flow equation is invariant of the pressure downstream of the orifice. This is in line with the physical phenomena occurring during critical flow, where a shock wave is established at the orifice, causing the flow rate to remain constant and unaffected by fluctuations in the downstream pressure.

Moreover, to determine whether the flow through the orifice is either subsonic or sonic in the model, the pressure ratio across the orifice is compared to that of the critical pressure ratio of the operating medium. This critical pressure ratio is defined as the ratio at which the flow is accelerated to a velocity equal to that of the local velocity of sound in the fluid. Subsequently, this can be obtained from Equation (3.37) via substitution of the appropriate ratio of specific heats for a given operating medium. For atmospheric air at room temperature, the ratio of specific heats is 1.4. Hence the critical pressure ratio is:

$$\frac{P_{th}}{P_u} = \left(\frac{\gamma+1}{2} \right)^{\frac{\gamma}{1-\gamma}} = \left(\frac{1.4+1}{2} \right)^{\frac{1.4}{1-1.4}} = 0.528 \quad (3.41)$$

Thus, if the pressure ratio across the orifice is less than 0.528, the flow through the orifice is subsonic and Equation (3.36) applies. Conversely, if the pressure ratio across the orifice is greater than 0.528, the sonic orifice flow relationship given by Equation (3.40) is used.

Discharge Coefficient

In addition to the flow effects through the airbag venting mechanisms, the inefficiencies inherent to this flow phenomenon are also captured in the single airbag model. This is represented by the C_D term in all of the orifice flow equations presented in the previous section, and is intended to represent the inefficiencies inherent to orifice flow. In particular, this refers to the losses due to frictional and fluidic viscous effects as the gas flows through the orifice, which varies as a function of the pressure ratio across the orifice.

To model this effect, data obtained from orifice flow experiments conducted by Perry [67] was used to form an empirical relationship relating pressure ratio to discharge

coefficient. During these experiments, Perry varied the pressure ratio across a sharp-edged orifice such that both subsonic and sonic flow conditions were obtained. With this, the measured flow rate through the orifice was obtained and compared to the corresponding theoretical value, thus allowing for the discharge coefficient to be obtained. The results of this series of experiments, along with the results of a regression fit of the data, as used in the single airbag impact model, are shown below in Figure 3-8.

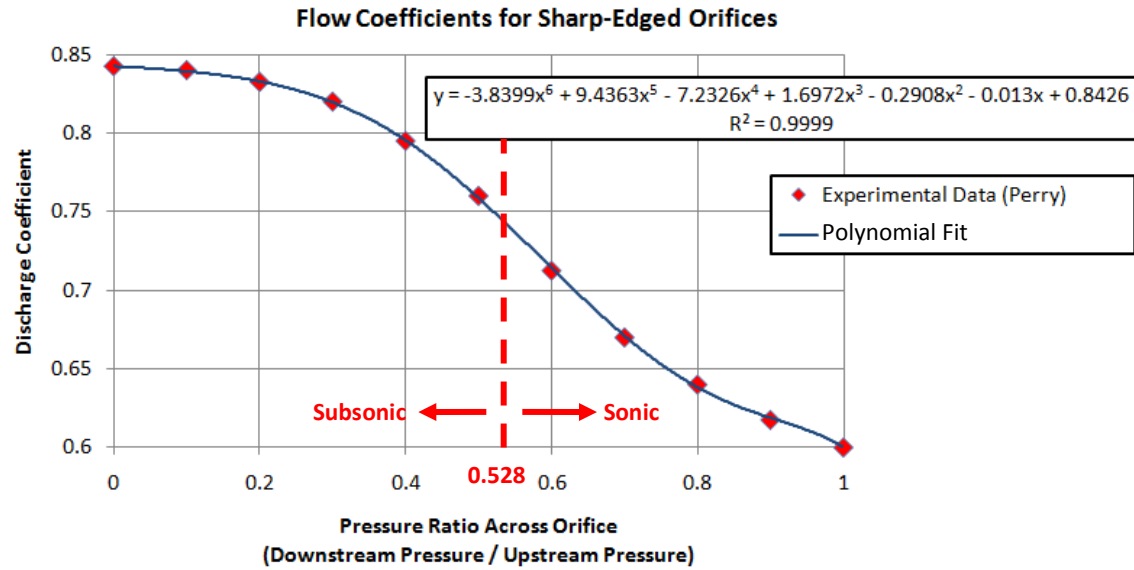


Figure 3-8: Data used to Model the Discharge Coefficient within the Single Airbag Impact Model

3.1.3 The Integrated Single Airbag Impact Model

In this section, the governing equations from each of the previously discussed functional modules will be integrated into the overarching framework presented in Figure 3-4. In addition, the underlying assumptions behind the model equations and structure will be discussed, allowing for shortfalls in the model prediction to be identified.

Model Structure

Upon combining each of the functional modules into the top level model framework, a clear model structure emerges, as shown in Figure 3-9. Note here that a timestep of 0.002 seconds was used to correspond with the sample rate of the data acquisition units used during later

testing. Additionally, a simple Euler time stepping scheme was employed as a first estimate to the system performance.

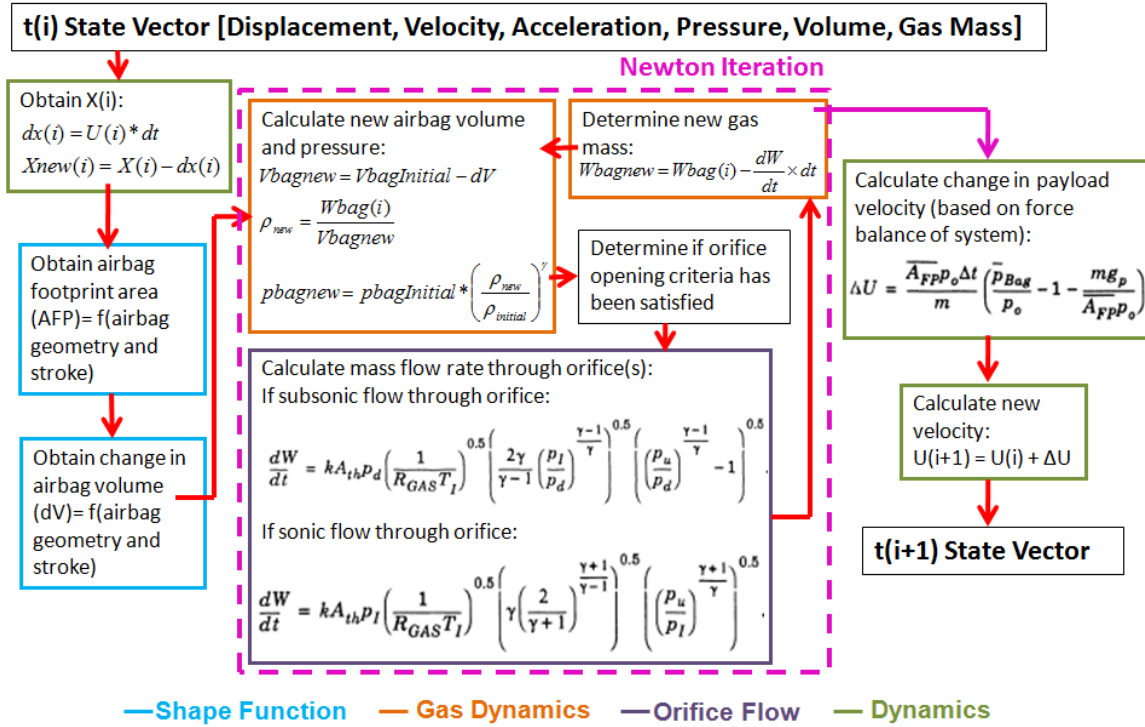


Figure 3-9: Single Airbag Impact Model Functional Flow Block Diagram

Here, it can be seen that there is an iterative interaction between the gas dynamics and orifice flow components of the model. This is because the orifice flow module requires pressure information from the gas dynamics module, which in turn requires knowledge of the mass of gas within the airbag, which is dependent on the orifice flow conditions.

To resolve this circular dependence, the pressure and gas mass values at each time step are solved for simultaneously by applying Newton's method. Commonly used as a gradient based optimization method, this iterative approach uses local gradient information about a given point to determine a direction to move within the solution space. For the case where a root of a real valued function is being searched for, the method travels along this direction until it obtains a solution with a zero objective value. If the initial guess is sufficiently close enough to the root, this resulting solution will be an improved approximation to the root when compared to the previous guess. By repeating this process in an iterative manner, the

obtained solution will gradually move closer towards the root of the function. This method is summarized by the following equation:

$$x_{n+1} = x_n - \frac{f(x_n)}{f'(x_n)} \quad (3.42)$$

Where n is an index representing the n^{th} iteration, f is the real valued function, x is the approximation to the root of f , and f' is the first derivative of f with respect to x .

For the case here, the real valued function is obtained by combining Equation (3.24) with either (3.36) or (3.40), depending on the flow velocity through the orifice. The derivation of this function is summarized below, in Equations (3.43) and (3.44).

$$P_{t+\Delta t} = P_t \left(\frac{\rho_{t+\Delta t}}{\rho_t} \right)^{\gamma} = P_t \left(\frac{w_{t+\Delta t}}{\rho_t V_{t+\Delta t}} \right)^{\gamma} = P_t \left(\frac{w_t - \Delta t \times dw(P_{t+\Delta t})/dt}{\rho_t V_{t+\Delta t}} \right)^{\gamma} \quad (3.43)$$

At a given timestep t , the pressure at the next timestep $t+\Delta t$ is desired. Thus, the real valued function in this case is:

$$f(P_{t+\Delta t}) = P_t \left(\frac{w_t - \Delta t \times dw(P_{t+\Delta t})/dt}{\rho_t V_{t+\Delta t}} \right)^{\gamma} - P_{t+\Delta t} \quad (3.44)$$

With this, Newton's method can be applied by differentiating Equation (3.44) and substituting the result into Equation (3.42). That is:

$$P_{t+\Delta t, n+1} = P_{t+\Delta t, n} - \frac{f(P_{t+\Delta t, n})}{f'(P_{t+\Delta t, n})} \quad (3.45)$$

Note that the fully expanded version of this Newton iteration relationship, including the complete representation of the function derivatives, is presented in Appendix B.

Model Assumptions

As alluded to throughout this chapter thus far, several simplifying assumptions have been made in the development of the single airbag impact model. Here, these assumptions will be made explicit in order to aid in later comparisons of the model predictions with experimental data. These are listed below as follows:

1. *The motion of the system occurs only in one vertical direction*

That is, the model only captures one degree of freedom. This is perhaps one of the most fundamental assumptions made in the model and is made apparent by the fact that the underlying system equation is derived from a balance of forces only occurring in the vertical direction.

2. *The impact occurs in a quasi-equilibrium manner over the duration of the event*

This implies that the gas properties such as pressure, temperature, and density are constant throughout each airbag at each time increment. Furthermore, between each time increment, the values of these properties adjust instantaneously.

3. *Gas compression and expansion occurs adiabatically within the airbags*

This is the crux behind the isentropic process assumption used within the model to predict the gas properties at the end of each timestep, given knowledge of the current gas properties and the geometry and venting characteristics of the airbag.

4. *The operating medium within the airbags is assumed to act as an ideal gas*

Similar to that previously described, this assumption is fundamental to the prediction of the gas properties from one time increment to the next. As will be discussed in Section 4.1.1, the operating gas used throughout this development has been fixed to atmospheric air. As a result, the ideal gas assumption is an accurate approximation for the purposes of this design effort.

5. *No airbag material elasticity effects are accounted for*

This assumption is captured by the implementation of the simple, geometry shape function described in the previous section.

6. *The flow area of each orifice is unaffected by the crush-up dynamics of the airbag*

That is, the orifice area remains unobstructed throughout the impacting event. This can be a good approximation to the dynamics of a physical system if the venting mechanisms are located on the airbag such that they remain unimpeded at all times.

7. *The mass of the airbag itself is neglected in the impact dynamics*

As was mentioned in the original thermodynamics analysis of the airbag impact attenuation problem, the contribution to the system mass and energy by the airbag itself is insignificant when compared to those of the supported mass and the gas internal to the airbag.

8. *No aerodynamic drag of the supported mass or the airbag is considered*

Similar to the first assumption, this assumption arises from the original vertical force balance performed to obtain the system equation. Also, because the initial condition of the system is set to the moment of first contact between the airbag and the ground surface, this assumption is a good approximation to the physical system

Of all of the aforementioned assumptions, Assumption 5 is most likely to have the greatest impact on the predicted performance of the system. This is because there is the least evidence to support the validity of this assumption, which effectively states that the changing geometry of the airbag during impact follows the path defined by the shape function given by Equations (3.21) and (3.22). As was found in the thermodynamics analysis presented in Section 3.1.1, the efficiency of the energy transfer between the supported mass and the operating medium internal to the airbags is directly related to the manner in which this geometry changes. In engineering devices such as engines or compressors, the effect of this boundary work is typically measured directly from the device during operation [63]. This is due to the fact that it is difficult to accurately predict the pressure versus volume path of the system *a priori* – an issue also inherent in the airbag impact attenuation problem.

One method in which this path can be more accurately predicted is by using a finite element method to investigate the fluid-structure interaction effects occurring between the airbag material and the operating gas. In order for this to be performed, Assumption 2 can no longer be held, as the entire pressure field is required to characterize the effect of the gas on the material and vice versa. Characterizing this pressure field requires solving the Navier-Stokes equations, which can be a highly time intensive exercise for a single design case, due to the potentially small timesteps required to meet the Courant-Friedrichs-Lowy condition for solution convergence. As a consequence of this time penalty, it was deemed unnecessary to implement a higher fidelity scheme to predict the airbag performance, especially considering the fact that at this stage of development, all design is at the conceptual level and the nature of design space is poorly understood. As will be seen in Chapter 5, confidence was ultimately established for this single airbag model via validation with experimental data.

3.2 Human Injury-Risk Modeling

In Section 1.2, one of the key questions highlighted as being necessary to meet the objectives of this work was:

Can an airbag-based system maintain an astronaut's injury-risk levels to within acceptable tolerances during a nominal land-landing?

In this section, the metric used to quantify these injury-risk levels will be introduced. Following this, an analysis of the underlying equation governing this metric will be analyzed in an attempt to gain useful insight into the nature of mitigating injury risk to the occupant during an impacting event.

3.2.1 The Brinkley Direct Response Index

To ensure that the Orion CEV, along with other Constellation program vehicles, are capable of accommodating all of the safety and basic comfort needs of their crew during all phases of flight, NASA has released the “Constellation Program Human-Systems Integration Requirements” (HSIR) document [9]. This document lists a set of requirements which must be met by a spacecraft for it to be considered human-rated.

In relation to crew impact attenuation systems, the primary metric specified by the HSIR for gauging system performance is the Brinkley Direct Response Index (DRI). This index measures the risk of injury to an occupant when subjected to a given measured acceleration profile by comparing the output of a dynamics model of the human body, with limiting values representing varying levels of risk to injury. Here, a lumped parameter model is utilized, whereby the dynamic response of a human is approximated as the response of a spring-mass-damper system to a given acceleration profile in each of the three orthogonal axes, referenced to the center of the torso. Moreover, a simplifying assumption is made where the effects of the applied acceleration profile in each of these three axes are uncoupled. Specifically, this dynamic system is modeled with the following relationship:

$$\ddot{X}(t) + 2\xi\omega_n \dot{X}(t) + \omega_n^2 X(t) = a(t) \quad (3.46)$$

Where:

- \ddot{X} is the relative acceleration of the dynamic system with respect to the reference point (or center of the torso) in either one of the x-, y-, or z-directions
- \dot{X} is the relative velocity of the dynamic system with respect to the reference point in either one of the x-, y-, or z-directions
- X is the relative displacement of the dynamic system with respect to the reference point in either one of the x-, y-, or z-directions. Here, a positive value corresponds to a compression
- a is the measured acceleration profile from the reference point in either one of the x-, y-, or z-directions. In regards to the model structure, this is obtained from the acceleration time history produced by the single airbag impact model
- ξ is the damping ratio of the dynamic system representing the response in the given x-, y-, or z-direction
- ω_n is the natural frequency of the dynamic system representing the response in the given x-, y-, or z-direction
- t is a time coordinate; and the

Reference Point, x, y, and z directions are defined by Figure 3-10.

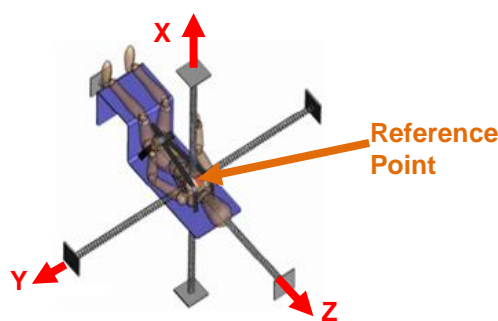


Figure 3-10: Brinkley Reference Frame

With this, the Brinkley DRI is obtained by solving the system given by Eq. (3.46) and inputting the result into the following relationship:

$$DRI(t) = \frac{\omega_n^2 X(t)}{g} \quad (3.47)$$

Where g is the acceleration due to the Earth's gravity, used here as a normalizing factor.

Moreover, the damping ratio and natural frequency values to be used in the aforementioned lumped parameter model as specified by the NASA HSIR are as follows:

Table 3.2: NASA HSIR specified natural frequencies and damping ratios to be used in the Brinkley Dynamic Response Model [9]

	x	y	z
ω_n	62.8	58.0	52.9
ξ	0.2	0.09	0.224

Furthermore, the limiting injury risk Brinkley DRI values as specified in the NASA CxP HSIR are presented below in Table 3.3.

Table 3.3: NASA HSIR Specified Brinkley DRI Limits [9]

Brinkley DRI Limit Level	x		y		z	
	DRI_x < 0	DRI_x > 0	DRI_y < 0	DRI_y > 0	DRI_z < 0	DRI_z > 0
Very Low (0.05%)¹ (Previous Nominal)	-22.4	31	-11.8	11.8	-11	13.1
Low (0.5%)¹ (Current Nominal)	-28	35	-14	14	-13.4	15.2

¹Note that these percentage values correspond to the likelihood of injury to the occupant at any location in the body.

It is important to note here that when originally proposed, the NASA HSIR dictated that a system must maintain the level of injury-risk to its occupant in the “very low” range throughout a transient acceleration event for it to be considered human-rated. Recently however, this requirement has been relaxed to a “low” limiting injury risk level. This decision was based on recommendations made by an independent group of industry, academic, and NASA experts tasked to determine if the HSIR specified occupant protection criteria were too conservative. It was realized that the “very low” Brinkley limit requirement was originally mandated so that deconditioned crew members could be safely returned to the ground. This capability was deemed as not necessary for Constellation Program vehicles during the original specification of the system requirements, hence allowing for the initial Brinkley limit to be relaxed to a “low” injury-risk level [1].

In addition to the DRI limit values specified by NASA, limiting values corresponding to higher levels of injury-risk have also been derived for use in evaluating the safety of systems subjected to high transient accelerations. These were obtained from the original Brinkley study [68], which focused on determining human acceleration tolerance measures for use in aircraft ejection seat design; and are given below in Table 3.4.

Table 3.4: Brinkley Limits for Moderate and High Risks of Injury [68]

Brinkley DRI Limit Level	<i>x</i>		<i>y</i>		<i>z</i>	
	DRI_x < 0	DRI_x > 0	DRI_y < 0	DRI_y > 0	DRI_z < 0	DRI_z > 0
Moderate (5%)¹	-35	40	-20	17	-12	18
High (50%)¹	-46	46	-30	22	-15	22.8

¹Note that these percentage values correspond to the likelihood of injury to the occupant at any location in the body.

Finally, since the DRI is a time-dependent function, a parameter called the β -function is commonly used to determine if a system has remained below a given Brinkley limit over the duration of an acceleration event. As shown in Equation (3.48), this function corresponds to the root sum square of the relative DRI values in each of the three orthogonal axes.

$$\max\{\beta\} = \max \left\{ \sqrt{\left(\frac{DR_x(t)}{DR_x^{\lim}} \right)^2 + \left(\frac{DR_y(t)}{DR_y^{\lim}} \right)^2 + \left(\frac{DR_z(t)}{DR_z^{\lim}} \right)^2} \right\} < 1 \quad (3.48)$$

Here, a maximum beta value of less than one corresponds to the system satisfying a given injury-risk level over the duration of an impacting event.

3.2.2 Injury-Risk Mitigation

With a formal model now established, further insights into the mechanisms influencing injury-risk can be obtained by analyzing the governing equations. This can be accomplished by firstly observing the fact that any acceleration input can be considered as a Fourier spectrum. For each amplitude (\tilde{p}) and frequency (ω) component of this spectrum, a sub-

Brinkley index problem can be solved. This appears in the form given by Equation (3.49), shown below:

$$\ddot{X}(t) + 2\xi\omega_n \dot{X}(t) + \omega_n^2 X(t) = \frac{\Delta\omega}{2\pi} \tilde{p}_j e^{i\omega_j t} \quad (3.49)$$

Where j is the j^{th} component of the Fourier spectrum, and $\Delta\omega$ is the frequency step to which the Fourier spectrum is discretized to.

Here, the solution to this spring-mass-damper system is well established in the structural dynamics discipline, and is given by:

$$X_j(t) = \frac{\Delta\omega}{2\pi} H(\omega_j) \tilde{p}(\omega_j) e^{i\omega_j t} \quad (3.50)$$

Where $H(\omega_j)$ is the transfer function relating a unit applied acceleration to a displacement X , given by:

$$H(\omega_j) = \frac{1/\omega_n^2}{1 - \left(\frac{\omega}{\omega_n}\right)^2 + 2i\xi\frac{\omega}{\omega_n}} \quad (3.51)$$

Now, since the damping ratio and natural frequency values used in the lumped parameter model are constant, the spring-mass-damper system is linear. Because this is the case, superposition applies, and the total response of the system given a driving acceleration profile can be calculated by the summation of the responses to each of the individual amplitude-frequency components of the response. That is:

$$X(t) = \frac{\Delta\omega}{2\pi} \sum_j H(\omega_j) \tilde{p}(\omega_j) e^{i\omega_j t} \quad (3.52)$$

Next, substituting Equation (3.52) into the Brinkley DRI equation given by Equation (3.47), and observing the fact that mitigating injury risk is directly proportional to

minimizing the magnitude of the overall system response; the following expression is obtained:

$$|DR| = \omega_n^2 |X(t)| / g = \frac{\omega_n^2 \Delta\omega}{2\pi g} \sum_j A(\omega_j) |\tilde{p}(\omega_j)| \quad (3.53)$$

Where $A(\omega_j)$ is the dynamic amplification function, given by:

$$A(\omega_j) = \frac{1}{\sqrt{\left[1 - \left(\frac{\omega_j}{\omega_n}\right)^2\right]^2 + 4\xi^2 \left(\frac{\omega_j}{\omega_n}\right)^2}} \quad (3.54)$$

Upon plotting the dynamic amplification function against varying frequencies for each of the three Brinkley axes, it can be seen that as the frequency of the system acceleration response approaches the natural frequency of the lumped parameter model, the magnitude of the response is magnified significantly. As can be seen in Figure 3-11, this magnification factor can range from 2.25 to 5.5, depending on the Brinkley direction being investigated.

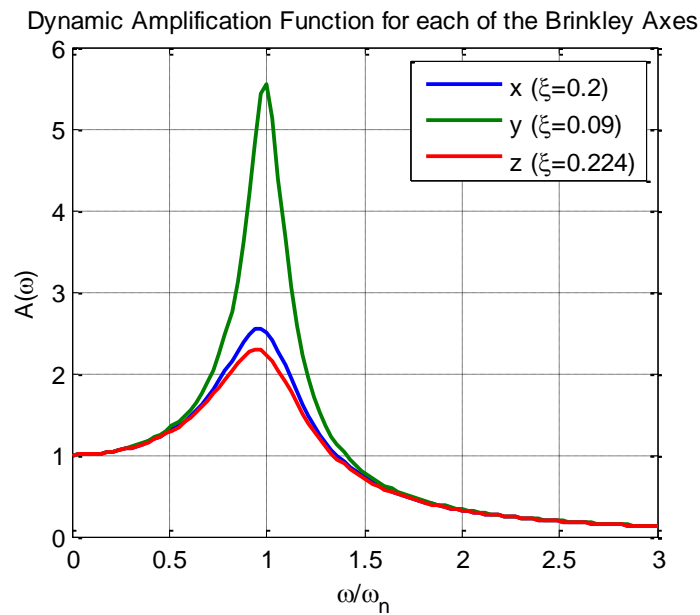


Figure 3-11: Magnification Effects of the Dynamic Amplification Function

Hence, when considering this observation in the context of Equation (3.53), it can be observed that improved impact attenuation performance occurs when both:

1. The magnitude of the acceleration of the impacting event ($|\tilde{p}(\omega_j)|$) is minimized; and
2. The frequency content of the acceleration response is weighted away from that of the natural frequency; and is preferably weighted towards frequencies beyond a factor of $\sqrt{2}\omega_n$, where dynamic damping is achieved

These observations have implications on the airbag venting characteristics and the system configuration, and also provide some intuition when interpreting both model-predicted and experimentally obtained results.

3.3 Photogrammetric Methods for Impact Analysis

In the previous sections of this chapter, the airbag impact attenuation problem has been treated from the perspective of predicting the system performance based on a set of idealized equations, given a design vector and a set of initial conditions. In this section, an alternative method known as photogrammetry will be discussed, whereby vision-based tracking techniques will instead be used to extract data from high speed camera footage.

Commonly used in the analysis of impact tests, this method involves placing a series of illuminated dots on the test setup. This illumination can be achieved by a color contrast between the dot and the background to which it is attached via the use of reflectivity, or via the installation of LED lights to artificially increase the relative brightness. During post-processing of the high speed camera footage, the position of these points is tracked frame by frame using the dot illumination as an identifying property. By numerically differentiating the position of these tracking points, important information such as impact velocity and maximum system acceleration can be gleaned. This process is summarized below in Figure 3-12.

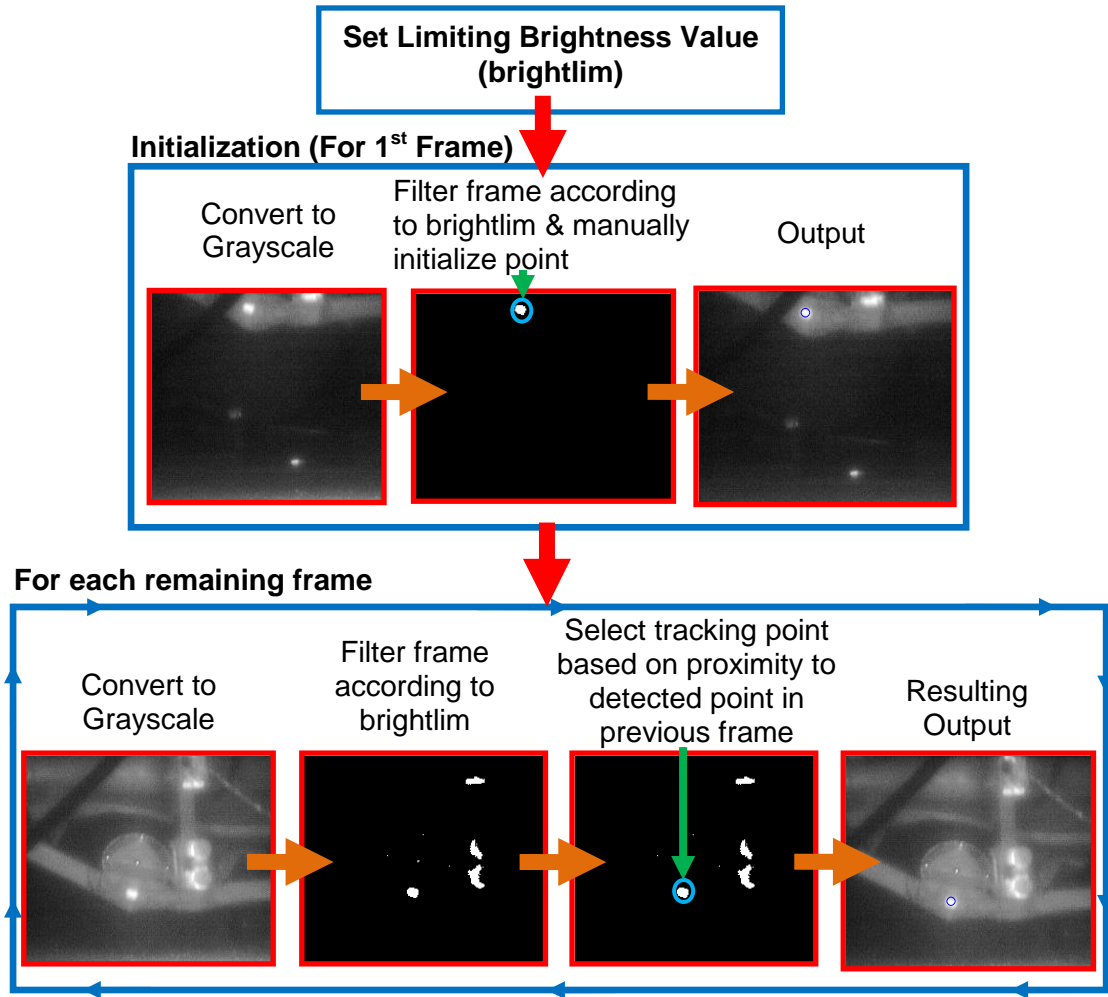


Figure 3-12: Dot Detection Algorithm Functional Flow Block Diagram

In addition to linear dynamics information, photogrammetry can also be used to yield attitude data of the system, by comparing the position of multiple strategically placed tracking points. In the case that the captured frame is not large enough to track multiple points, an alternative, line-detection method can be used. Based on the Hough transform technique, this method is based on processing each frame with firstly an edge detection algorithm, and then with a line detection algorithm. The output of this is a set of all lines detected in each frame. With this, a rule based filtering scheme is then used to detect and store lines corresponding to edges of interest within the frame. By repeating this process for each frame, attitude time history data can be obtained by measuring the gradient of the detected edges of interest. This process is summarized in Figure 3-13.

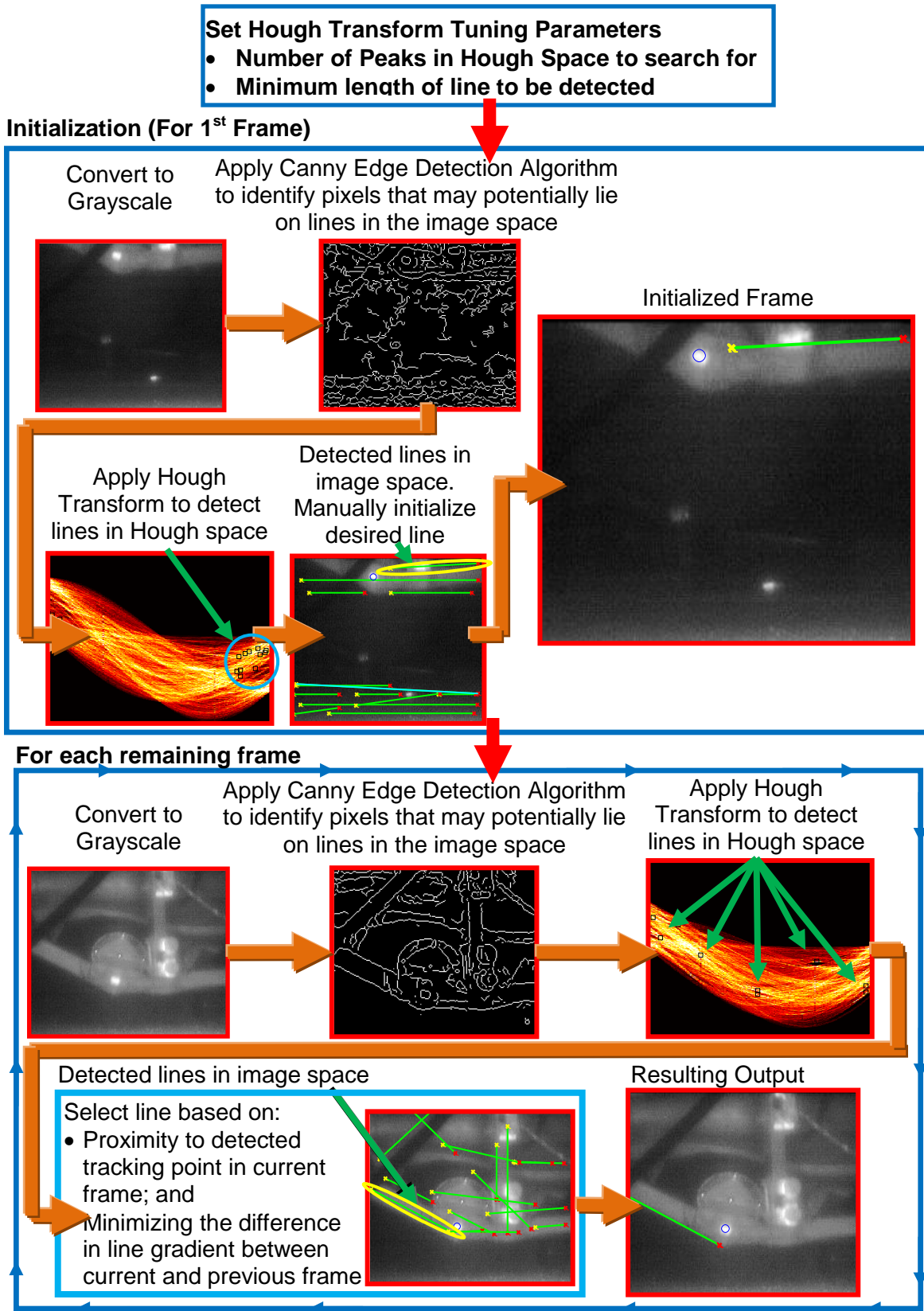


Figure 3-13: Line Detection Algorithm Functional Flow Block Diagram

Hence, with both attitude and position data obtained, it was then possible to resimulate the impact dynamics of the system, thus further aiding in the analysis of each drop. This entire photogrammetric analysis process is summarized in Figure 3-14.

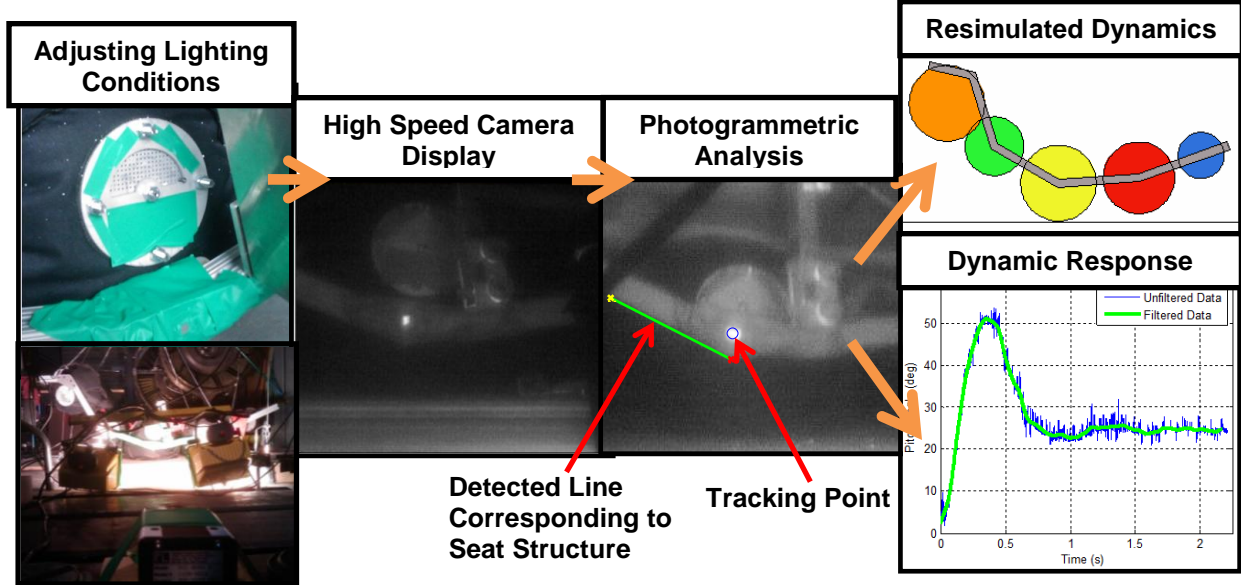


Figure 3-14: Summary of Photogrammetric Analysis Process

As will be seen in the subsequent chapters, photogrammetry will play an extremely valuable role in understanding the underlying physical mechanisms which occur during drop tests of each generation of the personal airbag system. Furthermore, this technique has allowed for the influence of these mechanisms on the injury-risk to the occupant to be analyzed and understood.

3.4 Chapter Summary

Over the course of this chapter, the techniques used to model and predict the performance of a mass supported by a single airbag were presented. This commenced with a first order thermodynamics analysis of the airbag-based impact attenuation problem, where it was highlighted that the airbag geometry and venting characteristics were fundamental to the efficiency of energy transfer between the supported mass and the airbag gas; and the amount of energy attenuated from the system, respectively.

Next, these insights were used as the basis for the development of a single airbag impact model. Here, the equations governing airbag geometry, gas dynamics, and orifice flow were introduced and integrated into a single framework. In addition, key assumptions of this single degree of freedom model were also discussed, along with their implications on the performance of the physical system during testing.

Following this, the Brinkley Direct Response Index (DRI) was introduced as the NASA mandated metric for quantifying and gauging human injury-risk during transient acceleration events. A related analysis of the underlying equation governing this metric found that injury-risk was related to both the magnitude and the frequency content of the acceleration environment subjected to the system occupant.

Finally, the method of photogrammetry was introduced, whereby dynamics data from high speed camera footage of impacts is extracted using vision based techniques to detect and track predetermined dots and lines on the drop test article. Here, functional flow block diagrams of each of these algorithms were presented to show the inner workings of these algorithms.

Thus with these tools and techniques established, design of a personal airbag system can be performed. The following chapters describe each of the three spirals of system development undertaken during this effort, and how these tools were used and evolved to meet the design objectives of each design cycle.

Chapter 4

Analog-Airbag System Development

Although not directly related to meeting the overall objectives of this work, an analog-airbag system was developed and tested from January through to April 2009, with the intention of developing the enabling products and processes required for future generations of the system development. It is this first generation system which will be the focus of this chapter.

As will be seen in the first section of this chapter, this development spiral originally began with the intention of developing a full-scale personal airbag system to evaluate its feasibility. However, difficulties with fabricating robust airbags which met both design requirements, and the real world pressures of schedule and cost constraints, led to the ultimate move toward building and testing an analog system. Interestingly though, many important insights into the manufacturability, operation, and ultimate performance of a personal airbag system were obtained from this first development effort. These will be further expanded upon in the second part of this chapter.

4.1 Analog-Airbag System Design

In order to design the first generation system, a simplified approach was employed, whereby a baseline airbag configuration was assumed, and the single airbag impact model was used to size each airbag individually within the configuration. Although this approach did not capture the interaction effects between each of the airbags and the human body, it was deemed appropriate for a first approximation to the performance of a first generation system. The following sections further elaborate upon the details of each of these phases of design.

4.1.1 System Configuration

Two primary considerations were made in the selection of the baseline system configuration; being its stability upon impact, and the manufacturability of the system. To address the former concern, a multi-airbag arrangement, as depicted in Figure 4-1, was chosen to mitigate any gas-shifting effects which might occur with a single airbag configuration. Moreover, this arrangement is inherently simple to manufacture, as it consists of elemental units which are within the size constraints of the available manufacturing equipment. This second attribute hence satisfies the latter requirement.

Additionally, incorporating multiple airbags rather than a single airbag adds a degree of redundancy within the system by maintaining some functionality if one airbag were to fail. Moreover, using multiple airbags would have a comparable mass penalty to that of a single airbag configuration [65], whilst also allowing for the introduction of a further degree of reconfigurability in the system via the ability to vary the design of each of the airbags. The configuration chosen as the basis for this initial design is shown in the figure below.

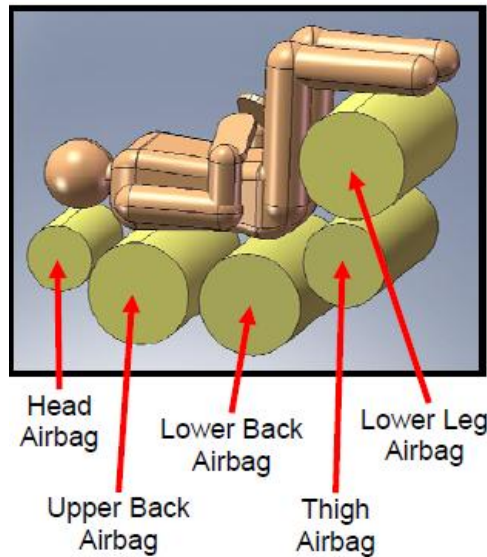


Figure 4-1: Baseline Airbag Configuration

It can be observed from Figure 4-1 that as an initial estimate for the multi-airbag arrangement, airbags have been placed under key mass concentrations in the human body when in the semi-supine position, based on the findings of the historical review performed in Chapter 2. Here, the airbags are situated to support the head, upper and lower back, thigh,

and lower leg regions of the body. In addition, the geometry of these airbags has been fixed to be cylindrical in shape, and their operating medium has been fixed to be atmospheric air. The former decision was based primarily on manufacturability considerations; whilst the latter was based on safety considerations for the astronaut crew when in the cabin of the Orion CEV, as well as the added benefit of commonality with the atmospheric environment of the cabin.

It should be reiterated here that at the time that this configuration was chosen, airbags, rather than their analog equivalents were intended as the primary means of impact attenuation. As a result, it was intended for each of the airbags within the system to incorporate venting mechanisms to facilitate a “stuck” landing profile, as per the conclusions made in Chapter 2. These mechanisms would be designed to completely dissipate the kinetic energy of the occupant on impact, such that no bouncing would occur, and the resulting Brinkley DRI remained beneath the “low” injury-risk level limit.

In addition, the development of airbags would require a choice of operating gas, the initial pressure of this gas, and specific airbag geometric dimensions – parameters which all play a role in the energy conversion processes which occur during impacting events. The process utilized to determine the value of these variables is described in the next section.

4.1.2 Airbag Sizing

To size each of the airbags in the first generation airbag system, the single airbag impact model was extensively used to generate an objective space to which a preliminary optimization could be performed. Specifically, this involved determining parameters for each of the five airbags by discretizing a 50th percentile male aviator human model [59] into the five key segments identified in Figure 4-1, to define the mass to be supported by each airbag. With this, a range of parameters was input into the model for each airbag to develop a design space over which to optimize. These were obtained from spacing constraints about the human body as well as initial simulation runs with the model, and are given in Table 4.1. Note that as a first approximation, these values were obtained for the system with a zero pitch angle landing at the nominal Orion impact velocity of 7.62m/s (25fps), and with a cabin pressurized with atmospheric air at sea level pressure. Also, the airbag vents were constrained to stay open once opened in this analysis, thus replicating the same venting profile employed in all

previous vented airbag systems reviewed in Chapter 2. As a result, the opening condition, measured here by a threshold acceleration value; along with the size of the venting orifice, are parameters which were also considered as variables in the design space.

Table 4.1: Parameter Values Forming the Optimization Space for Each Airbag

	Mass (kg)	Airbag Dimension Range		Airbag Pressure (atm)	External Orifice	
		Radius (m)	Length (m)		Area to cross sectional area ratio	Opening Condition (g's)
Head	4.74	0.09-0.11 [0.005]				
Upper Back	14.43	0.13-0.2 [0.01]				
Lower Back/Pelvis	26.05	0.13-0.2 [0.01]	0.3-0.6 [0.05]	1-1.1 [0.05]	0.1-0.6 [0.05]	5-50 [5]
Thighs	15.83	0.1-0.2 [0.01]				
Lower Leg	8.37	0.1-0.2 [0.01]				

NB. [x] indicates the length of the discretization step over the variable range

Hence, with a set of dynamic performance values for each design parameter combination obtained for each airbag, these design spaces were optimized using the following objective function:

To minimize the velocity at the end of the airbag stroke, over the set of solutions where the magnitude of the largest induced acceleration is less than 45G's over a period of less than 0.04 seconds

The choice of this objective was based on both energy dissipation and injury-risk level considerations, with the minimal velocity criterion aimed at minimizing the resulting bounce as much as possible; and the acceleration criterion based on minimizing the resulting Brinkley DRI. Here, the acceleration limit of 45G's over 0.04 seconds was chosen based on data from the literature on human tolerance to transient acceleration environments [69, 70].

Additionally, it should be noted that initial executions of the single airbag impact model indicated that the objectives of minimizing Brinkley DRI and velocity at the end of the airbag stroke were not necessarily mutually supportive. It was later discovered in future development spirals that this prediction was not entirely accurate, due to the implementation of an airbag shape function in-line with that originally used in the Mars Pathfinder airbag design code. As a consequence, the shape function described in Section 3.1.2 was implemented for the second and third spirals of system development. For the design and development of the first generation system however, the original observations and assumptions were maintained based on the available insight at the time.

Hence with this original model, the final results of the preliminary system design effort and the corresponding model-predicted performance were obtained. These are shown below in Table 4.2 and Figure 4-2 respectively.

Table 4.2 – Airbag Parameter Values for First Generation CIAS Design

	Head Airbag	Upper Back Airbag	Lower Back Airbag	Thigh Airbag	Lower Leg Airbag
Radius (m)	0.11	0.17	0.18	0.14	0.18
Length (m)	0.35	0.6	0.6	0.6	0.6
Internal Pressure at Impact (kPa)	106.4	101.3	106.4	101.3	101.4
Total Orifice Area (m²)	0.008	0.009	0.01	0.006	0.01
Orifice Opening Acceleration (G's)	15	30	35	30	25
Corresponding Orifice Opening Pressure (kPa)	120	130	150	145	120

It is interesting to note that in Table 4.2, the internal pressure at impact is very close to that of the cabin pressure. This implies that the solution to the trade-off between an airbag which is likely to bounce due to high pressure, and one which is likely to cause the occupant to impact the ground due to low pressure; is such that the airbag maintains its approximate equilibrium shape. It will be later observed in Section 5.5, that this was a consistent trend found during each iteration of system development.

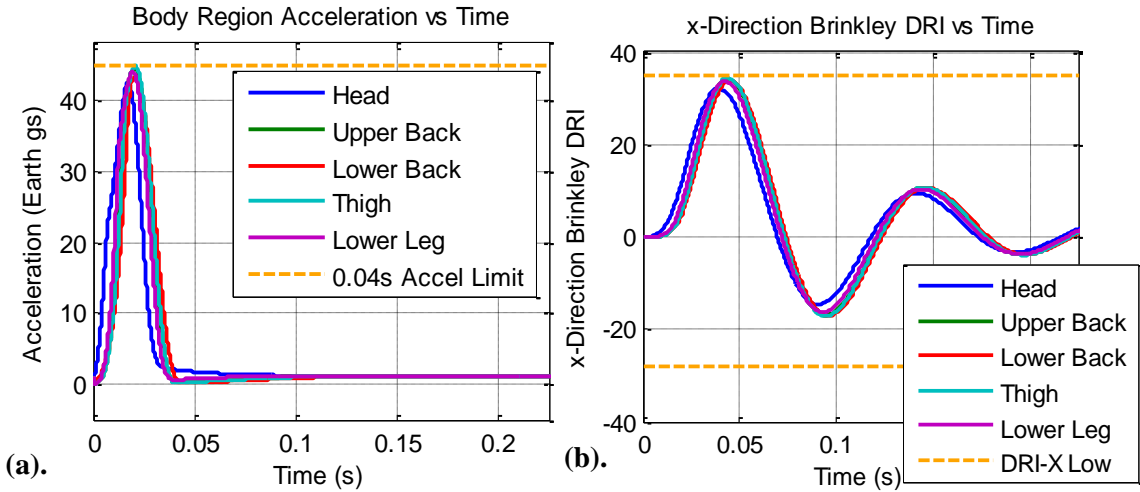


Figure 4-2: Predicted Performance for the First Generation Personal Airbag System
(a). Vertical Acceleration Time History (b). X-Axis Brinkley DRI Time History

From Figure 4-2(a), it can be seen that the maximum acceleration induced on the system remains below values corresponding to a low injury-risk level. This is particularly evident by the fact that the maximum DRI values in Figure 4-2(b) are within the low injury-risk level ranges given in Table 3.3, as was predicted by the literature [69, 70]. Hence, with this, enabling products were developed to support and test this finalized airbag configuration. This is described in the next section.

4.1.3 Test Hardware and Infrastructure Design

With a complete airbag configuration defined, a means of facilitating tests to evaluate their performance is required. To achieve this, a seat structure was designed to support both the airbags and an occupant, and a test rig was designed to simulate the range of impact angles and vertical impact velocities anticipated during Orion crew module landings. Figure 4-3 shows an overview of these components, whilst Figures 4-4 and 4-5 present more details of their respective designs.

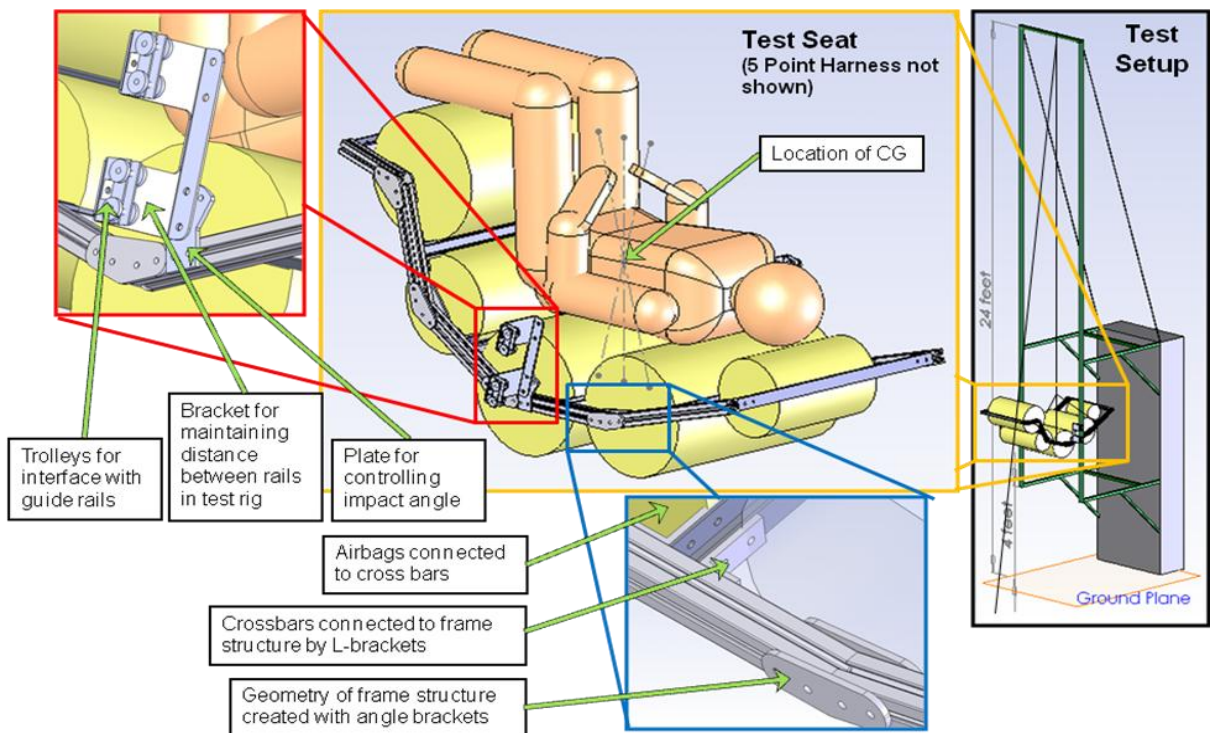


Figure 4-3: Test Article and Infrastructure Design Features

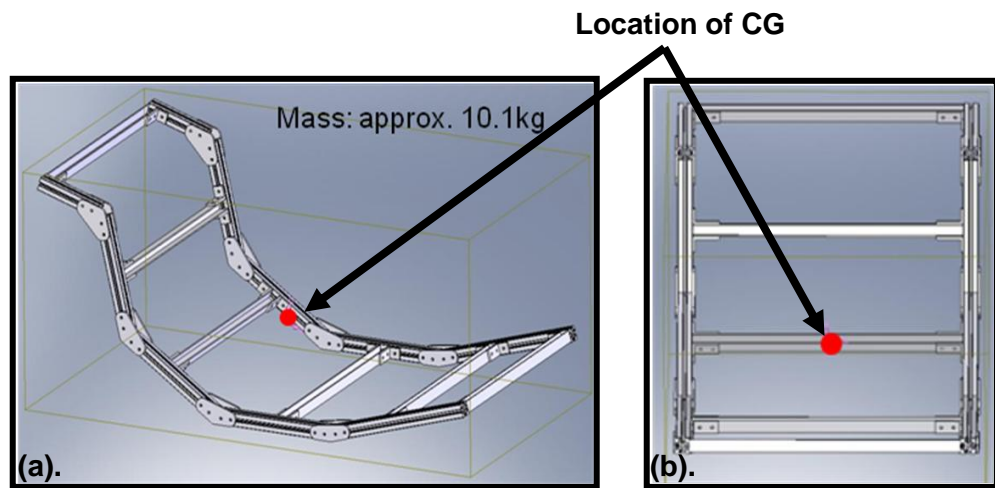


Figure 4-4: Detail of Seat Frame Design (a). Isometric View (b). Front View

One notable feature of the seat frame design is that it was purposefully designed to be reconfigurable, and thus able to be adjusted for investigations into future airbag configurations. This reconfigurability was achieved by using grooved extrusions, which allowed the flexible location of simple brackets which could be moved to change the shape of

the structure. In addition, this simple design also made the system easy to manufacture, an added benefit which assisted in the mitigation of manufacturing errors and resulting schedule slips.

With regards to the drop test rig, the concept of trolleys sliding through rails to guide the motion of an object, like that employed in rollercoasters, was chosen. Here, a simple design consisting of standard Unistrut® components was utilized for its ease of assembly and interfacing with the test area. This test area also provided an upper bound to the height of the test rig, being 24feet.

Although preliminary calculations indicated that under nominal conditions, a drop height of 10 feet would equate to the nominal Orion impact velocity of 7.62m/s (25fps), the test rig was designed to the maximum available height to enable future experiments with off-nominal impact velocities. Additionally, 4 feet of clearance was left at the bottom of the test rig to allow for the drop article to experience its natural dynamics at impact. This is summarized in Figure 4-5.

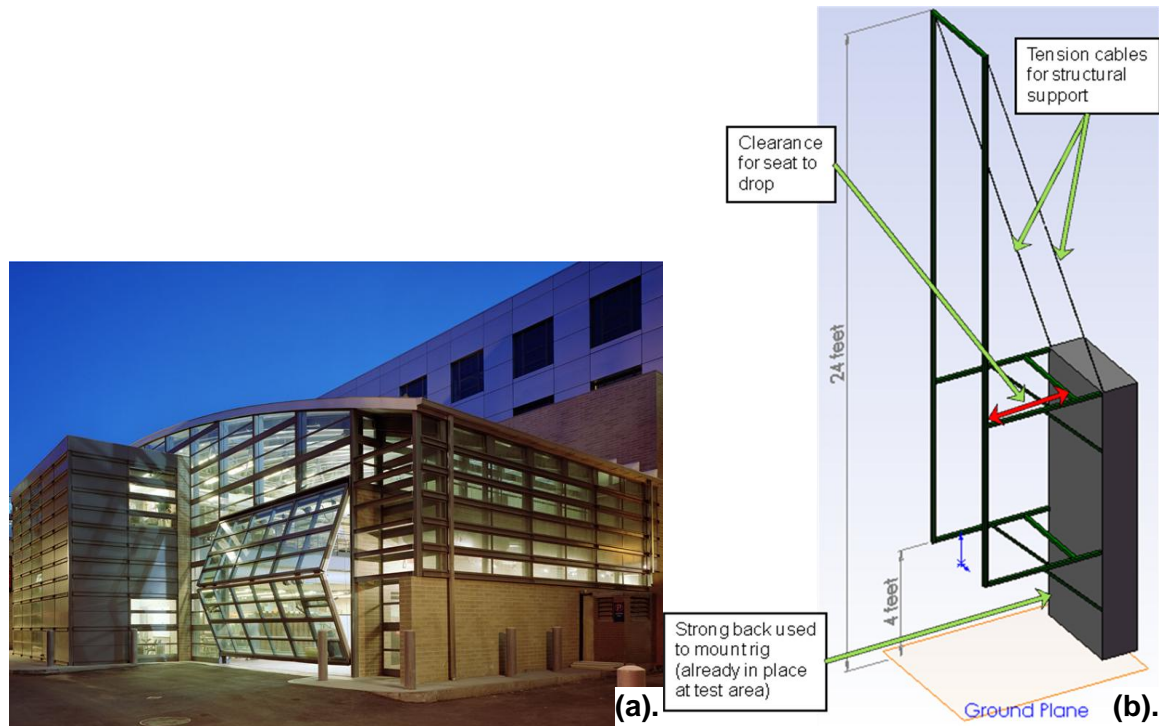


Figure 4-5: Drop Test Infrastructure (a). The Drop Test Location at the MIT Neumann Hangar (b). Drop Test Rig Design

Finally, to emulate the dynamic response of a human occupant, a 50th percentile male Hybrid II Anthropomorphic Test Device (ATD); more commonly referred to as a crash test dummy, was loaned from the NASA Langley Research Center Landing Impact Research Facility. To measure its dynamic response and risk to injury, tri-axial accelerometers were installed inside its chest. The ATD used throughout this research, prior to its delivery to MIT, is shown below in Figure 4-6.

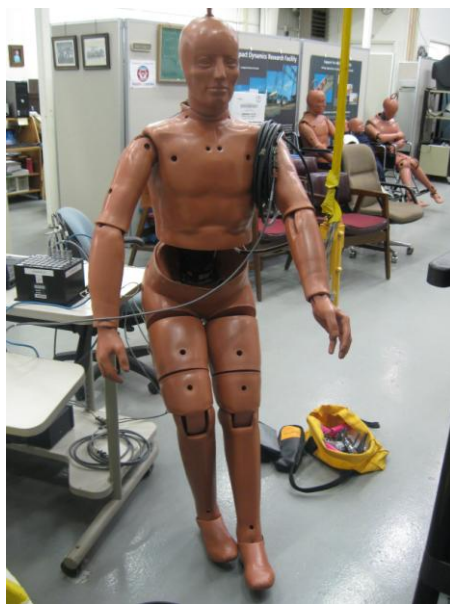


Figure 4-6: Anthropomorphic Test Device used during all Drop Test Campaigns

4.1.4 Airbags to Beanbags

As the supporting infrastructure for the first generation personal airbag system was being designed and built, a separate, parallel effort to fabricate airbags took place. It soon became apparent that this task had several additional design variables not accounted for during the preliminary modeling effort, including material type, stitch patterning, and inflation and venting valve selection. These parameters were eventually defined, with the exception of the venting valve, which became a prohibiting factor.

As was observed in the Chapter 2, venting has been facilitated by some form of burst valve in the majority of previously implemented airbag-based landing attenuation systems. These would open either passively or actively when a predefined acceleration level or

internal pressure was reached. Active systems used a pyrotechnic cutter to rip a designed pattern within the bag; whilst passive systems used disks with precision machined weak points designed to fail at a predetermined pressure load. Clearly, pyrotechnic cutters would not be appropriate for a system located in close proximity to an astronaut in a pressurized cabin; so the passively actuated burst disk was originally baselined for the first generation CIAS.

Upon further investigation into the procurement of commercially available burst disks, however, it was found that they would be prohibitive in cost and lead time given the pressing schedule of the project and its available resources. As a result, it was decided to perform the first test campaign with an analog airbag system, rather than with that originally designed. This analog was chosen to be beanbags – fabric bags filled with polystyrene beans. By moving to this option, the issue of burst disks could be temporarily avoided as there was no longer a requirement to have a hermetically sealed vent prior to impact. Material porosity and sealing was also no longer an issue as the beans forming the analog operating medium had a substantially larger volume than that of their predecessor, making them easier to contain.

Hence with this decision, the objectives of the first generation test campaign also changed. Whilst previously, the primary objective was to evaluate the performance of an airbag-based impact attenuation system; it had now transformed to evaluating the performance of the test equipment and procedures, whilst also obtaining operational and results analysis experience. Although these sets of objectives are not directly related, some valuable lessons were still able to be learned from this initial test campaign, as will be discussed in Section 4.3.4.

4.1.5 Analog-Airbag System Manufacture

As was mentioned in the previous section, the decision to move to a beanbag based system resulted in the significant easing of sealing requirements. One outcome of this was that leakage across the seams was no longer an issue, allowing for simpler manufacturing techniques to be employed, as well as more workable fabrics to be used.

Specifically, PVC-backed high strength polyester was selected as the beanbag material due to its ease of procurement, its workability, and its high strength. Moreover, this fabric was stitched together to form the cylindrical airbag shape using a straight stretch stitch with

nylon thread. Commonly used in construction of parachutes due to its high strength, this stitch involves making three stitches in the forward direction, followed by two stitches in the reverse direction; effectively producing a triple layer of stitching per seam.

Furthermore, to quantify the strength of both the selected beanbag fabric and its seam, a series of tensile strength tests were performed. From this, it was found that the seam failed in tension at 26.7MPa, whilst the fabric failed at 40.5MPa. Although these values were lower than the expected 73MPa maximum hoop stress in airbags of the same dimensions, it was decided to proceed with the original manufacturing choices due to the uncertainty in the similarity between the loading conditions of airbags, compared to beanbags. Figure 4-7 shows the tensile strength test setup, along with the failure mode of the seam.

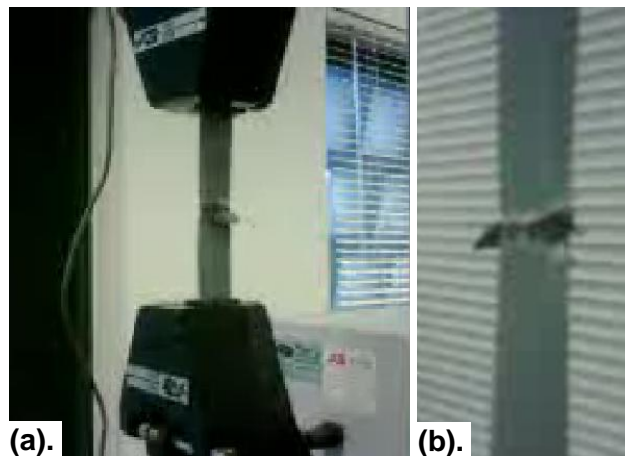


Figure 4-7: High Strength Polyester Tensile Strength Testing (a). Straight Stretch Seam Sample (b). Straight Stretch Seam at Failure

In addition, fill valves were developed to enable simple filling of the beanbags with polystyrene beans. Inspired by the design of salt container lids, these valves were to be placed on the sides of each beanbag to avoid affecting their crush-up dynamics during impact. Figure 4-8 presents an exploded view of the fill valve design.

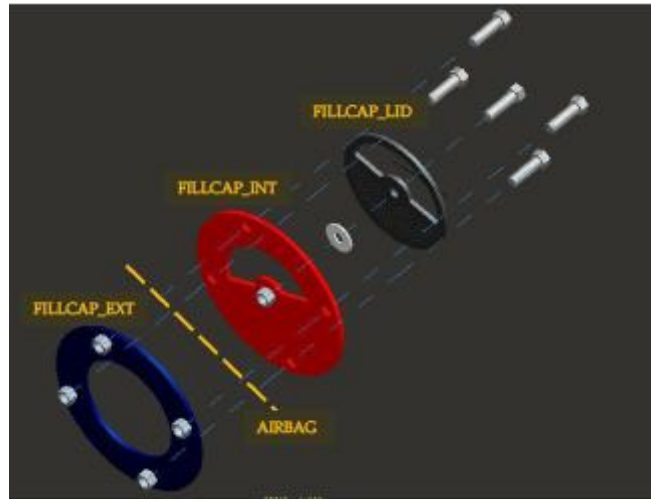


Figure 4-8: Exploded View of Beanbag Fill Valve Design

Hence, with the design of each of the individual beanbag components defined, the beanbags were manufactured and integrated onto the seat structure, which was in turn integrated with the drop test rig. Figures 4-9 and 4-10 show the various components of the system, as well as their integrated state.

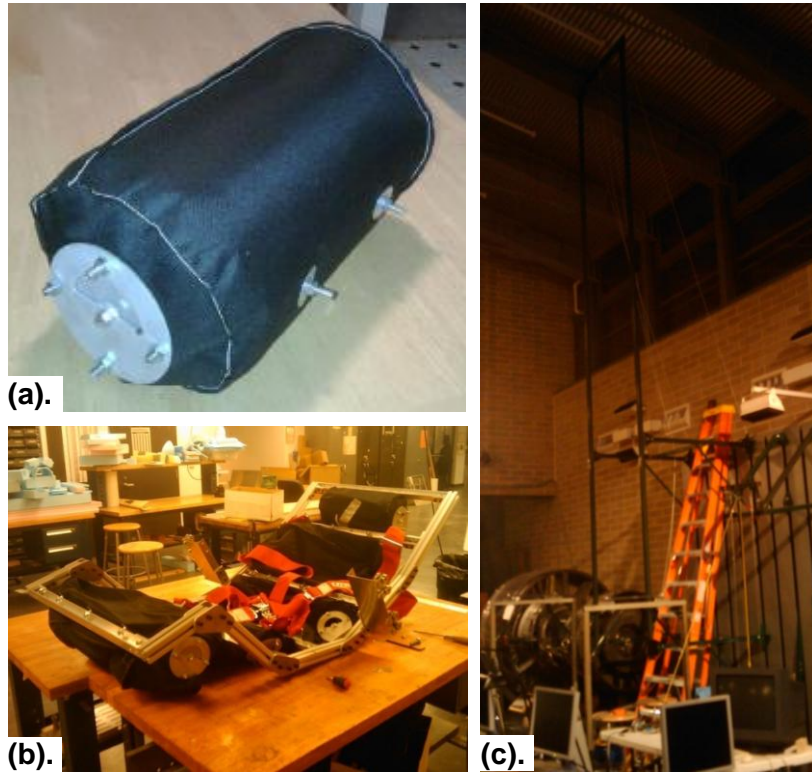


Figure 4-9: System Components (a). Integrated Beanbag (note the fill valve installed on the side) (b). Initial Fit Test of Beanbags with Seat Structure (c). Drop Test Rig

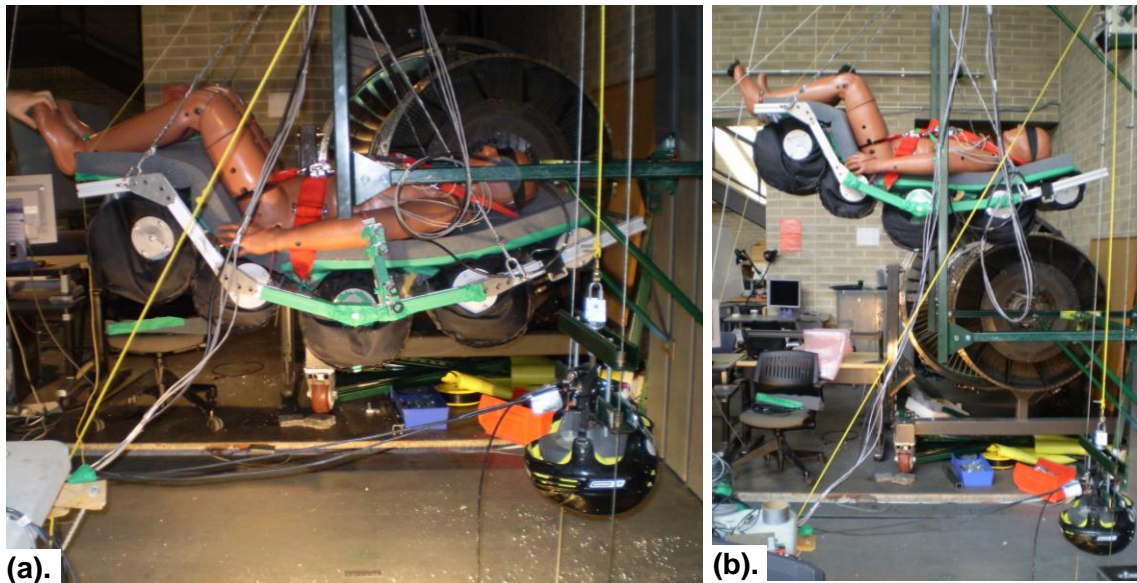


Figure 4-10: Integrated First Generation System (a). Close up view, showing ATD sitting atop a liner and supported by a five point harness, as per recommendations made in Section 2.4 (b). System Hoisted onto Drop Test Rig

4.2 Analog-Airbag System Drop Test Plan

With the first generation system manufactured and integrated, a test plan was developed to achieve the newly defined objectives discussed in Section 4.1.4. This plan involved performing drop tests with the fully integrated system from increasing heights until a failure occurred. Specifically, this consisted of performing drops at a zero impact angle at increasing increments of one foot. Note that this zero impact angle used was based on approximations made in the optimization exercise discussed in Section 4.1.2. This was deemed appropriate based on the newly formed test objectives. Hence by testing in this manner, trends in the system dynamics and its load attenuation capability could be ascertained at varying impact velocities, thus allowing for a performance envelope to be generated. Additionally, this would also enable for the failure modes of the system to be investigated.

With regard to data acquisition, a combination of accelerometers embedded in the chest of the ATD, and high speed camera footage was used. Accelerometer data allowed for the Brinkley DRI time history of each drop to be calculated, whilst high speed camera footage allowed for the dynamics of the system to be studied via the use of photogrammetry (See Section 3.3). Together, this data allowed for the injury-risk level of the system to be related

to its configuration via comparison of the DRI time history with the system dynamics. Figure 4-11 shows the test setup used to perform these drops.

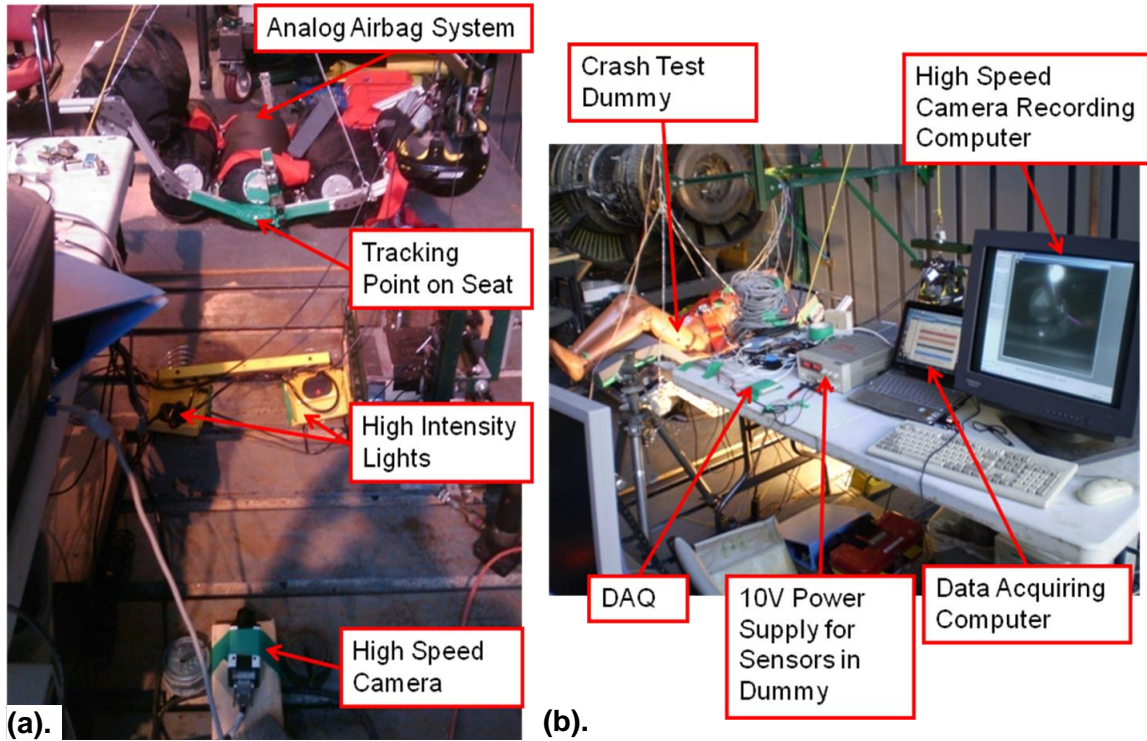


Figure 4-11: First Generation System Test Setup
 (a). Photogrammetric Lighting Arrangement (b). Data Acquisition Center

4.3 Analog-Airbag System Test Results & Analysis

In late April 2009, testing of the first generation personal airbag system prototype commenced. As drops were being performed, the limitations of the 1-DOF model became immediately apparent, with unforeseen two-dimensional effects significantly contributing to the system dynamics. Specifically, this refers to a consistent pitching moment which was experienced during all drops, where the system would bounce and pitch forward after impacting the ground, and experience a forward sliding motion before coming to rest. As the drop height increased, this pitching and sliding motion became more prominent. Figure 4-12 shows a breakdown of this motion.



Figure 4-12: Typical Dynamic Response Seen During Testing
 (a). Impact (b). Bouncing and Pitching (c). Sliding

It was evident from these initial observations that this motion was due to a moment imparted on the system by an offset distance between its center of gravity and the location of the impact. Later analysis revealed that as the system bounced and pitched, its center of rotation changed from being at the lower back beanbag to the lower leg beanbag. As the system was coming to rest after the maximum pitch angle was achieved, its geometry caused the lower portion of the system to slide forward as the center of gravity was returning to the ground. Clearly, because the model used for this first generation design was based on one degree of freedom in the vertical direction, this imparted moment and subsequent pitching motion was not captured.

Additionally, further comparison of the 1-DOF model output and the observed system dynamics indicated that the shape function used to relate the stroke of the bag to its geometry was not entirely accurate, thus influencing the behavior of the subsequent results. Consequently, this motivated the refinement of this shape function, as described in Section 4.1.1.

Hence, as a result of these discrepancies, it was decided to inspect the system for damage after a preliminary set of drops without the ATD. During this inspection, no damage was observed, resulting in the decision being made to proceed with drop testing with the ATD until system failure. After a series of successful and uneventful drops, the system experienced a failure from a drop height of 5 feet, with the lower back beanbag rupturing on impact. Upon detailed analysis of the high speed camera footage for this drop, it was concluded that this failure was due to high pressure in the bag causing a rupture at a local stress concentration generated at the interface between the bag and its fill cap. At the initiation of this rupture, a tear formed in a direction 45 degrees to that of the fiber – the direction in which the beanbag material is the weakest. This conclusion is supported by experience with local stress concentration induced tears gained during preliminary testing, as well as by studying the

beanbag material's failure properties post-testing. Figure 4-13 shows the system immediately after experiencing this failure. Additionally, the reason as to why it was the lower back beanbag that failed was because the system configuration and the test impact angle meant that it was the first to contact the ground, causing it to bear the majority of the impact load of the system.



Figure 4-13: Test Failure from a 5 foot Drop Height

Thus, with the testing campaign completed as a result of this failure, a detailed analysis of the dynamics of each drop commenced. This consisted of using both information obtained from photogrammetric analysis of the high speed camera footage and accelerometer data, processed with a Brinkley model in the following manner:

1. Using photogrammetry, time histories of vertical displacement, velocity, acceleration, and pitch angle were obtained
2. Based on the obtained time histories, time stamps were calculated for important stages in the system dynamics throughout the drop. These stages included the time of impact, the moment at which the end of stroke of the lower back beanbag occurred, and the time at which the maximum forward pitch angle was achieved
3. Using the fact that the maximum vertical acceleration occurs at the end of the first stroke, the timestamp for this event was used to time synchronize the accelerometer data (ie. the

- time at the end of the first stroke corresponds to the time of the maximum vertical acceleration as measured by the ATD's accelerometers)
4. With time synchronized accelerometer and photogrammetrically obtained system dynamics data (and hence resimulated dynamics), dynamically significant information can be extracted. Because the resulting Brinkley DRI time histories are also time synchronized with the accelerometer data, this allows for comparison between dynamic events and their injury-risk level

Note that a detailed comparison of dynamic histories at the photogrammetrically tracked point, and the position corresponding to the Brinkley frame of reference, showed that a negligible time lag between dynamic events occurring at these locations existed between them, thus justifying the validity of this analysis approach. Also, the fact that the photogrammetric analysis and the accelerometer data are referenced to different regions within the test article means that a direct comparison between their outputs cannot be made directly.

4.3.1 Considerations Regarding Measurement Uncertainty

As with any type of experiment, the uncertainty in the obtained measurements is an important consideration to make when performing analysis of the subsequent results. For the case here, these primarily arose from the photogrammetric techniques used to analyze the high speed camera footage, and the accuracy of the accelerometers embedded in the ATD.

With regard to the accelerometer derived error, independently performed calibration tests indicated that their output was accurate to within $\pm 0.4G$'s. Contrastingly, errors arising from the photogrammetric analysis were estimated instead, based on observations made during post-processing of the high speed camera data. This was so because changing lighting conditions and minute angular distortions affecting the image frame prevented a more analytical method of obtaining error values from being used. Specifically, these errors appear in the form of inaccurately tracked pixels shaping the tracking point, and misdetection of lines corresponding to the seat frame. These correspond respectively to the point tracking and line detection algorithms implemented as part of the photogrammetric analysis.

For the error arising from the point tracking algorithm, it is estimated that the calculated position of the illuminated tracking point is within ± 2 pixels of the true location as viewed by

the high speed camera. This estimation corresponds to a displacement error of approximately $\pm 4\text{mm}$ and is based on close examination of the final output of the algorithm used. Correspondingly, the attitude data obtained via line detection was estimated to have an accuracy of $\pm 4^\circ$, with this value being based on a later study performed to investigate the differences between the method used here and other point tracking based attitude estimation techniques. Moreover, the implementation of the human inspection of image frames, where a line corresponding to the seat structure could not be directly detected by the Hough transform algorithm; also contributed to the aforementioned estimated error value. Scenarios where such an inspection was required occurred in frames where a loose cable, stray polystyrene beans, or other such objects obstructed part of the camera's view.

Related to these error sources is the period in time at which their values peak. As expected, the uncertainty in the photogrammetric data is at a maximum at the turning points in the obtained dynamics profiles; where significant dynamic events take place. Specifically, this refers to the fact that the largest point-tracking derived position error occurs at the end of the stroke of the lower back beanbag, which is the first to contact the ground. Similarly, the largest line detection derived angular error occurs at the peak of the first bounce of the system, where it obtains its maximum pitch angle.

4.3.2 Typical Results

Since the results of each test indicate largely the same trends, the results of a single test case will be presented here to show what was typically obtained. Here, this test case will be a drop from an initial height of 3 feet. A summary of the results for all drop tests conducted is summarized in Table 4.4. Figure 4-14 shows the photogrammetrically obtained data obtained from this test.

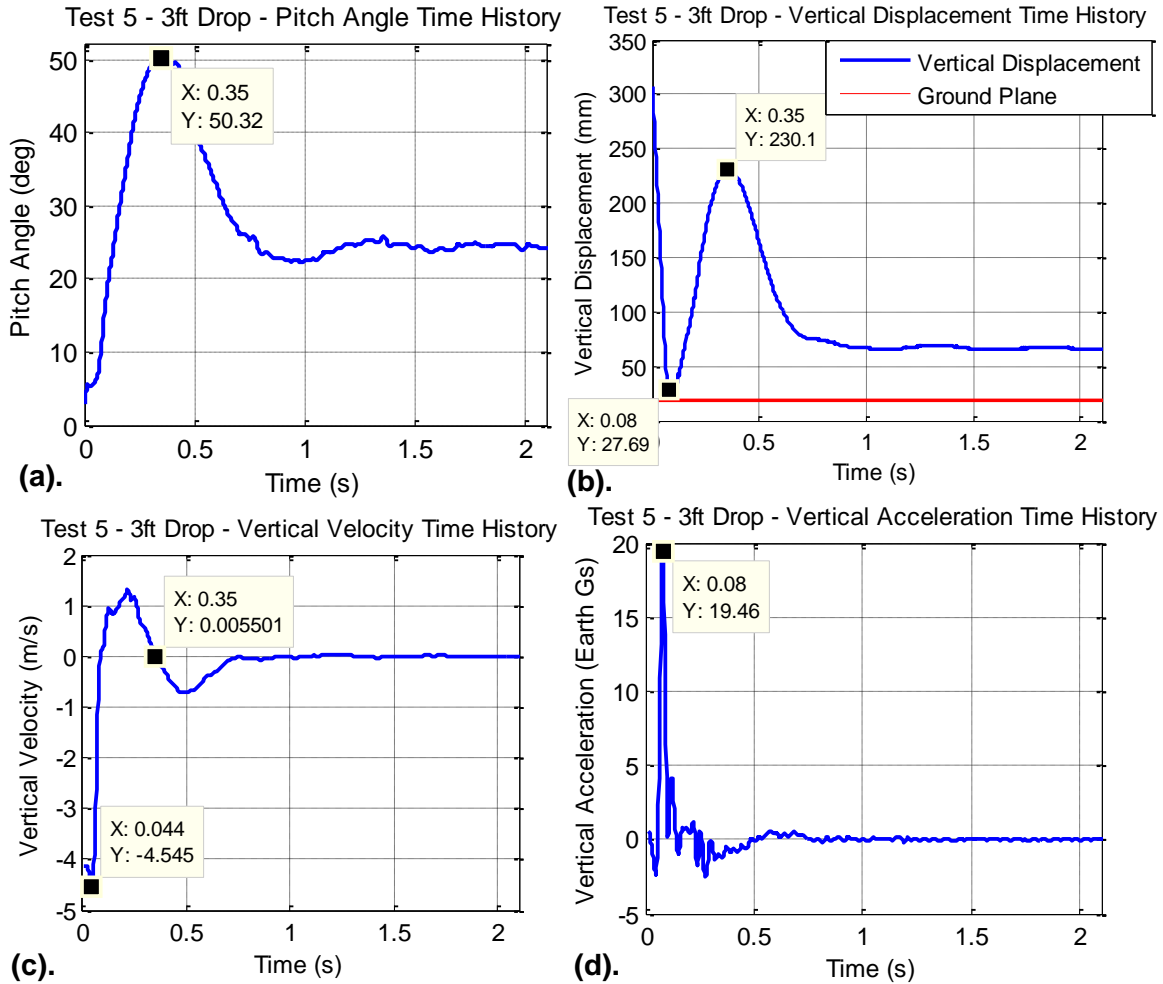


Figure 4-14: Photogrammetrically Obtained Test Results for a 3 foot Drop
 (a). Pitch Angle Response (b). Vertical Displacement Response (c). Vertical Velocity Response (d). Vertical Acceleration Response

Using this information, the timestamps of significant dynamic events and their associated dynamic values can be calculated. This in turn allows for a time synchronization with the data obtained from the ATD embedded accelerometers to be performed, hence enabling for the effect of each event on the acceleration response in the Brinkley frame to be studied. Additional information can also be obtained from comparison of the acceleration response with dynamics resimulated from the original photogrammetrically obtained data. This is summarized below in Table 4.3 and Figures 4-15 and 4-16.

Table 4.3: Time Breakdown of Significant Dynamic Events for a 3ft Drop Test

Event (Numbered event in Figure 4-15)	Time (s)	Method of Identification	Reference Figure	Dynamic Value
Time of Impact (1)	0.044	• Time of max. negative velocity	Figure 4-14(c)	Impact velocity = 4.5m/s
Time of End of First Stroke (2)	0.08	• Time of min. vertical displacement • Time of max. spike in acceleration profiles	Figure 4-14(b) Figure 4-14(d)	Max. acceleration = 19.46G's
Time at Height of Bounce (6)	0.35	• Time where vertical velocity = 0 • Time at max. vertical displacement after the end of the first stroke • Time of max. pitch angle	Figure 4-14(c) Figure 4-14(b) Figure 4-14(a)	Max. pitch angle = 50.3° Height of bounce = 230.1mm

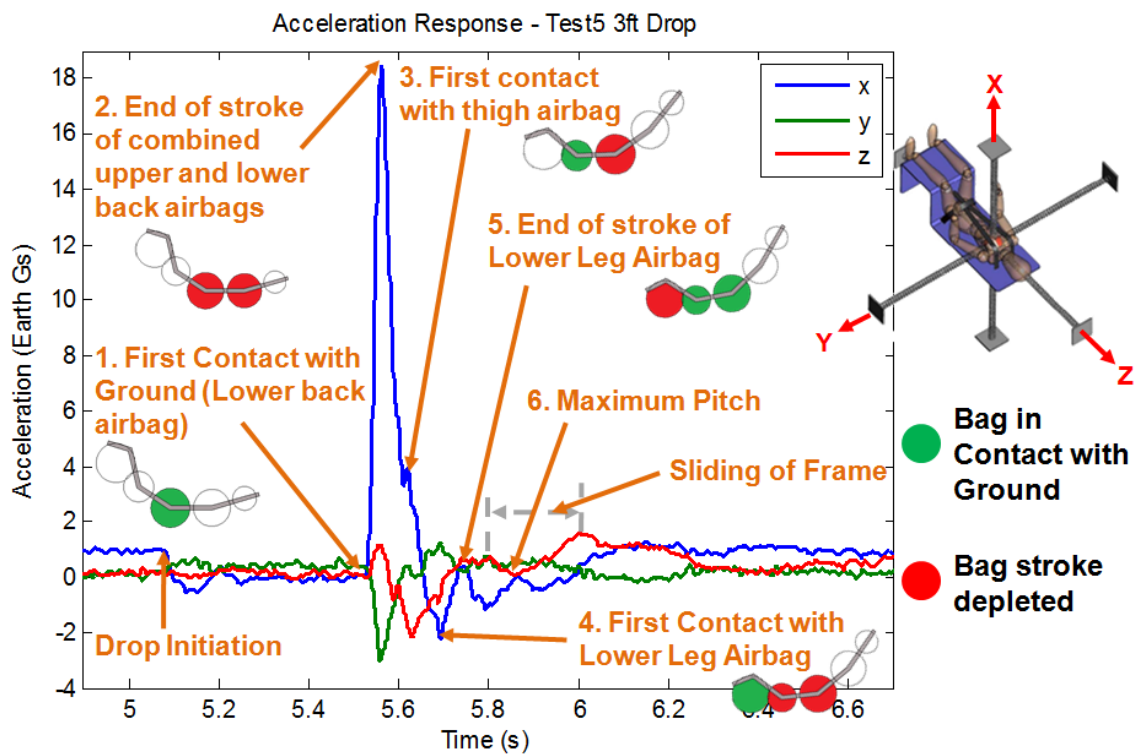


Figure 4-15: Dynamic Breakdown of Accelerometer Data obtained from a 3 foot Drop Test
(Note that the time scale shown here corresponds to that of the accelerometer, rather than the high speed camera, as given in Table 4.3)

As can be seen in Table 4.3, the system impacts the ground at approximately 4.5m/s, a velocity far less than the expected Orion landing velocity of 7.62m/s (25fps). Between 0.04 and 0.05 seconds after this impact, the maximum ATD experienced acceleration of 18.4G's occurs in the vertical x-direction at the end of the stroke, as depicted in Figure 4-15. Following this, the system begins to pitch forward, as previously discussed. Approximately 0.13 seconds after the end of the first stroke, the instantaneous center of rotation of the system moves to the lower leg bag, as it comes into contact with the ground. When the stroke of this bag is depleted, the system starts to slide forward before attaining its maximum pitch angle of 50.3°. From here, the forward sliding slows, as the pitch angle decreases and the system comes to its final resting position. For the current test case, this final resting position is achieved approximately one second after the initiation of the drop.

Hence with a basic understanding of the system dynamics obtained, a comparison can be made between it, and the resulting injury-risk level. Figure 4-17 shows the Brinkley DRI for this test case, normalized with the low injury-risk Brinkley limit (as found in Table 3.3); and its corresponding low, moderate, and high injury-risk beta numbers.

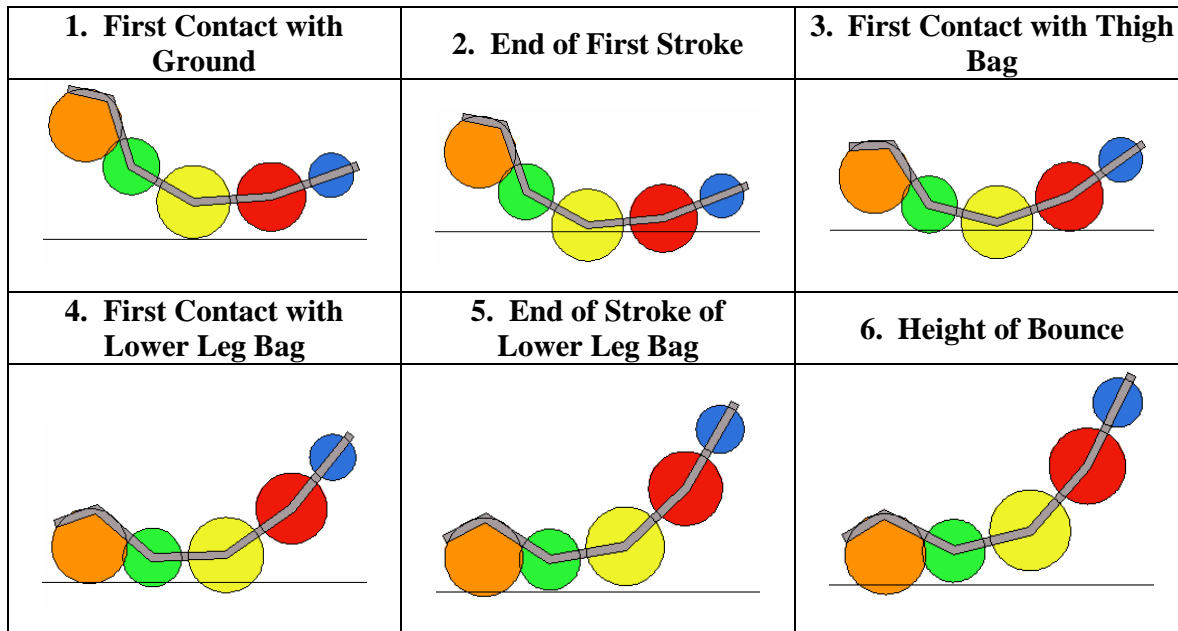


Figure 4-16: Resimulated System Dynamics for a 3 foot Test Drop

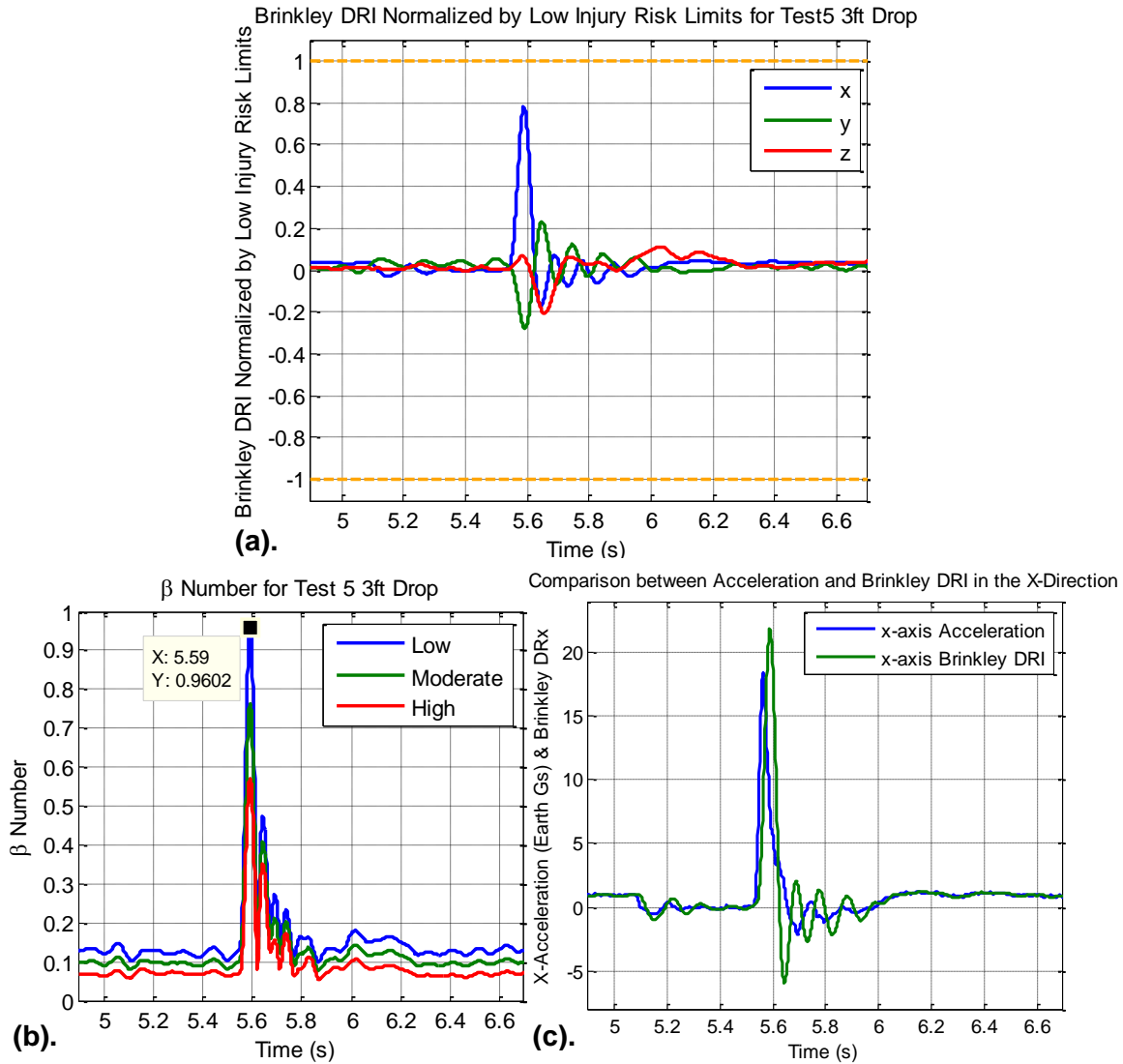


Figure 4-17: Injury-Risk Responses for a 3 foot Test Drop
 (a). Scaled Brinkley DRI (b). Low Injury-Risk β -Number (c). Comparison between Acceleration and Brinkley DRI Response

It can be concluded from Figure 4-17(b) that the injury-risk level for this drop is low, as demonstrated by the value of the low injury-risk β -number remaining less than one for the duration of the impact event. More importantly however, is the fact that the largest contribution to the injury-risk is from the acceleration in the x-direction at the end of the first stroke of the system. This can be seen in Figure 4-17(a), where the contribution from the x-direction is clearly the most significant; as well as in Figure 4-17(c), where it is observed that the largest magnitude spike in the Brinkley DRI corresponds to the moment at which the

initial stroking capability of the system has been depleted. This indicates that the load attenuating capability of the bag which first contacts the ground has the greatest influence on the resulting injury-risk of the impact event, which is to be expected. However, the fact that the Brinkley DRI experiences another spike of noticeable magnitude after this initial spike indicates that some substantial residual kinetic energy remains in the system. Close inspection of the high speed camera footage suggests that the first acceleration spike is due to the lower back bag bottoming out and allowing the seat structure to impact the ground. Only after subsequent bouncing, pitching, and sliding, is this energy removed entirely.

Although the magnitudes of the peaks in the DRI response remain below the low injury-risk threshold for this test case, this bottoming-out event will become significant for drops which more closely emulate the impact velocity of the Orion vehicle's landing scenarios, as will be seen in the next section. It is anticipated that the implementation of venting-type airbags will significantly reduce the magnitude of these DRI peaks, and hence the influence of the resultant bottoming-out event. Incorporating anti-bottoming airbags, like those of Orion's original external airbag system discussed in Section 2.2.4, would also greatly assist in the load attenuation performance of the system. With these additions, it is expected that the magnitude of the initial acceleration spike which occurs upon impact will decrease; whilst the time period over which it occurs will increase. This would result in a lower initial DRI peak and a significant reduction in magnitude of the DRI's secondary peak, thus improving the overall occupant protection capability of the system.

4.3.3 Trends with Varying Drop Height

With the typical system dynamic response characteristics now identified; variations in each of these characteristics with varying drop heights, and their effect on the injury-risk level to the occupant can be investigated. These trends are summarized in Table 4.4 and Figures 4-18 to 4-21.

Table 4.4: Summary of Photogrammetric Analysis Results for all Drop Tests Performed

Drop Height (ft)	Impact Velocity (m/s)	Height of Bounce (mm)	Max Pitch Angle (deg)	Max x-Acceleration (ATD) (Earth G's)	Max Brinkley DRI-X	Risk to Injury (HSIR Specs)
1	2.5	83.8	48.5	8.9	12.1	Very low
1	2.7	94.7	42.5	9.6	12.7	Very low
2	3.7	147.8	47.1	14.2	18.2	Very low
2	3.7	155.2	47.5	14.3	17.9	Very low
3	4.5	211.4	51.0	18.4	21.9	Very low
3	4.7	225.7	48.5	16.5	21.1	Very low
4	5.3	N/A	N/A	22.9	26.3	Low
4	5.5	243.0	50	22.3	26.0	Low

NB. A “N/A” indicates that it was not possible to obtain the indicated data due to surrounding debris obstructing the high speed camera lens.

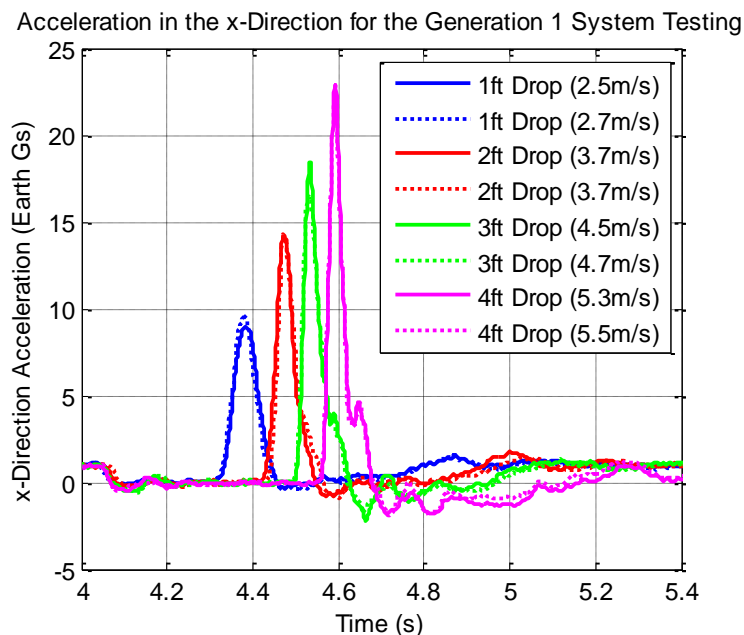


Figure 4-18: X-Direction Acceleration for all Generation 1 System Drop Tests

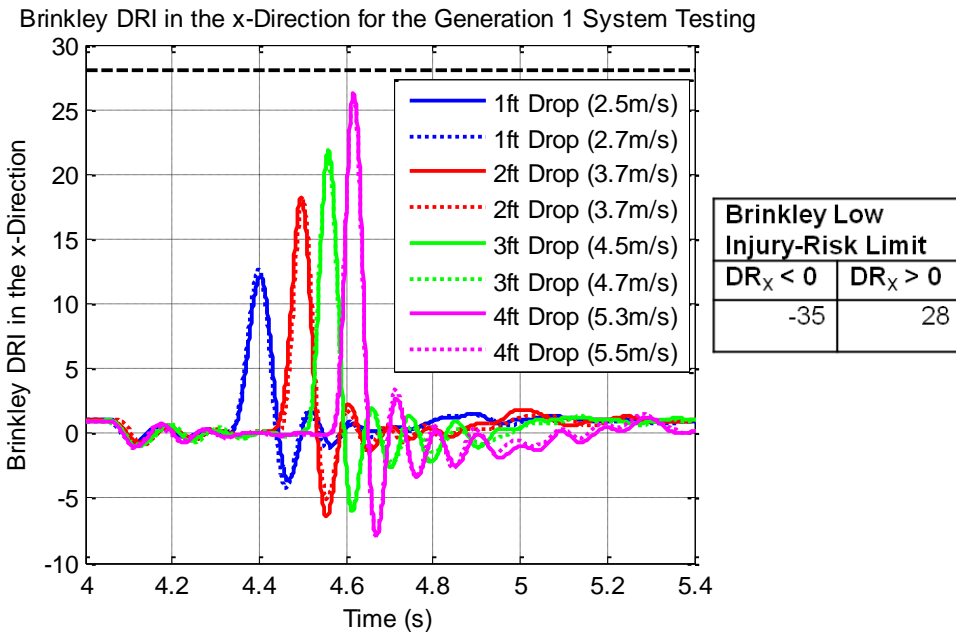


Figure 4-19: X-Direction Brinkley Index for all Generation 1 System Drop Tests

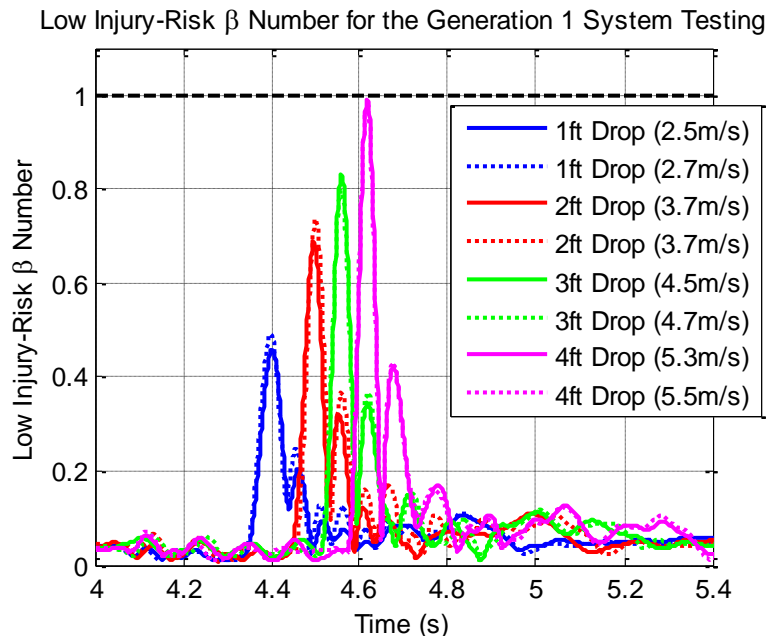


Figure 4-20: Low Injury-Risk β -Number for all Generation 1 System Drop Tests

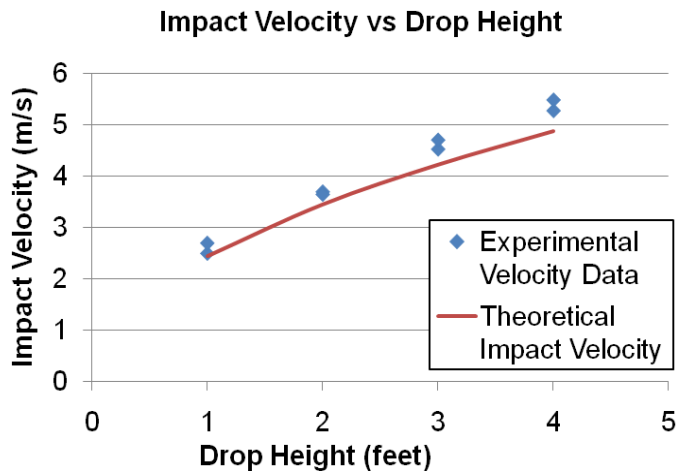


Figure 4-21: Impact Velocity for all Generation 1 System Drop Tests

Note that in Figures 4-18 to 4-20, the same color plots correspond to drops from the same initial height and that in Figure 4-21; the experimentally obtained impact velocity values are higher than those calculated based on the initial drop height. This is due to the manner in which the drops were initiated. Specifically, this refers to the fact that the test rig operator is required to pull down on a quick release mechanism supporting the test article to initiate a drop. This downward pull imparts an additional acceleration on the system, thus increasing its impact velocity. Also, this discussion will focus mainly on the system response in the x-direction as it is the most critical in terms of minimizing the overall injury-risk level at the zero impact angle tested (as was found in the previous section).

Upon first inspection of Figure 4-18, it can be immediately observed that the drop tests performed are indeed repeatable, as indicated by the consistent trends in the system response when the drop height is fixed. Additionally, it is also seen that the maximum impact acceleration, and hence injury risk, increases with drop height, which is to be expected. More significant however, is the fact that for all drops, the low injury-risk β -number remains beneath a value of 1, signifying that a low risk of injury exists for all cases (Figure 4-20). It should be observed, however, that at the 4foot drop cases, the peak low injury-risk β -number comes very close to unity. Hence, based on the increasing injury-risk trend with increasing impact velocity, it can be concluded that the current system would not adequately attenuate impact loads in the nominal landing case. This was indeed expected prior to the commencement of this test campaign due to the fact that analog airbags were used.

A more detailed examination of the acceleration responses shown in Figure 4-18 confirms the fact that all drops display largely the same dynamic trends. These are reflected in the corresponding DRI response, where all drops exhibit a secondary spike of approximately one third the magnitude of the initial impact-induced spike (Figure 4-19). In addition, close inspection of high speed camera footage for each drop, indicated the consistent occurrence of a bottoming-out event corresponding to the time at which the initial acceleration spike occurs. This, in turn, provides further evidence for the need for anti-bottoming bags to be introduced into the next generation system design. Furthermore, this bottoming out was also found to be attributed to the location of the seat structure relative to the bags. In its current configuration, the structure reduces the available bag stroke by one half, causing the bags to bottom out earlier. Consequently, future systems should be designed such that the seat structure enables for the bags they support to expend their entire stroke.

4.3.4 Summary of Analog-Airbag Test Campaign Findings

A first generation analog airbag-based CIAS test article was developed and subjected to a series of drop tests. It was found that for all drops with impact velocities of up to 5.3m/s (a velocity below that of the Orion nominal landing velocity) the system was able to maintain a low-injury risk level. At this maximum attained impact velocity, however, the system was nearing the limits on acceptable performance, indicating that during a nominal landing, the system would not adequately protect the Orion crew members from the imparted loads.

Although this was the case, several lessons were learned which will contribute significantly to future, airbag-based versions of the system. These include:

- The need for the seat supporting structure to be positioned such that it is conducive to maximum bag stroke expenditure, as was observed by the consistent bottoming-out occurring in all tests via the high speed camera footage
- The fact that the highest risk to injury occurs at the end of the combined first stroke of the system, as indicated by the presence of an initial acceleration and corresponding Brinkley DRI spike in all of the responses obtained
- The need to account for two-dimensional effects in the impact dynamics, even though the drops themselves were executed only in the vertical plane.

- The fact that the most probable failure mode in the system is due to local stress concentrations causing the bags to rupture

In addition, the infrastructure required for performing drop tests was implemented and experience in both operating this equipment and performing drop tests in a safe manner was gained. Moreover, experience was also gained in fabricating and integrating all components required for a prototype personal airbag system, thus meeting the objectives of this spiral of system development.

4.4 Chapter Summary

In this chapter, the development and testing of the first generation personal airbag system was described, and the subsequent results and analysis presented. Even though analog-airbags were used in this system, this development cycle yielded important insights into the design and operation of a personal airbag system.

The first and foremost of these, is the importance of obtaining a practical means for venting gas in a manner safe enough for operation in close proximity to an occupant, situated in a pressurized cabin environment. Related to this, is the challenge of making airtight airbags which are strong enough to withstand multiple stress cycles, as well as the local stress concentrations which will inevitably occur within the airbag skin. Finally, the importance of the configuration of the seat relative to the airbags was also highlighted, especially by the consistently observed bottoming-out events and pitch dynamics during impact. It is these issues which formed the basis of the second spiral of system development, which will be described in the next chapter.

Chapter 5

Single Airbag Impact Dynamics Investigation

One of the key outcomes of the analog-airbag system development was the identification of the need to develop the key processes and technologies required to implement and operate impact attenuating airbags. This formed the basis for the second spiral of system development, where the ultimate objective was to develop a working single airbag drop test article and to characterize its impact dynamics via testing, thus producing a baseline dataset for the 1-DOF airbag model to be validated against.

In order to accomplish these objectives, the fundamental challenges of venting mechanism implementation and airbag air-tightening were first explored through dedicated studies. Resolving these issues then allowed for a drop test article to be built and subjected to a drop test campaign - the results of which could be used to refine the original airbag impact model. Before undertaking these activities however, a baseline configuration and related requirements were first required. The processes employed to determine these, as well as the details of each of the subsequent development tasks; will be detailed throughout this chapter.

5.1 Single Airbag System Development

With the key areas of investigation for the single airbag impact dynamics investigation firmly established, the overarching system concept was revisited as the first step in the design of the single airbag drop test article. From here, a design of experiments was performed to explore the design space and determine venting performance requirements. The results of this were in

turn used as the baseline set of specifications for the development of a suitable valve. As will be later discussed, a decision was made to develop valves in-house due to the lack of commercially available options. Concurrently, methods were also explored for leak-proofing fabrics so that airbags could be implemented. The following sections further expand upon each of these phases of the single airbag system design.

5.1.1 System Configuration

Based on the lessons learned and insights obtained from the development and testing of the first generation personal airbag system, the following updated system configuration was conceptualized:

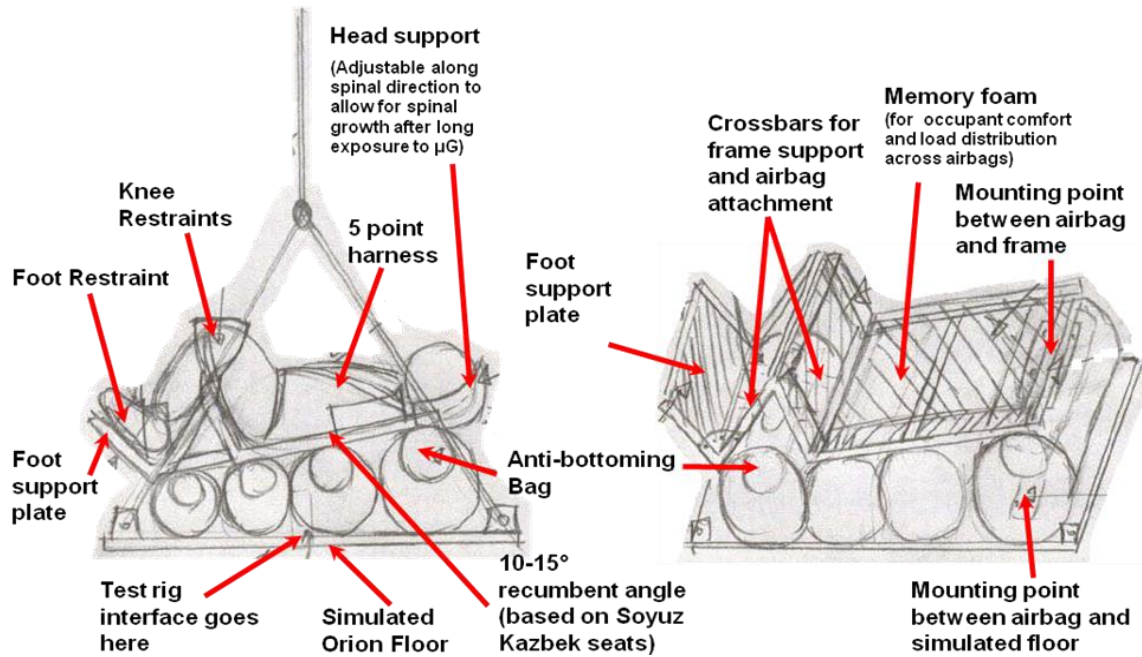


Figure 5-1: Generation 2 Personal Airbag System Configuration

As can be seen in Figure 5-1, there are several notable differences between this and the original system configuration. These are primarily:

- The fact that the system now rests on a simulated floor.

This design decision was based on the realization that the pitch dynamics consistently observed during the first generation test campaign did not replicate the expected dynamics of the system once installed with the cabin of the Orion CEV. Here, the intent

of the floor was to constrain the airbag system in a manner similar to that of an actual personal airbag system.

- The sitting position of the occupant is such that they are in a single plane.

This was again a result of the observed pitch dynamics during the first generation test campaign. Here, it was found that having the occupant sit in a single plane would mitigate the effects of differential airbag stroking, and hence unexpected pitch dynamics during impact. This was especially the case since a multi-airbag configuration was being utilized.

- The seat structure is now situated at the very top of the airbags.

This arose directly from the lesson learned that the seat structure should always be situated such that it maximizes the available stroke in the airbags

- Anti-bottoming airbags are now located within each primary airbag, to mitigate the effects of bottoming-out on the system occupant

Also, as was employed in the first generation system, a liner and five point harness have been included in the system design to support the crash test dummy, as per the recommendations made in Section 2.4.

In addition to these system level changes in configuration, subtle modifications were also made at the individual airbag level, as shown below in Figure 5-2.

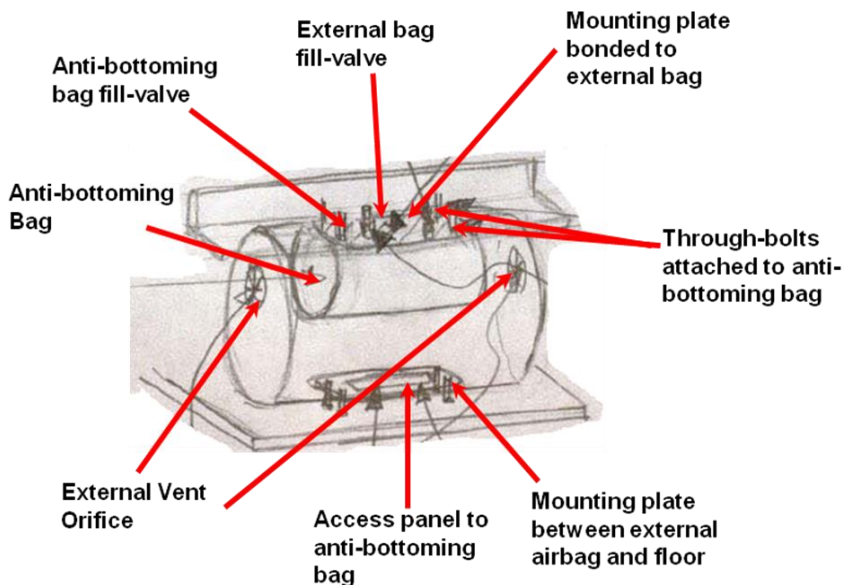


Figure 5-2: Generation 2 Individual Airbag Configuration

Here, it can be seen that valves are located on both sides of the airbag. This was the result of observations made during the first generation test campaign, where because all of the fill valves were located on the same side of each bag; any air internal to the bags was released on only one side of the bags during impact, causing the entire system to tilt towards one side. This can be seen below in Figure 5-3(a). Also note that the filling mechanisms were designed with a series of holes to allow some air to escape during impact, thereby reducing the stresses induced within the bean bag material. Figure 5-3(b) shows a detailed view of these filling mechanisms.

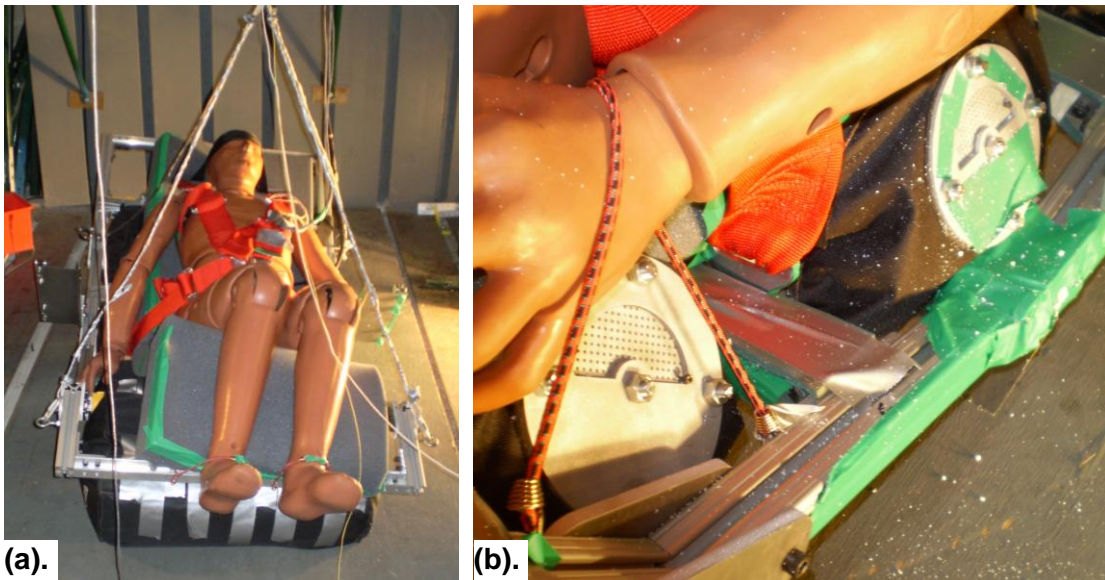


Figure 5-3(a): Tilting of the First Generation System after a 3ft Drop

(b): Detail of the Filling Mechanisms used on the First Generation System

Furthermore, it was also decided to implement a layer of gasketing at any hard point to fabric interface in the airbag. Although not shown in Figure 5-2, the intent of this addition was to provide better stress distribution across any hard edges within the airbag, thereby reducing the magnitude of the generated local stress concentrations, and hence the likelihood of a rupture from occurring.

In addition, for the purposes of this study, the geometry of the airbag to be used in the drop test article was constrained to be that of the head airbag of the first generation system – that is, a $\varnothing 220\text{mm} \times 350\text{mm}$ cylinder. This decision was based on the desire to construct multiple full size prototypes to refine manufacturing and interfacing techniques with venting

mechanisms and other hard points. By choosing a smaller geometry, less material would be required to develop each prototype, thus reducing development costs. Smaller geometries also lead to quicker manufacturing and easier overall handling, hence reducing development time. Moreover, this geometry further led to the decision to fix the value test mass to be equivalent to the mass of a human head - that is, 2.27kg (5lbs).

5.1.2 Design of Experiments

In addition to the high level architecture and geometric dimensions for the drop test article defined in the previous section, parameters related to the inflation and venting characteristics of the system are required to completely define the system. In particular, these are the airbag inflation pressure, the orifice area, and the condition by which the orifice opens, measured here by a threshold acceleration value.

It should firstly be noted however, that for the current study, the inflation and venting characteristics found in the first generation design process are no longer valid. This is due to the earlier discovery of inaccuracies in the initially implemented model shape function, as described in Section 4.1.2. As a result, a repeat of the sizing process is required to obtain updated design values via improved performance predictions using the model incorporating the final shape function presented in Section 3.1.2.

To perform this process, a recursive form of the “One at a Time” Design of Experiments method was used. Here, the values baselined in the first generation system development were used as an initial guess, and one variable was selected and optimized over before moving onto the next variable. In order to optimize over a certain variable, the Brinkley response for each design vector along the dimension of the variable was plotted, and the value corresponding to the lowest Brinkley DRI magnitude selected. One advantage of this visual form of optimization is that the relative sensitivities of the system performance to changes in each of the design variables could be easily seen. These sensitivities were also used to determine the order in which each variable would be optimized over, with the most sensitive variable being chosen first. Hence once all variables had been optimized over, the process was repeated to ensure that the final design vector remained “optimal”. Note that the final obtained solution is not necessarily optimal due to the fact that this method does not account

for interaction effects between the variables. As a result, the recursive step of cycling through the individual variable optimizations was implemented to compensate for this.

This process was initiated with the first generation head airbag design vector, given as follows:

$$x_0 = \begin{bmatrix} \text{Radius}(m) \\ \text{Length}(m) \\ \text{Inflation Pressure}(kPa) \\ \text{Orifice Diameter}(in) \\ \text{Orifice Opening Acceleration}(G's) \end{bmatrix}^T = \begin{bmatrix} 0.11 \\ 0.35 \\ 106.4 \\ 2.8 \\ 15 \end{bmatrix}^T \quad (5.1)$$

Note here that “orifice diameter” refers to the diameter of one of the two orifices located on either side of the airbag, as indicated in Figure 5-2. Hence the total venting area in the airbag is given by: $2 \times \pi(\text{Orifice Diameter})^2/4$

From here, the Brinkley response of the system was determined with each of the three parameters varied while all others were held constant. The results of this are shown in Figures 5-4 to 5-6. Note that all simulations conducted as part of this exercise were for a single airbag impacting at the nominal Orion landing velocity of 7.62m/s (25fps).

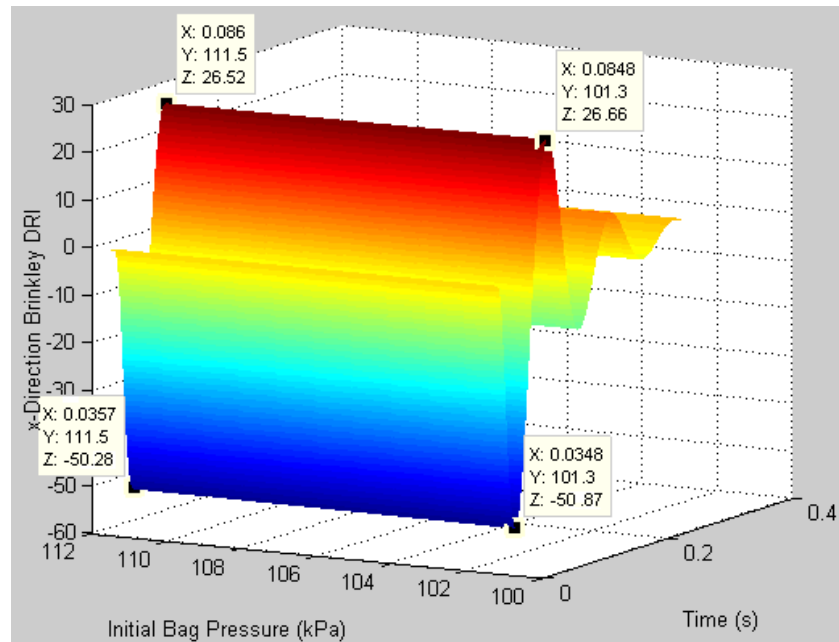


Figure 5-4: Brinkley Response with fixed x_0 and Varying Inflation Pressure

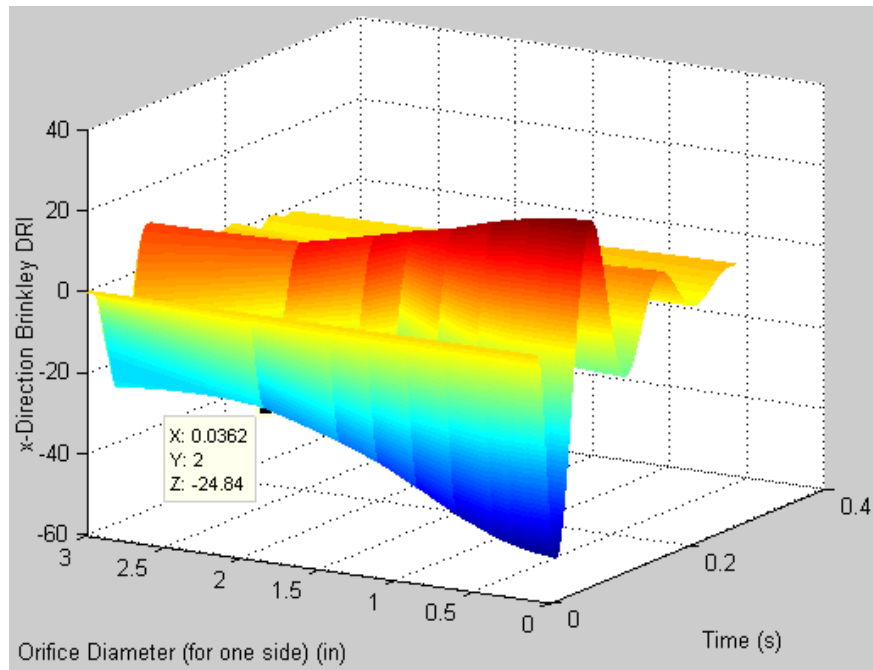


Figure 5-5: Brinkley Response with fixed x_0 and Varying Orifice Diameter

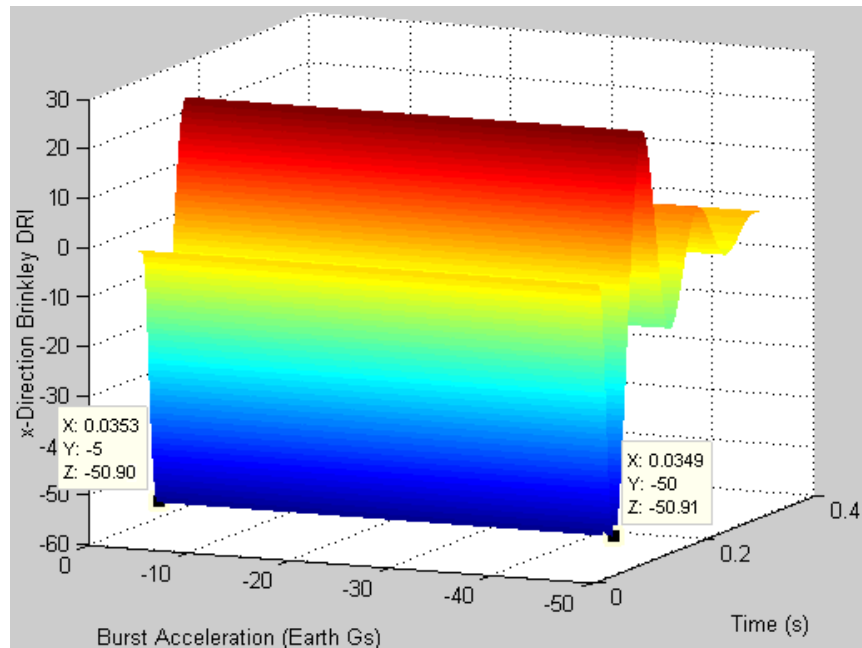


Figure 5-6: Brinkley Response with fixed x_0 and Burst Acceleration

Here, it can be seen that the injury-risk response is most sensitive to changes in venting orifice diameter, with the optimal configuration having a diameter of 2 inches bringing the

Brinkley response to within low injury-risk limits. Also of interest is the fact this Brinkley response does not change monotonically in a given direction with varying orifice diameter. This suggests that there is a trade-off between having a larger orifice area to remove energy from the system during impact, and a smaller orifice area to prevent excessive air from escaping the system, causing the stroke to decrease at a rate where the effects of bottoming-out become prominent.

Hence with this finding, the orifice diameter was fixed to a value of 2 inches and the Brinkley index was determined for variations over each of the two remaining parameters. Here, the baseline design vector was given by:

$$x_1 = \begin{bmatrix} \text{Radius}(m) \\ \text{Length}(m) \\ \text{Inflation Pressure}(kPa) \\ \text{Orifice Diameter}(in) \\ \text{Orifice Opening Acceleration}(G's) \end{bmatrix}^T = \begin{bmatrix} 0.11 \\ 0.35 \\ 106.4 \\ 2 \\ 15 \end{bmatrix}^T \quad (5.2)$$

The results of this next step are as follows:

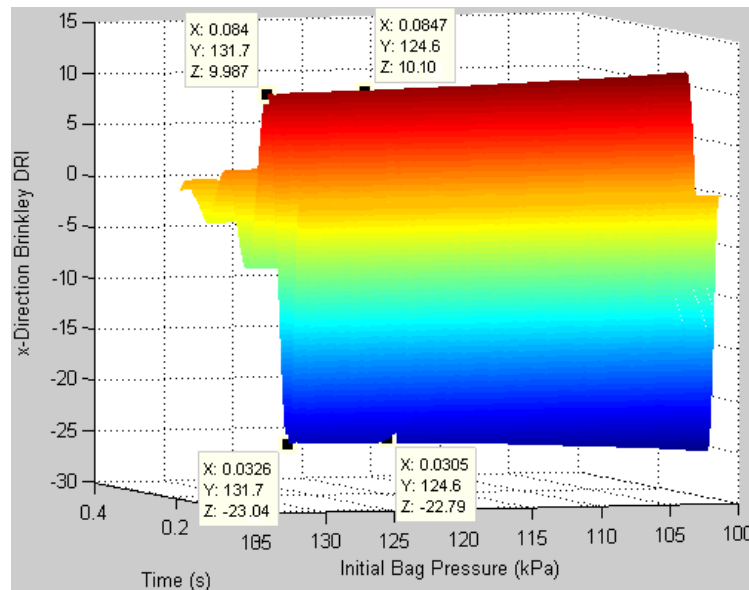


Figure 5-7: Brinkley Response with fixed x_1 and Varying Inflation Pressure

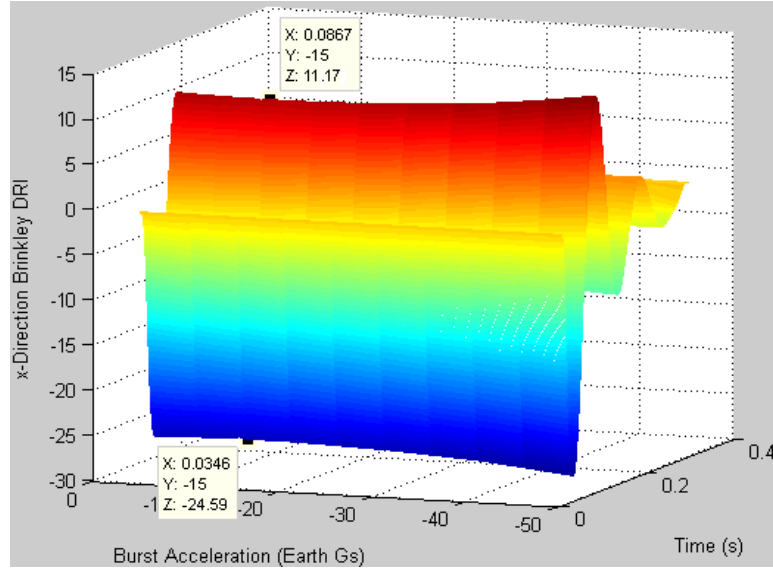


Figure 5-8: Brinkley Response with fixed x_1 and Burst Acceleration

From Figures 5-7 and 5-8, it can be seen that between the two investigated variables, the system performance is most sensitive to changes in the orifice burst acceleration. In addition, it is interesting to observe that the optimal burst acceleration is 15Gs, which is the same value as that of the baseline design vector used to generate this result. As a consequence, the performance sensitivity to varying inflation pressure presented in Figure 5-7 can be used to determine the “optimal” value, found here to be 124.6kPa.

Related to this, is the fact that Figure 5-7 indicates that the performance of the system is highly insensitive to perturbations in the airbag inflation pressure. This is highlighted by the fact that a 10kPa variation in the inflation pressure yields a difference of less than 1 in the corresponding Brinkley index. This subsequently has major implications on the operational aspects of a personal airbag system, particularly by the fact that precise inflation of the airbags is not required for robust system performance. This in turn leads to less stringent requirements on inflation mechanisms and pressure gauges, which is an unforeseen benefit of airbag-based impact attenuation.

Furthermore, Figure 5-8 indicates that the performance sensitivity relative to changes in this burst acceleration increases overall, when the orifice diameter is set to 2 inches, compared to the original baseline of 2.8 inches (see Figure 5-6). This implies that an interactive dependency exists between the choice of orifice diameter and the orifice opening condition in terms of overall impact attenuation performance. This makes intuitive sense as both these variables dictate the venting characteristics of the airbag.

Finally, the curvature along the changing variable axis apparent in both Figures 5-7 and 5-8 indicates that trade-offs exist in their selection. Inspection of the governing equations of the impact model indicates that these tradeoffs, like that of the orifice area, are related to the venting characteristics of the airbag. Specifically, this refers to the fact that the choice of burst acceleration affects the time at which the orifices open, and hence the amount of energy released from the system; while the choice of inflation pressure affects the flow properties of the gas through these orifices when they are open. In both cases, there is a balance between not releasing enough energy from the system via the venting of gas; and venting too much gas initially during the impact to the point that bottoming-out effects become apparent.

Thus, the first “optimal” design vector was found to be:

$$x^* = \begin{bmatrix} \text{Radius}(m) \\ \text{Length}(m) \\ \text{Inflation Pressure}(kPa) \\ \text{Orifice Diameter}(in) \\ \text{Orifice Opening Acceleration}(G's) \end{bmatrix}^T = \begin{bmatrix} 0.11 \\ 0.35 \\ 124.6 \\ 2 \\ 15 \end{bmatrix}^T \quad (5.3)$$

With this initial “optimal” baseline established, the recursive component of the method was executed, whereby the optimality of the solution was checked by repeating the “One at a Time” process. Here, this commenced with once more investigating the sensitivity of the system performance with varying orifice area – the parameter previously found to be most sensitive. The result of this is as follows:

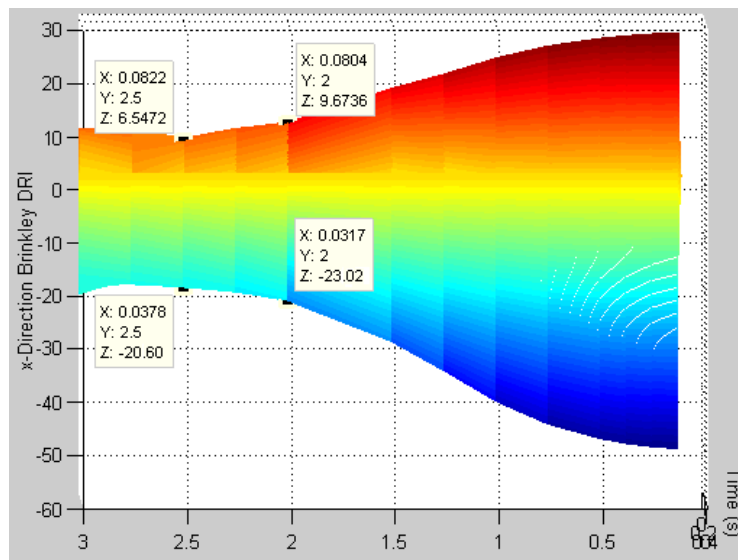


Figure 5-9: Brinkley Response with fixed x^* and Varying Orifice Diameter

From Figure 5-9, it can be seen that the optimal venting area has now moved to one with a 2.5inch diameter. The baseline diameter of 2inches, however, also results in a relatively strong impact attenuation performance when compared to other dimensions. This in turn indicates that the performance of x^* is near optimal. Because the objective of this study is to characterize the impact dynamics of a single airbag, this near-optimal design was deemed adequate for its purposes. Additionally, the equivalent diameter for the desired venting mechanisms was relaxed to lie between 2 and 2.5inches, thus increasing the number of available options for valve procurement. Consequently, the final baseline design vector to be used as a starting point for subsequent design activities was set to:

Table 5.1: Baseline Design Vector for a Single Airbag with Burst Valves

Parameter	Value
Test Mass	5 lbs (2.27kg)
Radius	110mm
Length	350mm
Total Vent Orifice Area	2 x $\emptyset(2\text{-}2.5")$ holes
Initial Airbag Pressure	125kPa = 1.23atm
Burst Acceleration	-15G's
Corresponding Burst Pressure	Approx. 130kPa (4psig)

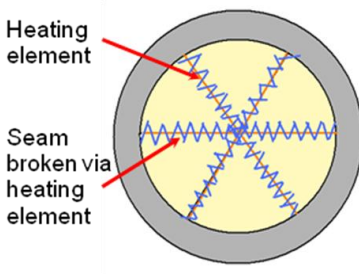
It should be noted here this design vector is baselined specifically for an airbag employing burst type venting mechanisms. That is, mechanisms which open, and stay open once triggered. In the case that the venting concept changes, the values for these design variables would need to be revisited.

5.1.3 Valve Development

Although basic venting criteria were now defined for the single airbag drop test article, no decision had been made as to how this capability would be physically implemented. To address this, a series of venting concepts were developed and presented to the NESC for their input. These concepts, along with their advantages and disadvantages, are summarized below in

Table 5.2.

Table 5.2: Venting Mechanism Concepts Presented to the NES

	Pressure Relief Valve	Heating Element Actuated Burst Disk	Microcontroller Actuated Solenoid Valves
			
Actuation Method	Passive Air pressure pushes against a spring, pushing open a poppet	Active Pressure transducer or accelerometer signal is used to turn on a heating element which melts a seam holding the valve closed	Active Pressure transducer or accelerometer signal is used by a microcontroller to command a set of solenoid valves
Notes	Suggested by NES. Widespread commercial use	Suggested by NES. Inspired by plastic burst disks used in hypervelocity impact guns	Investigated by the PSU team as part of a separate project
Pros	- Simple system. - May be commercially available	- Lightweight - Orifice opening condition able to be varied - Orifice diameter can be sized as desired	- Very robust system – both opening condition and opening area can be varied. Can be made adaptive to various landing conditions based on microcontroller logic
Cons	- Relatively limited operational flexibility in terms of opening conditions and orifice sizes	- Time delay from signal to valve opening may be an issue - Some added complexity - In house development likely required	- Significant added complexity, which increases the number of potential failure modes - Potentially very heavy

Upon discussion of the aforementioned concepts with the project stakeholders, it became apparent that there was a desire to minimize system complexity as much as possible, as this would reduce the number of potential failure modes which could occur during the critical phase of landing. In addition, a concept which was quick to implement was also desired, due to the project time constraints and the fact that the overall objective was to determine

feasibility, rather than focus on developing robust means for airbag venting. As a result, the pressure relief valve concept was baselined as the venting mechanism of choice.

Survey of Commercially Available Pressure Relief Valves

As was previously mentioned, one of the major advantages of opting for pressure relief valves as the method of venting is that they are commonly used, and hence widely available. With this in mind, a survey of commercially available valves was conducted to generate a list from which the final valve could be chosen. Upon doing this however, it was discovered that the requirements generated in Section 5.1.2 were largely mutually exclusive in the context of marketed pressure relief valves. Specifically, this refers to the fact that:

- Pressure relief valves with large outlet diameters are typically used in industrial applications and operate at a high pressure; whilst
- Low pressure valves tend to have very small outlet diameters

This final observation can be observed from

Table 5.3, which gives a sample of the valves offered by McMaster-Carr® which operate within the required pressure range.

Table 5.3: Pressure Relief Valves Offered by McMaster-Carr®

	Opening Pressure	Venting Diameter	Height	P/N
Brass Pop-Safety Valve	10, 15, or 20psig	1"	5.75"	9024K15
Bronze Quick Exhaust Remote-Discharge ASME Pop-Safety Valves	15psig	2"	2.25"	4699K7
Bronze Low-Pressure Pop-Safety Valves (NPT Female Side Outlet)	5,6,8,10 or 12psig	1"	1.8125"	4699K13
Cast Iron Quick-Exhaust ASME Pop-Safety Valves	2-60psig	2"	3.75"	8175K12
Brass Adjustable Vacuum/Pressure Relief Valve	Adjustable from 0-20psig	3/4"	2.75"	48935K45

In addition, it was found that only custom designed and built valves were capable of meeting the determined requirements. However, these were prohibitive in both cost and delivery time.

As a consequence, it was decided to develop pressure relief valves in-house. Although this contradicted one of the key rationales for selecting this concept, it was deemed as the easiest concept to mature when compared to the other options. This would in turn reduce development time, enabling more time to be focused on meeting the primary project objectives.

Pressure Relief Valve Conceptual Development

One notable valve concept found during the search for commercially available valves was the flapper valve. First observed in a catalogue from the custom valve design company ValveTech Inc., this concept was simple, able to facilitate large venting areas, able to have its opening pressure easily adjusted, and had a minimal geometric footprint. As a result of this, a flapper valve of similar design was designed to meet the earlier defined venting requirements, and built for testing. Figure 5-10 shows a comparison between the ValveTech design, and the first generation flapper valve build in-house.

 VALVETECH, INC. Flapper Valve P/N11070	First Generation Personal Airbag System Valve
 <ul style="list-style-type: none"> • Developed for the Orbital Sciences X-34 Propulsion System Tanks • Low pressure operation • Low leakage with gaseous helium 	 <ul style="list-style-type: none"> • Outlet area size to be between 2 and 2.5" • Springs sized to open at a pressure of approximately 130kPa

Figure 5-10: Comparison between ValveTech flapper valve and valve developed in-house

Pressure Relief Valve Leakage Testing and Proofing

In order to test the performance of the first generation flapper valve, a series of leakage tests were conducted. Specifically, this involved mounting the valve onto a pressure vessel, and observing the pressure time history as this vessel was inflated to determine its venting characteristics. In addition, leak detection fluid was applied about the seat of the valve to visually indicate the opening of the valve. This test setup is summarized in Figure 5-11.

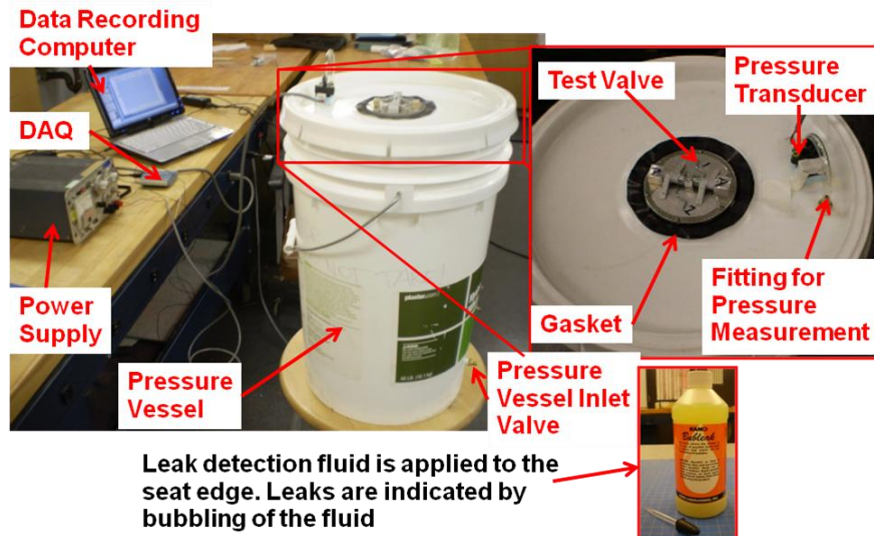


Figure 5-11: Flapper Valve Leakage Testing Setup

Upon conducting these tests, it was immediately observed that leakage was a major issue with this first prototype; so much so that the pressure within the pressure vessel was found to have never increased above that of atmospheric. Figure 5-12 shows the extent of this leakage, as captured by a video camera monitoring these tests.

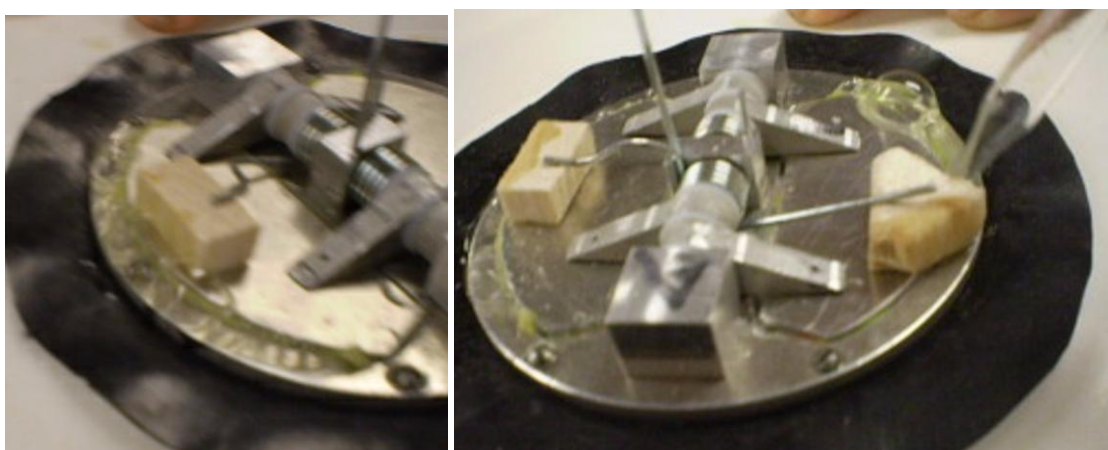


Figure 5-12: Close up views of leakage of First Generation Flapper Valve

Close inspection of the valves after this set of tests indicated that one of the prime contributions to this leakage was the lack of a sealing material located between the opening flap and the valve seat. Instead, a metal-to-metal seat had been originally implemented to determine if this provided an adequate seal. As the results of this test campaign indicated that this was clearly not the case, an investigation into the appropriate sealing material was initiated. This involved procuring potential sealing materials, installing them onto the test valve, and subjecting the valve to a set of leakage tests. Such materials included silicone sealant, neoprene rubber, and memory foam. Moreover, this set of tests highlighted the need to preload the valve springs, a consideration not previously made as this feature was not observed on the original ValveTech concept (see Figure 5-10). Tables 5.4 and 5.5 summarize the results of all tests performed in this investigation.

Table 5.4: Summary of Leakage Tests Conducted during the Sealing Material Investigation

Test No.	Valve Config.	Observations	Conclusion	Image
1	Original (metal to metal seat)	Significant leaking felt by hand. Leak fluid seeped through Pressure transducer indicated no change in container pressure	Perform control test of pressure transducer. Sealing required at seat	
2	Dummy Valve (Control Test)	Pressure transducer indicated expected increase in container pressure Container bulged significantly	Pressure transducer has an adequate accuracy and works as expected Container cannot withstand expected burst pressures	
3	Neoprene Backed Flaps	Slight improvement on Test 1. Significant leaking observed. Leak fluid seeped through Pressure transducer indicated no major pressure increase	Covering entire hatch restricts room for material to deform and hence seal Neoprene is too firm for this application	

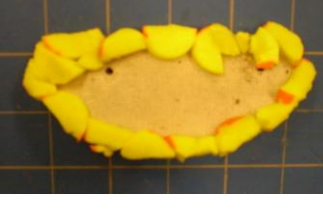
4	Dow Corning Silicone Sealant on Seat	Performance similar to the observed in Test 3	Silicone rubber did not fill all gaps in seat. Silicone sealant is not viscous enough for this application Preloading required on spring to provide downward force	
5a	Memory foam backed flaps with preloaded springs	Leakage still observed, however it is improved upon the initial tests Significant leak fluid bubbling observed	Although this material conforms well to the seat and flap, its porosity causes it to leak. Hence this material has been ruled out .	
5b	Ear plug (vinyl) foam backed flaps with preloaded springs	Much improved performance over previous tests Some leak fluid bubbling observed from areas of imperfect material application	This material has potential for providing the required sealing capability. Leakage was traced to imperfections in the installation of this material	

Table 5.5: Summary of Leakage Tests Conducted during the Sealing Material Investigation

Test No.	Valve Config.	Observations	Conclusion	Image
6a	Marian Chicago Vinyl foam tape backed flaps with preloaded springs	See 5b	This material has potential for providing the required sealing capability. See Test 5b	
6b	Dennis RCR Vinyl foam tape backed flaps with preloaded springs	Leakage analogous to that observed in Test 5a	This material has been ruled out . See Test 5a	
7a	ULine Vinyl Foam backed flaps with preloaded springs	Sealing capability is better than un-preloaded springs, however its leakage is greatest relative to all previous conducted preloaded tests	The firmness of this material is too high for this application. This causes it to not conform well to the seat surfaces. Hence, this material has been ruled out	

7b	Original Neoprene backed flaps with preloaded springs	Leakage analogous to that observed in Test 7a	Preloading the springs did not significantly improve the sealing ability of this material. Hence, this material has been ruled out See Test 7a	
----	---	---	--	--

As can be seen in the results presented in the above tables, all materials except for vinyl foam rubber were found to be inadequate for the flapper valve application. Here, the idea for exploring this material arose from the observation that the material used for industrial earplugs was viscoelastic, and had a completely closed cell, non-porous structure – properties ideal for sealing applications. When performing leakage tests with this material however, some minor leakage across the valve seat was still observed. It was hypothesized that this was a consequence of the seat area being too small for the material to provide an effective seal. As a result, a second generation flapper valve was developed with a substantially larger seat area to investigate this hypothesis. This is shown below in Figure 5-13.



Figure 5-13: Second Generation Flapper Valve

As depicted in Figure 5-13, the second generation valve consists of largely the same components as that of the first generation, with the only differences being the design of the valve body and the pieces used to connect the outlet hatches to the valve mandrel. The intent of this was to leverage parts which had already been manufactured, thus enabling the effect of the increased seat area to be quickly studied.

Upon integration and testing of this valve however, it became apparent that an error had been made earlier in the selection of the valve springs. Originally, it was believed that the torque values specified by the spring manufacturers corresponded to the state at which the

spring was unloaded. Testing of the springs indicated that this was not the case, and that the torque values instead indicated the resistive force produced by the spring when deformed at a 90° angle. Consequently, these spring calculations were revisited and the appropriate spring selected. This led to the development of the third generation valve, which was subsequently proved to meet all leakage requirements through leakage testing. This final valve design is shown in Figure 5-14.

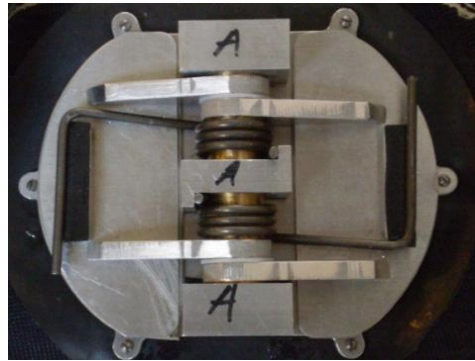


Figure 5-14: Third Generation Flapper Valve

Here, it can be seen that the overall size of the third generation flapper valve has increased substantially when compared to its earlier generations. This is the result of the increased geometry of the stiffer springs driving the increase in the size of its supporting components, and hence the size of the entire valve.

Third Generation Valve Characterization Testing

With a leak-proof flapper valve design established, a series of characterization tests were performed to determine the valve burst pressure as a function of spring pre-load angle. In doing so, a data set was produced, which could be used for refinement of the venting module of the single airbag impact model. Here, a similar setup to that used for the leakage tests was employed, where the valve was mounted onto a pressure vessel and inflated to observe its behavior. To characterize the valve performance, this process was repeated for different preload angles of its torsional springs. Specifically, preloading was facilitated by using strips of both rubber and aluminum to vertically displace the leg of each torsional spring, thereby

imparting an angular offset. Figure 5-15 shows the test setup used, whilst Figure 5-16 shows the results obtained.

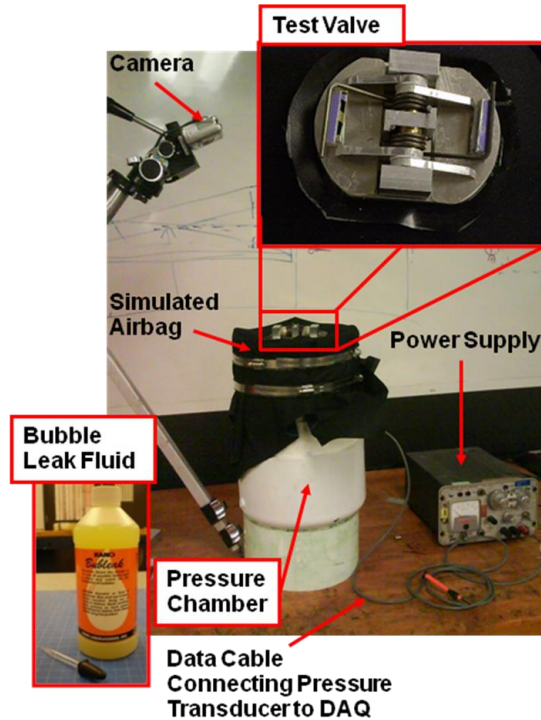


Figure 5-15: Third Generation Flapper Valve Characterization Test Setup

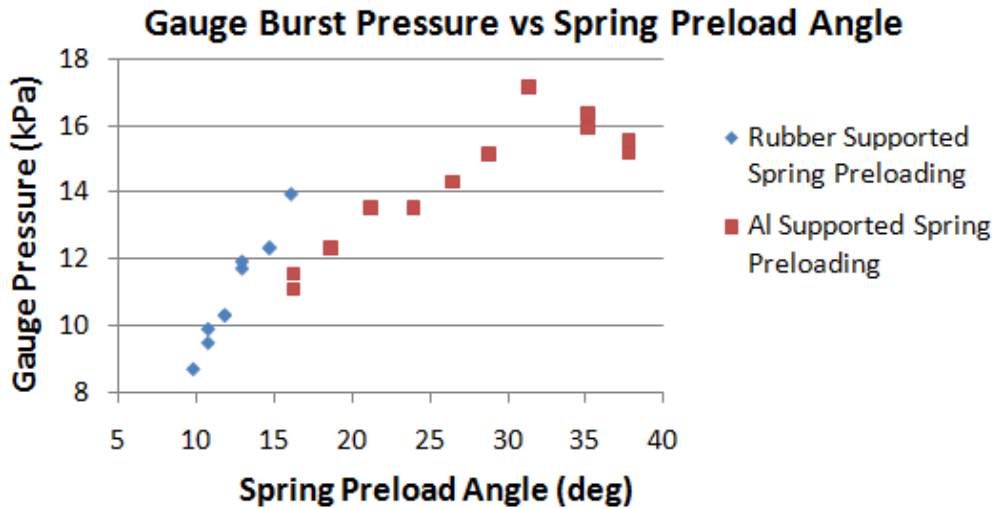


Figure 5-16: Third Generation Flapper Valve Characterization Testing Results

An interesting result observed during this test series is that when rubber was used to support the preloaded springs, the valves tended to burst at a higher gauge pressure. It was

hypothesized that the reason for this was the improved load distribution across the contact face between the torsional spring legs and the preload blocks, when compare to that of the harder aluminum surface. As a consequence, a rubber strip was implemented at this contacting surface in all subsequent valves.

In addition, the results presented in Figure 5-16 indicate that the burst pressure of the valve does not increase monotonically with an increasing spring preload angle. This is due to the fact that the effective downward force of the torsional spring is a function of the preload angle multiplied by its cosine, rather than just the preload angle alone. This can be seen by considering the idealized spring model shown in Figure 5-17.

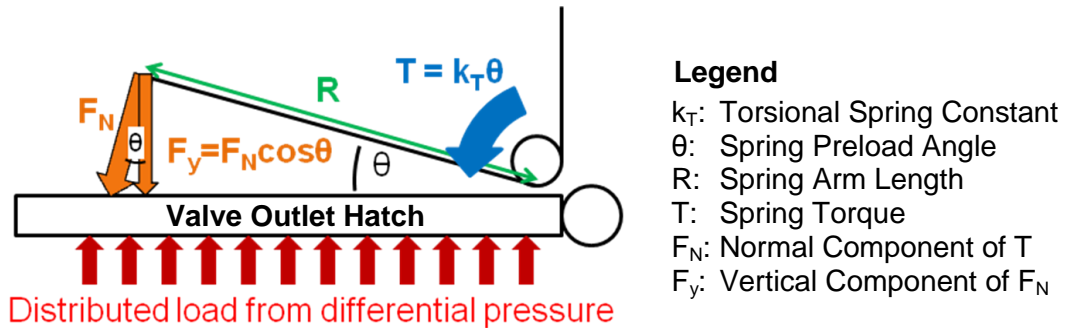


Figure 5-17: Idealized Valve Torsional Spring Model

From Figure 5-17, it can be seen that the force imparted by the torsional spring on the outlet hatch of the valve is given by:

$$T = k_T \theta = R F_N \quad (5.4)$$

Note that it is the vertical component of the normal force imparted by the spring, which acts to counteract the net force applied by the air pressure on the inside surface of the outlet hatch. Assuming a uniform pressure field, this relationship can be expressed as:

$$F_y = P_{DIFF} A \quad (5.5)$$

Where A is the area of the outlet hatch exposed to the airbag internal gas, and P_{DIFF} is the differential pressure across this outlet hatch which must be overcome for the valve to open.

Finally, combining Equations (5.4) and (5.5) with the force decomposition relationship shown in Figure 5-17, reveals the nonlinear relationship between the valve burst pressure and the spring preload angle.

$$P_{DIFF} = \frac{k_T \theta}{RA} \cos \theta \quad (5.6)$$

Furthermore, in addition to characterizing the valve performance, this series of tests also allowed for the concept used to mount the valves onto the fabric airbags to be validated. Here, this was accomplished by using a technique whereby the gasketed airbag fabric was sandwiched between the valve and a mounting plate. Figure 5-18 shows a detailed view of this mounting concept. Also note that the final result can be seen in the test setup shown in Figure 5-15.

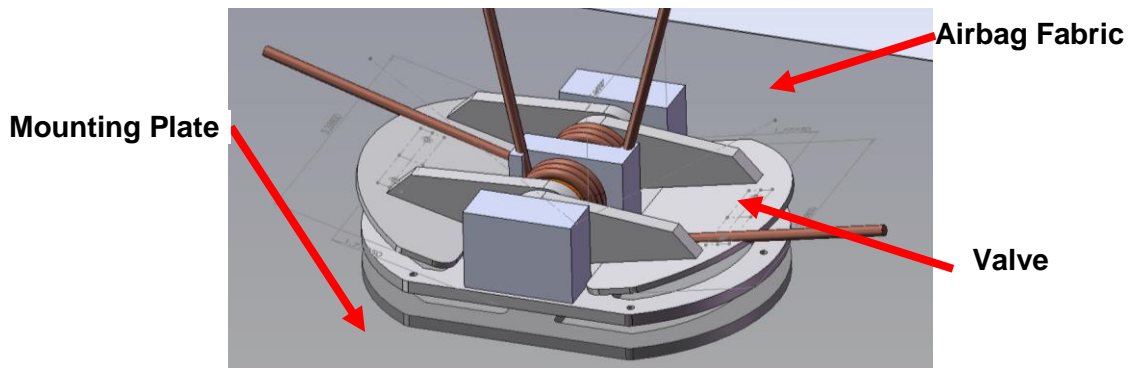


Figure 5-18: Flapper Valve Mounting Concept

5.1.4 Airbag Material Testing and Leakproofing

In addition to identifying the importance of developing a practical means of venting, the development and testing of the first generation system also emphasized the need for a stronger material to be used in the fabrication of airbags. This was particularly highlighted by the local stress concentrations which ended the first generation drop test campaign. To address this, the choice of airbag material was revisited, ultimately resulting in 200 denier High Strength Vectran being chosen as the preferred material for the next full scale personal airbag system prototype. For the single airbag drop test article however, it was decided to

continue to use high strength polyester due to its comparatively less stringent performance requirements. This decision was further supported by the fact that it would result in savings in development time, as well as maximize utilization of existing resources, thereby reducing project costs.

Used as the primary material on all of NASA's Mars rover airbag landing systems [44], as well as on the originally planned Orion CEV external airbag system; Vectran is an engineering fiber spun from a liquid crystal polymer. As a result of this, it has very high strength, low creep, and is chemically stable - properties which are all suitable for airbags designed to be subjected to multiple drop tests. With these advantages, however, are two main drawbacks, with the first of which being that when woven into a sheet form; Vectran is highly porous and hence prone to leakage. Secondly, because of its exceptionally high strength, Vectran is extremely difficult to cut, thus making it generally harder to work with.

Therefore, to quantify the benefits of Vectran and to develop methods to address its drawbacks, a series of investigations were held to resolve all uncertainties related to its implementation. These are described in the following sections.

Vectran Tensile Strength Testing

To determine the precise strength of Vectran under the anticipated loading conditions throughout an airbag impact attenuation event, a series of tensile strength tests were conducted between June and July 2009. Specifically, this involved inserting samples of Vectran in both its sheet and stitched form into a tensile strength testing machine to determine the yield stress of the fabric, as well as to characterize the seam strength as a function of the number of rows of straight stretch stitch (as described in Section 4.1.5). The objective of this latter set of tests was to obtain a baseline dataset from which the appropriate seam stitch patterning could be determined for construction of Vectran airbags. Figure 5-19 shows the samples used for these tests.

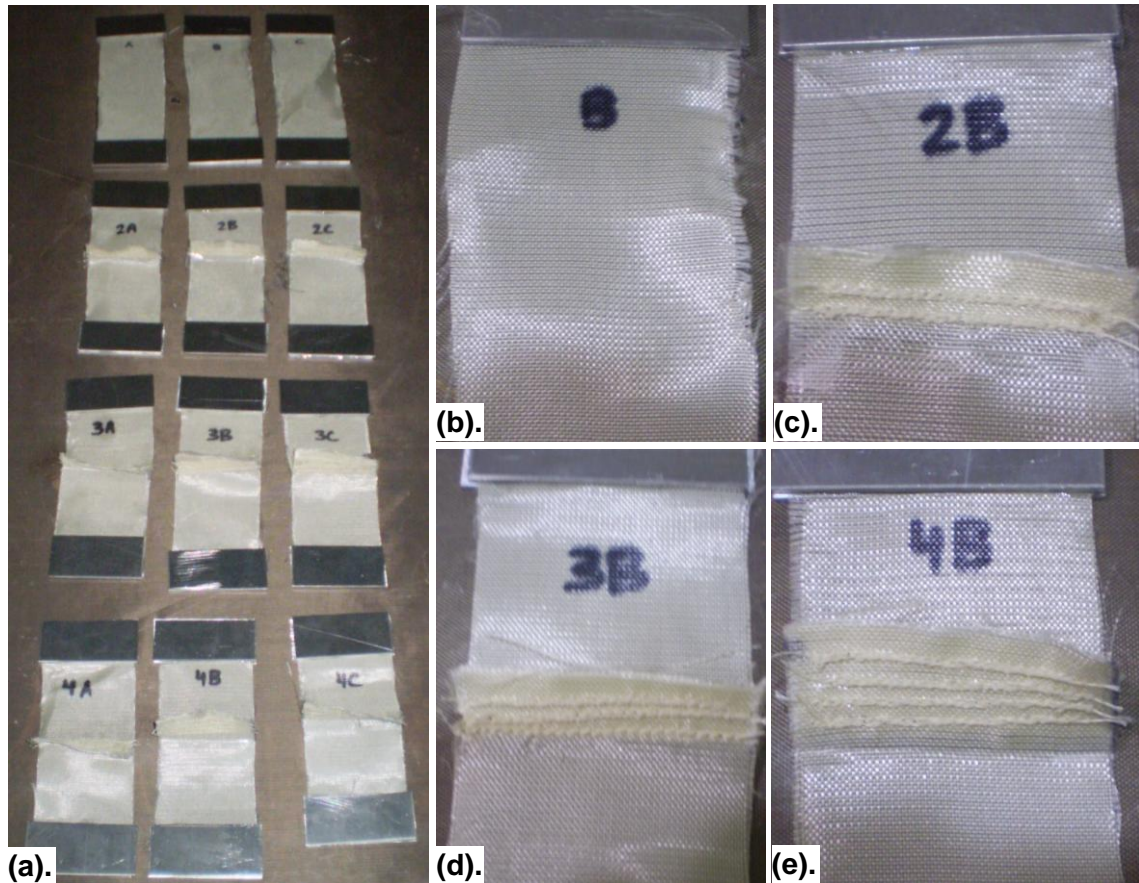


Figure 5-19: Vectran Tensile Test Samples (a). Entire Sample Set (b). Vectran Sheet (c). Two Stitch Sample (d). Three Stitch Sample (e). Four Stitch Sample

During these tests, it was found that for all samples, the tensile failure experienced by the fabric was not due to the strength of the yarn or the stitch, but rather the strength in the connection between the fibers of the fabric. In addition, for the stitched samples, this weaker connection caused the seam to slide along the fabric, creating large gaps in the fabric as it stretched. This has implications on leakage through the airbag at the seams during impact. Figure 5-20 summarizes these observations, whilst Table 5.6 summarizes the tensile strength values obtained.

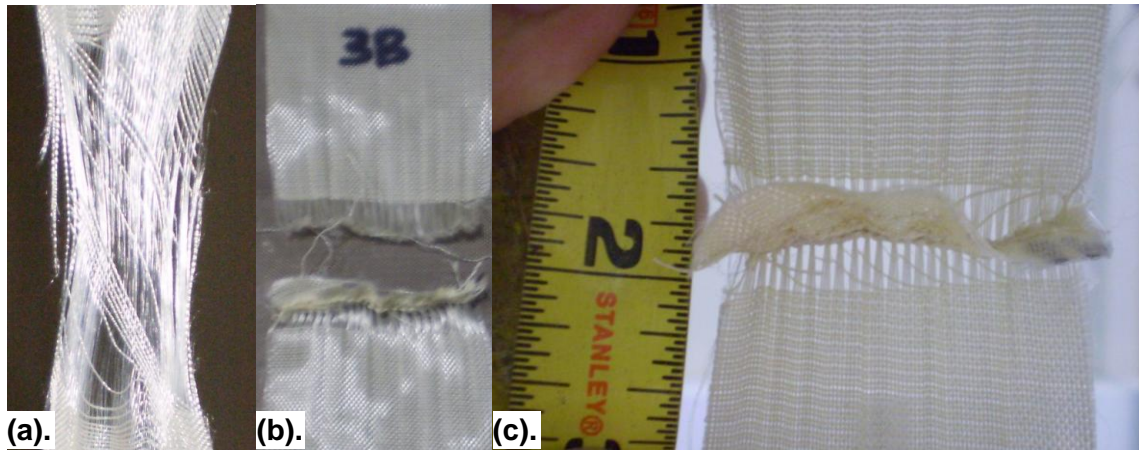


Figure 5-20: Vectran Tensile Strength Test Results

(a). Vectran Sheet (b). Three Stitch Sample (c). Detail of Stitched Sample
Showing Large Gaps Created as Seam Slides Along Fabric

Table 5.6: Vectran Tensile Strength Testing Results

Test Case	Minimum Observed Tensile Strength (MPa)
Vectran Sheet	565
Four Stitch Sample	125
Three Stitch Sample	105
Two Stitch Sample	25

From Table 5.6, it can be seen that in its sheet form, Vectran has significantly high tensile strength. When stitched however, this strength decreases substantially, especially when moving from three to two rows of stitches. This indicates that besides tears arising from local stress concentrations, an airbag constructed of Vectran is also likely to fail at the seams.

Material Leakproofing

During the performance characterization of the third generation flapper valve, it was observed that even though no leakage was found around the vicinity of the valve, the pressure vessel was not able to maintain pressure as long as expected. As a result, an investigation was initiated to determine whether the nylon-backed high strength polyester was indeed airtight, as had been previously assumed. Here, a fabric sample was mounted onto a pressure vessel,

wetted, and inflated in the search for the formation of bubbles on the fabric surface. Upon performing this test, a clear causal effect was observed between the inflation of the pressure vessel and the formation of bubbles across the surface of the fabric. This hence verified earlier suspicions that the fabric was not airtight, and therefore not adequate for use as an airbag material in its standard state. This bubbling effect can be seen in Figure 5-21.

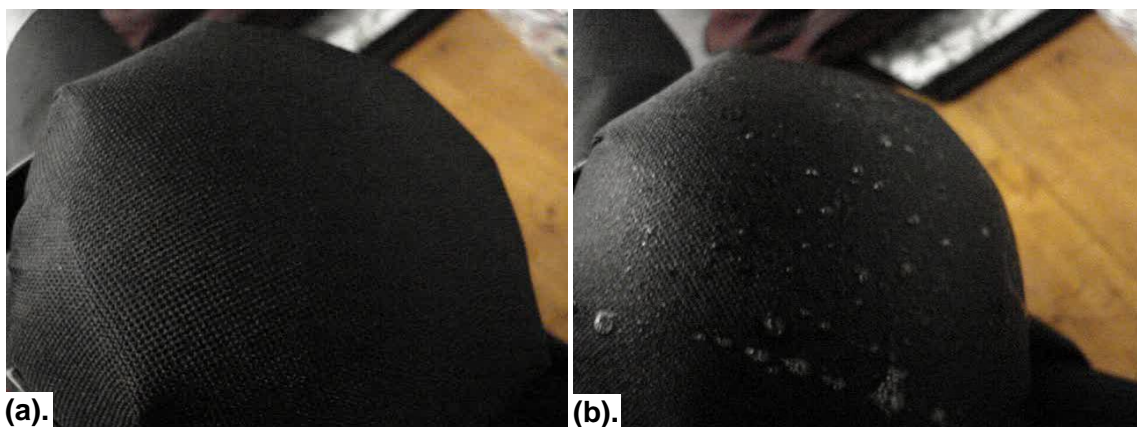


Figure 5-21: High Strength Polyester Leakage Testing (a). Sample Prior to Pressure Vessel Inflation (b). Sample During Pressure Vessel Inflation

As a consequence of this finding and the previous observations regarding the leak-prone structure of Vectran; an online search was conducted to determine a means for easily leakproofing porous fabrics. From this, it was found that commercially available liquid latex was a suitable candidate.

Typically used in cosmetic applications to emulate fictitious features on the human body, liquid latex was recommended as being a very good fabric leakproofing agent, especially when multiple layers were applied in orthogonal directions [71, 72]. To determine the exact number of layers required to effectively leakproof both high strength polyester and Vectran fabric; samples of liquid latex were procured, applied to various fabric samples in multiple layers, and leakage tested. Note here that leakproofing methods were investigated for both high strength polyester and Vectran, as they would be used in the single airbag drop test article, and future generations of the personal airbag system, respectively. Table 5.7 summarizes the samples tested, while Figure 5-22 shows the test setup and liquid latex sample used.

Table 5.7: Liquid Latex Coating Test Matrix

Sample	Material	Coatings	Side
1	High Strength Polyester	3	Polyester
2	High Strength Polyester	3	Nylon-backed
3	High Strength Polyester	3	Both
4	High Strength Polyester	4	Polyester
5	High Strength Polyester	4	Nylon-backed
6	High Strength Polyester	4	Both
7	Vectran	3	One
8	Vectran	3	Both

NB. The high strength polyester consists of one nylon-backed side, and one bare side. In this test series, liquid latex was applied to each side individually, as well as to both, to determine the required coating configuration.

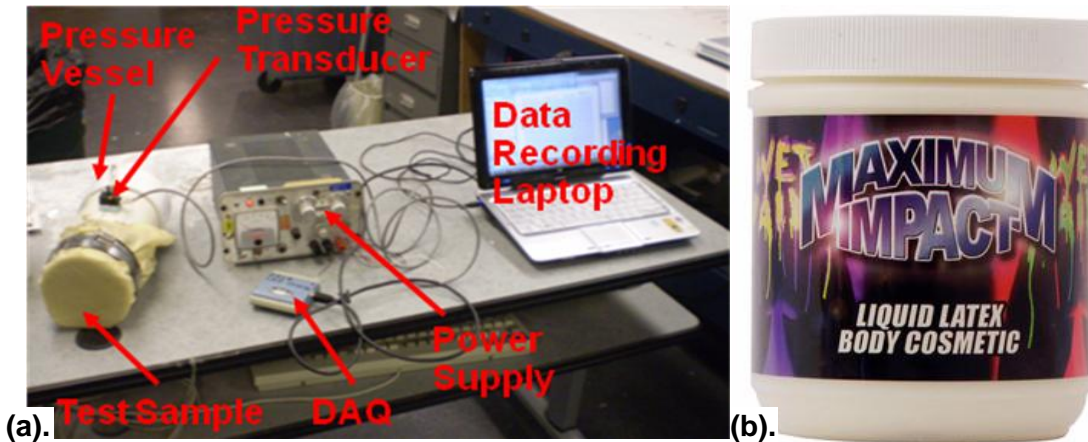


Figure 5-22: (a). Liquid Latex Coating Test Setup (b). Procured Liquid Latex Sample

From this series of tests, it was found that the minimum number of coatings required for adequate air retention was three on any side of the high strength polyester fabric, and three on both sides of the Vectran fabric. Figure 5-23 shows the air retention capabilities of these treated samples when subjected to a leakage test. Note especially the inflated profile of both fabrics in this figure.

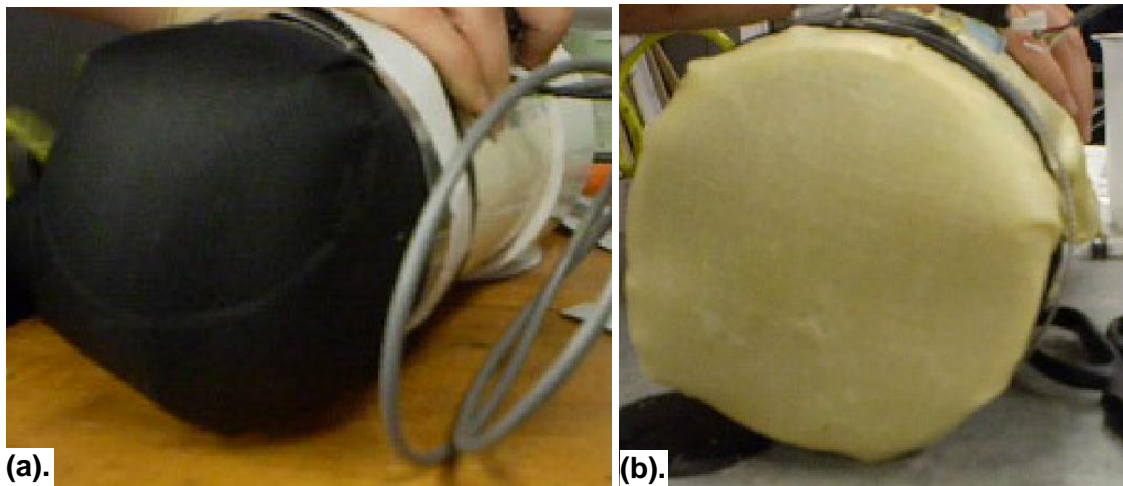


Figure 5-23: Leakage Test Results (a). High Strength Polyester with Three Coatings of Liquid Latex on the Nylon-Backed Side (b). Vectran with Three Coatings of Liquid Latex on both Sides

In addition, an investigation was held to address the potential leakage across the seams, observed during tensile strength testing. Here, a small scale airbag was built, attached to a pressure vessel, and leakage tested with different sealants applied at the seam. From this, silicone paint was chosen as the preferred sealant. Figure 5-24 shows the manner in which this sealant is applied at the airbag seam, as well as the leakage test setup employed.

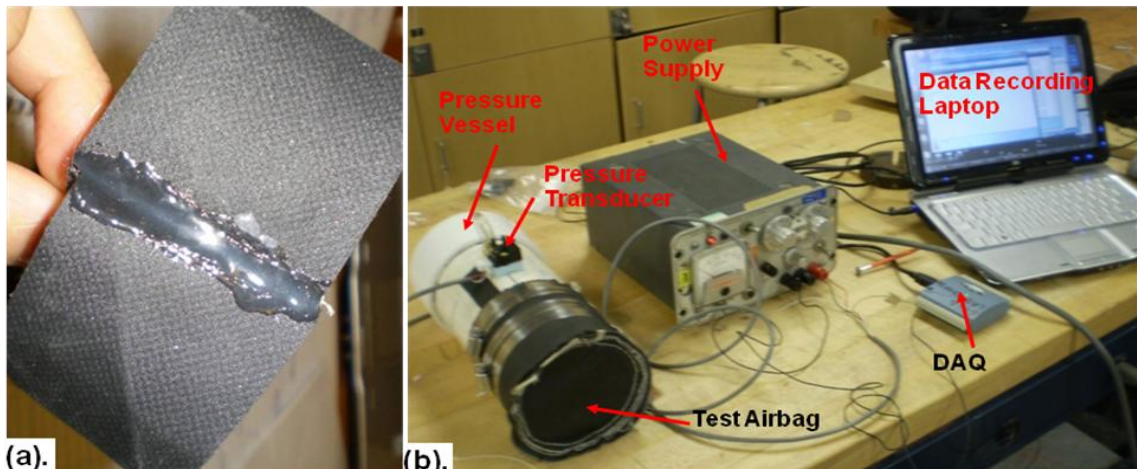


Figure 5-24: (a). Silicone Paint Applied to Fabric Seam
(b). Seam Sealant Leakage Test Setup

5.1.5 Pressure Relief Valve Vented Airbag Optimization

In Section 5.1.2, a design of experiments was conducted to size the venting and inflation properties of the single airbag drop test article based on a concept employing burst-type venting mechanisms. The obtained result then formed the basis for the subsequent valve development activity, which concluded that pressure relief valves were a more practical form of airbag venting. As a consequence of this misalignment between the original design of experiments results and the developed means of implementation, the inflation characteristics of the system need to be recalculated for one incorporating pressure relief valves.

This firstly requires incorporating a model of the venting profile of the developed pressure relief valves into the single airbag impact model. Here, this was accomplished by firstly using Newton's Method to solve the transcendental Equation (5.6) for the displacement angle of the valve springs. Subtracting the preload angle from this value and incorporating the geometric properties of the third generation flapper valve allows for the orifice area to be calculated, which along with the airbag pressure; can be substituted in the orifice flow equations given by Equations (3.36) and (3.40) in Section 3.1.2.

With this modified impact model established, an optimization was performed to determine updated inflation values. Since the venting area was now fixed to that of the third generation flapper valve, the remaining parameters to be updated were the airbag inflation pressure, and the valve opening pressure - the latter of which would be implemented by setting the valve torsion springs to the appropriate preload angle.

Because only two variables were required to be determined, a full factorial analysis was employed, rather than a One at a Time approach. In doing so, the globally optimal design vector could be obtained at a relatively small increase in computation cost compared to that of the One at a Time method. This was because the total number of function evaluations required to enumerate the design space was low in the absolute sense, due to the fact that only two variables were being optimized over. Figure 5-25 shows this design space for the single airbag system incorporating pressure relief valves, impacting at the nominal Orion impact velocity of 7.62m/s (25fps), and supporting a 2.5kg mass.

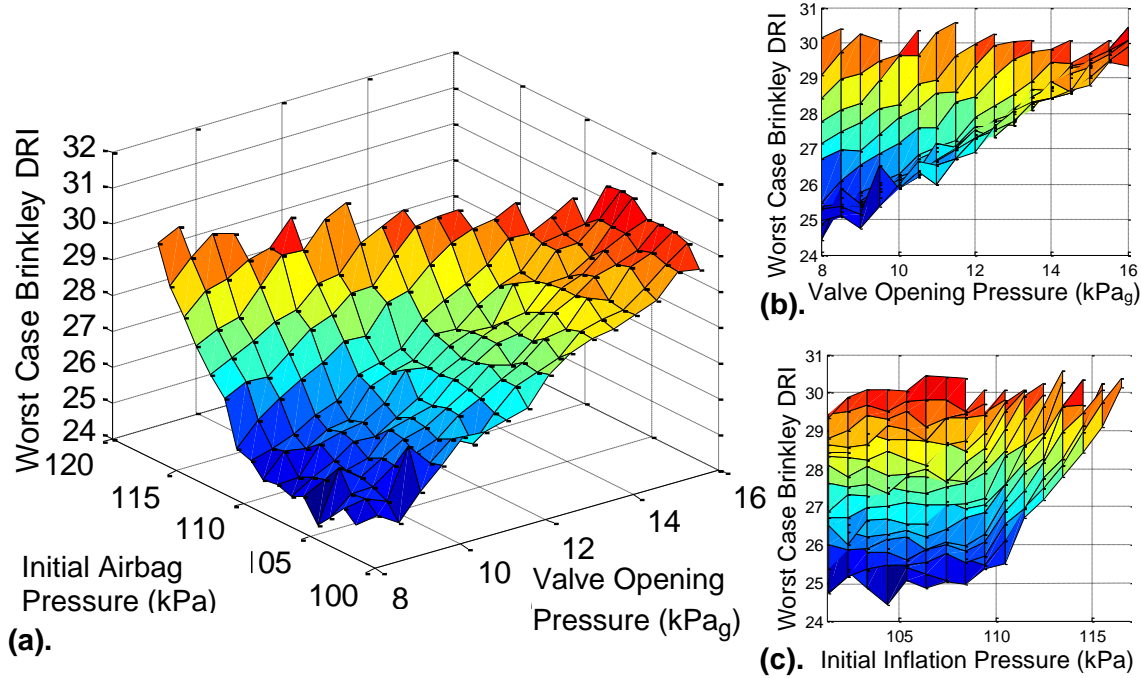


Figure 5-25: (a). Pressure Relief Valve Vented Airbag Design Space (b). Brinkley DRI vs Valve Opening Pressure (c). Brinkley DRI vs Airbag Inflation Pressure

Observing the obtained design space, it can be seen that the injury risk decreases as the valve opening pressure decreases. This can be explained by the fact that a lower opening pressure results in the valve opening earlier, and hence venting more energy from the system prior to the complete expenditure of the airbag stroke. At the lower opening pressure values between 8 and 9kPa_{Ag} however, the design space indicates that the system performance becomes less sensitive to variations in this variable. This is likely the result of the less significant effect on mass flow rate through the orifices as this pressure is varied over this lower end of the opening pressure spectrum.

Also of relevance is the fact that the design space appears to flatten out as the airbag inflation pressure decreases to less than 110kPa. This is in-line with the observations made in the Design of Experiments exercise performed for the burst valve vented airbag configuration, discussed in Section 5.1.2. Here, it was found that the system performance was least sensitive to the initial inflation pressure of the airbag, implying that during operation, precise inflation of the system was not required for near optimal performance.

Consequently, based on the results of this optimization study, the following values were chosen for the design of the single airbag drop test article.

Table 5.8: Final Design Vector for the Single Airbag Drop Test Article

Parameter	Value
Radius	110mm
Length	350mm
Total Vent Orifice Area	2 x (2 to 2.5") dia. holes
Initial Airbag Pressure	101-110kPa (1-1.09atm)
Valve Burst Pressure	8-9kPa gauge
Corresponding Spring Preload Angle	9-10deg (with vinyl rubber backing)

Note that ranges have been defined for both the airbag inflation pressure and the valve burst pressure, to take advantage of the less sensitive region of the design space. The corresponding predicted performance of this configuration under nominal landing conditions at an inflation pressure of 105kPa, over the specified range of valve burst pressures is presented in Figures 5-25 and 5-26.

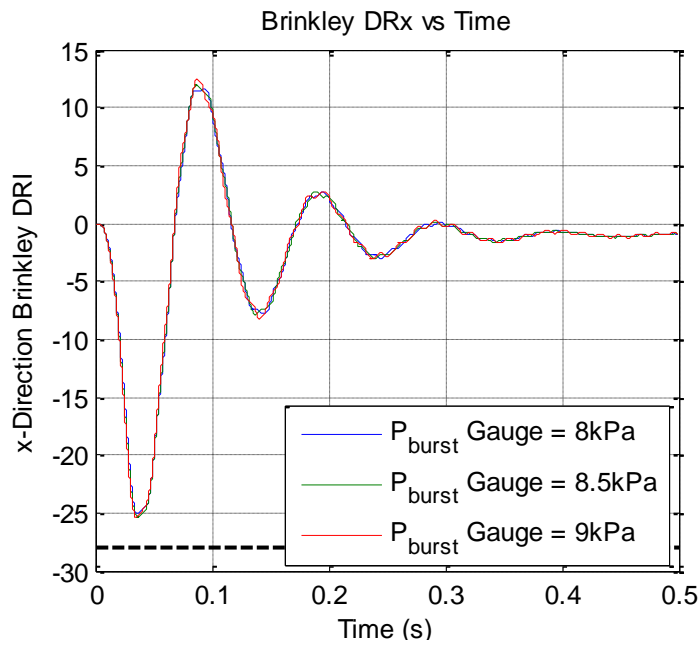


Figure 5-26: Predicted Brinkley Response for the Single Airbag Test Article

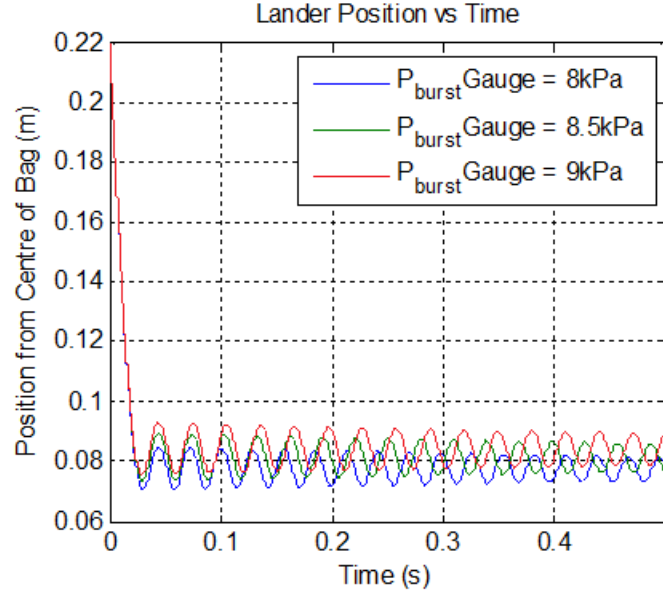


Figure 5-27: Predicted Vertical Displacement Response for the Single Airbag Test Article

From Figure 5-26, it can be seen that as indicated in the optimization study, the Brinkley response is largely insensitive to variations in the lower valve opening pressure range. Furthermore, for all specified valve opening pressure values, the system is predicted to meet the Brinkley low injury-risk criteria.

Of more interest however, is the vertical displacement response shown in Figure 5-26(b). Here, a lightly damped oscillatory behavior is predicted to occur within the airbag system after its initial stroke. This is the result of the pressure relief valve closing and hence no longer releasing gas after this first stroke. When this occurs the only form of damping arises from the frictional effects between the gas molecules within the airbag – an effect not explicitly captured in the single airbag model. As a consequence, the mass supported atop the airbag experiences an oscillatory motion as its potential energy is converted into kinetic energy and vice versa. The light damping observed is a result of the non-linear interaction between the airbag pressure and its shape function. This is demonstrated by the structure of the original system equation presented in Section 3.1.2, and shown again below:

$$m\ddot{x} + (P_{bag}(x) - P_{atm})A_{FP}(x) = mg \quad (5.7)$$

Here, it can be observed that this equation is in the form of a mass-spring system, with a nonlinear spring stiffness, given by:

$$k = \frac{1}{x(t)} \left(P_{bag}(x, t) - P_{atm} \right) A_{FP}(x) = \frac{1}{x(t)} \left(\overbrace{P_{bag}(x, t - \Delta t) \frac{w}{\rho V(x)}}^{\text{Pressure}} - P_{atm} \right) A_{FP}(x) \quad (5.8)$$

Now, consider that when the pressure relief valves are closed, the mass of gas within the airbag remains constant. Consequently, the airbag stiffness becomes a nonlinear function of only the pressure and geometric variables. Because these variables change at near proportional rates, their interaction results in a light damping effect. Note that if the effective stiffness were to be purely constant, no damping would occur, and the system would experience simple harmonic motion after the end of the initial stroke.

5.1.6 Single Airbag Drop Test Article Manufacture

With the fundamental issues of venting and airbag leakproofing resolved, as well as the inflation and venting characteristics finalized; an integrated system was designed and fabricated. Figure 5-28 shows the final integrated system design.

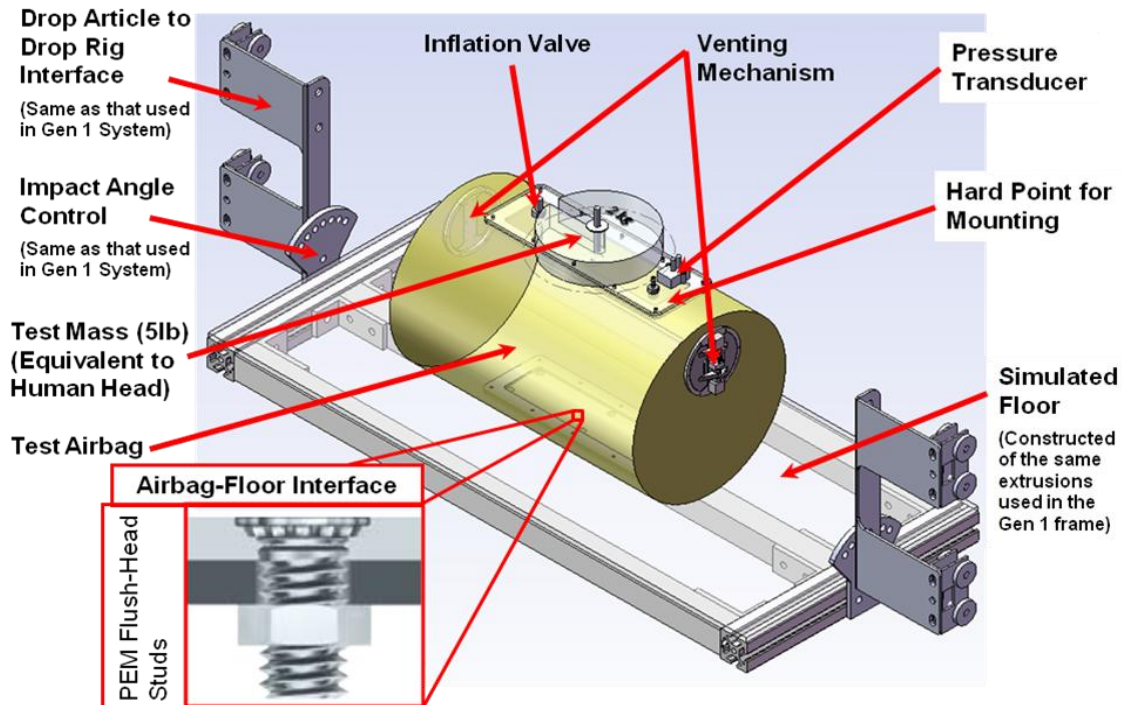


Figure 5-28: Final Integrated Single Airbag Drop Test Article Design

In order to save on manufacturing time and costs, several components of the single airbag drop test article were reused from the first generation personal airbag system. In particular, these included the extruded sections used in the simulated floor, as well as the brackets used to interface the system with the drop test rig. An added advantage of reusing these components was that a flawless interface with the drop test rig was guaranteed, as components which had previously been successfully operated were being used.

Furthermore, as can be seen in Figure 5-28, hard points were incorporated into the airbag to both support the payload mass, and allow for interfacing between the airbag and the simulated floor. In addition to supporting the payload mass, this top plate also acted as a mounting point for all instrumentation, including a pressure transducer, accelerometer, and LED lights; the latter of which intended for use with photogrammetric analysis. Figure 5-29 shows a detailed view of this top plate, along with the locations of the LEDs installed throughout the system.

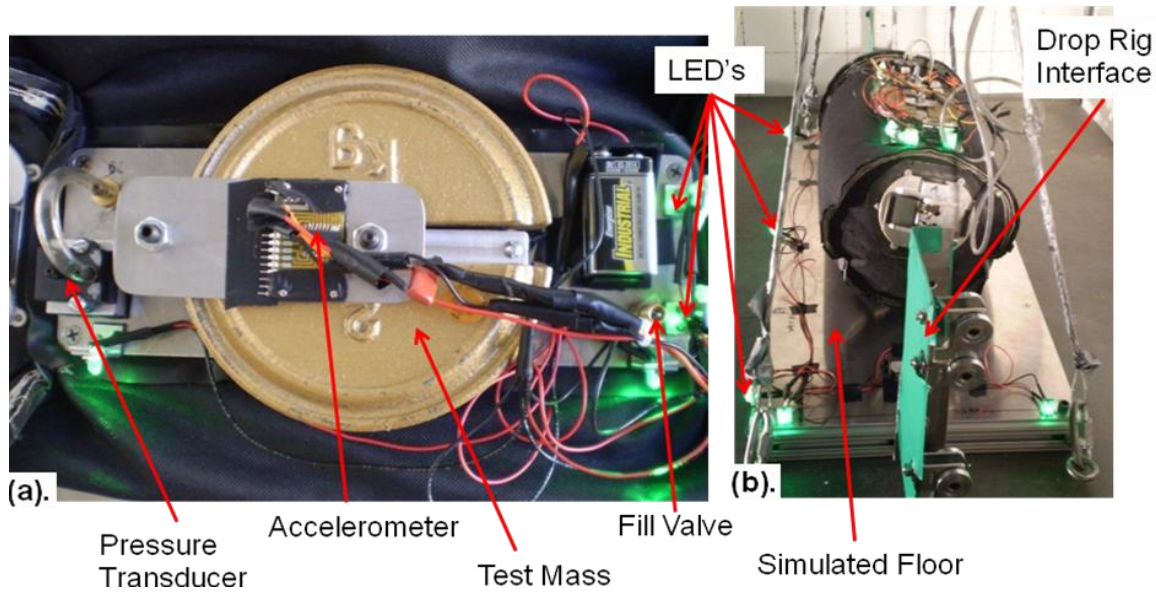


Figure 5-29: Single Airbag Drop Test Article (a). Instrumentation (b). Location of LEDs

Here, it can be seen that LEDs have been installed on both the top of the airbag and the simulated floor. The intention of this is to allow airbag stroke to be measured during impact via photogrammetric methods. Also, tracking LEDs on the simulated floor would enable for the impact velocity analogous to that of a landing spacecraft, to be determined.

Moreover, Figure 5-29(a) shows the scheme used to support the payload mass. Specifically, a sandwich type configuration was used to fix the translational degrees of freedom of the mass, whilst a block inserted into the slit of the mass fixed its rotational degrees of freedom. Since all test masses were of the same dimensions, this fastening scheme allowed for tests with differing test masses to be performed – an attribute which formed the basis of a series of checkout tests performed prior to the main test campaign. In addition, the proximity of the plate to the geometric center of the mass provided an ideal location for the installation of an accelerometer. This was particularly beneficial as this location corresponded to the location of the payload mass in the single airbag impact model, thus allowing for a direct comparison between the test results and the model predictions. The final single airbag drop test article, integrated onto the drop test rig, can be seen in Figure 5-30.

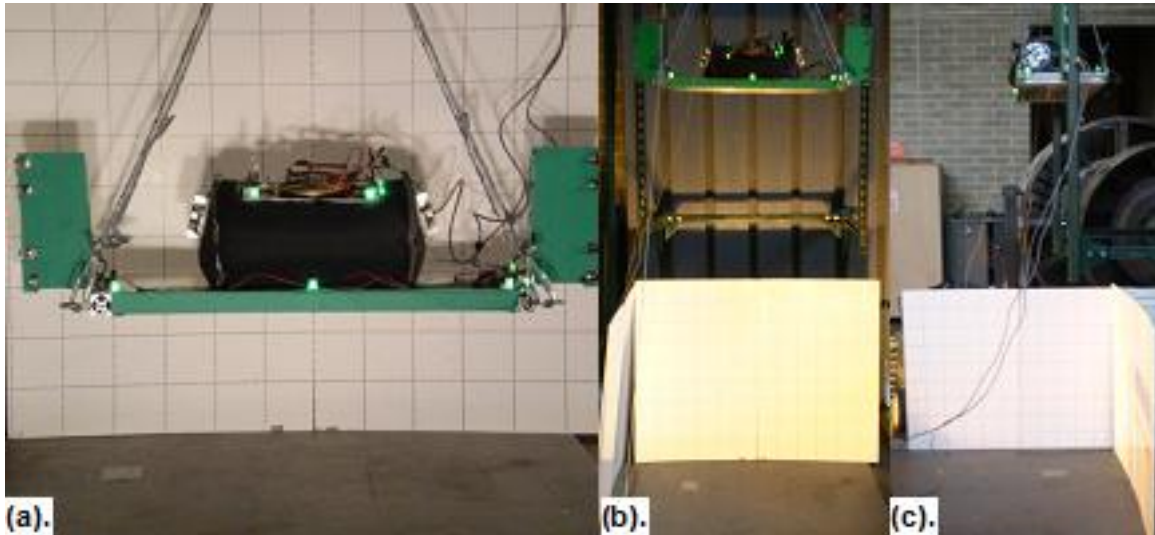


Figure 5-30: Single Airbag Drop Test Article
(a). Front View Detail (b). Front View of System Integrated with Drop Test Rig
(c). Side View of System Integrated with Drop Test Rig

5.2 Single Airbag System Drop Test Plan

At the start of this chapter, it was mentioned that the ultimate objective of this development spiral was to characterize the impact dynamics of a single airbag and in doing, refine the single airbag impact model. To meet this objective, drop tests were performed using the single airbag drop test article with both varying test masses, and varying impact velocities.

Specifically, two test sessions were performed, consisting firstly of a system checkout, followed by the impact dynamics characterization. Here, the first test session consisted of fixing the drop height to 1 foot, and performing drops with the test mass increasing incrementally from 500g to the nominal mass of 2.5kg. The intent of this test series was to identify any flaws which may have existed in the system design and/or fabrication prior to subjecting it to full scale test conditions.

Upon completion of this first test session in an intact state, the drop test article would be subjected to the second test session, where the test mass would be fixed to the nominal 2.5kg, and drops would be performed from drop heights increasing in 1foot increments. These tests would continue until the nominal Orion impact velocity was achieved at a drop height of approximately 10feet; or a failure in the system was experienced. Note that for both test sessions, drops would be performed at each test condition three times to ensure that a consistent and repeatable data set was obtained.

With regards to data acquisition, an accelerometer and pressure transducer were used together with two perpendicularly separated high speed cameras tracking LEDs situated on the test article, as described in Section 5.1.6. As was the case with the first generation test campaign, photogrammetry would be used to analyze the high speed camera footage in order to obtain impact dynamics data. Moreover, the accelerometer and pressure transducer data would be used as the baseline for refining the single airbag impact model. Figure 5-31 shows the test setup used during this test campaign.

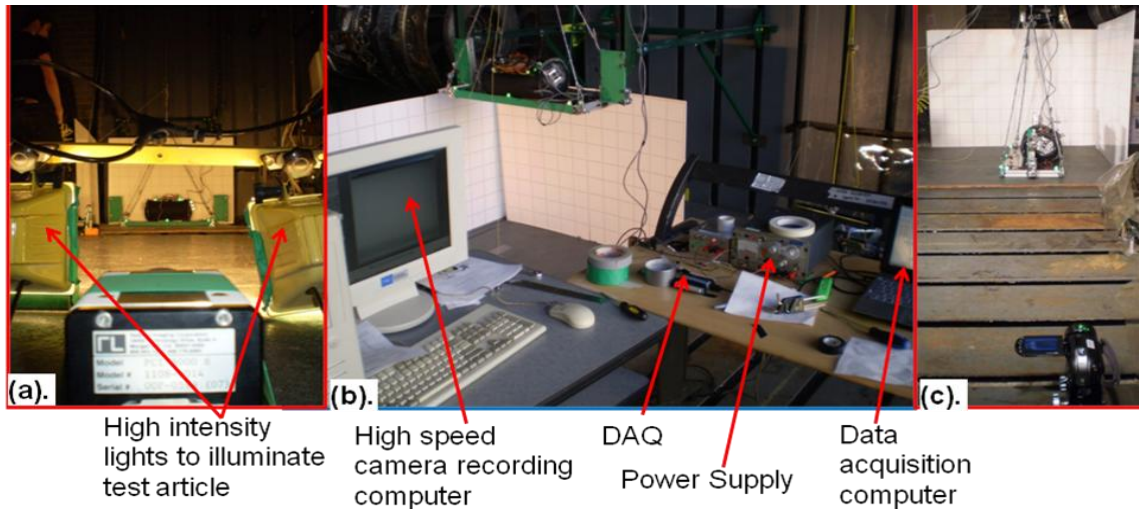


Figure 5-31: Single Airbag Drop Test Setup (a). View from High Speed Camera 1
 (b). Data Acquisition Center (c). View from High Speed Camera 2

5.3 Single Airbag System Test Results & Analysis

Over the course of mid-March 2010, the single airbag drop test campaign was conducted. As tests were being performed, a consistent dynamic, comparable to that predicted by the single airbag impact model, was observed. This involved the system experiencing a primary stroke after initial contact with the impacting surface, followed by a recoil and damped oscillations before finally coming to rest. Figure 5-32 summarizes this motion.

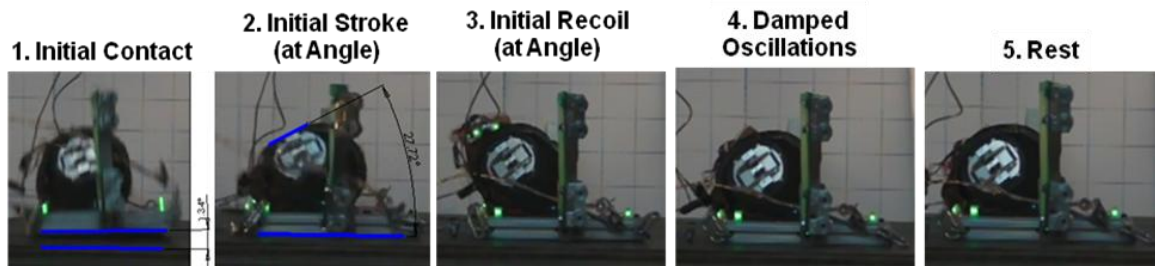


Figure 5-32: Typical Dynamic Observed During all Single Airbag System Drop Tests

An interesting aspect of this dynamic, previously unforeseen during simulations, is the tendency for the payload mass to tilt at a pitch angle during the impact. This is a result of the uneven pressure field within the airbag making it difficult for the mass to balance atop the system. Since the single airbag impact model assumes a uniform pressure distribution, and neglects the real-world effects of geometric interactions between the payload and the airbag; this effect could not be predicted. However, even though this was the case, the overall similarities between the observed dynamic and the predicted performance indicated that the system could potentially perform to design specifications.

This appeared to be indeed the case throughout the first test session, where the system remained intact and nominal performance was observed. Midway through the second test session however, this outlook was disproven; with a rip in the airbag occurring after the first 6 foot drop was performed. Specifically, this occurred at the contacting surface between the edge of the test mass and the airbag, as shown in Figure 5-33.

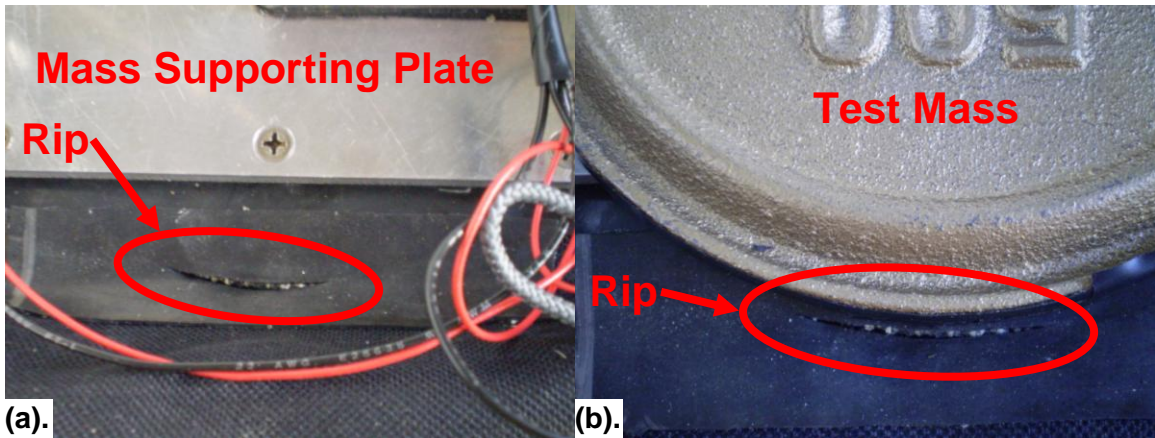


Figure 5-33: Single Airbag Drop Test Article Failure at 6 foot Drop Height (a). Rip with Payload Mass Removed from System (b). Rip with Payload Mass Installed on System

Close inspection of the rip indicated that it was a result of a local stress concentration occurring at the contact edge between the airbag and the test mass as it stroked. This stress concentration was so high, that it caused a rip to occur through both the layer of gasketing and the airbag material itself. This is particularly apparent when observing Figure 5-33(b), where the shape of the rip can be seen to match the geometry of the test mass. Moreover, this result further reiterated the need to move to Vectran as the primary airbag material for future developments of the airbag system.

Regardless of this early conclusion to the test campaign however, several valuable insights were made from the test results. These are discussed in the following sections.

5.3.1 Test Session 1 Results Analysis

As was previously mentioned, the single airbag drop test article performed nominally and remained intact throughout all drop tests performed in the first test session. From a photogrammetric analysis of the high speed camera footage, it was found that all tests had an impact velocity of between 2.3 and 2.5m/s. Figures 5-33 to 5-35 show all results obtained for this session.

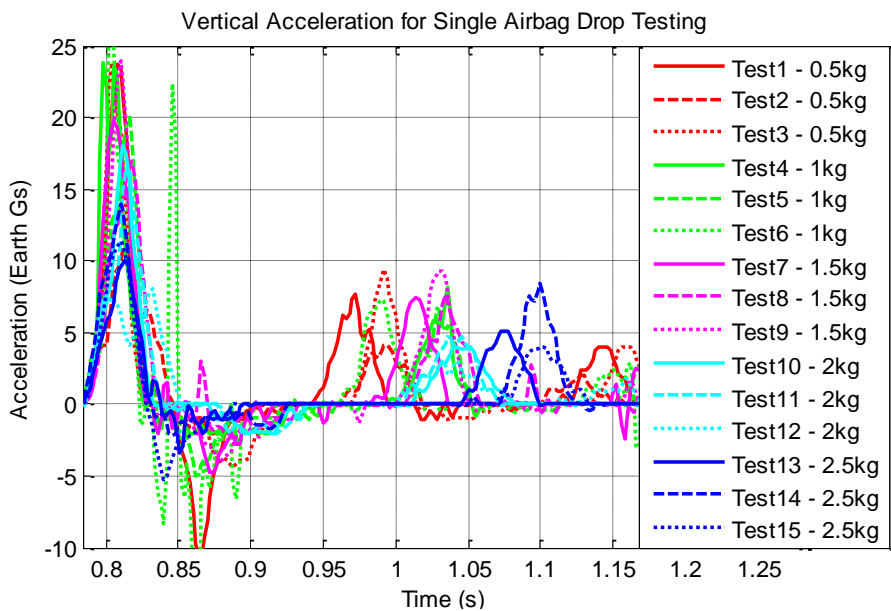


Figure 5-34: Single Airbag Drop Test Session 1 Accelerometer Data

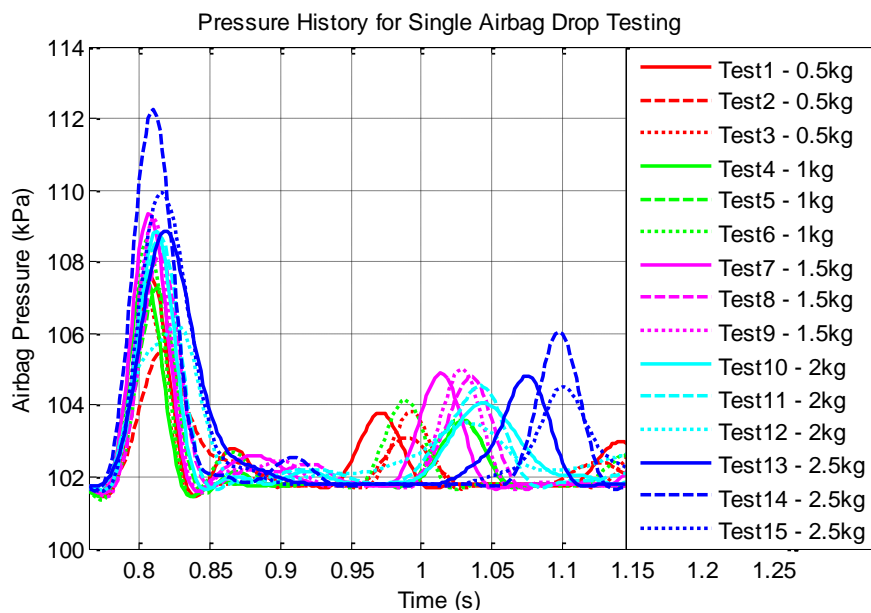


Figure 5-35: Single Airbag Drop Test Session 1 Pressure Transducer Data

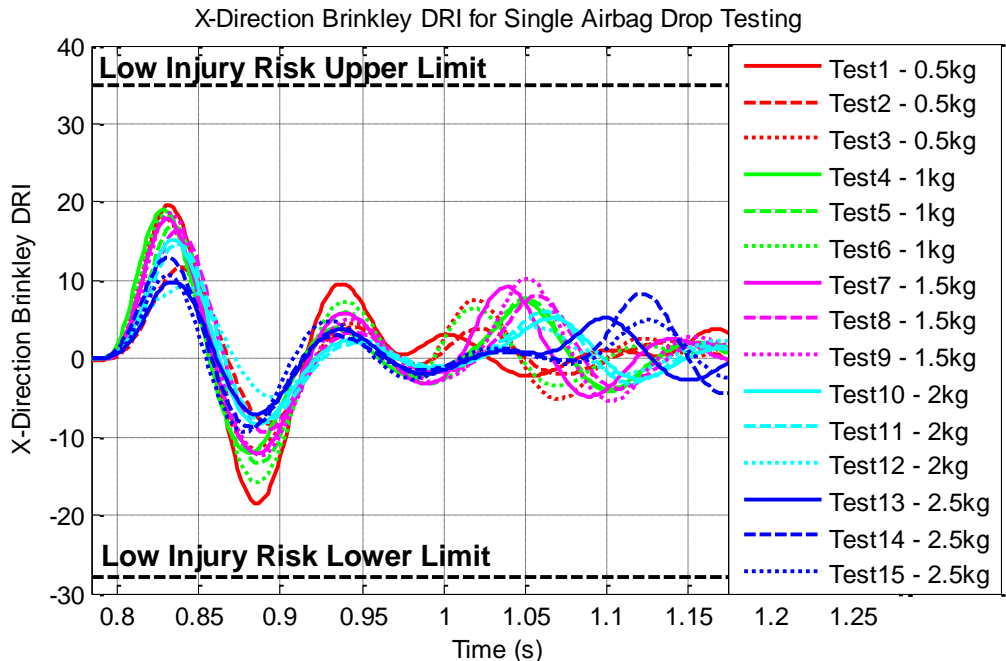


Figure 5-36: Single Airbag Drop Test Session 1 Pressure Transducer Data

From these test results, it can be seen that all tests remained well within the Brinkley low injury-risk limits, indicating potential for the system to perform as designed. More interestingly however, is the fact that these results suggest that an increasing test mass corresponds to a decreasing peak acceleration, and hence a maximum Brinkley Index. This seemingly unintuitive result can be explained by the fact that a higher mass causes the airbag pressure to remain higher for a longer period of time. This in turn causes the pressure relief valves to remain open for longer, allowing more gas, and hence energy, to escape from the system. The result of this is improved overall impact attenuation.

5.3.2 Test Session 2 Results Analysis

As was performed for the analysis of the first generation system test campaign, a detailed photogrammetric analysis was performed with the high speed camera footage captured during all drop tests, in order to extract key dynamics information. Since a similar dynamic was observed for all drop tests, the photogrammetric analysis of a sample test case will be presented here. Following this, the entire data set obtained during this test session will be presented and analyzed.

Typical Results

Here, the results obtained from the third drop performed at a height of 4 feet will be analyzed. Figures 5-37 and 5-38 show the output from this photogrammetry analysis.

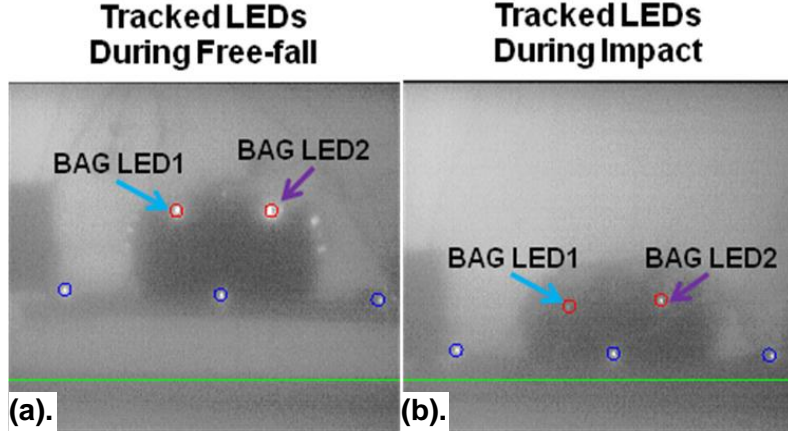


Figure 5-37: Photogrammetric Analysis of High Speed Camera 1 Footage
 (a). Frame Captured During Free-fall (b). Frame Captured During Impact

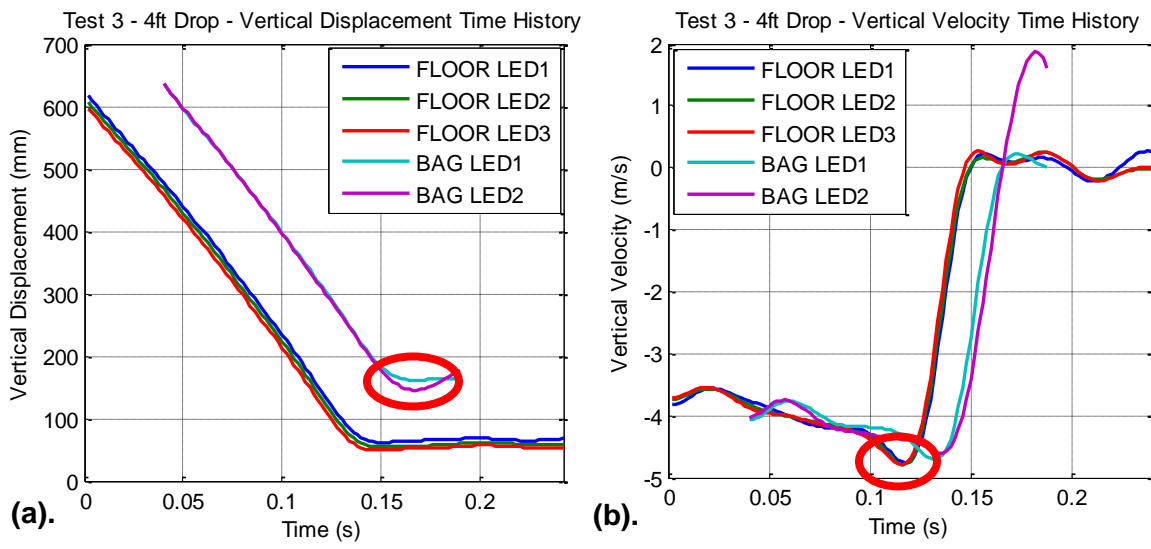


Figure 5-38: Dynamics Data Extracted from Photogrammetry
 (a). Vertical Displacement Time History, with Maximum Stroke Highlighted
 (b). Vertical Velocity Time History, with System Impact Velocity Highlighted

From Figure 5-38, it can be found that during this particular drop; the system impacts the ground at 4.8m/s, causing the airbag to experience a maximum stroke of 34% of the total available stroke. Note here that the airbag LEDs could not be tracked beyond the timestamp of 0.18seconds because they became obstructed by the airbag as it stroked during the impact.

Furthermore, using the fact that the maximum stroke and the peak acceleration occur at the same time, the accelerometer data can be tagged with the dynamic events identified in Figure 5-32. The result of this is shown below.

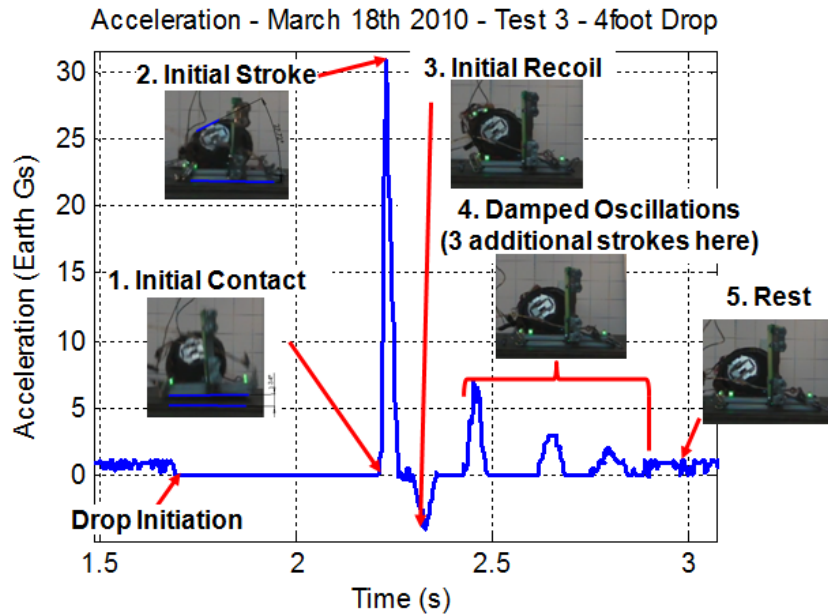


Figure 5-39: Accelerometer Data for a 4foot Drop

One interesting attribute observed in all accelerometer data analyzed was that after the initial stroke and recoil, the acceleration never again decreased below a value of zero G's. Although the period at which the data appears to be truncated to zero G's corresponds to when payload mass was mid air, some negative acceleration was expected to initiate this upward component of the oscillatory motion.

It was initially hypothesized that this trend was due to either an artificial error introduced through filtering of the data during post processing; or through errors in the operation of the accelerometer itself. Upon investigation of these potential error sources, it was found that the raw unfiltered data displayed this same truncated trend, and that there were no errors in the accelerometer's ability to detect negative acceleration loads, thus disproving these hypotheses.

Examining the pressure data (See Figure 5-40(a)) however, provides insight into the physical mechanisms occurring during this event. Here, it can be seen that the internal pressure within the airbag is equal to the local atmospheric pressure during these latter recoil periods. Since there is a zero pressure difference here, there is no additional force being applied on the payload mass during these recoil periods.

Conversely, immediately after the first stroke, the pressure is observed to decrease beneath atmospheric pressure for a brief period of time. This negative gauge pressure is a result of the airbag volume expanding immediately after its maximum stroke, due to the elasticity in the airbag fabric. This expansion and resulting negative pressure difference causes a suction effect in the airbag, which in turn imparts an upward force on the mass which is registered as a negative acceleration on the accelerometer. Because the material elasticity is so low, this suction effect does not occur in subsequent strokes, which have significantly lower peak accelerations. Rather, it is only the increase in pressure due to the stroking of the airbag which initiates the upward motion of the mass during the latter recoil stages.

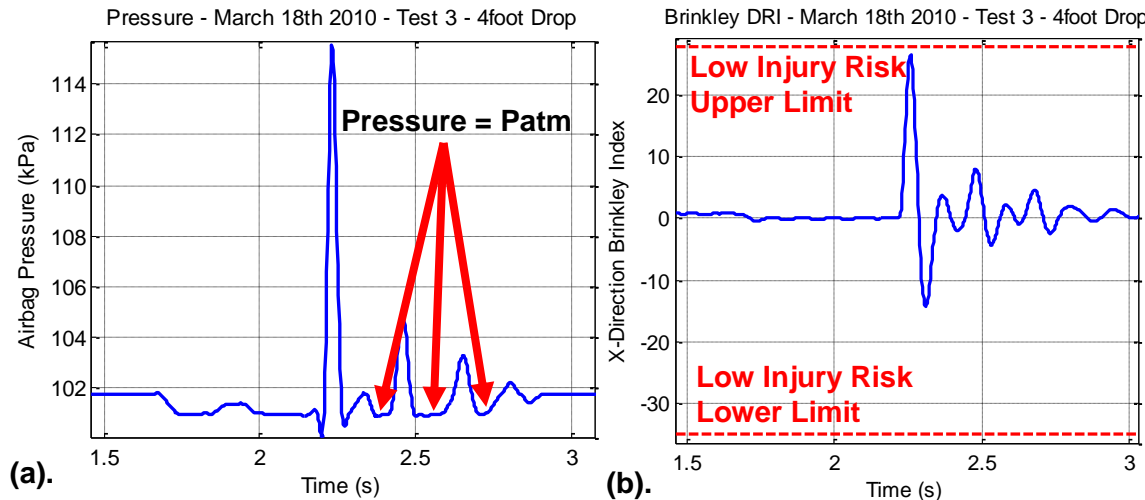


Figure 5-40: Pressure Transducer Data for a 4foot Drop

Finally, observing the Brinkley Index data shown in Figure 5-40(b) indicates that for this particular drop test, the Brinkley Index remains beneath the low injury-risk limits and hence passes NASA's safety requirements. Additionally, the synchronized occurrence of injury-risk level peaks with acceleration peaks prevalently seen in the first generation system test campaign can again be observed here.

Trends with Varying Drop Height

Upon examination of the data obtained for all drop tests performed with the single airbag drop test article, it can be seen that the general dynamic trends observed in the previously presented sample analysis consistently appear. Table 5.9 and Figures 5-41 to 5-43 summarize this data.

Table 5.9: Summary of Sensor and Photogrammetric Analysis Results for the Single Airbag Drop Test Campaign

Drop Height (ft)	Impact Velocity (m/s)	Max Airbag Acceleration (G's)	Max Brinkley DRI	Max Airbag Pressure (kPa)	Floor Impact Pitch Angle (deg)	Max Pitch Angle (deg)	Max Stroke (mm)
1	2.4	9.972	9.784	108.9	20.13	59.53	144.4
1	2.5	14.02	12.92	112.2	16.74	45	145.0
1	2.3	11.38	10.68	109.9	24.12	53.86	129.6
2	3.5	15.85	14.32	110.4	28.01	40.89	159.9
2	3.6	29.12	18.46	113.3	12.12	50.42	156.2
2	3.3	14.43	16.41	112.1	17.62	37.15	159.8
3	4.1	34.84	21.19	115	5.94	39.07	155.1
3	4.1	31	23.59	114.7	3.36	30.2	151.6
3	4.2	13.87	12.83	109	-6.6	22.73	N/A
4	4.8	32.65	24.6	115	4.87	20.21	152.4
4	4.8	28.15	27.16	115.8	5.24	21.95	166.7
4	4.8	30.96	26.45	115.5	7.91	26.31	164.5
5	5.2	37.15	25.1	115.2	0	20.04	186.3
5	5.3	36.79	23.64	115	N/A	N/A	N/A
5	5.3	24.78	25.89	115.4	1.34	27.72	142.3
6	5.8	38.15	23.28	115.8	7.34	47.57	N/A

NB. “N/A” implies that the high speed camera footage captured did not provide enough information to extract the stated variable.

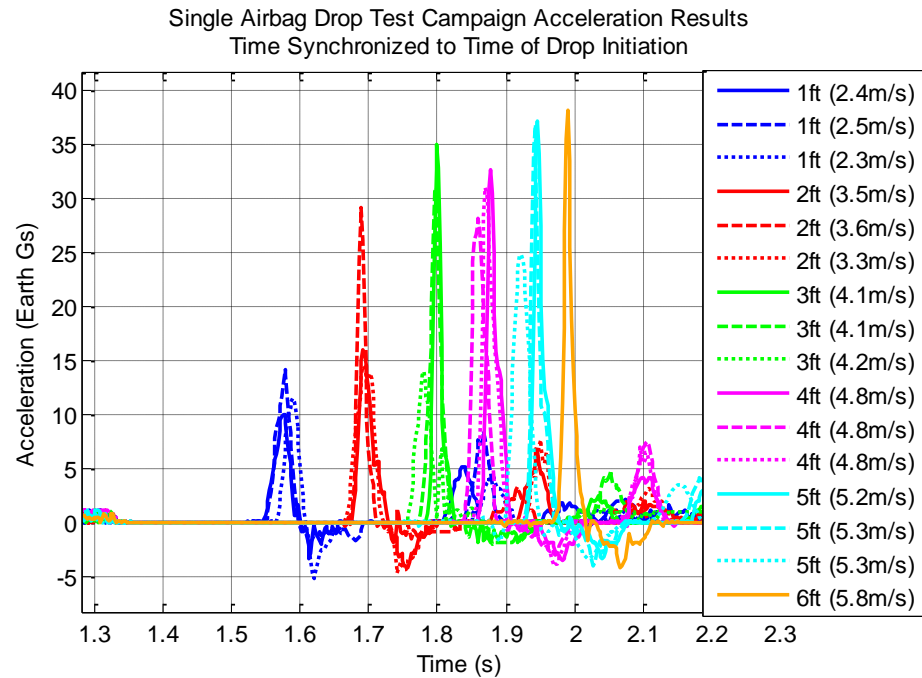


Figure 5-41: X-Direction Acceleration for all Single Airbag System Drop Tests

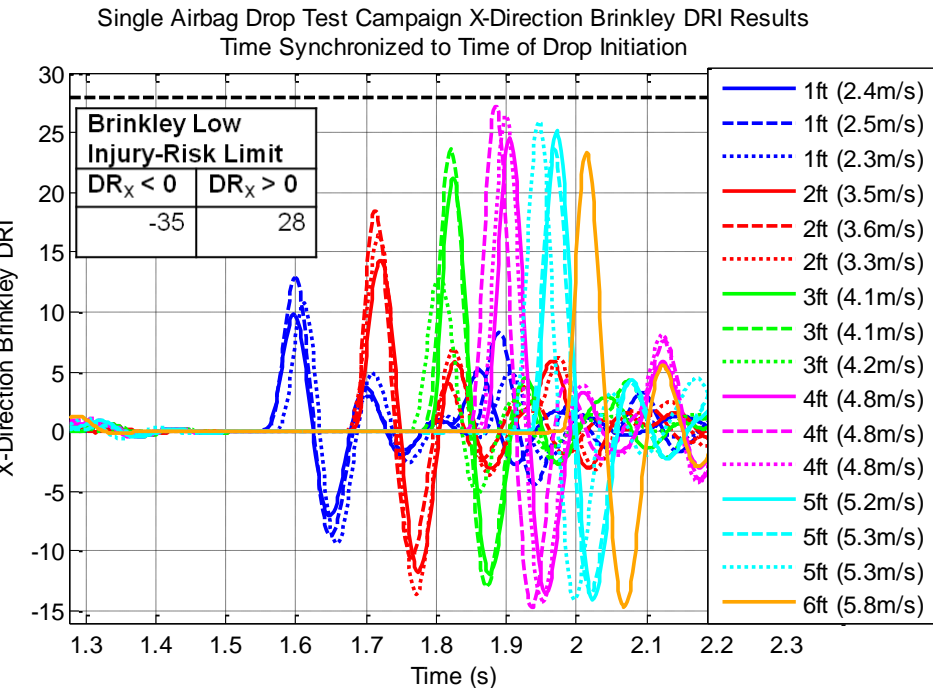


Figure 5-42: X-Direction Brinkley Index for all Single Airbag System Drop Tests

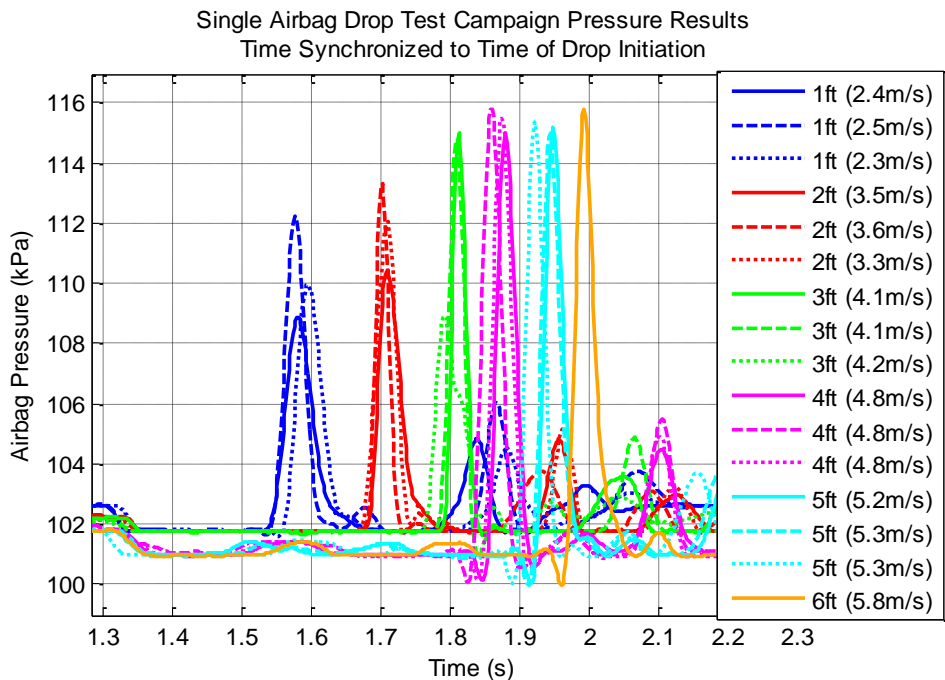


Figure 5-43: Airbag Pressure for all Single Airbag System Drop Tests

Here, it should be noted that in Figure 5-43, the difference in airbag pressures during freefall between the 1 to 3 foot drop tests and the 4 to 6 foot drop tests; was due to the fact

that these sets of tests were performed on different days with differing ambient pressure conditions

Hence from these test results, it can be seen that as expected, the acceleration and pressure spikes experienced by the system generally increase with the impact velocity. In the cases where this trend is not as apparent, the drop was initiated from a height which was too low for the system to be engaged in the test rig. Consequently, during the execution of these drops, pitch, yaw, and roll angles were sometimes unintentionally imparted on the drop test article during the triggering of the quick release mechanism. As the airbag made contact with the ground, any imparted attitude angle caused some shearing of the airbag, thereby reducing the available stroke and increasing the magnitude of the resultant acceleration spike. The presence of this unintended impact attitude is highlighted in the “Floor Impact Pitch Angle” column of Table 5.9.

More importantly, however, is the fact that all drops remained underneath the Brinkley low injury-risk limits, indicating a safe impact environment. Interestingly, the peak Brinkley Index appears to clearly decrease as the drop height moved from 5 feet to 6 feet. This can be explained by the tear which was experienced in the airbag at the 6 foot height. Although it led to the premature ending of the drop test campaign, this tear allowed for more gas to be vented from the airbag during the initial stroke, as compared to the normal means of venting through pressure relief valves. By releasing more gas, more energy was effectively removed from the system, thus leading to improved impact attenuation performance.

Also of significance is the proximity of the peak Brinkley Index response to the upper bound for low injury-risk. This suggests that although the system met the injury-risk requirements for all tests performed, it is likely to exceed the low injury risk limits as the impact velocity is increased towards that of the nominal Orion landing case. This motivates the need for the system dynamics model to be refined so that more accurate performance predictions to be made, thus enabling an improved system to be developed.

5.4 Single Airbag Impact Model Refinement

With a data set characterizing the impact dynamics of the single airbag drop test article obtained, an effort was undertaken to refine the impact dynamics model originally used to

size the system. Figure 5-44 shows an acceleration and pressure history comparison between the original model prediction and the experimental data obtained for the 4 foot impact case.

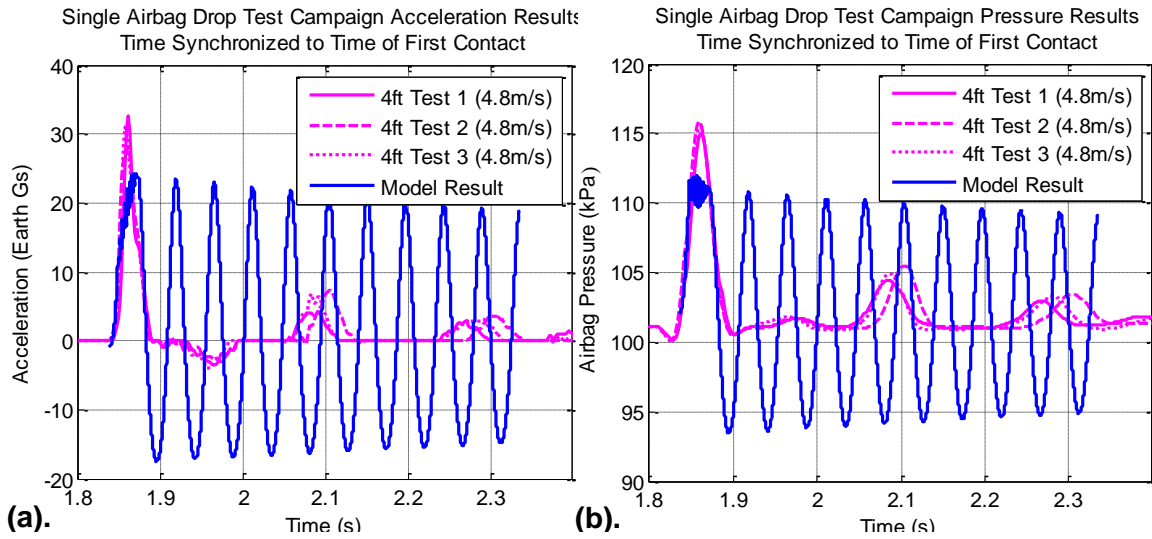


Figure 5-44: Comparison between Original Model Predictions and Experimental Data for a 4 foot Drop (a). Acceleration (b). Airbag Pressure

Here, it can be seen that the model-predicted oscillatory behavior discussed in Section 5.1.5 leads to a corresponding high amplitude oscillatory behavior in the acceleration and pressure response. Investigation into the cause of this trend found that it was due to the manner in which the airbag shape functions were implemented.

As discussed in Section 3.1.2, the purpose of the shape functions is to approximate geometry of the airbag as it compresses. During the downward stroke of the airbag, this is an adequate approximation, as the volume decreases and the footprint area increases. During the upstroke however, the inverse occurs and the volume expands, causing the pressure to decrease below atmospheric, producing the suction effect described in sample analysis case presented in Section 5.3.2. It is this suction effect which imparts the upward force on the payload mass, initiating the observed oscillatory motion.

Additionally, in the analysis performed in Section 5.3.2, it was observed that the aforementioned suction effect occurs only for a brief period of time after the initial stroke of the airbag, due to its material elasticity. This effect manifested itself in the form of a negative gauge pressure over this short time period. Since airbag material properties are not explicitly modeled in the single airbag impact model, this pressure effect was chosen as the basis for the refinement of the single airbag impact model.

Specifically, this was performed by implementing a condition whereby the internal airbag pressure is prevented from decreasing to a value beneath that of atmospheric. By doing this, the elasticity of the airbag geometry is implicitly limited, thus approximating the observed interaction between the airbag geometry and its material. Also, the implementation of this condition results in the previously mentioned suction effect being completely ignored. Because this effect was observed to occur over such a short period of time, this assumption was deemed appropriate for the desired level of fidelity of the refined model. Figure 5-45 shows a comparison between the 4 foot drop test results and the performance predictions of the updated single airbag impact model.

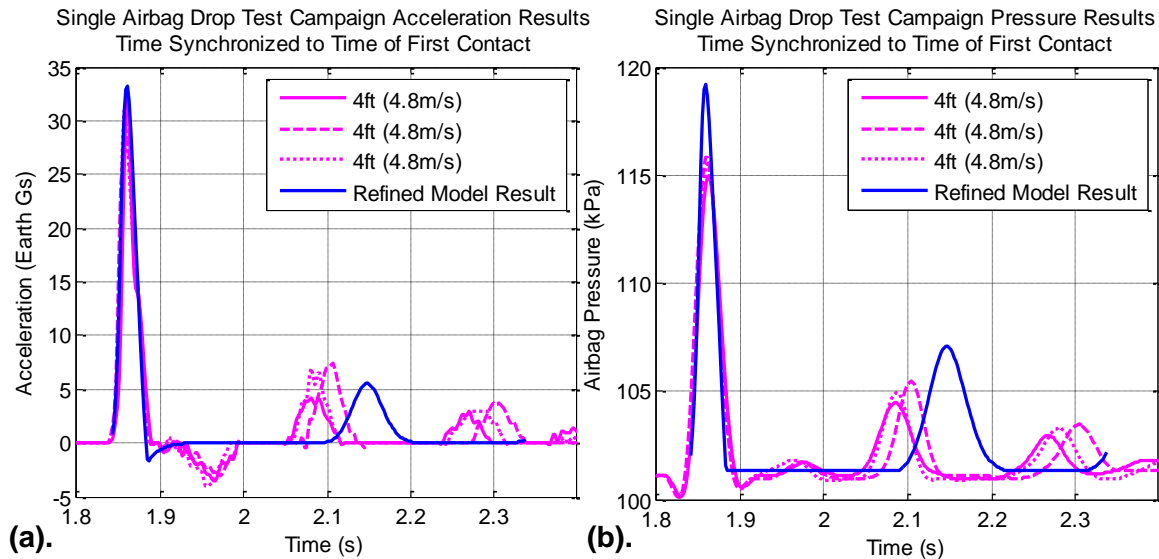


Figure 5-45: Comparison between Refined Model Predictions and Experimental Data for a 4 foot Drop (a). Acceleration (b). Airbag Pressure

From Figure 5-45, an immediate improvement in the model prediction can be observed. This is made apparent by the less than 1G difference in acceleration peak values between the datasets, as well as the similarity in their overall dynamic trends. Additionally, the minor differences between the predicted and experimentally obtained results can be attributed to the observations discussed in Section 5.3.2. In particular, this refers to the unintentional impact attitude imparted on the system during drop initiation, causing the test mass to recoil at an inclined angle. It is this angle which causes the secondary stroke to occur sooner than predicted for a purely vertical impact; as represented by the approximately 0.05s time delay in this phenomenon, shown in Figure 5-45.

Moreover, Figure 5-45 also indicates that the refined model slightly over-predicts the magnitude of the pressure peaks during the impacting event. This is due to the fact that even

though several measures were implemented to minimize leakage, the test airbag was not completely airtight. This led to slight reduction in its pressure and hence a discrepancy between its pressure history and that of the ideal, perfectly airtight case, assumed by the dynamics model.

Therefore, with the accuracy of the refined airbag impact model predictions showing promise, its performance was tested against the complete data sets obtained during Test Sessions 1 and 2. In turn, this allowed for the robustness of the model along both the dimensions of varying mass and varying impact velocity to be gauged. Here, the predicted acceleration and Brinkley DRI was used as the basis of performance evaluation as these are the primary metrics used to determine system feasibility.

Refined Airbag Impact Performance over Varying Payload Mass

Shown below is a comparison of the Test Session 1 and corresponding model-predicted acceleration responses:

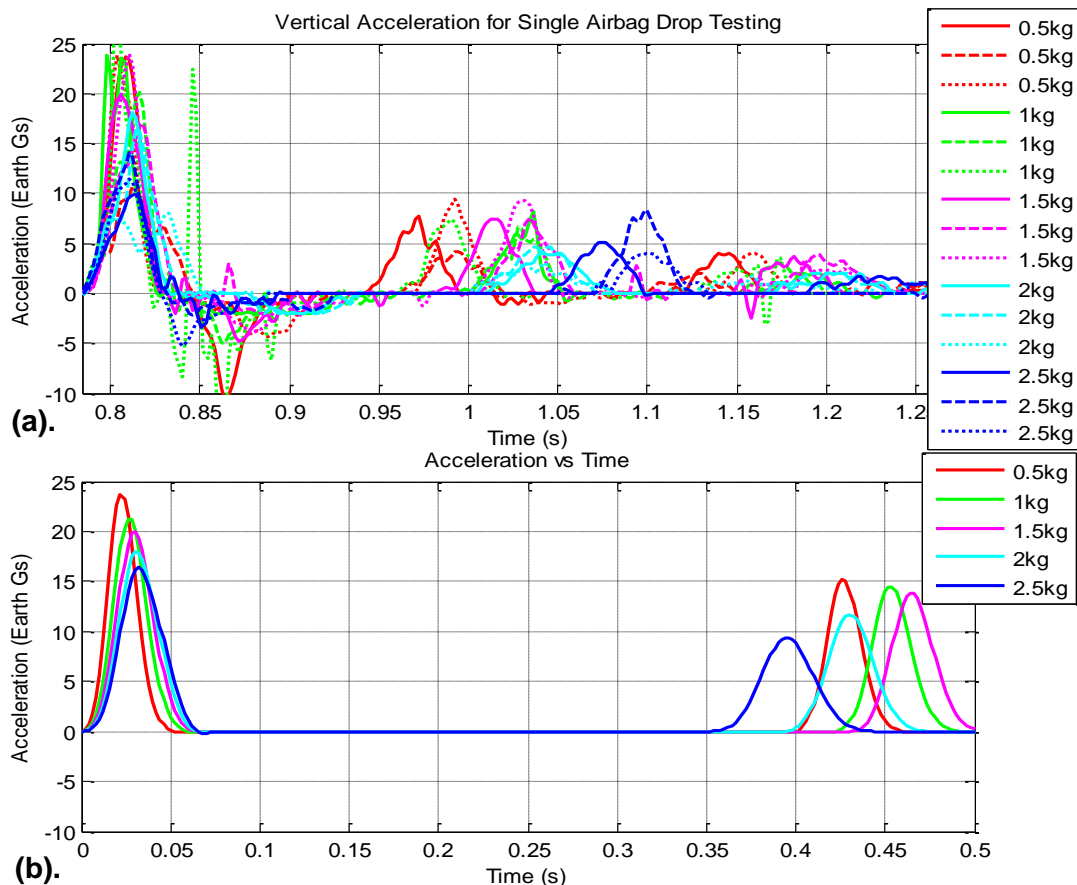


Figure 5-46: Acceleration Response over Varying Payload Mass
 (a). Experimentally Obtained Data (b). Updated Model Prediction

It can be seen in Figure 5-46 that the refined single airbag impact model captures the general acceleration trends to a relatively high degree of accuracy. Here, the decreasing peak acceleration with increasing payload mass trend observed during testing is clearly predicted, with the predicted peak acceleration value being within 1G of that experimentally observed. In addition, it should be noted that because all Test Session 1 drops were performed from a height of 1 foot, the system was not high enough to be initiated from the drop test rig. As a result, the same unintended impact angles as those mentioned in the previous section were imparted on the system, causing a highly variable time between the first and second stroke in the system during impact. These same trends can be found in a comparison of the corresponding Brinkley Indices, shown below:

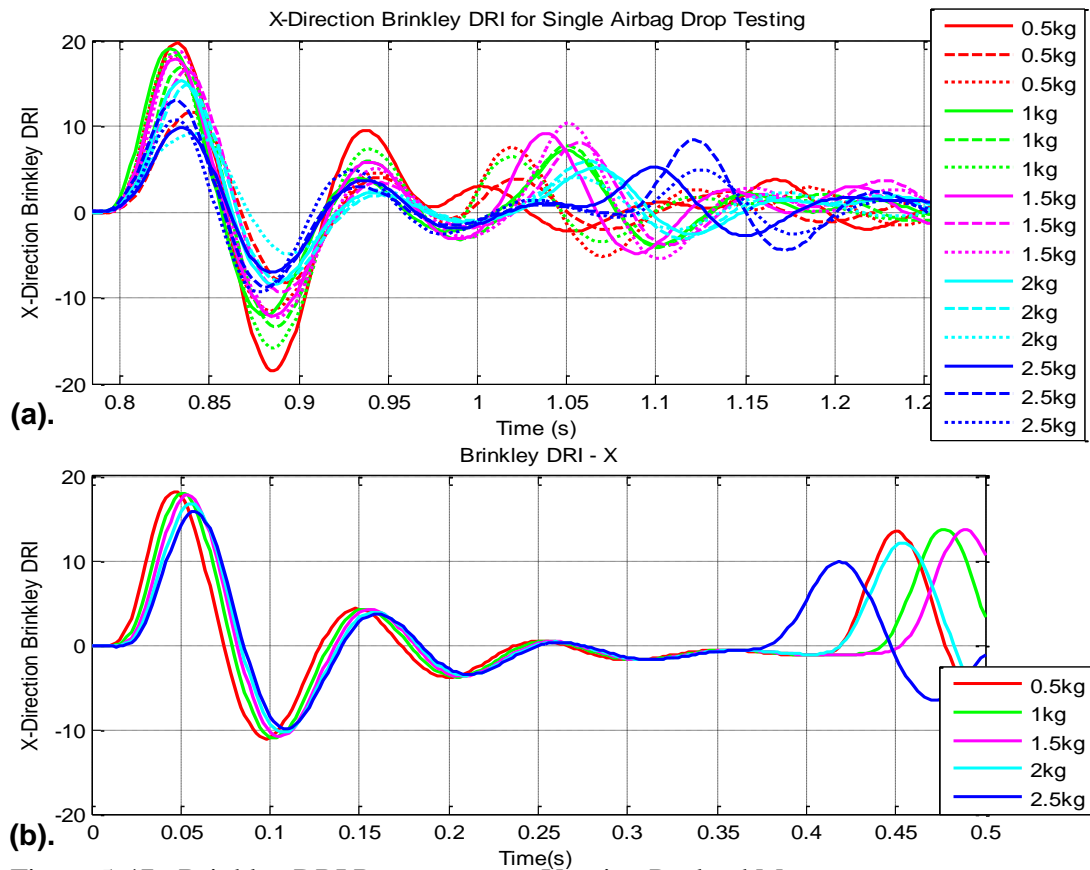


Figure 5-47: Brinkley DRI Response over Varying Payload Mass
 (a). Experimentally Obtained Data (b). Updated Model Prediction

Here, it can be observed that the slightly differing frequency content between the model-predicted and experimentally obtained acceleration responses results in a less accurate prediction of the peak Brinkley index values. This is especially apparent in the prediction of

the secondary Brinkley peak at approximately 1.1 seconds in the experimentally obtained results, and after 0.42 seconds in the model prediction. Interestingly, the difference between the peak Brinkley values increases slightly with increasing payload mass, indicating the growing influence of the combined impact attitude and test mass effects on the system response. Specifically, the difference in these peak Brinkley values is less than 1 for a payload mass of 0.5 kg, and closer to 3 for a test mass of 2.5 kg. Even though this discrepancy exists however, the fact that the model over predicts the Brinkley Index may prove beneficial in future design efforts due to its conservatism.

Refined Airbag Impact Performance over Varying Impact Velocity

Figure 5-48 shows a comparison between the experimentally obtained and model predicted acceleration responses over varying impact velocity:

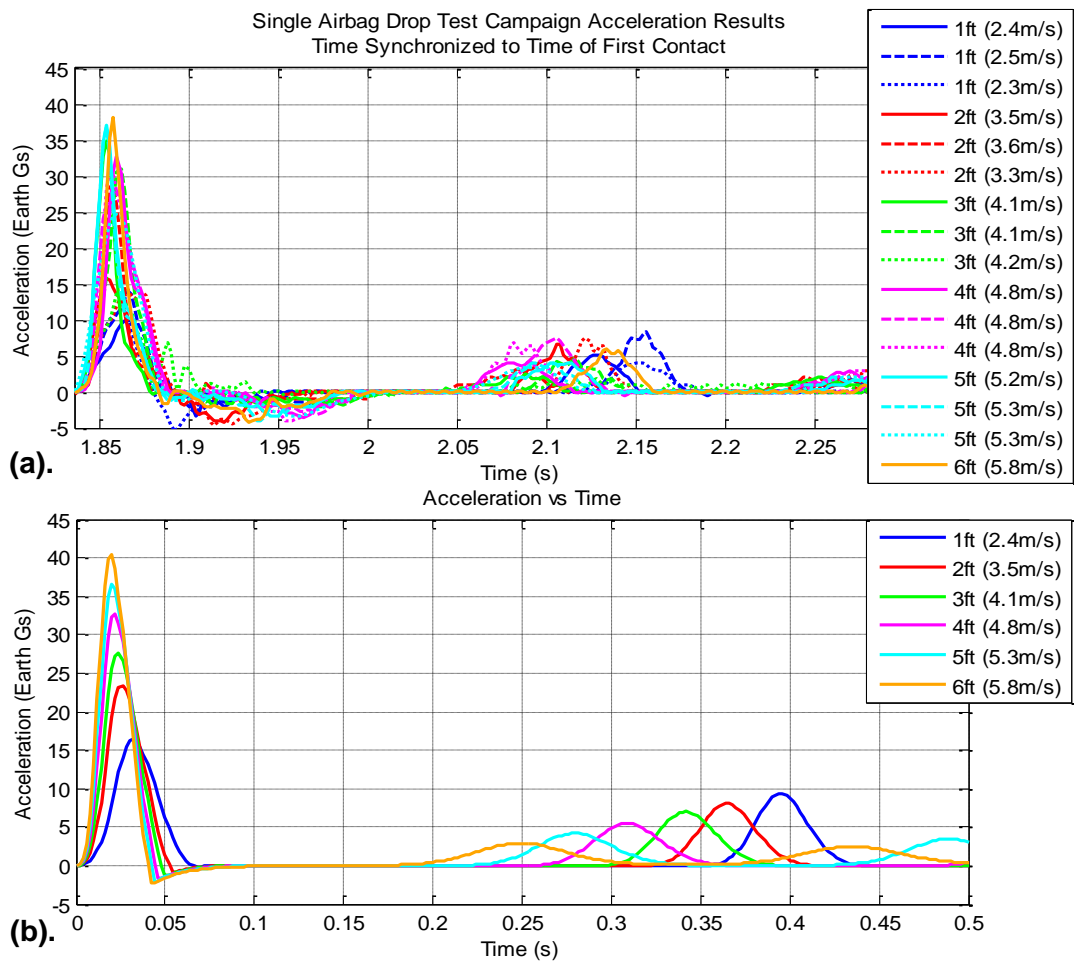


Figure 5-48: Acceleration Response over Varying Impact Velocity
 (a). Experimentally Obtained Data (b). Updated Model Prediction

Like that of the previous analysis over varying payload mass, it can be seen here that overall, the refined airbag impact model achieves a relatively accurate prediction over varying impact velocity. In particular, it captures the previously observed trends of increasing peak acceleration and decreasing time between first and second strokes, with increasing impact velocity. Moreover, the value of the peak acceleration is also accurately predicted, being within 2Gs of the corresponding experimentally obtained value. Although not as accurate as the acceleration predictions observed with varying payload mass, the over prediction of the peak acceleration leads to a slightly conservative estimate which is favorable from the design perspective. This conservatism is again reflected in the model prediction of the Brinkley response, shown below in Figure 5-49.

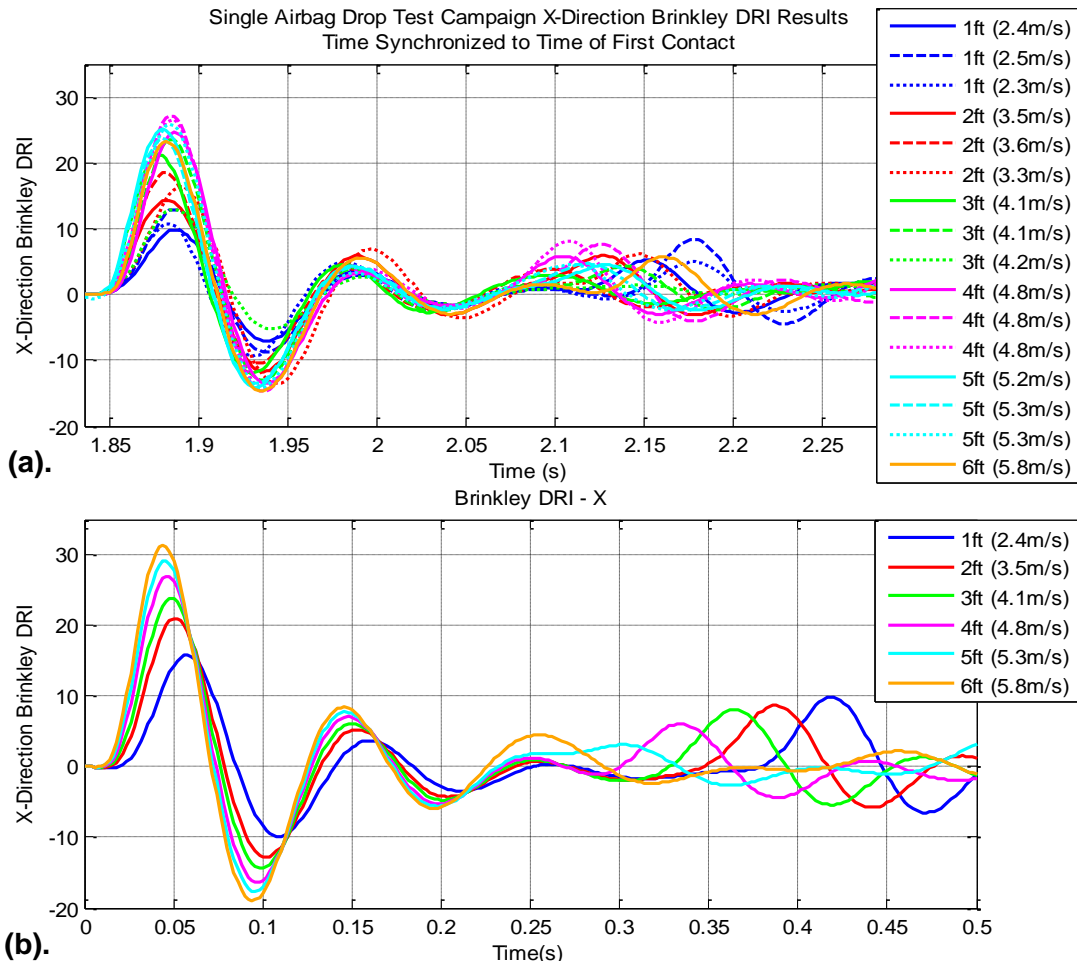


Figure 5-49: Brinkley DRI Response over Varying Impact Velocity
 (a). Experimentally Obtained Data (b). Updated Model Prediction

From Figure 5-49, it can be seen that like the comparison with varying payload mass, the model achieves a Brinkley Index prediction which captures the underlying trends whilst over-predicting the peak values. Interestingly, the peak Brinkley index prediction improves with increasing impact velocity here – a contrasting trend to that observed in the varying mass case, where the prediction improved with a reduction in the payload mass. A contributing factor to this may be that as the impact velocity is increased, the system is hoisted higher in the drop test rig. Consequently, the system spends a longer period of time traveling down the guide rails of the rig, resulting in drops which more closely mirror the perfectly vertical drops simulated in the impact model. It should further be noted here that the large discrepancy in the Brinkley prediction for the 6 foot drop case is a result of the test airbag rupturing during this test, allowing more gas to be vented and hence leading to a lower measured peak Brinkley DRI value.

Finally, it is important to highlight the fact that in all of the comparisons discussed in this section, a key discrepancy has existed between the modeled case and the test scenario. This refers to the fact that a simulated floor was implemented on the test article, but was not explicitly modeled as there was no a priori knowledge of its stiffness properties. By not implementing the floor in the model, the floor is implicitly assumed to be infinitely stiff, since the load transfer from the ground surface through the floor and to the airbag is completely efficient. Since the analyses performed throughout this section indicates that this assumption has a negligible effect on the accuracy of the model prediction, it was deemed unnecessary to implement the stiffness effects of the simulated floor into the single airbag impact model as part of its refinement.

5.5 Design Space Exploration

As the development and testing of the single airbag drop test article took place, a separate, detailed optimization study was concurrently performed in an attempt to gain insight into the effects of the geometry on the overall system performance. Whilst previously discussed attempts at optimization focused on only determining the inflation and venting properties of an airbag with fixed geometry, the intent of this study was to account for the interaction between the airbag geometry, inflation and valve burst properties; and to relate trends in the resulting single and multi-objective space, to trends in the design space. This was

accomplished by firstly attempting to optimize the design of a single airbag system with the single objective of minimizing the maximum Brinkley DRI; followed by an attempt to optimize the system over the dual objectives of minimizing both injury-risk and total system mass. These studies consisted of experimenting with a series of optimization schemes and comparing their results, as will be expanded upon in the following sections. In addition, note that because the pressure relief development was well underway when this study was performed, the venting area used in this study was fixed to that of the third generation flapper valve.

5.5.1 Single Objective Optimization

To optimize the single airbag system design over the single objective of minimizing the Brinkley index, the optimization problem was formulated as follows:

$$\begin{aligned}
 & \text{Minimize} \left(\begin{array}{l} \beta = \text{Maximum Injury Risk} \\ = \text{Maximum Brinkley Direct Response Index} \end{array} \right) \\
 & \text{Subject to:} \\
 & \quad 0.1 \leq R \leq 0.5 \quad [\text{m}] \\
 & \quad 0.3 \leq L \leq 0.85 \quad [\text{m}] \\
 & \quad P_{bagI} \geq 101325 \quad [\text{Pa}] \\
 & \quad \Delta P_{burst} \geq 0 \quad [\text{Pa}]
 \end{aligned} \tag{5.9}$$

Where p_{bagI} is the initial airbag inflation pressure and Δp_{burst} is the pressure relief valve opening pressure, measured as the pressure in addition to p_{bagI} required for the valve to open.

It is interesting to note here that the only constraints present within this problem correspond to bounds on the design variables. As was the case with all previous optimization attempts, this is due to the fact that only a single-airbag model is being studied. For a multi-airbag system however, additional constraints would be required to capture the interactions between each of the airbags. An example of this is that the sum of the airbag diameters (ie. the total length of the system), would have to be within some range of the sitting height of the occupant.

Hence with this formulation now composed, a series of methods was used to study trends in the problem solution. These included a Design of Experiments method, a gradient based

method, and a heuristic optimization method. Each of these methods is expanded upon throughout the rest of this section.

Design of Experiments – Orthogonal Arrays

In order to obtain initial trends in the objective with respect to the design variables, the Design of Experiments method was used to perform a preliminary sampling of the design space. Here, the factors were chosen to correspond to each of the design variables in the problem, being the: airbag radius, length, bag pressure and burst pressure. Three levels of values for each factor were selected to represent an even spread across the design domain, as shown in the following table:

Table 5.10: Factors and Levels for the Design of Experiments

Factor	Level 1	Level 2	Level 3
A: Radius (m)	0.2	0.3	0.4
B: Length (m)	0.3	0.5	0.7
C: P_{bagI} (atm)	1.0	1.1	1.2
D: ΔP_{burst} (kPa)	8	12	16

For this study, the orthogonal arrays method was used to study the design space. This involves sampling the space along orthogonal combinations of design variables to ensure a balanced spread, thereby better capturing its interactions when compared to the One at a Time method employed in Section 5.1.2. An added advantage of this method is that because it enforces balance, the resultant sensitivities better represent the entire design space compared to the One at a Time method, where the sensitivities obtained ignored all interaction effects between the design variables. For the case here, the $L_9(3^4)$ set of orthogonal arrays was used, with the corresponding results shown below in Table 5.11

Table 5.11: Orthogonal Array Analysis Results

	A: Radius	B: Length	C: p_{bagI}	D: d_{p_{burst}}	DRx
Experiment 1	A1: 0.2	B1: 0.3	C1: 1.0	D1: 8	36.72
Experiment 2	A1: 0.2	B2: 0.5	C2: 1.1	D2: 12	45.62
Experiment 3	A1: 0.2	B3: 0.7	C3: 1.2	D3: 16	54.82
Experiment 4	A2: 0.3	B1: 0.3	C2: 1.1	D3: 16	43.65
Experiment 5	A2: 0.3	B2: 0.5	C3: 1.2	D1: 8	52.53
Experiment 6	A2: 0.3	B3: 0.7	C1: 1.0	D2: 12	57.39
Experiment 7	A3: 0.4	B1: 0.3	C3: 1.2	D2: 12	46.94
Experiment 8	A3: 0.4	B2: 0.5	C1: 1.0	D3: 16	55.68
Experiment 9	A3: 0.4	B3: 0.7	C2: 1.1	D1: 8	57.15

To calculate the effect of each design factor and level, the overall mean of the Brinkley DRI, m , is first calculated. Following this, the main effect of each design factor and level is calculated by averaging the Brinkley DRI values when that factor and value is fixed. For the case that the radius is 0.2m (ie. Factor-Level: A1), this is given by:

$$m_{A1} = \frac{DRI_1 + DRI_2 + DRI_3}{3} \quad (5.10)$$

With this, the main effect of a level A1 is calculated by:

$$\text{Effect of radius level A1} = m_{A1} - m \quad (5.11)$$

Repeating the same procedure the effects of all the factors and levels can be obtained. These are shown in Table 5.12.

Table 5.12: Main Effect of Design Variables determined from Orthogonal Array Analysis

Main effect of A1	-4.33
Main effect of A2	1.13
Main effect of A3	3.20
Main effect of B1	-7.62
Main effect of B2	1.22
Main effect of B3	6.40
Main effect of C1	-0.13
Main effect of C2	-1.25
Main effect of C3	1.37
Main effect of D1	-1.26
Main effect of D2	-0.07
Main effect of D3	1.33

From these results, it can be seen that A1, B1, C3 and D3 have the largest effect on the mean Brinkley Index for the corresponding design factor. In addition, since the objective is to minimize Brinkley DRI, a starting vector of [A1 B1 C2 D1] will be selected for subsequent optimization studies. This corresponds to:

$$x_0 = (0.2m, 0.3m, 1.1atm, 8kPa) \quad (5.12)$$

An interesting point to note is that the results of this exercise indicate that smaller geometries lead to lower Brinkley DRI values and hence improved impact attenuation performance, which seems unintuitive. As will be seen in the following sections, this trend was consistently observed with all optimization schemes used. Consequently, an investigation was performed in an attempt to explain this phenomenon. This will be discussed later in this section.

Gradient Based Optimization – Sequential Quadratic Programming

For the gradient-based optimization, a Sequential Quadratic Programming (SQP) method was chosen. This technique involves solving a local quadratic approximation to the Lagrangean to determine the search direction, performing a line search to determine the step length, and iteratively updating the solution to this approximation as it steps through the variable space. Here, the approximation to the Lagrangean consists of creating a quadratic approximation to the objective, and a linear approximation to the constraints. In addition, the Hessian term used in this method was approximated in a Quasi-Newton manner, using a Broyden-Fletcher-Goldfarb-Shanno (BFGS) method. This algorithm is summarized in Equation (5.13).

for $k = 1, 2, \dots$ **do**

- Solve local quadratic subproblem for search direction d_k :

$$\min Q(d_k) = J(x_k) + \nabla J(x_k)^T d_k + \frac{1}{2} d_k^T B_k d_k$$

subject to:

$$\nabla g_j(x_k)^T d_k + g_j(x_k) \leq 0 \quad j = 1, \dots, m_1$$

$$\nabla h_i(x_k)^T d_k + h_i(x_k) = 0 \quad i = 1, \dots, m_2$$

(5.13)

- Perform line search to determine step length α such that Lagrangean is minimized
- Update solution: $x_{k+1} = x_k + \alpha d_k$
- Compute update to Hessian, B_{k+1} , using BFGS method
- Check for convergence: $\nabla L = 0$

end for

Where J is the objective function, g is the set of m_1 inequality constraints, h is the set of m_2 equality constraints, and L is the Lagrangean.

Here, the SQP method was chosen based on the fact that for the single airbag system, no simple analytical expression is available to express the objective function. Rather, the objective value is obtained from the solution to a highly non-linear set of numerically solved equations. Because SQP uses an approximation to the Hessian rather than requiring an analytical form of one, the method lends itself naturally to this problem. In addition, the fact that SQP is designed to inherently handle constraints allows it to easily accommodate the bound constraints of this problem.

Scaled Case

As was mentioned in the previous section, the result of the Design of Experiments was used as an initial guess for an unscaled run of the SQP. Figure 5-50 shows the iteration history and solution of this run.

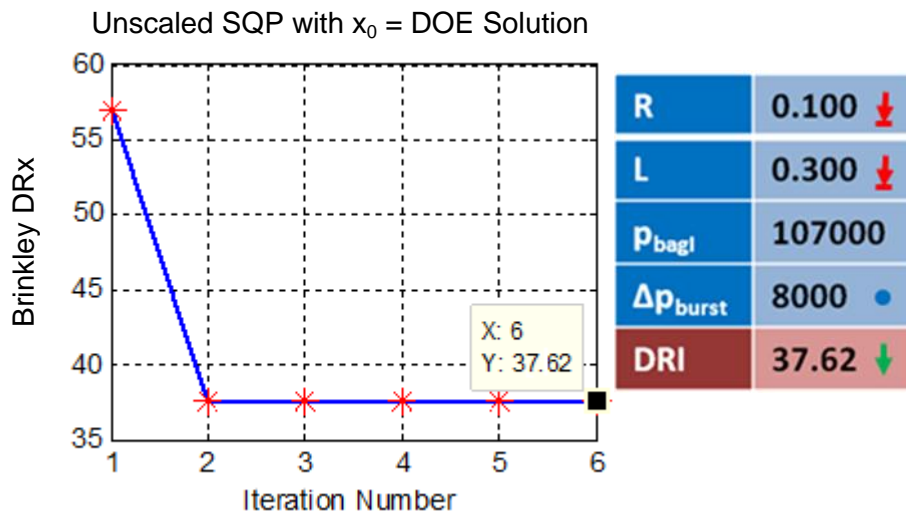


Figure 5-50: Unscaled SQP Iteration History and Solution

Here, it can be seen that like the result of the Design of Experiments, the geometric component of the solution hits the lower bounds. The reasons behind this will be explored later in this section. Contrastingly, a change in the burst pressure resulted in a significant reduction in the Brinkley Index.

Unscaled Case

In an attempt to obtain a better gradient-based solution, the SQP scheme was rerun with a scaled design vector. This vector was determined by calculating the Hessian of the system at the optimal solution, which in turn, was obtained with the use of a second order accurate finite difference approximation to the second derivative. This is given as follows:

$$f''(x) \approx \frac{f(x + \Delta x) - 2f(x) + f(x - \Delta x)}{\Delta x^2} \quad (5.14)$$

Here, the value of Δx was chosen to be $\Delta x = 1 \times 10^{-8}$, based on enforcing the condition whereby the rounding error is comparable in magnitude to the truncation error. With this, the diagonal terms of the Hessian were calculated to be approximately:

$$\begin{aligned} H_{11} &= 6.671 \times 10^{12} \\ H_{22} &= 1.004 \times 10^{12} \\ H_{33} &= -61733220 \\ H_{44} &= 0 \end{aligned} \quad (5.15)$$

As can be seen from this result, three of the four diagonal terms are in need of scaling. The magnitude of scaling required can be calculated by attempting to make the order of the Hessian terms equal to one. Thus, the scaling terms can be calculated using the following relationship:

$$\text{Scaling Factor} = O(H_{ii}^{-0.5}) \quad (5.16)$$

Therefore:

$$\text{Scaling Factor} = L = \begin{bmatrix} 10^{-7} & & & \\ & 10^{-7} & & \\ & & 10^{-4} & \\ & & & 1 \end{bmatrix} \quad (5.17)$$

With this, the SQP scheme was re-run, yielding the results given in Figure 5-51.

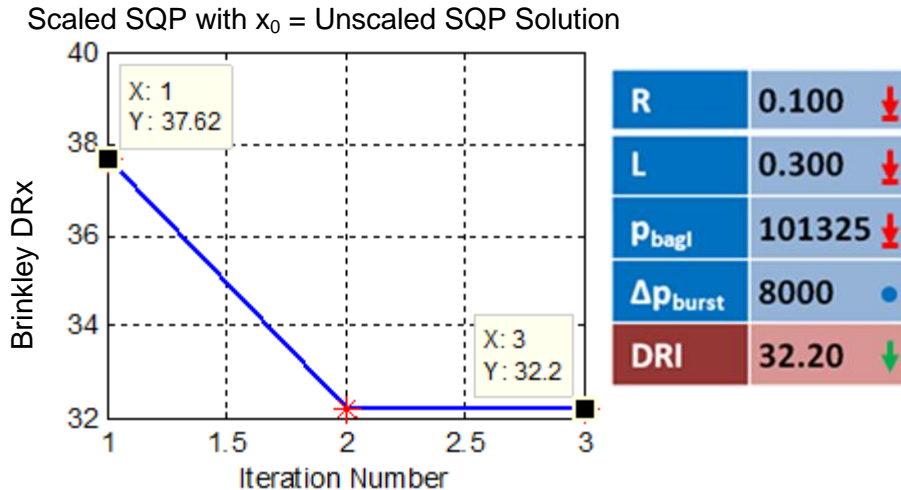


Figure 5-51: Scaled SQP Iteration History and Solution

Again, it can be seen that the overall impact attenuation performance of the system has improved after this run. Here, this is due a reduction in the inflation pressure – a trend also observed during the optimization exercise performed in Section 5.1.5. Also observed is the fact that the consistent trend towards smaller geometries has once more occurred. This will be investigated in later in this section.

Heuristic Methods – Simulated Annealing

In addition to gradient-based methods, heuristic techniques were also used to solve the single-airbag single objective optimization problem. This was due to the fact that the large search space and complex interactions between the non-linear governing system equations results in the potential for many local optima to occur. Because of their inherent randomness, heuristic techniques are capable of identifying the global optimum of the problem under these conditions.

Here a Simulated Annealing (SA) method was used, primarily due to its requirement for less function evaluations when compared to other methods. Inspired by the concept of annealing in metallurgy, this method involves starting with an initial design vector with an initial temperature, to represent the probability of the optimizer selecting a suboptimal design as it steps through the design space. As the optimizer moves through the design space, this temperature decreases toward a value of zero, eventually adopting a steepest descent type behavior. To determine subsequent iterates, a random perturbation of the current vector is taken and its objective is evaluated and compared to that of the current. If this new vector

achieves a lower objective value, it is accepted. However, if the new vector has a higher objective value, it is subjected to the “Metropolis Step”, where a random number is generated and compared to the Boltzmann Probability, thus providing an opportunity for it to be accepted as the next iterate. This Boltzmann probability is given by:

$$P(k, T) = \exp\left(-\frac{\Delta E_k}{T_k}\right) \quad (5.18)$$

Where ΔE_k is the difference in energy or objective value between the current and previous iterates, and T_k is the current temperature of the system. Moreover, the simulated annealing algorithm is summarized below in Equation (5.19).

Define initial state (x_0), temperature (T_0), and limiting number of iterates before decreasing temperature (T_E)
while $T_k > T_{min}$ **or** $k < k_{max}$... **do**
 • Evaluate Objective: $E(x_k)$
 while $m \leq T_E$
 ○ Perturb Configuration: $x_k \rightarrow x_{k+1,m}$
 ○ Evaluate Energy of Perturbed Configuration: $E(x_{k+1,m})$
 ○ Compute Energy Difference: $\Delta E_k = E(x_{k+1,m}) - E(x_k)$
 if $\Delta E < 0$
 ▪ Accept $x_{k+1,m}$ as the new iterate
 break
 else Perform Metropolis Step
 ▪ Create a random number, v in [0,1]
 if $\exp\left(-\frac{\Delta E_k}{T_k}\right) > v$
 - Accept $x_{k+1,m}$ as the new iterate
 break
 else
 - Keep x_k as the current iterate
 - Try a different Perturbed Configuration: $m \rightarrow m+1$
 end if
 end if
 end while
 • Determine System Temperature for next Iterate: $T_{k+1} = (T_1 / T_0)^k T_k$
end while

For the case here, the optimal values obtained from the SQP analysis were selected as the starting point for the Simulated Annealing scheme; with the upper and lower bounds for the perturbation in each design variable chosen to be the same as those listed in Equation (5.9). Furthermore, the major parameters for the system were selected based on previous experimentation with various combinations of settings. These are summarized in Table 5.13 below:

Table 5.13: Simulated Annealing Tuning Parameters

SA Parameter	Values	Rationale
T ₀ - initial system temperature	500	Guarantees a good initial sampling of the design space
Cooling Schedule	Exponential	Proven to be effective in terms of the optimality of the final result and computation time
dT Temperature Increment	0.1	Experimentation showed that this value was appropriate for the problem at hand
Equilibrium Condition	20	Ensures that enough configurations are evaluated before moving to the next temperature state

With these final tuning parameters, the following results were obtained:

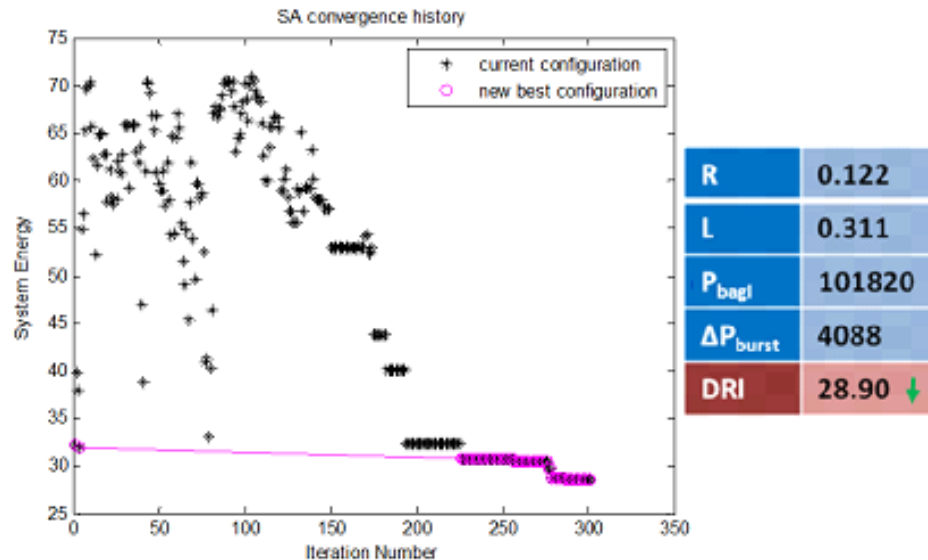


Figure 5-52: Simulated Annealing Iteration History and Solution

Observing the SA iteration history, it can be seen that the algorithm first samples through different parts of the design space at the initial temperature state. As the temperature reduces,

the scheme behaves more like a gradient based method and concentrates on a specific region of the design space. The optimal solutions are found near the termination of the algorithm.

With respect to the optimal solution obtained, it is interesting to note that unlike the gradient based schemes, none of the design variable bounds have been hit. This is the case even with an improved Brinkley Index. The reason for this behavior will be explored in the next subsection.

Single Objective Optimization Results Analysis

In this section, the trends in the results observed in the various single objective optimization runs will be analyzed. Specifically, the following will be investigated:

- The unintuitive trend towards a smaller airbag geometry for improved Brinkley DRI
- The fact that the simulated annealing analysis yielded a result with an improved Brinkley Index but without hitting the lower bounds of the design variables; as was observed with all previous optimization cases; and
- The sensitivities within the system

Correlation between Smaller Airbag Geometries and Improved Brinkley Index

Throughout the single objective optimization analysis, it was continually observed that the optimal solution tended toward the lower bound of the geometric design variables, indicating that a smaller airbag is preferable for impact attenuation. This counter-intuitive observation can be explained by comparing the orifice opening area time histories between two differently sized airbags, shown below.

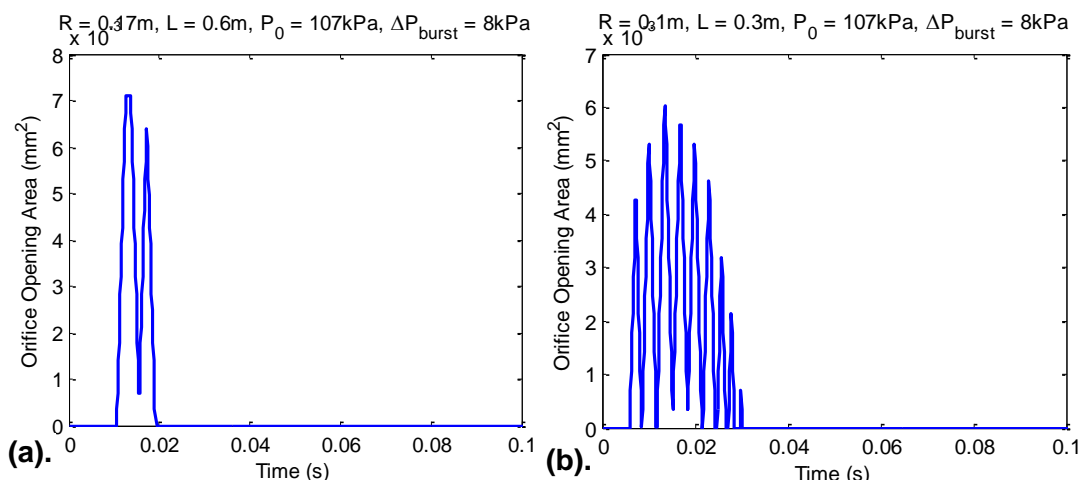


Figure 5-53: Comparison of Orifice Opening Area under Different Airbag Geometries
 (a). Airbag of Radius 0.17m and Length 0.6m
 (b). Airbag of Radius 0.1m and Length 0.3m

Here, it can be seen that under the same impact conditions, the smaller airbag maintains a higher pressure over a longer period of time, which results in the pressure relief valve remaining open for a longer time period. Since the system reduces the energy from the impacting object by venting gas from the system, a longer time for gas release results in a better impact attenuation performance.

However, it should be noted that there are limiting factors to how small the airbag geometry can feasibly be – one of which, being the amount of physical stroke available to damp the impacting system. Hence there appears to be two opposing factors which influence the direction in which the size of the optimal airbag should move. One which drives the system towards lower geometries to maximize the amount of time over which the venting orifice remains open, thereby allowing for more energy to be attenuated from the system; and one which pushes towards increasing the system geometry to avoid bottoming-out. Based on these observations, it appears that the optimum geometry would be one which minimizes the geometry such that bottoming-out does not occur.

The SA Solution Not Lying at the Lower Bounds of the Geometric Variables

In the previous subsection, it was found that the result from the Simulated Annealing analysis had improved upon that of the gradient based methods. One unexpected observation made however, was that when the SA optimal was reached, the geometric variables did not hit their lower boundaries, as had been consistently observed earlier. To further investigate the reason for this, the design space was further examined. It became apparent that this phenomenon was related to how each scheme interpreted the design space. Shown below, are the Brinkley DRI indexes of the design space plotted over a coarse grid and a fine grid:

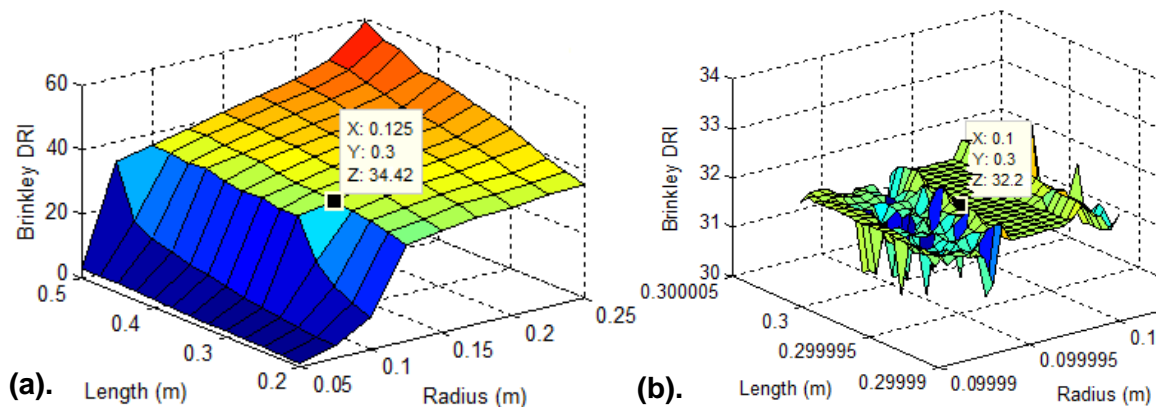


Figure 5-54: Brinkley DRI Space Plotted at (a). Coarse Resolution $\Delta x = 0.025$
(b). Fine Resolution $\Delta x = 10^{-6}$

Here, it can be observed that under different resolutions, the design space has varying levels of noise. This is a result of the manner in which the Brinkley Index is calculated – that is, by integrating over a time horizon to obtain dynamic time histories, and then by calculating the maximum Brinkley DRI value from this.

With this finding, the discrepancy in the trends obtained between the SQP and SA methods can be explained by the fact that the step sizes used by SQP to step across the design space, were large enough to avoid the low amplitude high frequency noise spikes. This resulted in it following gradients measured over longer spatial steps towards the lower bounds. Contrastingly the stochastic nature of the SA scheme allowed it to better sample within the noisy regions of the design space, thus enabling it to find better solutions.

Additionally, an important implication of this finding is that the noise content within a design space affects how the sensitivity analysis is performed. This is because the results of the analysis are dependent on how much noise is captured by the choice of step size when performing a finite difference approximation to a derivative in the design space. This is addressed in the next section.

System Sensitivities

Here, the sensitivities of the system objective with respect to the design variables will be explored. This is achieved by calculating the normalized gradient vector at the achieved local optimum. Due to the numerical form of the objective function, a forward difference method was used to identify the derivatives of the objective with respect to each design variable. The selection of a forward difference scheme was based on the fact that the lower boundaries of three of the four design variables are active under the SQP optimization result. A central or backward difference scheme would result in a step into an infeasible design domain.

Additionally, the selection of the magnitude of the step change in each design variable took into consideration the noisy nature of the design space. Here, these values were chosen such that they were large enough to avoid the high frequency noise present in the design space, while small enough to fulfill the finite difference accuracy requirement. The chosen step lengths are listed as follows:

Table 5.14: Step Length Selections for Sensitivity Analysis

Design Variable	Radius	Length	Bag Pressure	Burst Pressure
Step Change	10^{-3}	10^{-3}	10^{-3}	10^{-3}

Given this, the sensitivity of the objective function to each variable was calculated as follows:

$$\nabla \bar{J} = \frac{x^0}{J(x^0)} \nabla J = \frac{x^0}{J(x^0)} \begin{bmatrix} \frac{\partial J}{\partial R} & \frac{\partial J}{\partial L} & \frac{\partial J}{\partial P_{bagI}} & \frac{\partial J}{\partial P_{burst}} \end{bmatrix}^T = [9.86 \quad 17.38 \quad 12.89 \quad 0]^T \quad (5.20)$$

This result agrees with those previously observed, in that a decrease in airbag radius and length results in a lower Brinkley DRI. Additionally it is also seen that increasing the length of the airbag results in increasing the Brinkley Index by almost a factor of two, when compared to the effects of increasing the radius. This implies that modifying the length has the strongest effect in terms of improving impact attenuation performance amongst all of the design variables.

5.5.2 Multi-Objective Optimization

In addition to the single objective optimization, a multi-objective optimization study was also performed. Here, the additional objective of minimizing system mass was included into the problem formulation. Specifically, the system mass included the mass of the airbag, as well as the mass of the gas internal to it. Hence with this, the problem formulation becomes:

$$\begin{aligned} \text{Minimize} & \left\{ \begin{array}{l} \beta = \text{Maximum Injury Risk} \\ \quad = \text{Maximum Brinkley Direct Response Index} \end{array} \right\} \& \text{ System Mass} \\ \text{Subject to:} & \begin{array}{ll} 0.1 \leq R \leq 0.5 & [\text{m}] \\ 0.3 \leq L \leq 0.85 & [\text{m}] \\ P_{bagI} \geq 101325 & [\text{Pa}] \\ \Delta P_{burst} \geq 0 & [\text{Pa}] \end{array} \end{aligned} \quad (5.21)$$

In order to solve this multi-objective problem, a full factorial expansion over the objective space was performed. The choice of this method came after a series of experiments with the Multi-Objective Genetic Algorithm, where significant issues with clustering of Pareto points and significantly long computation times were observed. The result of this is presented in Figure 5-55.

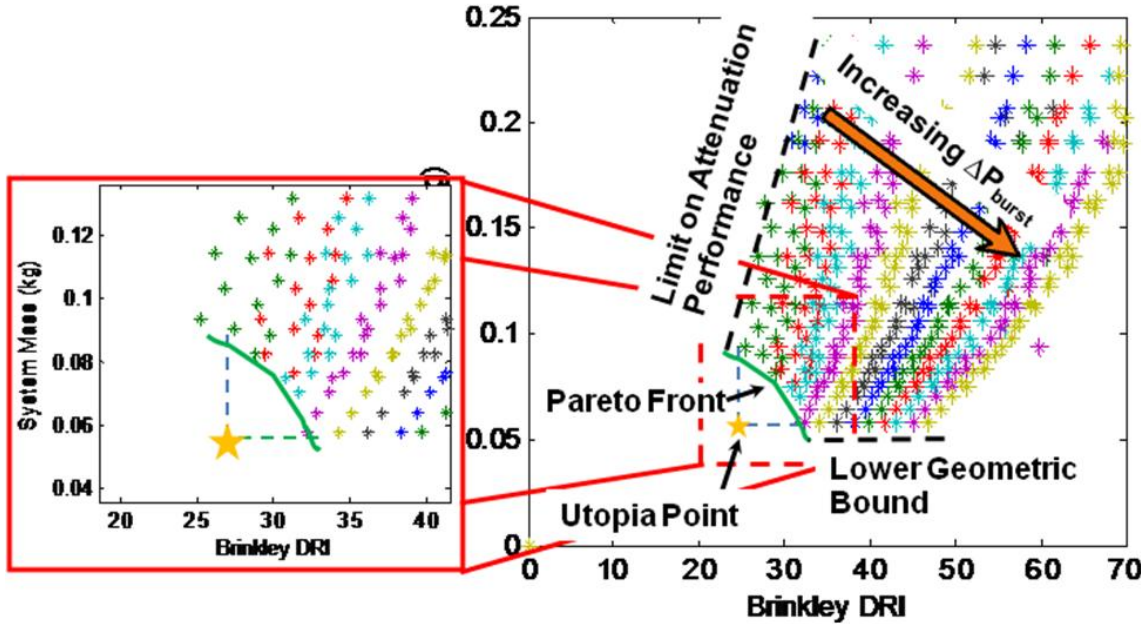


Figure 5-55: Full Factorial Expansion of the Objective Space. Design points of the same color correspond to those with the same burst pressure

Here, it can be observed that moving along the Pareto front corresponds to varying the valve burst pressure at the minimum airbag geometry such that bottoming-out does not occur. It is important to note that this trend was directly driven by the choice of the pressure relief valve concept implemented within the system, and that it would most likely change if the characteristics of the valve were made variable.

Furthermore, Figure 5-55 indicates that the trends found in the single objective optimization again hold true in the multi-objective case. In particular, this refers to the fact that at constant valve burst pressures, the objectives are mutually supporting. This in turn reflects the trend that smaller geometries (and hence lower masses) result in lower Brinkley DRI values, and hence improved impact attenuation. Moreover, it was found that the lower bounds at each of these constant burst pressure values corresponded to the minimum geometry such that bottoming-out of the system did not occur. The fact that these points also corresponded to the Pareto points within the objective space agrees with the conclusions made in the earlier single objective optimization analysis. This also explains the concave shape of the Pareto front, in that the non-dominant solutions along mutually supporting sets of objectives results in solutions being close to equidistant from the utopia point.

Furthermore, it is interesting to note that the observations discussed here would not have been so easily made if a full factorial method was not used, thus reinforcing the value of being able to visualize the relationship between both non-dominated and dominated design solutions.

5.6 Chapter Summary

In this chapter, the design, development, and testing of a single airbag drop test article was presented, followed by an analysis of the results and consequent refinement of the computational model used throughout this study. Through this effort, the practical issues of venting and airbag leakproofing, identified in the first generation system development, were addressed and their solutions validated through testing. Related to this was the development of the processes required for airbag system manufacturing, integration, and testing. Not only did these act to mitigate risk during the single airbag system development, they will inevitably prove to be valuable in future development cycles.

Furthermore, this development effort also yielded valuable insights into the interaction between the design variables. In particular, it was found that for airbag systems incorporating pressure relief valves, smaller geometries resulted in improved impact attenuation performance as long as bottoming-out did not occur. Moreover, it was found that for a fixed airbag geometry, the system performance was most sensitive to changes in the venting area due to its influence on the energy removal from the system.

Hence with this physical insight, a refined dynamics model, and the aforementioned processes established; the third project spiral was initiated to develop a full-scale multi-airbag system in order to determine the feasibility of the personal airbag system concept. This final spiral is discussed in the next chapter.

Chapter 6

Multi-Airbag System Development

In June 2010, after completing two full cycles of system development and having established the fundamental tools, processes, technologies and physical understanding of the airbag impact attenuation problem; the third and final development spiral was initiated in an attempt to definitively determine the feasibility of the personal airbag system concept. Here, the objective was to develop a full-scale multi-airbag system, and to subject it to a series of drop tests. The results of these tests would then be processed and compared to the Brinkley low injury-risk criteria, from which its performance, and hence its feasibility, could be quantified. The details of each of the stated of this final development cycle will be expanded upon throughout this chapter.

6.1 Multi-Airbag System Modeling

One of the major accomplishments achieved in the previous development cycle was the refinement of the single airbag impact model to a level where it was capable of robustly providing accurate performance predictions. In achieving this, a reliable foundation for the development of a multi-airbag system impact model was established. This is particularly the case given that because individual airbags can be modeled as non-linear springs, multiple airbags can be combined together via a structural dynamics framework. As was mentioned in Section 5.1.5, this spring-like behavior can be observed upon examination of the mass-spring structure of the system equation:

$$m\ddot{x} + (P_{bag}(x) - P_{atm})A_{FP}(x) = mg \quad (6.1)$$

Since the second term in the left hand side of Equation (6.1) is a function purely dependent on the system displacement, it can be considered to be analogous to a nonlinear spring with a stiffness given by:

$$k = \frac{1}{x(t)} (P_{bag}(x, t) - P_{atm}) A_{FP}(x) \quad (6.2)$$

With this observation in mind, Lagrange's Equation can be used to derive the system of equations for a multi degree of freedom model with multiple airbags as follows.

Consider the idealized personal airbag system depicted below in Figure 6-1.

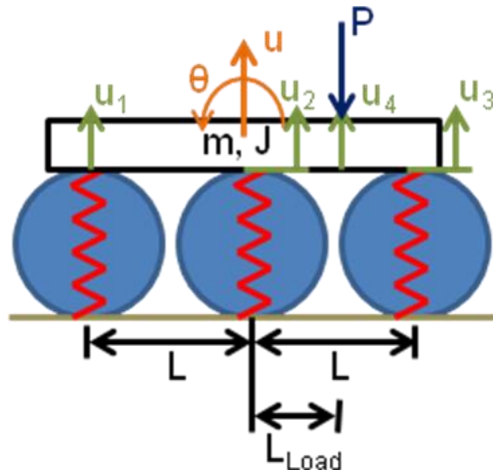


Figure 6-1: Baseline Two Degree of Freedom Multi-Airbag Model

Here, a two degree of freedom model is represented, with a rigid payload mass supported by a system of three equally spaced airbags. In particular, the degrees of freedom captured are the system vertical displacement, and its pitch angle. The choice of these was based on the fact that only the stiffness properties of the airbags in the vertical direction are known, hence limiting the ability to model the system in the lateral degrees of freedom. Even though this is the case, however, these two degrees of freedom capture all the dynamics of interest as they correspond to the Brinkley x-direction – the direction in which the injury-risk criteria is most difficult to meet. Moreover, because the system now consists of multiple airbags, the payload mass has mass and inertia properties, with the location of the center of gravity (CG)

represented in Figure 6-1 by the weight vector, p , acting at the location corresponding to L_{Load} .

Now, define the vector of generalized coordinates, q , as:

$$q = [u \quad \theta]^T \quad (6.3)$$

Where u is the vertical and θ the pitch angle degrees of freedom, as depicted in Figure 6-1. Here, the vertical displacement of the region of the payload mass atop each of the airbags, as well as the CG, can be represented in terms of these degrees of freedom. This is based on the fact that the payload mass is approximated as being a rigid body. The result of this is given as follows:

$$\begin{aligned} u_1 &= u - L \sin \theta \\ u_2 &= u \\ u_3 &= u + L \sin \theta \\ u_4 &= u + L_{Load} \sin \theta \end{aligned} \quad (6.4)$$

With the representation of all displacements within the system established, consider Lagrange's equation, given by:

$$\frac{d}{dt} \left(\frac{\partial K}{\partial \dot{q}} \right) - \frac{\partial K}{\partial q} + \frac{\partial V}{\partial q} + \frac{\partial D}{\partial \dot{q}} = \frac{\partial W}{\partial q} \quad (6.5)$$

Where K is the kinetic energy, V is the elastic potential energy, D is the damping on the system, W is the work done on the system, and t is a measure of time. Since there is no damping in the modeled system, and the kinetic energy is invariant of its displacement, Equation (6.5) can be reduced to:

$$\frac{d}{dt} \left(\frac{\partial K}{\partial \dot{q}} \right) + \frac{\partial V}{\partial q} = \frac{\partial W}{\partial q} \quad (6.6)$$

Now, each component of Equation (6.6) will be expressed in terms of the system degrees of freedom as follows:

Kinetic Energy Term:

The kinetic energy of the system can be expressed as:

$$K = \frac{1}{2} m\dot{u}^2 + \frac{1}{2} J\dot{\theta}^2 \quad (6.7)$$

Differentiating Equation (6.7) firstly with respect to \dot{q} , then with respect to t yields:

$$\frac{d}{dt} \left(\frac{\partial K}{\partial \dot{q}} \right) = \begin{bmatrix} m\ddot{u} \\ J\ddot{\theta} \end{bmatrix} \quad (6.8)$$

Elastic Potential Energy Term:

The elastic potential energy of the system is composed of contributions from each of the airbags, and can be expressed as:

$$V = \frac{1}{2} k_1 u_1^2 + \frac{1}{2} k_2 u_2^2 + \frac{1}{2} k_3 u_3^2 \quad (6.9)$$

Where k_i is the equivalent stiffness of airbag i , given by Equation (6.2).

Substituting Equation (6.4) into Equation (6.9) and differentiating with respect to q yields:

$$\frac{\partial V}{\partial q} = \begin{bmatrix} \frac{\partial V}{\partial u} \\ \frac{\partial V}{\partial \theta} \end{bmatrix} = \begin{bmatrix} k_1(u - L \sin \theta) + k_2 u + k_3(u + L \sin \theta) \\ -L \cos \theta [k_1(u - L \sin \theta) - k_3(u + L \sin \theta)] \end{bmatrix} \quad (6.10)$$

Work Term:

Finally, the work in the system is a function of the displacement contribution from the payload mass, and is given by:

$$W = pu_4 = p(u + L_{Load} \sin \theta) \quad (6.11)$$

Differentiating Equation (6.11) with respect to the generalized coordinate vector, q , results in:

$$\frac{\partial W}{\partial q} = \begin{bmatrix} \frac{\partial W}{\partial u} \\ \frac{\partial W}{\partial \theta} \end{bmatrix} = \begin{bmatrix} p \\ pL_{Load} \cos \theta \end{bmatrix} \quad (6.12)$$

Now, substituting each of the terms given by Equations (6.8), (6.10), and (6.12) into Equation (6.6), and accounting for the fact that the load p is equal to the weight force of the payload mass; yields the following system of equations:

$$\begin{aligned} m\ddot{u} + k_1(u - L\sin \theta) + k_2u + k_3(u + L\sin \theta) &= p = mg \\ J\ddot{\theta} - L\cos \theta[k_1(u - L\sin \theta) - k_3(u + L\sin \theta)] &= pL_{Load} \cos \theta = mgL_{Load} \cos \theta \end{aligned} \quad (6.13)$$

In matrix form, this can be represented by:

$$\begin{bmatrix} m & 0 \\ 0 & J \end{bmatrix} \begin{bmatrix} \ddot{u} \\ \ddot{\theta} \end{bmatrix} + \begin{bmatrix} k_1 & k_2 & k_3 \\ -Lk_1 \cos \theta & 0 & Lk_3 \cos \theta \end{bmatrix} \begin{bmatrix} u_1 \\ u_2 \\ u_3 \end{bmatrix} = mg \begin{bmatrix} 1 \\ L_{Load} \cos \theta \end{bmatrix} \quad (6.14)$$

With this system of equations now established, a finite difference scheme can be developed to determine its solution, thereby predicting the performance of the system. This is performed by firstly considering Equation (6.13). Let the stiffness terms in this set of equations be represented as follows:

$$\begin{aligned} F_1(u, \theta) &= k_1(u - L\sin \theta) + k_2u + k_3(u + L\sin \theta) \\ F_2(u, \theta) &= -L\cos \theta[k_1(u - L\sin \theta) - k_3(u + L\sin \theta)] \end{aligned} \quad (6.15)$$

With this, the vertical displacement equation from Equation (6.13) becomes:

$$m\ddot{u} + F_1(u, \theta) = mg \quad (6.16)$$

Rearranging this equation to reflect the fact that acceleration is measured positive down, yields:

$$a = -\ddot{u} = \frac{1}{m}(F_1(u, \theta) - mg) \quad (6.17)$$

Now, substituting the acceleration term with a second order accurate finite difference approximation to the second derivative yields:

$$\left(\frac{u(t + \Delta t) - 2u(t) + u(t - \Delta t)}{\Delta t^2} \right) = \frac{1}{m}(F_1(u, \theta) - mg) \quad (6.18)$$

Finally, rearranging Equation (6.18) to make the system vertical displacement in the next timestep the subject, yields the following timestepping performance prediction equation:

$$u(t + \Delta t) = 2u(t) - u(t - \Delta t) + \frac{\Delta t^2}{m}(F_1(u, \theta) - mg) \quad (6.19)$$

Similarly, the equivalent equation for the pitch angle can be found to be:

$$\theta(t + \Delta t) = 2\theta(t) - \theta(t - \Delta t) + \frac{\Delta t^2}{J}(F_2(u, \theta) - mgL_{Load} \cos \theta) \quad (6.20)$$

Note here that the values for F_1 and F_2 in the above equations can be determined every timestep using the output of the single airbag impact model applied to each airbag within the system.

Hence with this, the final multi-airbag model can be codified by generalizing the scheme defined by Equations (6.19) and (6.20) to handle any number of airbags, and incorporating the stiffness contributions from the single airbag impact model. The final result of this is summarized in Figure 6-2.

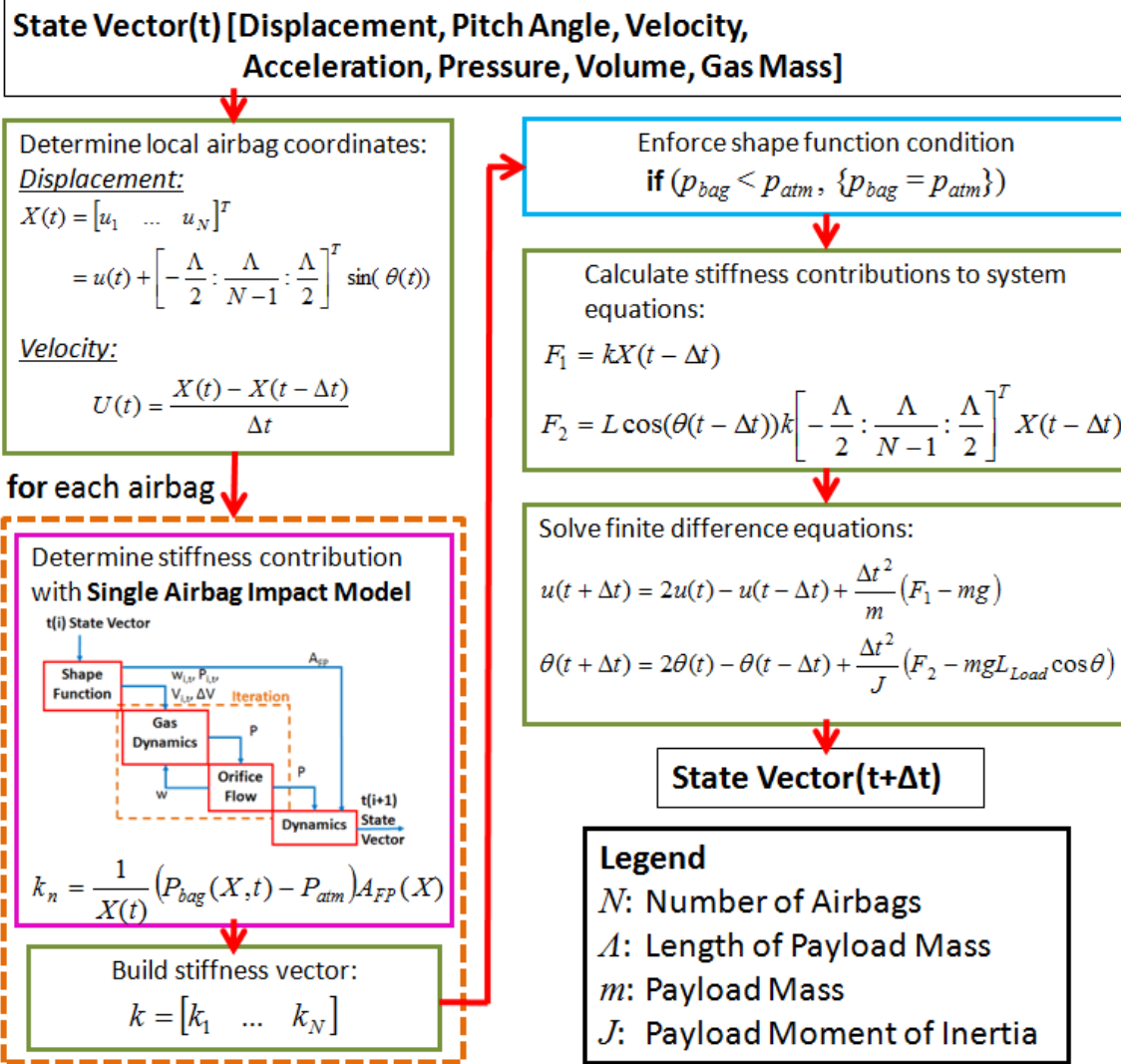


Figure 6-2: Multi-Airbag Impact Model Functional Flow Block Diagram

Following the execution of this model, the resultant acceleration history would be decomposed into the X- and Z- components of the Brinkley frame affixed to the payload mass: and then run through the injury-risk model described in Section 3.2.1 to determine the corresponding Brinkley DRI values.

6.2 Multi-Airbag System Development

With a working multi-airbag model developed, the design process was initiated for the second generation personal airbag system. Here, the objective was to design a multi-airbag system capable of maintaining the Brinkley DRI within low injury risk limits at nominal impact velocities of 7.62m/s (25fps) and at impact angles of both 0° and 30° pitch forward, as specified in Section 2.4. Specifically, this involved determining the specific configuration and design properties of each airbag, as well as designing and fabricating the airbag support structure to interface with the crash test dummy and the drop test rig during drop tests. Each of these design efforts is described in the following sections.

6.2.1 Airbag Configuration Design and Sizing

To determine an appropriate airbag configuration, an optimization problem was formulated so that the design space for each configuration could be explored. Here, the problem was formulated as follows:

$$\text{Minimize } J(x) = [\max(\text{Brinkley DR}_x) \quad \max(\text{Brinkley DR}_z)]^T$$

Where:

$$x = \text{Design Vector} = \begin{bmatrix} \text{Number of Airbags}(N) \\ \text{Airbag Radius}(R) \\ \text{Airbag Length}(L) \\ \text{Valve Burst Pressure}(\Delta P_{burst}) \\ \text{Orifice Area}(A) \end{bmatrix}$$

Subject to:

$$2R(N-1) \leq L = 1.5m$$

Geometric Constraint

Prevents interference between airbags on system

(6.21)

$$R_i = R$$

Commonality Constraints

$$L_i = L$$

Improves system robustness and eases manufacture

$$A_i = A$$

$$P_{bagI,I} = 102\text{kPa}$$

Fixed Inflation Pressure

Determined from experimental experience during Single Airbag Drop Test Campaign

$$\sigma = \max(P_{bag}(X))R/t < 540\text{MPa}$$

Hoop Stress Constraint

Ensures that airbag does not rupture during impact. Upper bounds determined from Section 5.1.4

From this formulation, it can be seen that the length of the payload mass (Λ) was fixed to a value of 1.5m. This was derived from the height of the anthropomorphic test device when in the semi-supine position. In addition, a commonality constraint was enforced, whereby all airbags were intentionally designed to have the same dimensions and inflation properties. In doing this, system robustness would be improved in that if any airbag were to malfunction during operation, it could easily be replaced by a common spare. Moreover, having a common design across all airbags resulted in a more streamlined system manufacture.

Furthermore, a fixed inflation pressure of 102kPa was also enforced during the design process. This value was determined from the single airbag drop test campaign, where it was found that even with the numerous measures implemented to mitigate leakage, the pressure still dropped to this approximate value between the time after inflation was complete, and the time at which the drop was initiated. This was the case even though the airbags were overinflated during all tests. Fortunately, as was found in Section 5.1.5, the system performance improves as the inflation pressure approaches that of atmospheric; and is least sensitive to changes in this variable in the low gauge pressure range.

Also, from preliminary executions of the multi-airbag model, it was found that the system experienced a significantly high injury-risk at impact angles of 30° compared to those at 0° . As a consequence, this design effort was focused primarily on sizing a system to meet its performance objectives when subjected to a 30° impact angle. Any system which performed adequately under this impact condition would easily meet the injury-risk requirements under a 0° impact condition.

Thus, with these constraints defined and the overall problem formulated; a two stage full factorial based methodology was employed to determine the “optimal” solution. Specifically, this involved firstly performing a coarse resolution full factorial expansion over the design space to filter out regions which experienced either bottoming out or hoop stresses which exceeded the limiting value of 540MPa. Here, five evenly spaced levels for each design variable were chosen, bounded such that they met the geometric constraints within the system. In addition, the commonality constraints were explicitly enforced by the manner in which the design variables were input into the multi-airbag model.

When a feasible bounding region was found, a second, high resolution full factorial analysis was performed. From this, the resulting objective space was visualized, and the hoop

stress criterion again used to filter out infeasible designs. This was required as it was found that stress infeasible designs were still able to pass the first phase due to the coarse resolution used. Hence, with the resulting feasible set of designs obtained, the minimum Brinkley DRI design was evaluated and if necessary, a decision to modify the configuration concept was made.

In total, this optimization process was iterated through three times, with each cycle exploring a unique airbag and valve configuration. Interestingly, in all of the three configurations, it was found that only designs with 2 or 3 rows of airbags with larger radii met the hoop stress criterion. The processes undertaken to move through and between each optimization cycle are summarized in the following sections.

Multi-Airbag System Design Iteration 1

As a first estimate, the system configuration conceptualized at the end of the first generation development effort, and summarized in Section 5.1.1 was baselined for the optimization study. Shown in Figure 6-3, this configuration consisted of a row of cylindrical airbags aligned the longitudinal axis of the seat structure. Additionally, the same pressure relief valves as used in the single airbag drop test article were to be located on either side of each airbag.

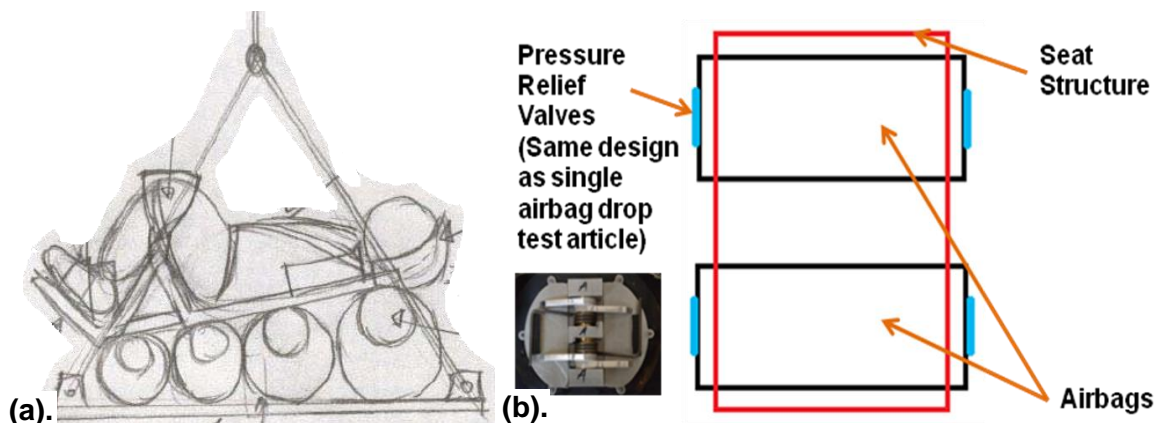


Figure 6-3: Baseline Airbag Configuration for the Multi-Airbag System Design Iteration 1
 (a). System Configuration updated at the end of the First Generation System Development

(b). Top View of the Baseline Configuration, showing valve locations

Table 6.1 summarizes the factors and levels used, whilst Table 6.2 summarizes the corresponding maximum model-predicted hoop stresses for each combination of number of airbags and airbag radius. Here, the bounding values for the airbag length and the valve burst pressure were based respectively on the practical dimensions required to support the width of the ATD, and the burst values able to be accommodated by the third generation flapper valve.

Table 6.1: Factors & Levels used for the first iteration of the Multi-Airbag System Design

Level	Factor					
	Radius				Length	Δp_{burst}
	N = 2	N = 3	N = 4	N = 5		
Level 1	0.11	0.11	0.11	0.11	0.65	8
Level 2	0.27	0.175	0.145	0.1275	0.6875	10
Level 3	0.43	0.242	0.18	0.145	0.725	12
Level 4	0.59	0.305	0.215	0.1625	0.7625	14
Level 5	0.75	0.375	0.25	0.18	0.8	16

Table 6.2: Maximum Hoop Stress Predictions (in MPa) for each Design Iteration 1 Radius-Number of Airbags Combination (Red = Bottoming Out Experienced, Orange = Failed to meet Hoop Stress Criterion, Green = Potentially Feasible Design)

	N = 2	N = 3	N = 4	N = 5
Radius Level 1				
Radius Level 2	692.864			
Radius Level 3	516.201	1045.790		
Radius Level 4	641.706	546.318	3757.573	
Radius Level 5	767.340	493.104	900.511	

During this initial process, it was found that the effects of hoop stress were most prominent in the airbags located towards the foot-ward end of the seat structure, as it was the first to contact the ground surface during the 30° impact condition. In addition, it was found that in general, the hoop stress had little sensitivity to variations in the valve burst pressure. Since by definition, the hoop stress is invariant of the airbag length, this resulted in very little difference in the hoop stresses experienced along the length and burst pressure dimensions, for a fixed combination of airbag radius and number of airbags. Consequently, this trend was exploited to efficiently filter out infeasible regions in the design space, as shown in Table 6.2. Specifically, this was performed by mapping the results shown in this table to the factors and

levels combinations shown in Table 6.1. For this particular optimization case, the feasible region was found to be:

$$\begin{aligned} \text{For an } N = 2 \text{ airbag configuration: } 0.27 < R < 0.59 \\ \text{For an } N = 3 \text{ airbag configuration: } 0.242 < R \leq 0.375 \end{aligned} \quad (6.22)$$

With this region established, a high resolution full factorial expansion was performed with the variable ranges defined in Table 6.3. Here, the resolutions for each factor were chosen to correspond to the minimum value which could be practically implemented.

Table 6.3: Variable Ranges used in the Multi-Airbag System Design Iteration 1 High Resolution Full Factorial Expansion

Factor	Lower Bound	Upper Bound	Resolution
N	2	3	1
R	0.27m	0.59m	0.01m
L	0.65m	0.8m	0.01m
ΔP_{burst}	8kPa	1kPa	16kPa

The figure below shows the resultant objective space, color coded using the airbag hoop stress criterion.

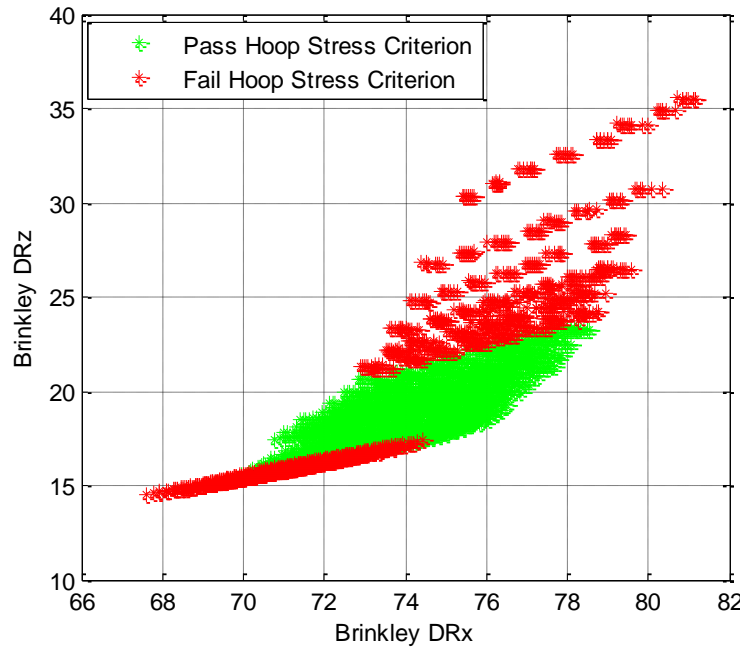


Figure 6-4: High Resolution Full Factorial Expansion for the first Multi-Airbag System Design Iteration

From Figure 6-4, it can be seen that as the x-direction Brinkley DRI decreases, the hoop stresses experienced by the airbag move in a non-monotonic manner; starting firstly at a high value, then decreasing to below the limiting value, and finally increasing again past this threshold. This can be explained by considering the trends found in the optimization study performed in Section 5.5. Here, it was found that smaller geometries tend to lead to lower peak Brinkley DRI values, due to their ability to maintain higher pressures for longer periods of time. Because hoop stress is derived from the multiplication between the airbag pressure and its radius, a trade-off exists as the radius decreases, and the corresponding pressure increases.

More importantly however, is the fact that even when ignoring the hoop stress criterion, the objective space in Figure 6-4 indicates that the best performing design has an x-direction Brinkley DRI of 67.59 – a value which far exceeds the limiting value of 28. As a consequence, a drastic configuration change is likely required to reduce the Brinkley DRI to within the required low injury-risk limits. It is this finding which formed the basis for the second design iteration, described in the next section.

Multi-Airbag System Design Iteration 2

As mentioned in the previous section, one of the key findings of the optimization studies performed during the single airbag system development was that smaller airbag geometries tended to lead to improved impact attenuation performance. In addition, it was also found that for a fixed geometry, the Brinkley response was most sensitive to changes in the venting area of the airbag, with larger areas leading to improved performance. Using these two facts, the baseline configuration used in the first design iteration was updated accordingly, as shown in Figure 6-5.

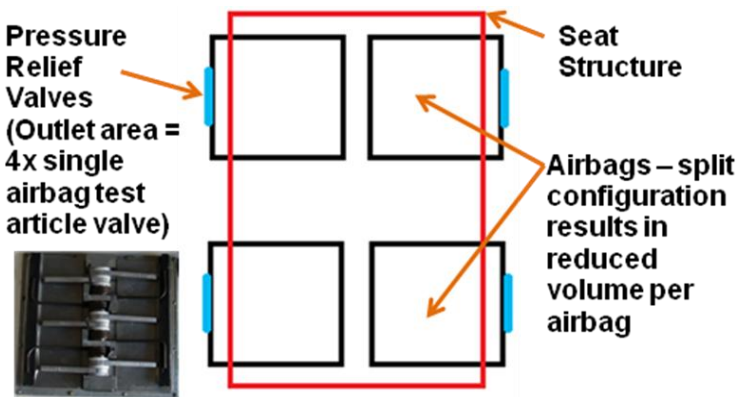


Figure 6-5: Baseline Airbag Configuration for the Multi-Airbag System Design Iteration 2

Here, it can be seen that a split-bag configuration has been chosen, in an attempt to reduce the volume of each airbag. The effect of this configuration change on the multi-airbag model is that the stiffness of each modeled airbag is doubled, since the stiffness of springs acting in parallel can be summed together to form an equivalent single spring. In addition, the venting area on each airbag has been increased by a factor of four, thereby requiring a new pressure relief valve design. Hence, with this, the levels and factors appropriate for an initial coarse full factorial study were determined. These are presented below:

Table 6.4: Factors & Levels used for the second iteration of the Multi-Airbag System Design. (Here, N refers to the number of rows of airbags in the longitudinal direction)

Level	Factor				
	Radius			Length	Δp_{burst}
	N = 2	N = 3	N = 4		
Level 1	0.11	0.11	0.11	0.15	8
Level 2	0.27	0.175	0.145	0.2125	10
Level 3	0.43	0.242	0.18	0.275	12
Level 4	0.59	0.305	0.215	0.3375	14
Level 5	0.75	0.375	0.25	0.4	16

From Table 6.4, it can be seen that the five airbag case has been neglected from this study due to the consistent bottoming out experienced in the first design iteration. The likely reason for this is that as the number of airbags increases, the maximum available airbag radius decreases such that it does not interfere with the adjacent airbag. At a certain point, the radius decreases to a point where it does not have enough stroke to avoid bottoming-out. Based on the observations made thus far, this point appears to be when the number of airbags within the system reaches a value of five. The results of this second iteration coarse resolution full factorial analysis are summarized in Table 6.5.

Table 6.5: Maximum Hoop Stress Predictions (in MPa) for each Design Iteration 2 Radius-Number of Airbags Combination (Red = Bottoming Out Experienced, Orange = Failed to meet Hoop Stress Criterion, Green = Potentially Feasible Design)

	N = 2	N = 3	N = 4
Radius Level 1			
Radius Level 2	692.864		
Radius Level 3	491.054	1045.79	
Radius Level 4	602.823	546.318	3757.573
Radius Level 5	745.764	488.688	900.511

Here, it can be seen that the feasible radius and number of airbag combinations obtained is exactly the same as that obtained during the first design iteration. This is a consequence of the previously discussed low sensitivity of the hoop stress performance to the valve burst pressure, as well as the fact hoop stress is invariant of airbag length. Moreover, this consistent finding suggests that as the number of airbags increases past three, the airbag radius decreases to a level where the contribution of the internal pressure to the hoop stress dominates that of the radius. This, in turn, results in hoop stresses which continually exceed the limit set by the Vectran fabric tensile strength.

Thus, performing a high resolution full factorial expansion over the same feasible region defined in Equation (6.22) using the same variable resolutions as those outlined in Table 6.3, the following objective space was obtained:

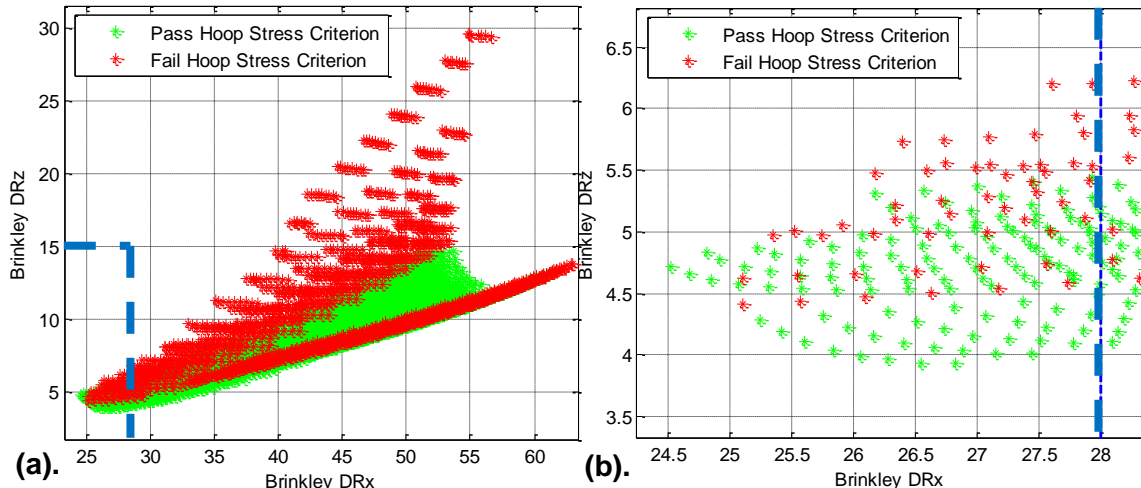


Figure 6-6: High Resolution Full Factorial Expansion for the Second Multi-Airbag System Design Iteration (with Brinkley Low Injury-Risk limits marked by the blue dotted line) (a). Entire Objective Space (b). Close Up of Feasible Region

Here, it can be seen that a significant number of designs meet both the hoop stress and injury-risk criteria, indicating potential for this baseline configuration. When viewing the objective space in terms of the system length, however, the additional issue of impact stability is highlighted. Figure 6-7 shows this same objective space color-coded by airbag length.

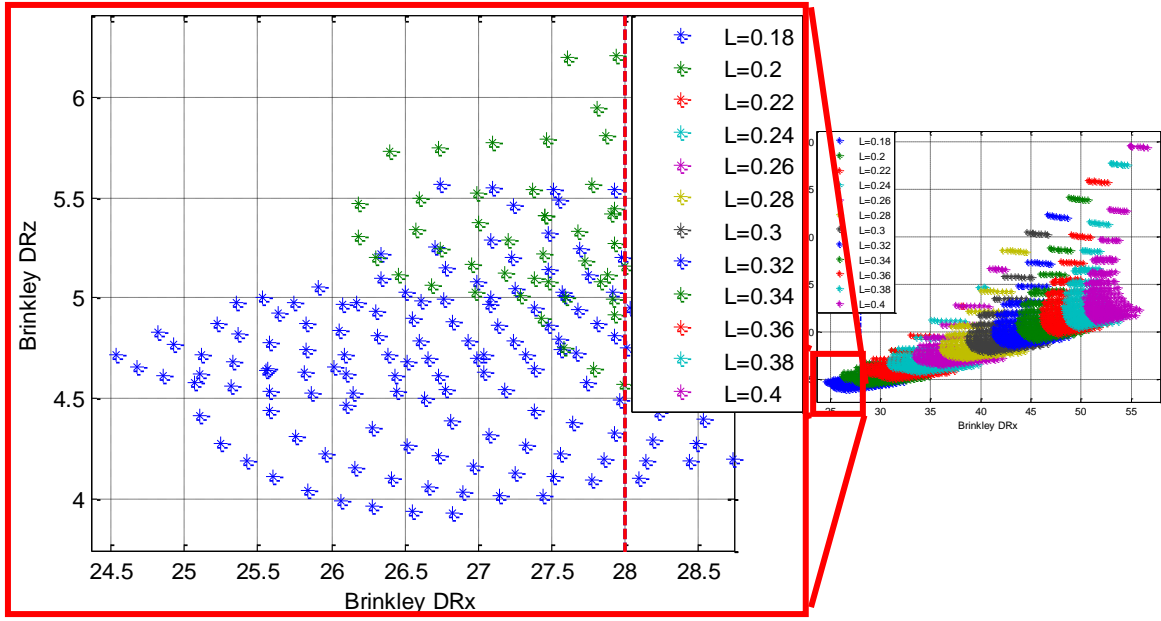


Figure 6-7: Second Multi-Airbag System Design Iteration Objective Space Filtered by Airbag Length

From the above figure, it can be seen that within the set of feasible system configurations, the largest airbag length is 0.2m. Further inspection of this set showed that all feasible designs had airbag radii ranging from 0.32m to 0.34m. This high radius to length ratio results in an airbag which is highly susceptible to local buckling, which in turn has implications on system stability during impact. As a result of this finding, a final configuration change was explored in an attempt to increase the optimal airbag length, thereby improving system stability.

Multi-Airbag System Design Iteration 3

In an attempt to find a feasible design with a larger length and hence improved impact stability, a final concept was explored. This consisted of taking advantage of the extra surface introduced by the split airbag configuration, and doubling the number of valves on each airbag. Here, the idea was that by allowing more gas to be vented, the geometry of the airbags could be allowed to grow whilst maintaining the same impact attenuation capability. This proposed configuration is depicted in Figure 6-8.

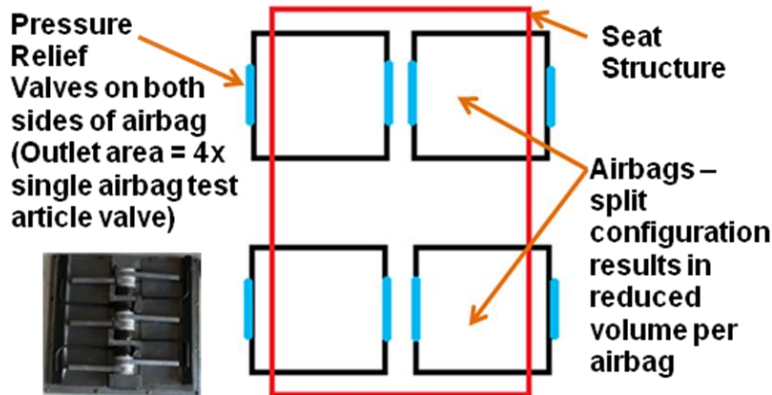


Figure 6-8: Baseline Airbag Configuration for the Multi-Airbag System Design Iteration 3

Since no change in geometry from the second design iteration was made to this final airbag configuration, the same factors and levels as presented in Table 6.4 were used for the coarse resolution full factorial analysis. Upon performing this analysis however, the same results as those found in Table 6.5 were obtained. This was a result of the previously observed insensitivity of the hoop stress to the valve burst pressure. In particular, this is likely due to the fact that the peak hoop stress occurs before any of the valves open.

Consequently, the same feasible region within the design space was used as an input to the high resolution full factorial analysis. The result of this shown below:

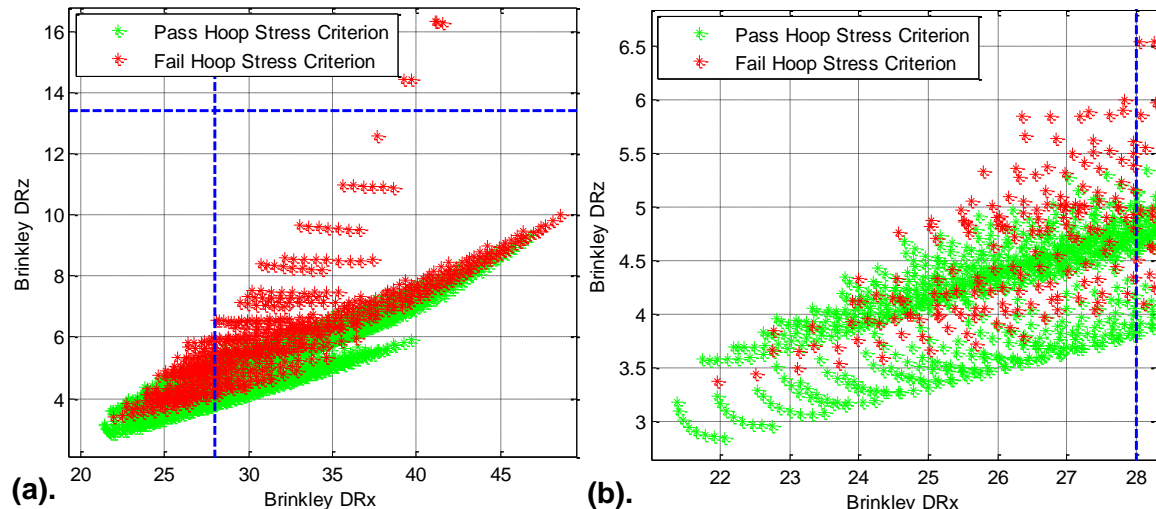


Figure 6-9: High Resolution Full Factorial Expansion for the Third Multi-Airbag System Design Iteration (with Brinkley Low Injury-Risk limits marked by the blue dotted line) (a). Entire Objective Space (b). Close Up of Feasible Region

As was the case with the previous design iteration, the objective space indicates that several designs are capable of meeting the hoop stress criterion. Moreover, filtering the objective space by the airbag length indicates that significantly more feasible design options are available. This result is presented in Figure 6-10.

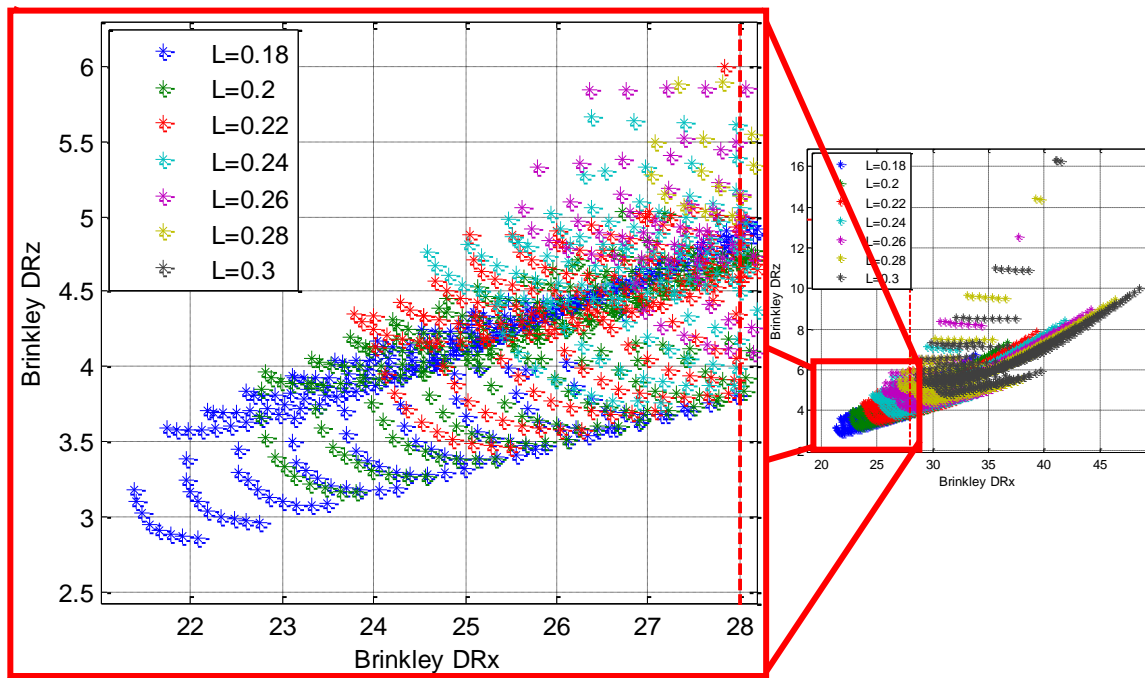


Figure 6-10: Third Multi-Airbag System Design Iteration Objective Space Filtered by Airbag Length

Here, it can be seen that the maximum airbag length from the set of Brinkley feasible designs has increased to 0.28m, from the 0.2m value observed in the previous design iteration. Closer inspection of the feasible design points indicated that these airbags had the same 0.32m to 0.34m radius range as those previously found. This in turn resulted in airbags with radii to length ratios high enough to be deemed adequate for impact stability.

Moreover, it was found that all designs with burst pressures above that of the minimum sampled value were dominated – an observation consistent with that made during the single airbag system development effort. As a result, the valve burst pressure was fixed to this minimum value.

With this, the hoop stress and airbag length criteria were used to simultaneously filter the objective space, thereby narrowing the potential design choices and allowing for the preferred design to be more easily identified. Here, the allowable airbag lengths were set to values of either 0.26m or 0.28m to provide more design options.

Additionally, a seam stress criterion was also introduced to further aid in the selection of the final design. Specifically, this referred to the results of the tensile strength tests described in Section 5.1.4, where it was found that a seam consisting of three rows of stitches failed at a tensile stress of 105MPa. In order to avoid this failure mode, a triple layer of fabric was proposed for the airbag seam construction to reduce the local stress accumulation by increasing the material thickness. The resultant stress through this triple layer seam was then limited to be less than 90MPa in order to provide some margin against this failure mode.

The combined result of these various filters on the objective space is presented below:

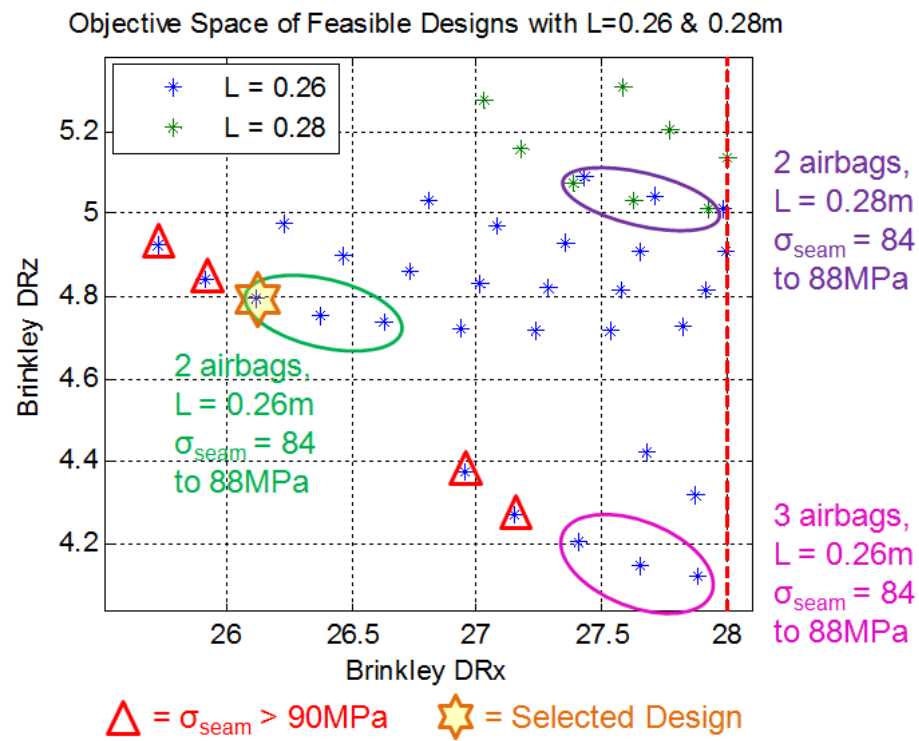


Figure 6-11: Objective Space Filtered by Max Hoop Stress < 540MPa & L = 0.26m or 0.28m

Here, it can be seen that with a higher airbag length of 0.28m, the Brinkley performance moves very close to the low injury-risk limit when compared to the 0.26m length case. It can be further observed that the additional system stiffness of the three-airbag configurations also increases the x-direction Brinkley Index from the two-airbag case by a comparable amount. Moreover, the seam stress criterion was found to have made four of the originally non-dominated designs infeasible, thus limiting the final choice of the system configuration to the set of designs encircled by the green ellipse. From this set, the design with the lowest x-

direction Brinkley Index was chosen due to the substantially higher difficulty in meeting the injury-risk criteria in the x-direction, compared to that of the z-direction. This design is highlighted by the yellow star in Figure 6-11, whilst its characteristics and predicted performance are summarized below in Table 6.6, and Figures 6-12 to 6-15 respectively.

Table 6.6: Final Second Generation Personal Airbag System Configuration

Design Variable	Value	Comments
Airbag Configuration	Split Bag 2-sided Venting	Allows for larger optimal airbag length, thereby increasing impact stability
Number of Airbags	2	Additional stiffness from extra airbags was found to be detrimental to minimizing Brinkley DRI
Valve Type	PRV with Outlet area = 4x Gen 3 Flapper Valve	Larger venting area improves Brinkley DRI
Valve Burst Pressure	8kPa	Minimum value able to be achieved in previous PRV without significant leakage
Airbag Radius	0.32m	Corresponds to minimum hoop stress and Brinkley DRx design
Airbag Length	0.26m	Corresponds to minimum hoop stress and Brinkley DRx design whilst still maintaining reasonable length for impact stability purposes
Airbag Inflation Pressure	102kPa	Achievable pressure based on past experienced leakage rates. A previous analysis also indicated that minimal Brinkley DRI designs favored lower initial inflation pressures

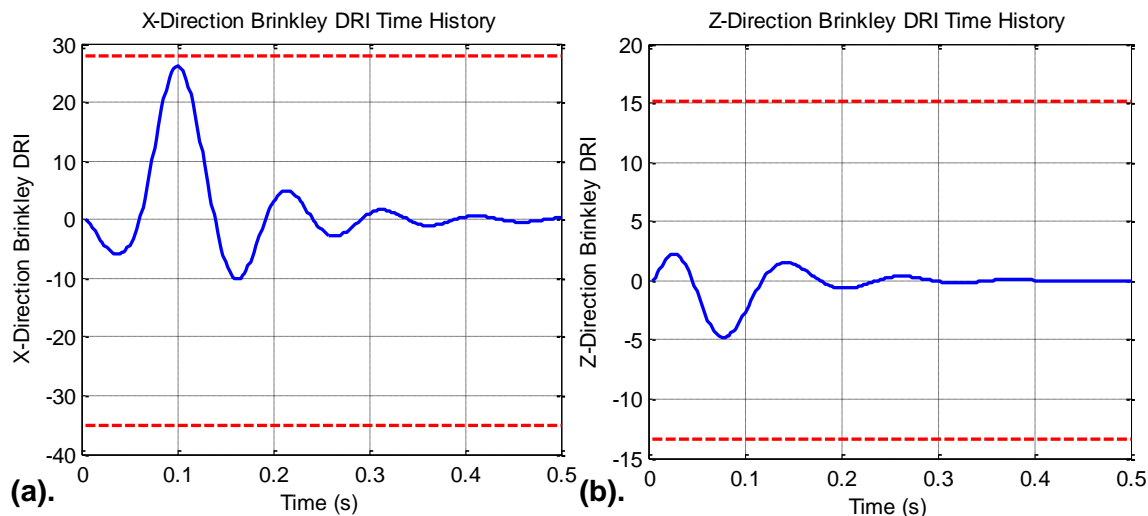


Figure 6-12: Predicted Brinkley DRI for the Nominal 30° Impact Case

(a). X-Direction Brinkley DRI (b). Z-Direction Brinkley DRI

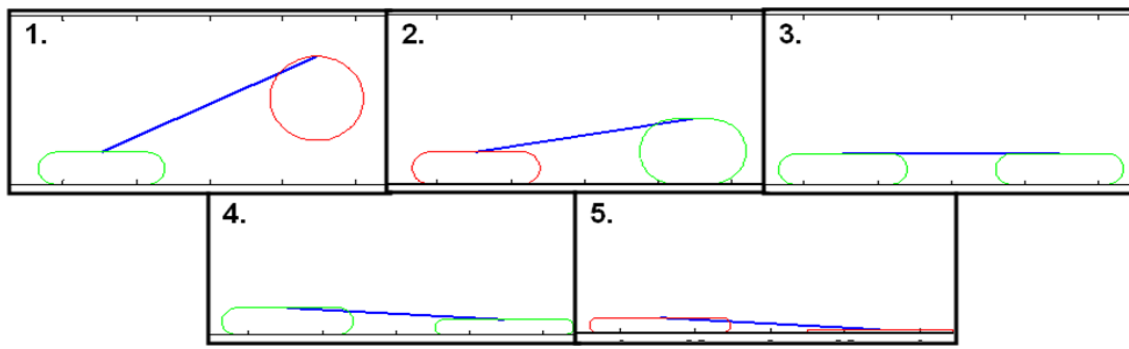


Figure 6-13: Predicted System Dynamic for the Nominal 30° Impact Case
(Red = Valve Closed, Green = Valve Open)

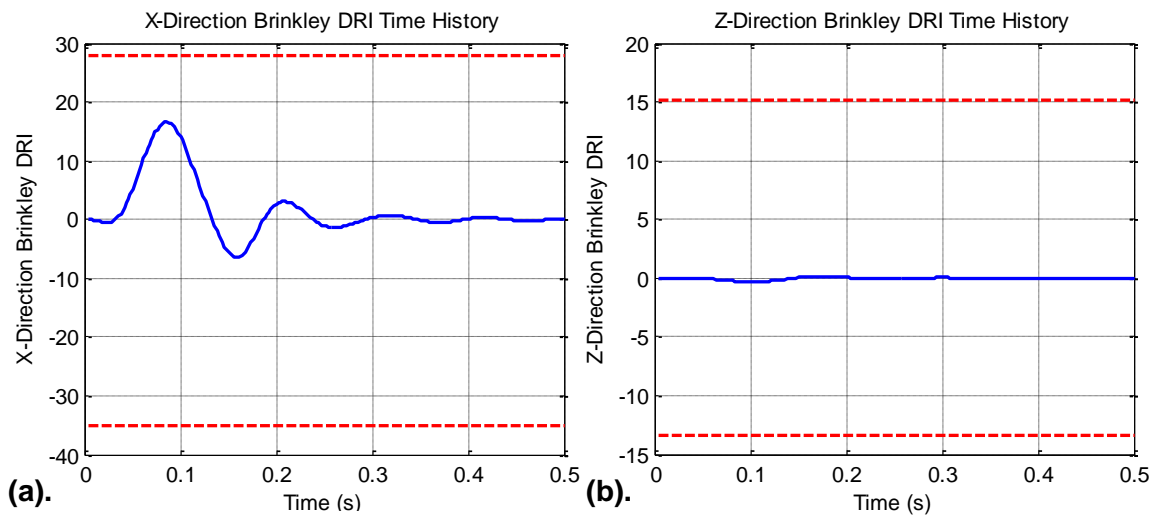


Figure 6-14: Predicted Brinkley DRI for the Nominal 0° Impact Case
(a). X-Direction Brinkley DRI (b). Z-Direction Brinkley DRI

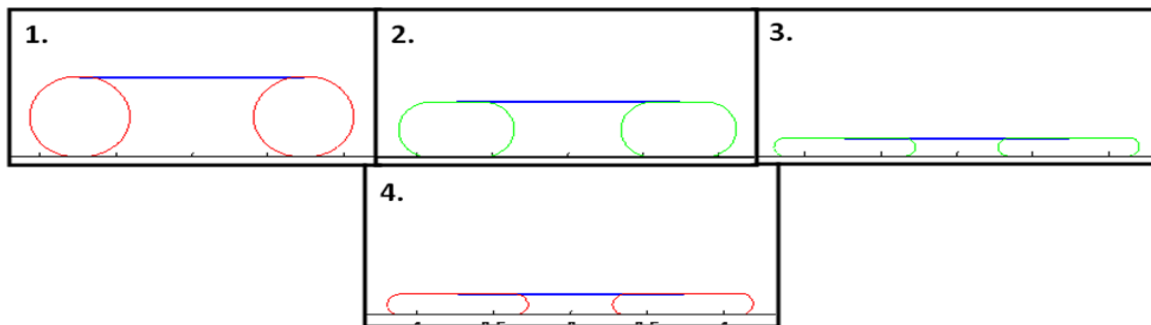


Figure 6-15: Predicted System Dynamic for the Nominal 0° Impact Case
(Red = Valve Closed, Green = Valve Open)

As can be seen from these figures, the final system configuration is expected to just meet the low-injury risk criteria during a 30° impact case, and to easily support a safe landing during the 0° impact cases. With this, an overarching concept was devised to integrate this final airbag configuration with both a seat support structure and a simulated floor to replicate the impact conditions experienced within the cabin of a landing spacecraft. Figure 6-16 depicts the baseline concept used for the development of the remaining components of the system.

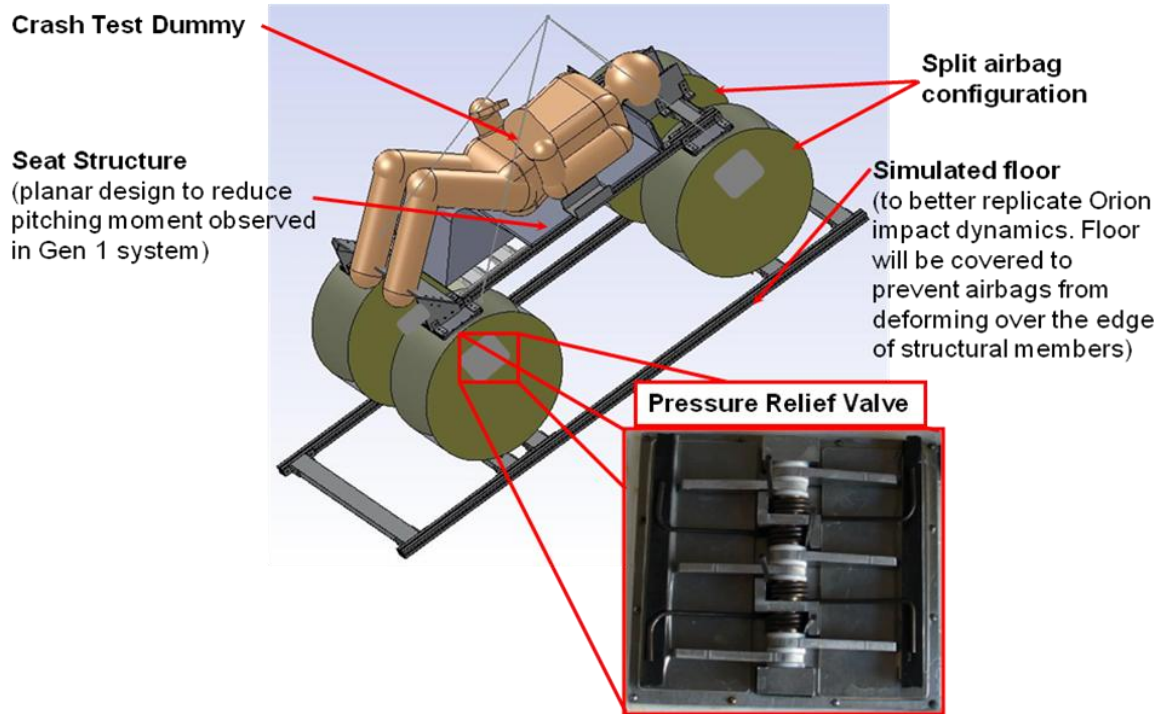


Figure 6-16: Overarching Multi-Airbag System Concept

6.2.2 Seat Support System Development

As the system configuration was being determined, a concurrent effort took place to develop a seat support system to accommodate the crash test dummy during drop tests. Based on the updated baseline seating configuration determined at the end of the first generation system drop test campaign, and described in Section 5.1.1; this system was designed to support the crash test dummy in a planar semi-supine position. Figure 6-17 shows the preliminary sketches used in the design of the system.

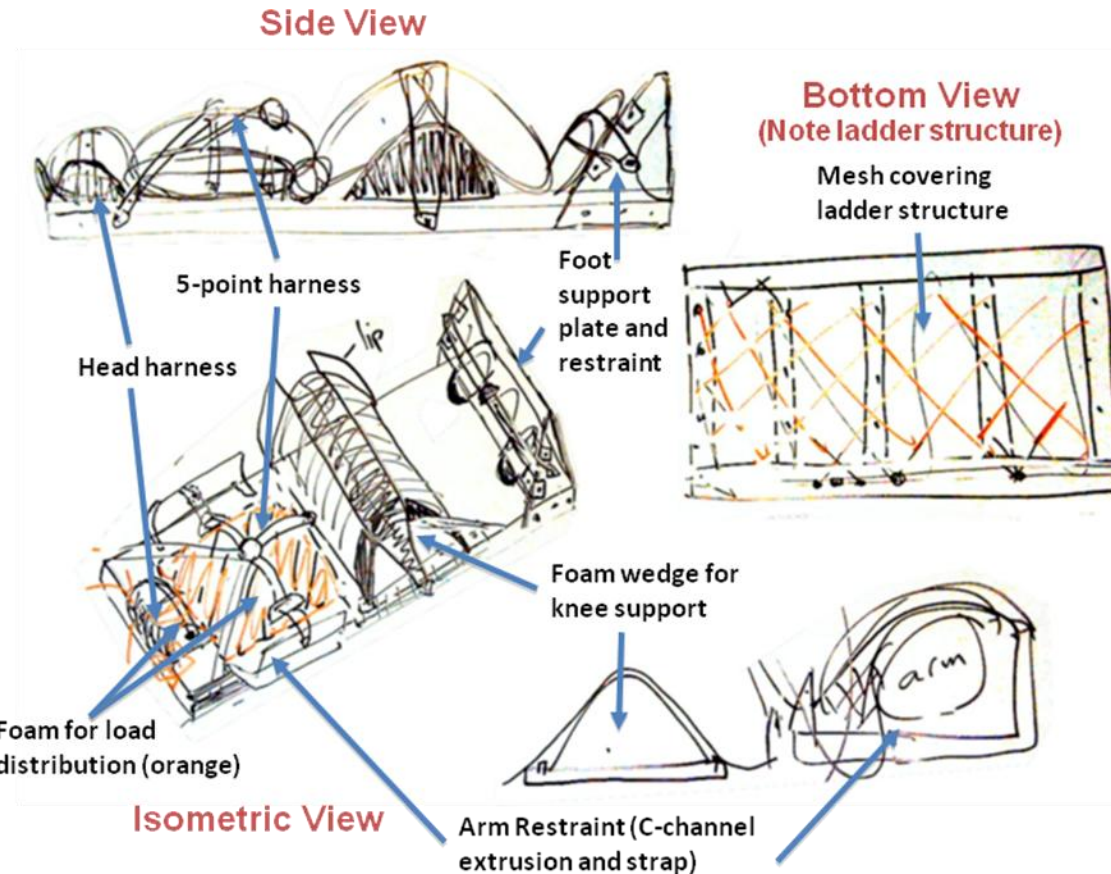


Figure 6-17: Original Seat Support System Sketches

To determine the specific dimensions of the system, a mock-up was built around the crash test dummy using duct tape. Figure 6-18 summarizes this process.

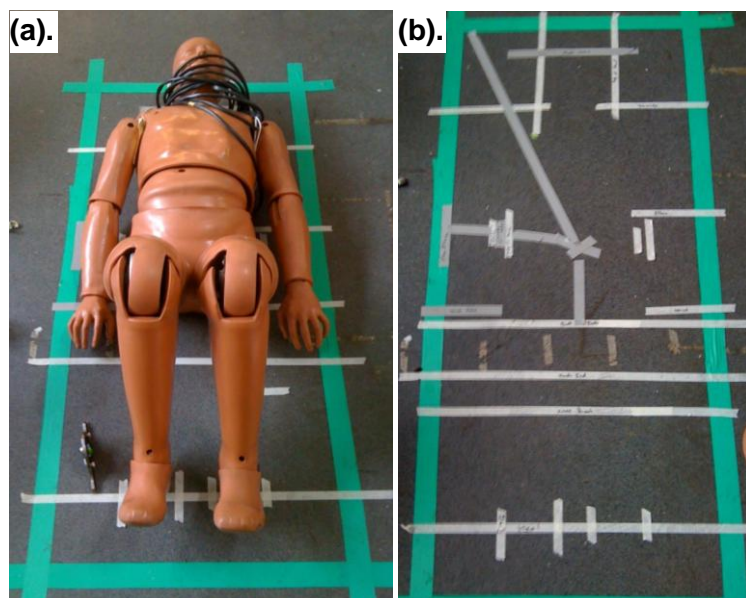


Figure 6-18: Seat Support System Sizing (a). Crash Test Dummy in Semi-Supine Position
(b). Registration Marks left over after System Mock-up

Moreover, to simplify the seat system manufacture, the same fundamental components and processes used for the first generation seat system were employed. In particular, this involved utilizing predominantly simple grooved extrusions and brackets to build the structure. Figure 6-19 shows the final manufactured seat support system, with and without the crash test dummy.

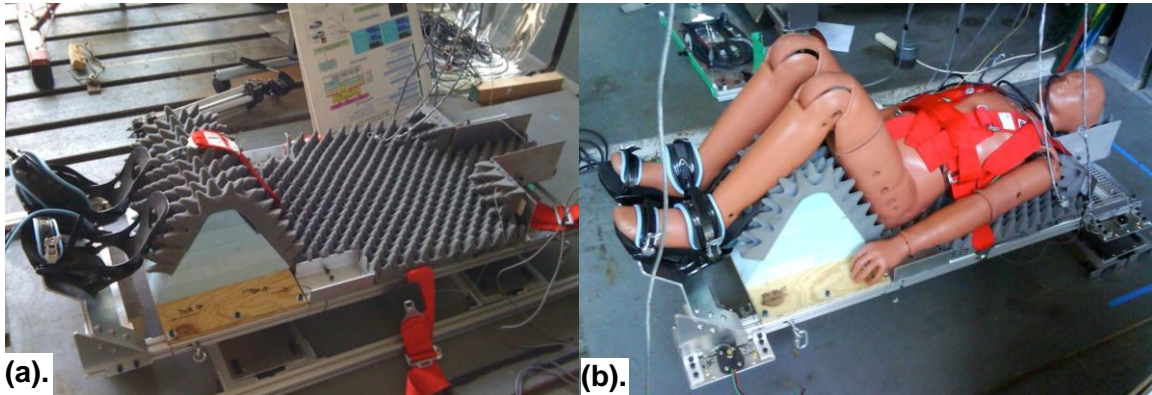


Figure 6-19: Final Manufactured Seat Support Structure (a). Without Crash Test Dummy
 (b). With Crash Test Dummy

6.2.3 Generation 3.1 Flapper Valve

As was mentioned during the airbag configuration study described in Section 6.2.1, the decision to increase the venting area in each airbag meant that another variant of the pressure relief valve was required. Using the same flapper valve concept as had been employed on all previous valve designs, the venting area was increased by a factor of four. In turn, this necessitated the implementation of an additional torsion spring on each outlet hatch, to counteract the effects of the airbag pressure on its increased area. Figure 6-20 shows the final flapper valve design used for the multi-airbag system.

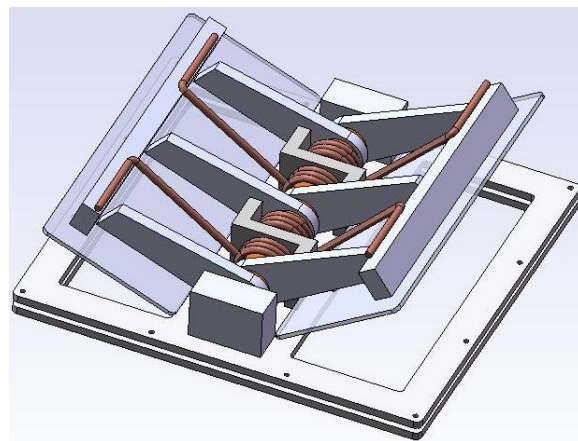


Figure 6-20: Generation 3.1 Pressure Relief Valve Design

Furthermore, the updated valve configuration meant that characterization testing was required to determine the appropriate spring pre-loading angle. As was previously performed, a test valve was built and mounted to a pressure vessel which was in turn, inflated with the valve set to various spring pre-load angles. Moreover, the pressure at which the valve opened was measured with a pressure transducer connected to the pressure vessel, with the opening event visually verified using leak detection fluid. In particular, the objective here was to determine preload angle corresponding to the 8kPa gauge burst pressure derived during the airbag configuration study. Figure 6-21 shows the test setup used.

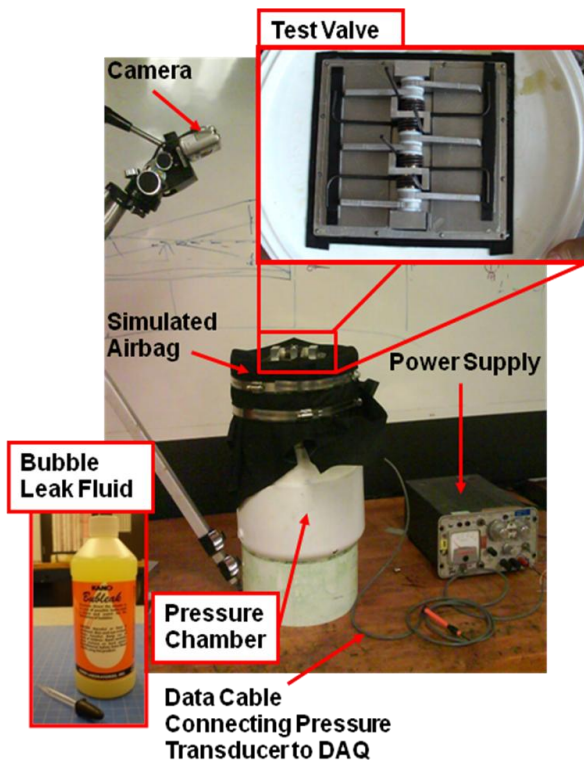


Figure 6-21: Generation 3.1 Pressure Relief Valve Leakage Test Setup

With the final pre-load angle determined, a major effort was undertaken to manufacture and integrate each of the eight valves required for the multi-airbag system. This process required additional care due to the numerous small parts required to be fabricated for each valve. Figure 6-22 gives a sense of the number of components that were required to be manufactured.



Figure 6-22: Manufactured Generation 3.1 Pressure Relief Valve Components

6.2.4 Airbag Manufacture

In order to manufacture each of the four airbags required for the multi-airbag system, the techniques developed during the second project-level development spiral were employed. Specifically these included:

- Fabric leakproofing; by applying four layers of liquid latex on each side of the Vectran fabric used to construct each airbag
- Airbag construction; using three rows of straight stretch stitch along each seam to sew the airbags together; and
- Seam sealing; by applying silicone paint to the inside of each of the airbag seams.

Moreover, a triple layer of fabric was introduced at each seam, as was mentioned briefly in the airbag configuration study. This consisted of adding strips of Vectran fabric at each of the seams to increase its thickness, thereby reducing the resulting stress build-up. Figure 6-23 depicts the configuration used to stiffen each seam.

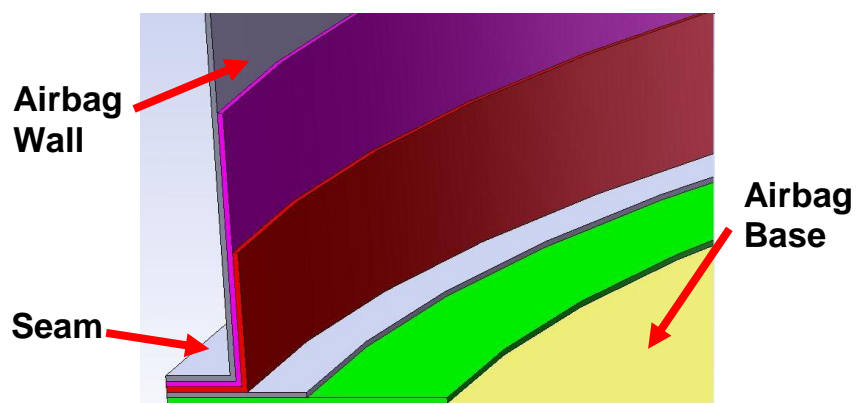


Figure 6-23: Airbag Seam Layering Scheme

Furthermore, it was realized prior to airbag manufacture that the final choice of location for the pressure relief valves should be made as late as possible, due to the uncertainties regarding the potential for valve blockage in the vicinity of the airbags. As a result, the first airbag was completely manufactured and subjected to a series of crush-up tests, where the local structure around the airbag during operation was simulated. This, in turn, allowed for unobstructed regions on the airbag surface to be identified, from which the final location of the pressure relief valves could be chosen. This process is shown in the figure below:

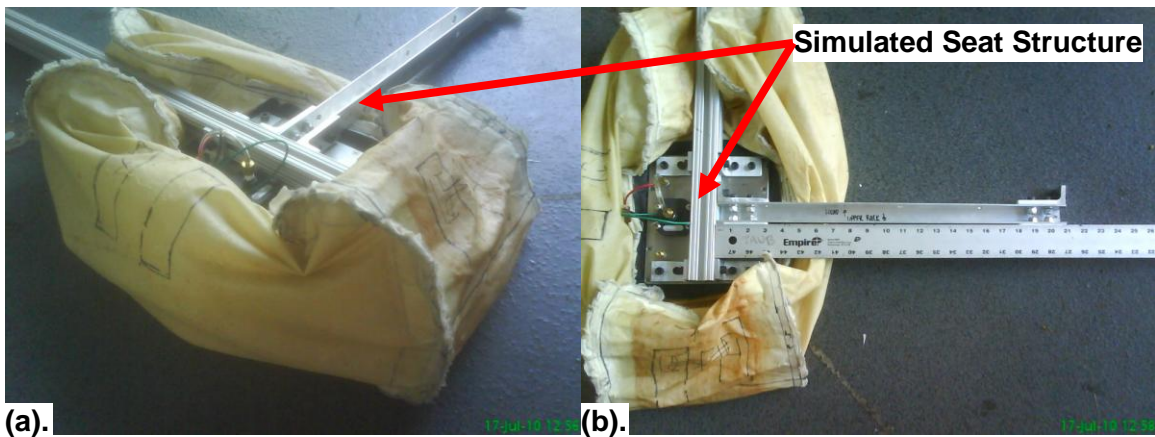


Figure 6-24: Airbag Crush-Up Test (a). Side View (b). Top View

Here, it can be seen that when integrated with a simulated seat structure, the only unobstructed regions on the airbag are on the front surface, and on the upper half of the circular cross section. As a consequence, these regions were chosen as the final location for the installation of the pressure relief valves. It should be noted here that even though this final choice of location differs from that originally proposed in the airbag configuration study, the resultant model performance prediction would have been exactly the same, as the model does not account for spatial effects within each airbag. Instead, a cumulative venting area, invariant of orifice location, is modeled. Figure... shows a final integrated airbag, including two pressure relief valves, and hard points on the top and bottom surfaces for interfacing with the seat structure and the simulated floor, respectively.

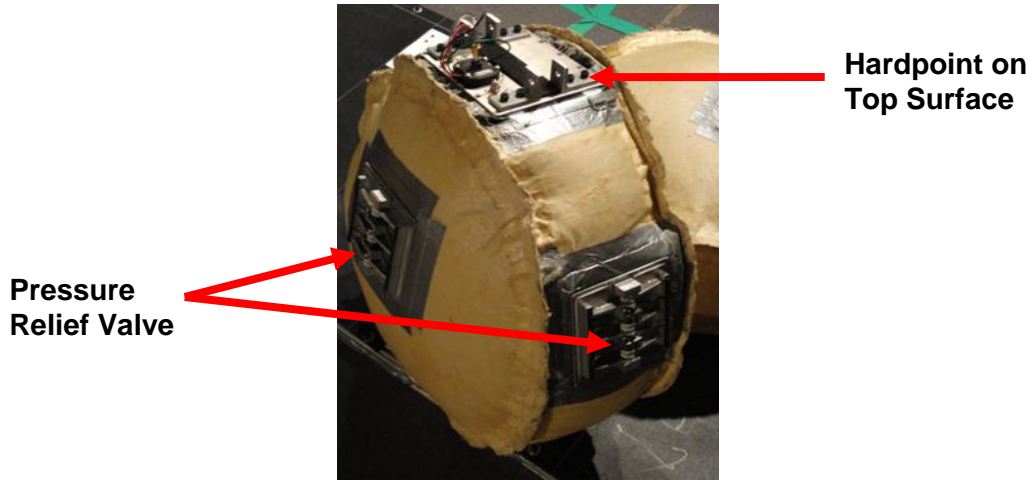


Figure 6-25: Integrated Airbag (Bottom Hardpoint not shown)

6.2.5 Multi-Airbag System Integration

Once manufacturing of each of components of the multi-airbag system was complete, the system was integrated and subjected to a series of hoist tests to ensure structural integrity of the test rig; and that correct interfacing and adequate clearance existed between the system and the drop test rig. In addition, these tests also allowed for the mass and center of gravity of the system to be measured. These values were in turn input into the multi-airbag model to improve its performance predictions. These tests are shown in Figures 6-26 to 6-27, with the final mass properties of the integrated system summarized in Table 6.7.

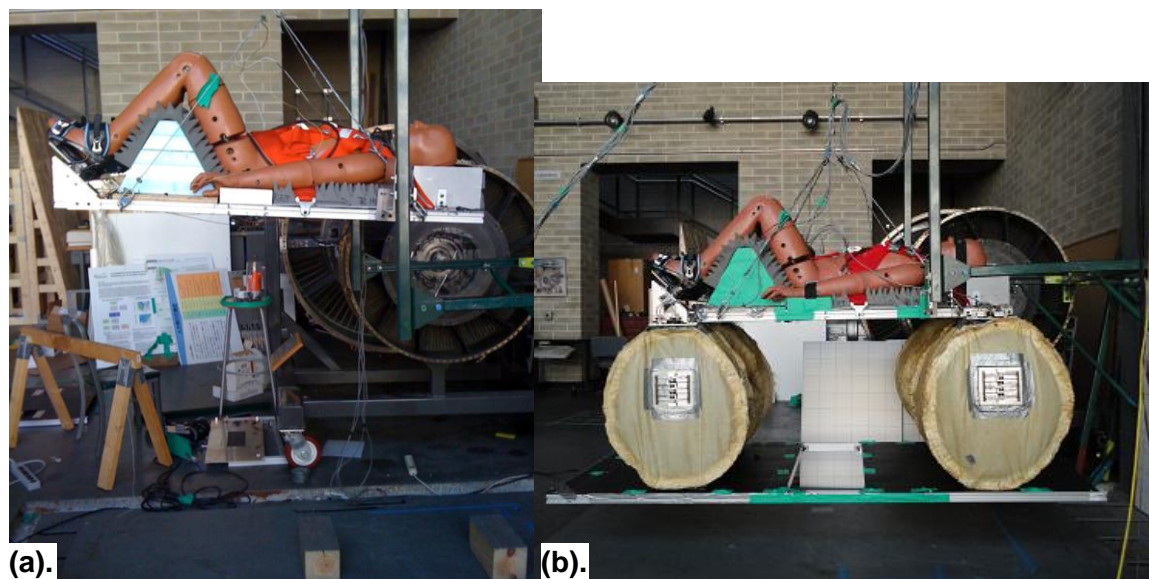


Figure 6-26: System Hoist Test (a). With Seat Structure and Crash Test Dummy Only
 (b). With Completely Integrated System

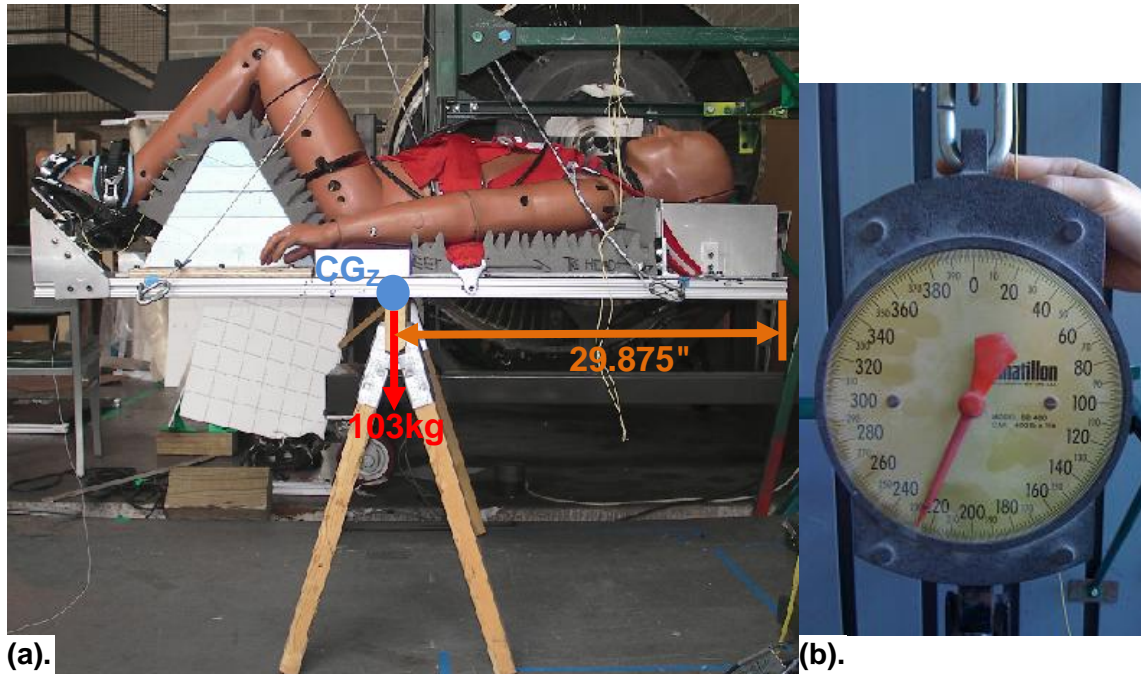


Figure 6-27: Center of Gravity Testing (a). Test Setup (b). Weight of Combined Seat System and Crash Test Dummy (Scale Reads 227lb)

Table 6.7: Multi-Airbag System Mass Properties

Component	Mass
Crash Test Dummy	75.3kg (166lb)
Seat Structure	27.7kg (61lb)
1x Integrated Airbag	4.0kg (8.8lb)
Simulated Floor	26.3kg (58lb)
Total Mass without Crash Test Dummy	70.0kg (154.3lb)
Total Mass with Crash Test Dummy	145.3kg (320.2lb)

For a six person crew, this value equates to a mass saving of 24% over the existing Orion Crew Impact Attenuation System, as compared to the originally estimated saving of 36%. As can be seen from the mass comparison performed in Appendix C, this saving primarily comes from the ability to avoid incorporating a 123kg (271lb) pallet in an airbag-based system. Moreover, the final volume of the airbags indicates a 16% increase in available volume in the CEV while on orbit, as compared to the original estimate of a 26% volume saving. This estimate is based on a baseline habitable volume of 12m³.

6.3 Multi-Airbag System Drop Test Plan

With the multi-airbag system completely integrated and its operation with the drop test rig verified, a test plan was developed to achieve the ultimate project objective of determining the feasibility of the personal airbag system concept. Specifically, this plan involved performing two test sessions, each of which focusing on evaluating the performance of the system at impact angles of 0° and 30° . As was discussed in Section 2.4, these impact angles were chosen based on the original NESC finding that flatter angles were preferred for land-landings; and on the fact that the proposed nominal impact angle of the Orion CEV is 30° .

Moreover, during each test session, drop tests would be performed from heights of 1 to 10 feet in 1 foot increments. At each height, a minimum of two drop tests would be performed to ensure that a repeatable data set was obtained. After the second drop at a given height was performed, a preliminary analysis of the results would be performed to determine whether or not a third drop was required to ensure repeatability. Here, the drop height would be measured from the lowest point on the simulated floor. Figure 6-28 shows the final, integrated multi-airbag system, whilst Figure 6-29 shows the drop configuration for each of the two test sessions.

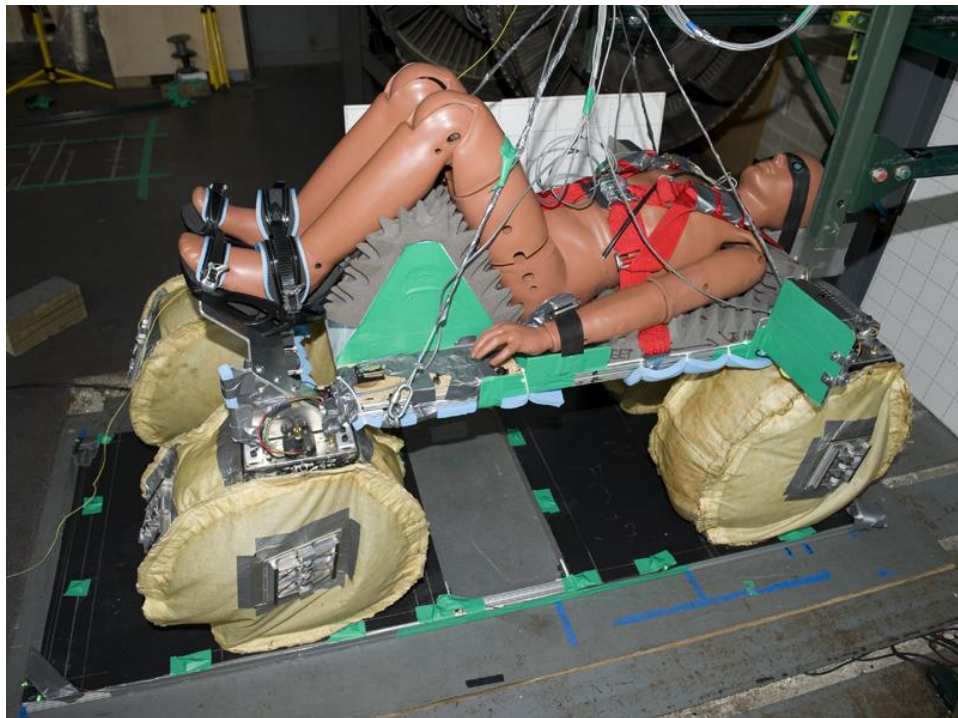


Figure 6-28: Fully Integrated Second Generation Personal Airbag System

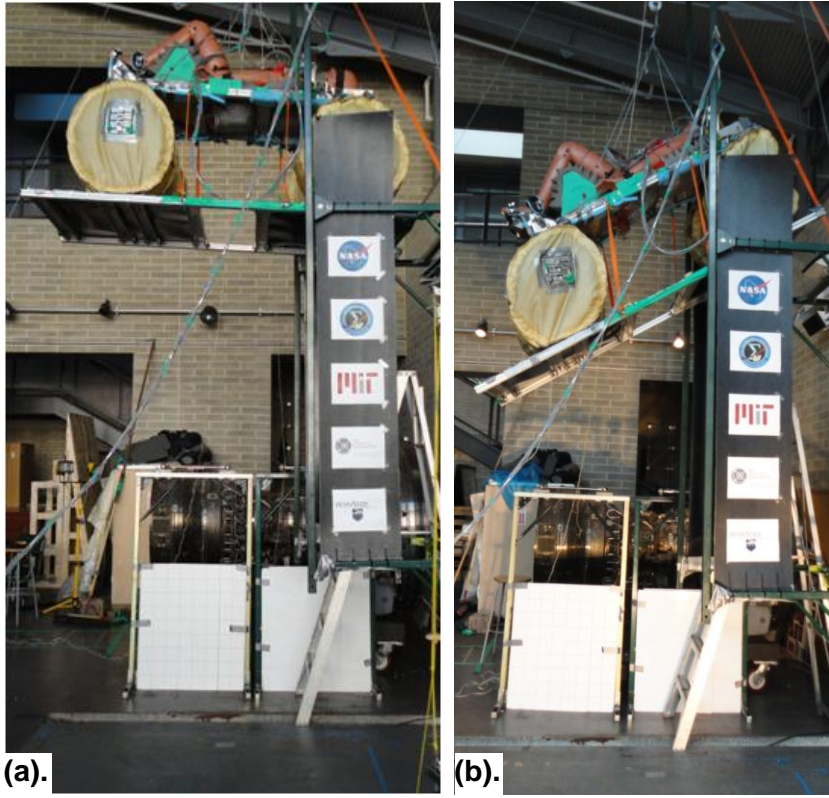


Figure 6-29: Drop Test Configuration
 (a). Test Session 1 - 0° Impact Angle (b). Test Session 2 - 30° Impact Angle

With respect to data acquisition, a combination of accelerometers, pressure transducers, and high speed camera footage was used. In particular, the previously used set of three tri-axial accelerometers embedded in the chest of the crash test dummy were used to evaluate the Brinkley response, whilst two perpendicularly separated high speed cameras were used to track LEDs installed about the seat support system and the simulated floor. As has been the case with all previous drop test campaigns, this footage was post processed using photogrammetric analysis code to extract transient dynamics data. In addition, pressure transducers were installed on each airbag in the same manner as used during the single airbag drop test campaign. This data allowed for valve performance to be observed, as well as providing a supplementary data set for time synchronization purposes. Figure 6-30 shows the locations of the sensors installed on the drop test article and the scheme used to identify each airbag, along with the test setup used throughout this drop test campaign.

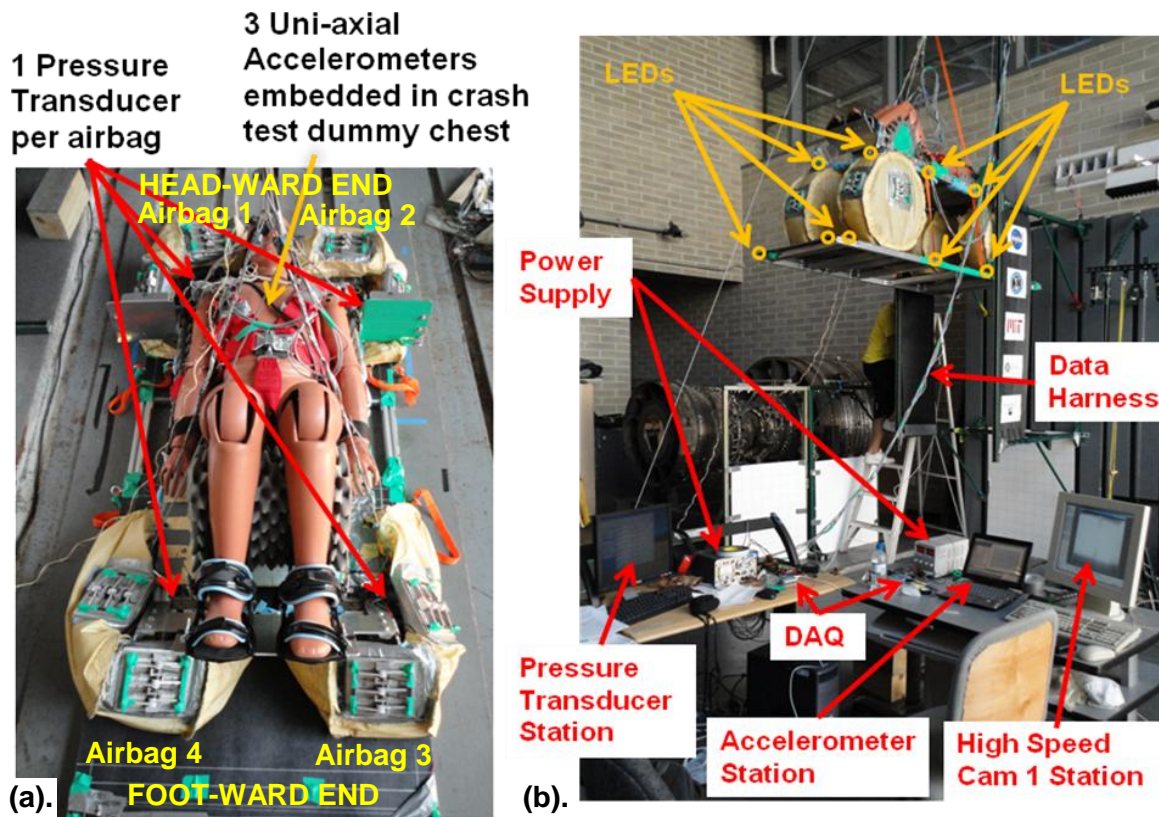


Figure 6-30: Multi-Airbag System Drop Test Setup (a). Airbag Identification Scheme and Sensor Locations (b). Data Acquisition Sensor and LED Locations

In addition to high speed cameras, high definition real-time cameras were also used to capture each drop from different viewing angles. These enabled parts of the system not captured by the high speed cameras to be observed during impact. Figure 6-31 summarizes the location and views of all cameras used during this test campaign.

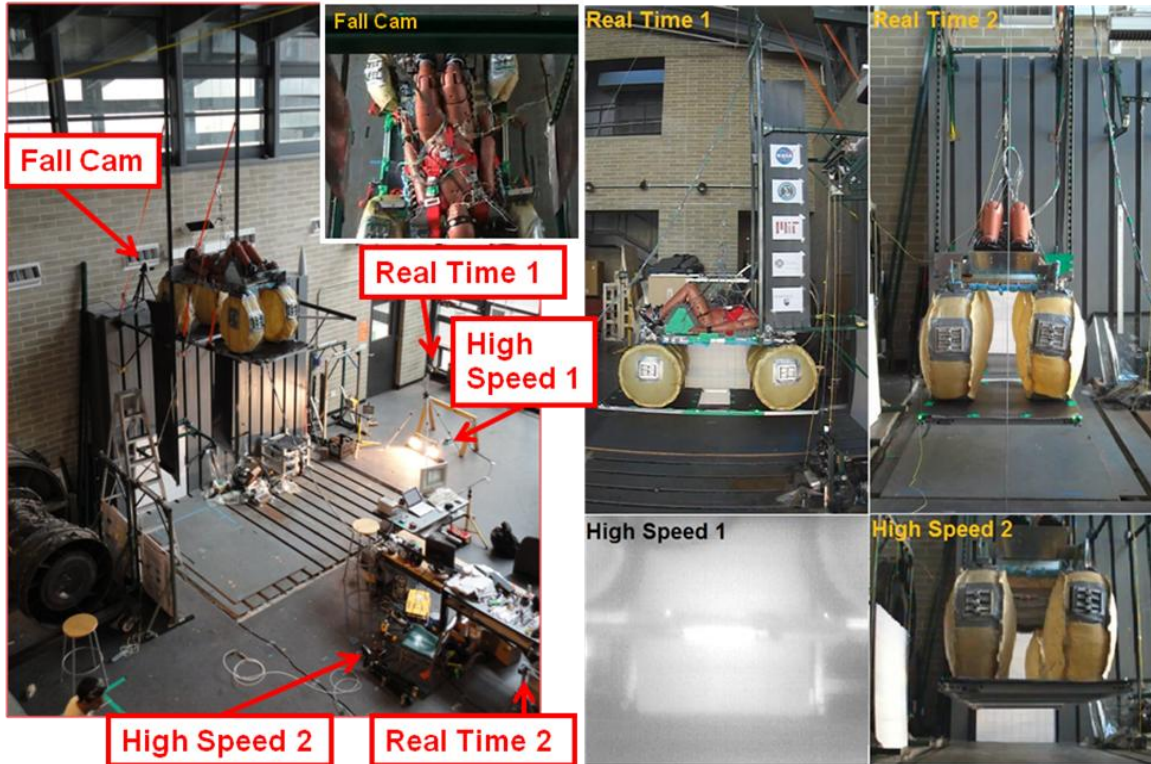


Figure 6-31: Multi-Airbag System Drop Test Campaign Camera Locations and Views

6.4 Multi-Airbag System Test Results & Analysis

Throughout the month of August 2010, the final drop test campaign was conducted; with a total of 38 drop tests successfully performed. Here, the first test session was successfully completed with a maximum impact velocity of 7.85m/s achieved – a value higher than that anticipated during the nominal landing of the Orion CEV.

During the second test session however, significant issues with airbag leakage were experienced, as continual drop cycles began to remove layers of liquid latex from the airbags. To mitigate this, leakage tests were performed after each drop, and an additional layer of liquid latex applied accordingly. When a drop height of 7 feet was reached though, a significant tear was found at the lower hard-point to fabric interface on Airbag 2. Closer inspection of the airbag and corresponding high speed camera footage indicated that, like all failures observed in previous drop test campaigns, this was a result of the formation of a local stress concentration. In particular, this was due to a shearing effect induced on the airbag as the seat structure slid forward relative to the simulated floor during the inclined impact.

Figure 6-32 shows a detailed view of this tear, whilst Figure 6-33 presents a dynamic breakdown of the 7 foot inclined drop.

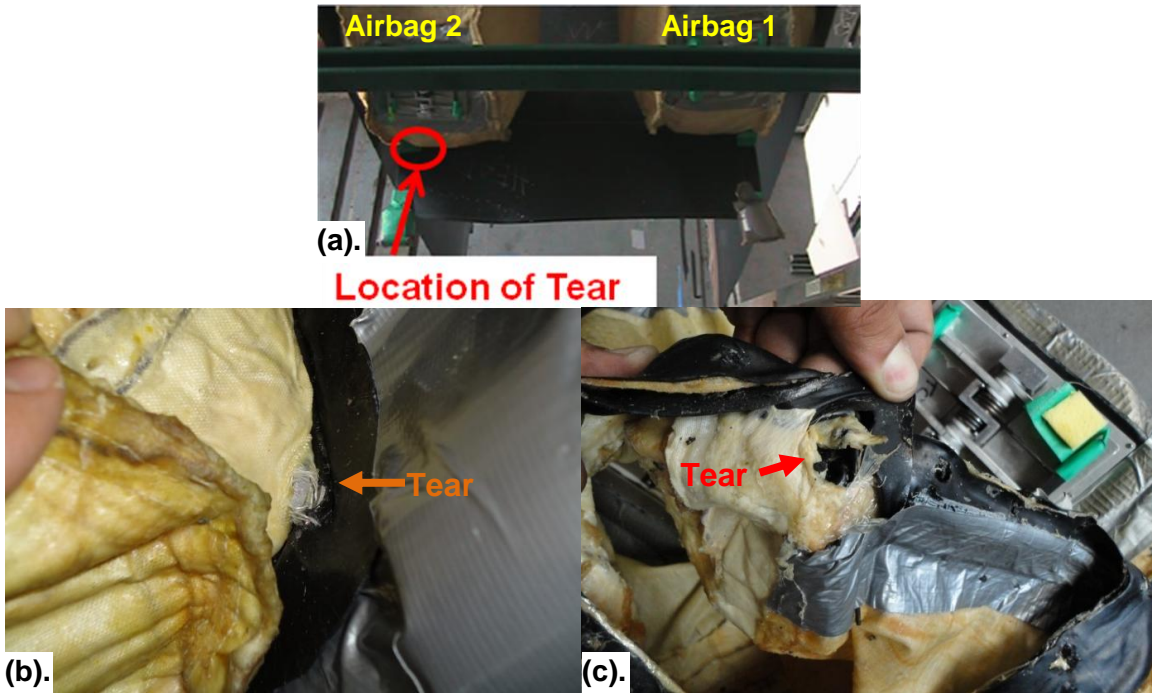


Figure 6-32: Airbag Failure Experienced during 7 foot Drop at 30° Impact Angle
 (a). Location of Tear on System (b). Tear as viewed from outside surface of airbag (c). Tear as viewed from inside surface of airbag

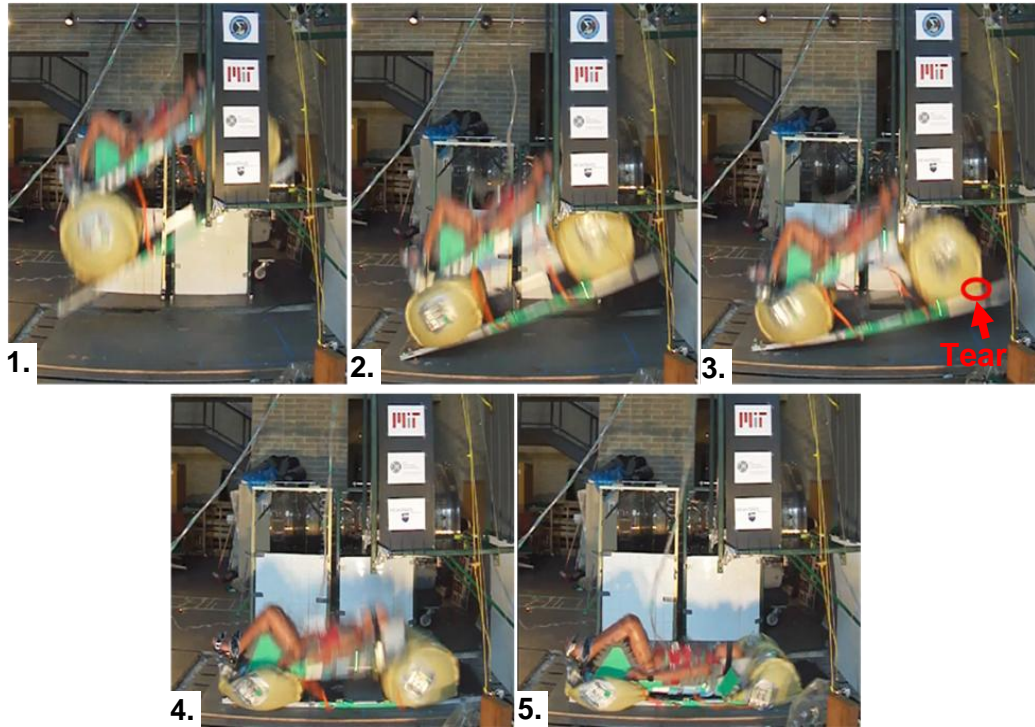


Figure 6-33: Frame by Frame Breakdown of the 7 foot, 30° Impact Angle Drop showing the Forward Shearing of the Seat Structure Relative to the Simulated Floor

Although this failure led to an early conclusion to the drop test campaign, a sufficient data set had been obtained to determine system feasibility. The following sections present a detailed analysis of the system impact attenuation performance during both test sessions. Firstly however, the performance of the pressure relief valves will be analyzed.

6.4.1 Pressure Relief Valve Performance

To gain insight into the performance of the pressure relief valves, the high speed camera footage taken during all drop tests was reviewed. Upon first glance, the valves appeared to perform nominally, opening in the manner anticipated. As a detailed inspection of each of the video files was being performed however, a consistent phenomenon was observed, whereby the side valves would open first, followed by the front valves. This asynchronous opening pattern indicated the presence of a pressure wave moving through each airbag as it compressed during the impact – an effect not captured by the single airbag impact code due to its assumption of a uniform pressure field. As a consequence, there was a likelihood of less air being vented than predicted; and therefore lower performance than anticipated. This will be explored in Sections 6.4.2 and 6.4.3. Figure 6-34 shows a frame by frame breakdown of a 10 foot, 0° impact angle drop test.

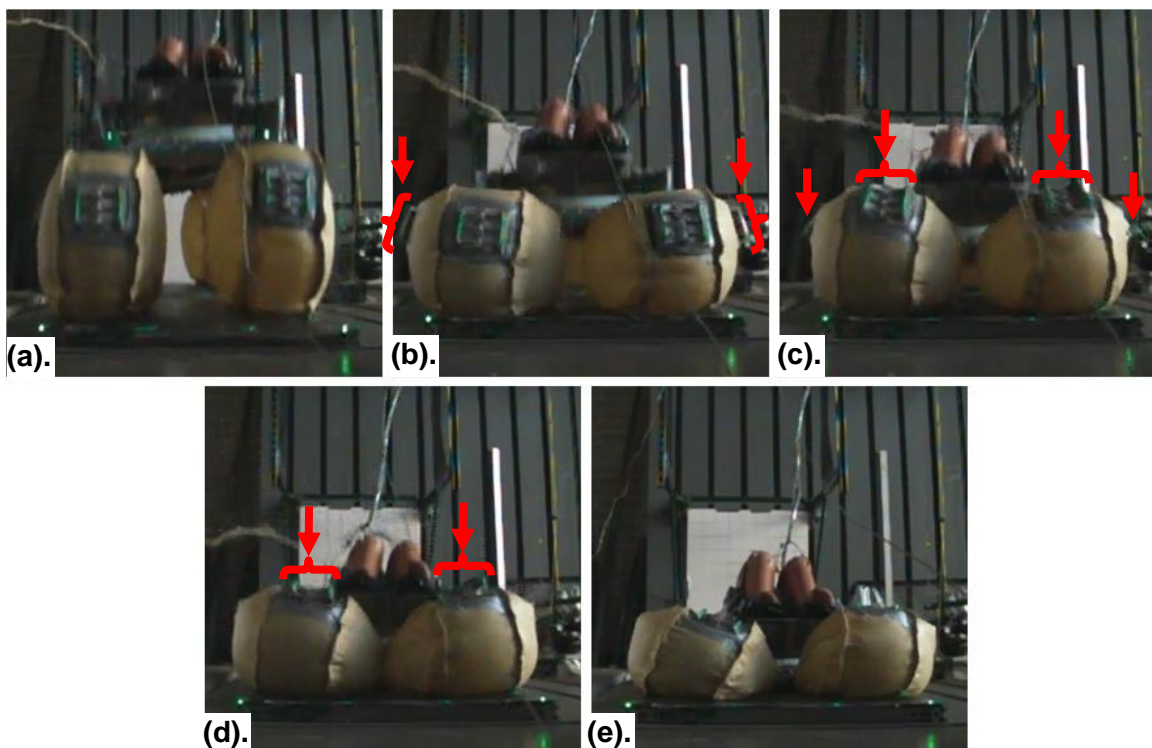


Figure 6-34: Breakdown of the Pressure Relief Valve Performance (a). Commencement of Airbag Stroke (b). Side Valves open (c). Front Valves Open as Side Valves begin to Close (d). Front Valves begin to Close (e). System Rest with all Valves Closed

Furthermore, in order to quantify the performance of the pressure relief valves, the pressure transducer time history for each drop was inspected. Figures 6-34 and 6-35 show the pressure transducer output obtained for all drop tests performed during both test sessions.

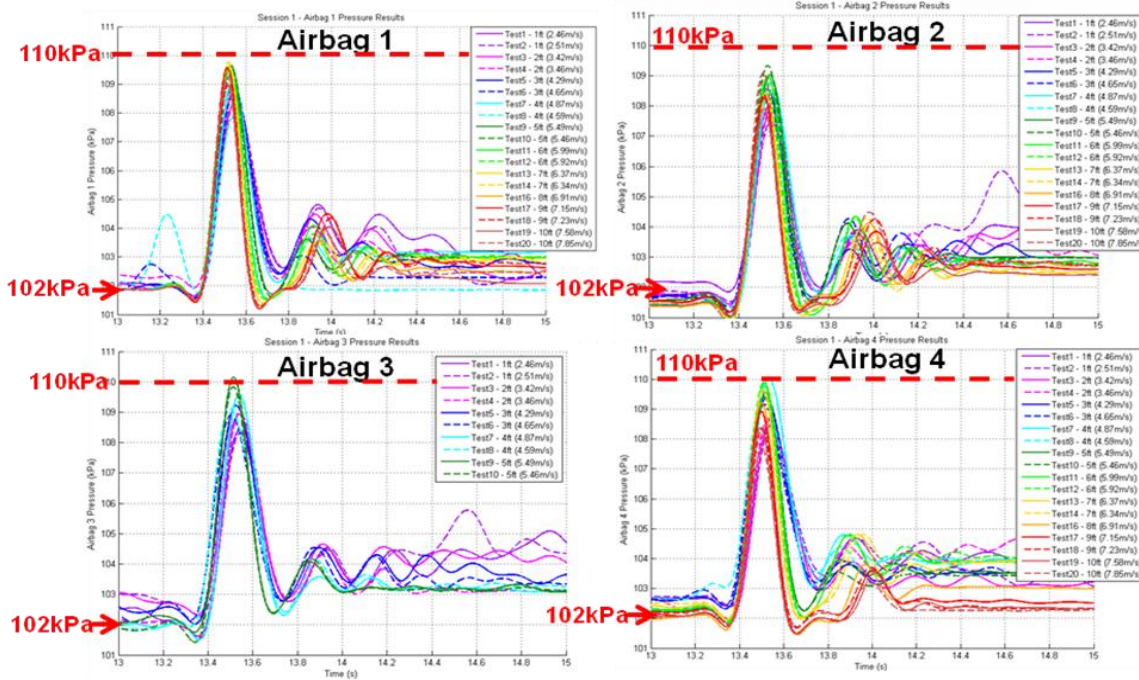


Figure 6-35: Pressure Transducer Output for all Test Session 1 Drop Tests

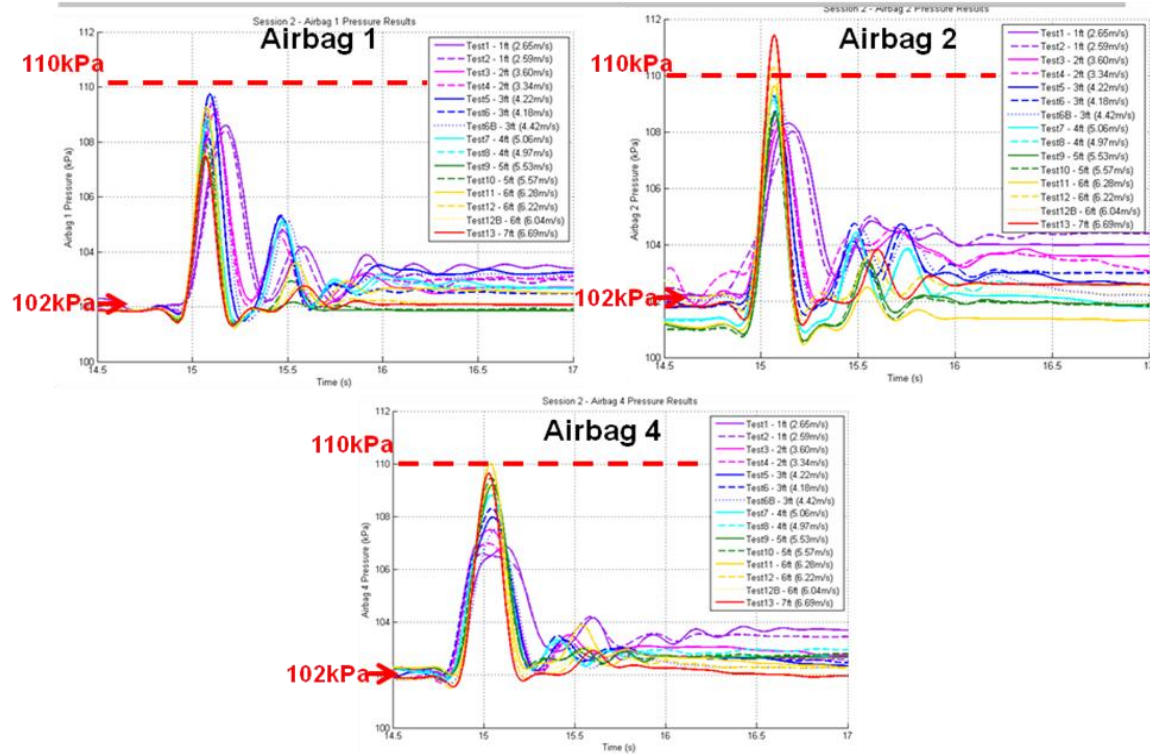


Figure 6-36: Pressure Transducer Output for all Test Session 2 Drop Tests

Note here, that midway through the first test session, the pressure transducer on Airbag 3 stopped working. As a consequence, no pressure transducer for this airbag is shown in Figure 6-36.

From these pressure results, it can be seen that the designed inflation pressure of 102kPa was achieved for all airbags during all drop tests to within 1kPa. More importantly however, is the fact that the peak pressures experienced in all airbags, during all tests occurred to within 1kPa of the designed burst pressure value of 8kPa above the inflation pressure. This in turn validates the development and characterization methodology used in the development of the valves.

6.4.2 Test Session 1 Results Analysis

As was earlier mentioned, all drops planned for the first test session were successfully completed, with the system performing nominally and remaining intact. To determine the impact velocity of each impact, a photogrammetric analysis was performed on the captured high speed camera footage, as had been done during all previous drop test campaigns. Figures 6-36 to 6-38 show the acceleration and injury-risk results obtained for all Session 1 drop tests, whilst Table 6.8 provides a summary of this data.

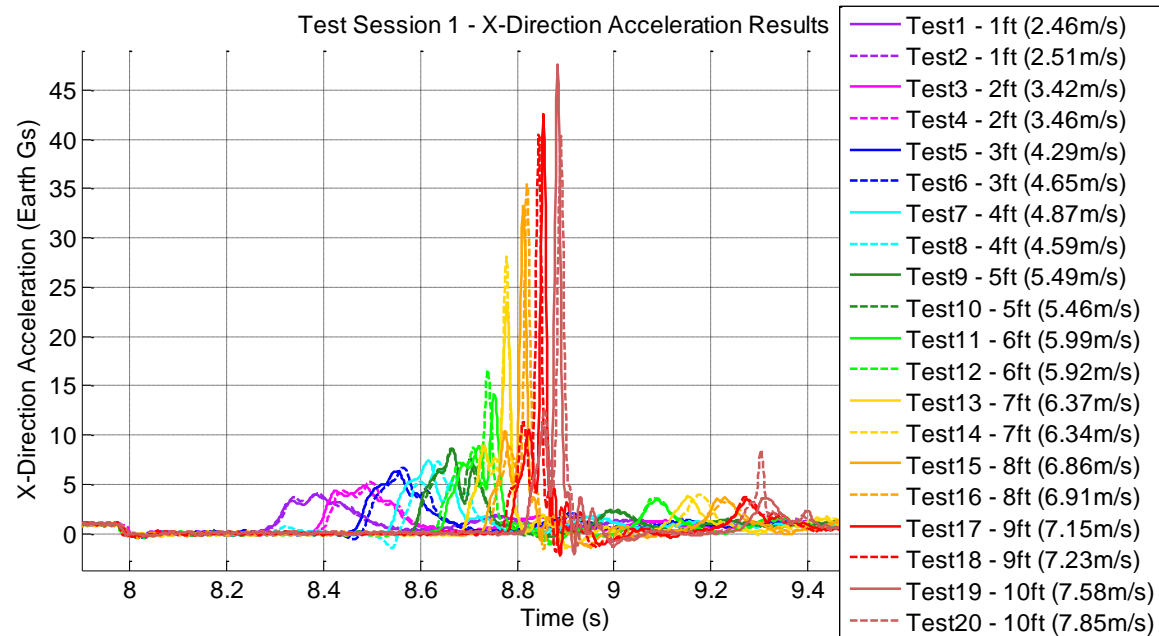


Figure 6-37: Test Session 1 X-Direction Acceleration Results

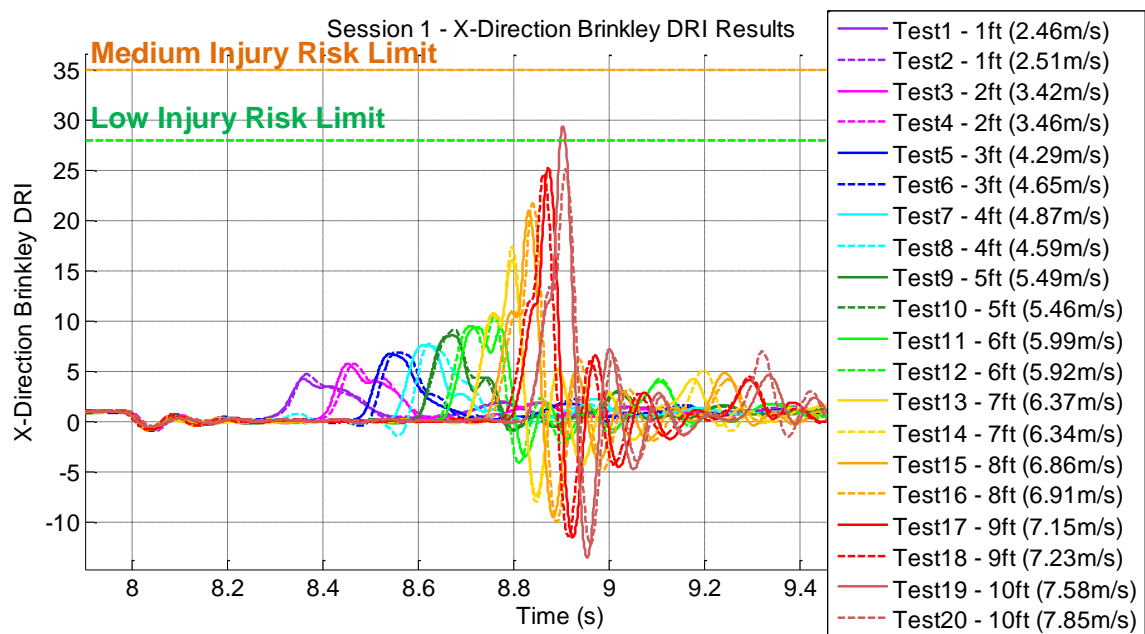


Figure 6-38: Test Session 1 X-Direction Brinkley DRI Results

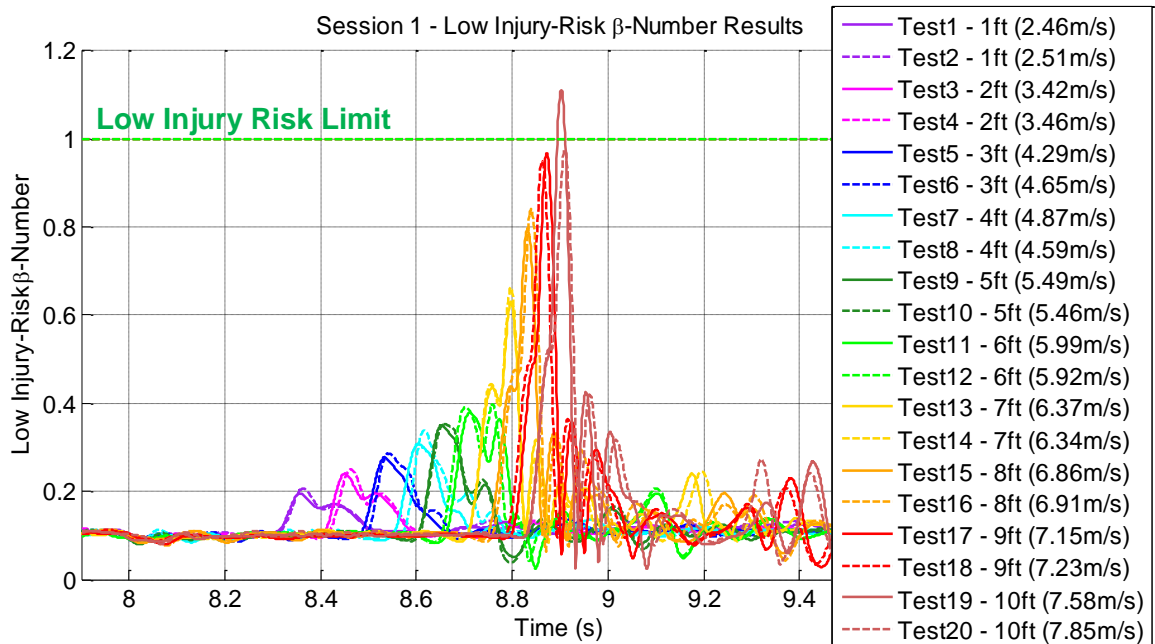


Figure 6-39: Test Session 1 Low Injury-Risk β -Number Results

Note here, that in the above figures, all test data has been time synchronized to the moment of drop initiation.

Table 6.8: Summary of Multi-Airbag System Drop Test Session 1 Results

Test No.	Drop Height (ft)	Impact Velocity (m/s)	Max X-Acceleration (G's)	Max Brinkley DRx	Max β-Number
1	1	2.46	4.004	4.23	0.152
2	1	2.51	4.128	4.71	0.170
3	2	3.42	4.923	5.77	0.207
4	2	3.46	5.302	5.77	0.210
5	3	4.29	6.356	6.73	0.241
6	3	4.65	6.689	6.90	0.252
7	4	4.87	7.427	7.59	0.272
8	4	4.59	7.384	7.70	0.293
9	5	5.49	8.575	8.57	0.308
10	5	5.46	8.643	9.12	0.328
11	6	N/A	14.208	9.42	0.340
12	6	5.92	16.562	10.51	0.376
13	7	6.37	23.444	16.10	0.606
14	7	6.34	28.068	17.38	0.634
15	8	6.86	33.178	20.95	0.770
16	8	N/A	35.472	21.73	0.809
17	9	7.15	42.474	25.28	0.934
18	9	7.23	40.451	24.70	0.919
19	10	7.58	47.544	29.46	1.083
20	10	7.85	40.298	25.09	0.944

NB. “N/A” implies that the high speed camera footage captured did not provide enough information to extract the stated variable.

From the Brinkley response and low-injury risk β-number results, it can be seen that at the 10 foot drop height, one of the drops stayed within the low-injury risk limit whilst the other exceeded it. Interestingly, the drop test with the higher impact velocity of 7.85m/s met the safety requirements whereas the 7.58m/s drop failed to meet them. Since the nominal impact velocity of the Orion CEV is 7.62m/s (25fps), this suggests that at a 0° impact angle, the system is at the limit of its impact attenuation performance in terms of meeting injury risk requirements for nominal landings. Moreover, because the system was designed to prove concept feasibility, any improvement in performance resulting from more rigorous design and analysis, should produce a system which consistently meets all Brinkley criteria under nominal, non-inclined landings conditions. As a result, it can be definitively stated that:

The airbag-based crew impact attenuation concept is feasible

In addition to this preliminary analysis, a more detailed investigation was conducted to determine why the as-built system had only just met the Brinkley low-injury risk criteria, when the predictions made during the design process indicated that it should have easily met the safety requirements. Here, this study focused on Test 19 – the only 0° degree drop test to exceed the low injury-risk limits. In particular, the acceleration time history was first inspected, where an unusual trend not observed during previous test campaigns was detected. Specifically, thus refers to the presence of two consecutive peaks occurring in the acceleration profile before a negative acceleration is experienced. What is interesting here is that the first peak is of lower magnitude than the second, a trend which is the opposite to that observed during the first generation system testing, where the first peak corresponded to an initial bottoming-out event. Figure 6-40 shows the Test 19 acceleration response, with these consecutive peaks highlighted.

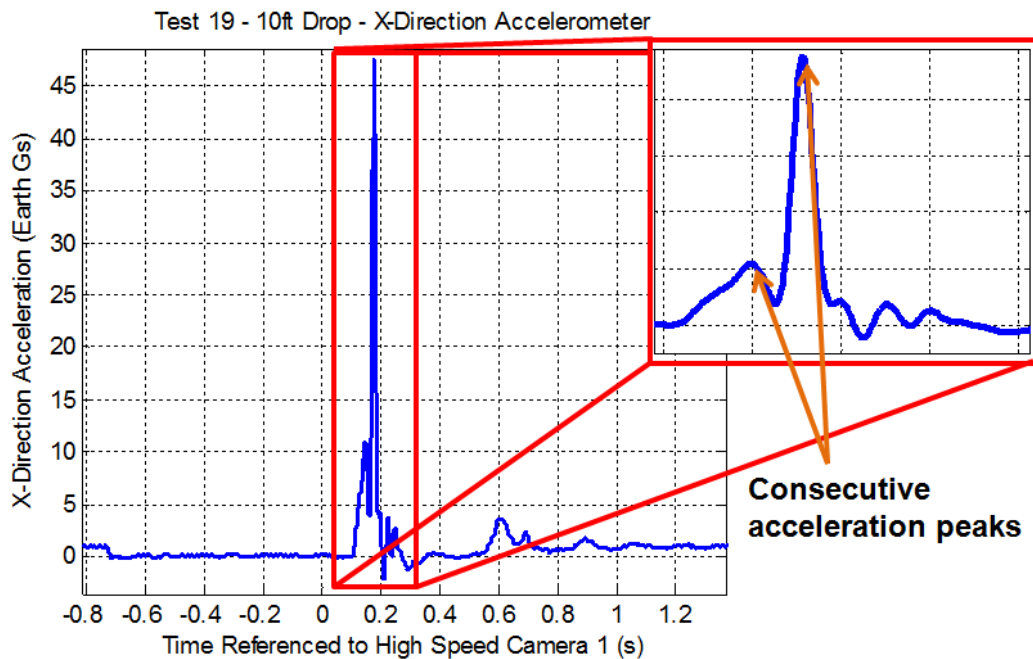


Figure 6-40: Test 19 Acceleration Response with Anomalous Consecutive Peaks Highlighted

In order to study the mechanics governing this acceleration response, all obtained data was time synchronized and over-plotted to observe the interactions between the measured properties. This commenced with a photogrammetric analysis performed on all high speed camera footage captured during each test. Following this, these data sets were time synchronized using the timestamp corresponding to the moment of impact of the simulated

floor LEDs. With this, the accelerometer data was then time synchronized with the high speed camera data, by using the fact that the maximum acceleration occurs at the moment of minimum transient vertical displacement. To synchronize this dataset with the pressure transducer data, an indirect method was used whereby the footage captured by High Speed Camera 2 was analyzed frame by frame to determine the time of maximum combined opening of the system pressure relief valves. With this timestamp found, an insight obtained from the single airbag impact model was used to synchronize the pressure data. Specifically, this is the observation that the maximum pressure occurs at the same time at which the combined valve opening area is at a peak, due to the dependence of the valve springs on the local pressure magnitude. Figure 6-41 summarizes this process.

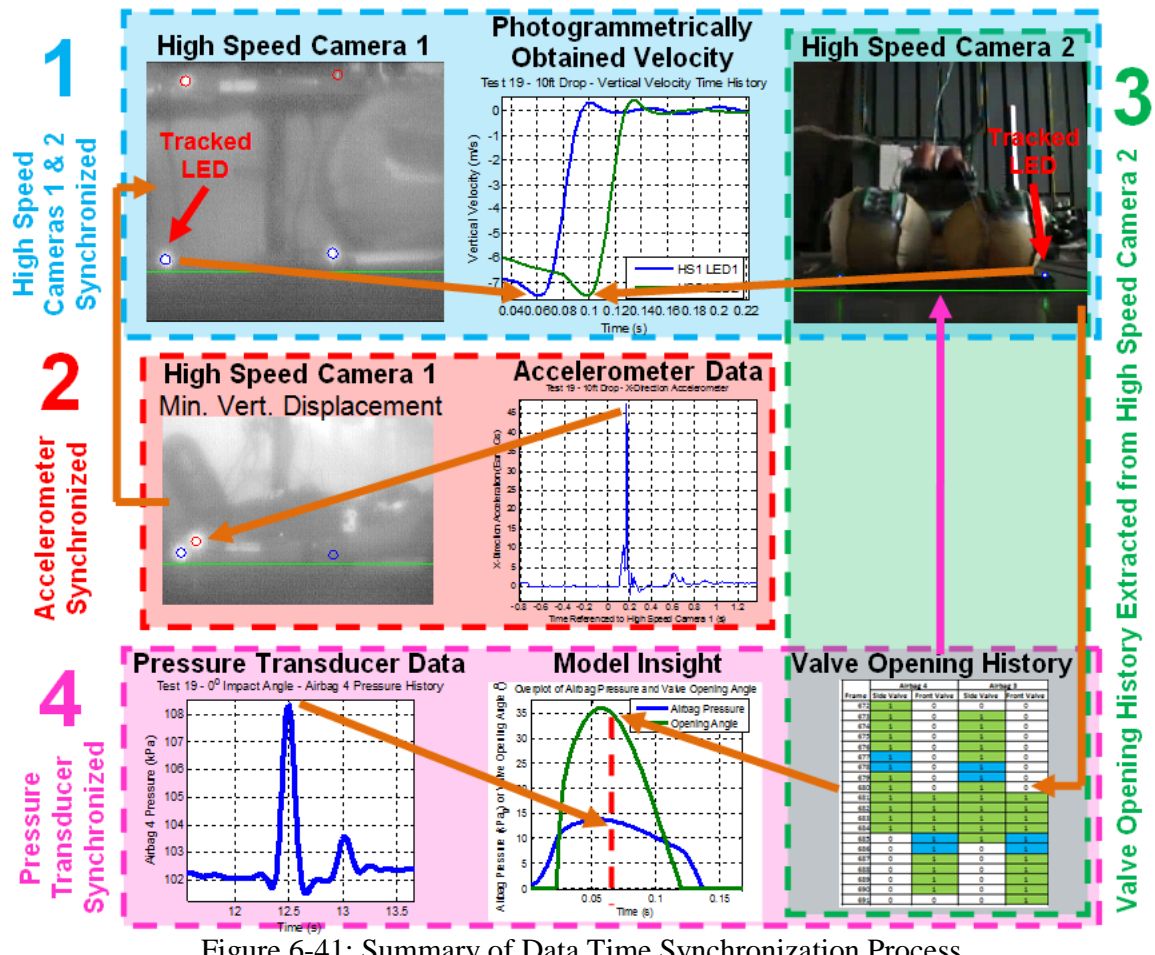


Figure 6-41: Summary of Data Time Synchronization Process

With regard to the last approximation made to time synchronize the pressure data, it should be noted that there is no guarantee that the pressure measured by the pressure transducers corresponds to the local pressure at the valves. Although this is the case, this approximation

allows for a time synchronization of the pressure data to within 20 milliseconds to be achieved – a value close enough for trends to be analyzed, and finer time synchronization adjustments to be made based on correlation with high speed camera footage.

Furthermore, to visually determine the valve opening history from the High Speed Camera 2 footage, a three level scoring system was used. Here, a value of zero was assigned to a given valve if it was observed to be closed during a particular frame, a value of 0.5 assigned if the valve was observed to be open, and a value of 1 given if the valve appeared to be experiencing its maximum opening angle. A representative set of results of this analysis can be seen by the blue, green, and white cells in the table labeled “Valve Opening History” in Figure 6-41. Moreover, the effects of this three level quantization scheme can be seen in the normalized and time synchronized data set, presented below in Figure 6-42.

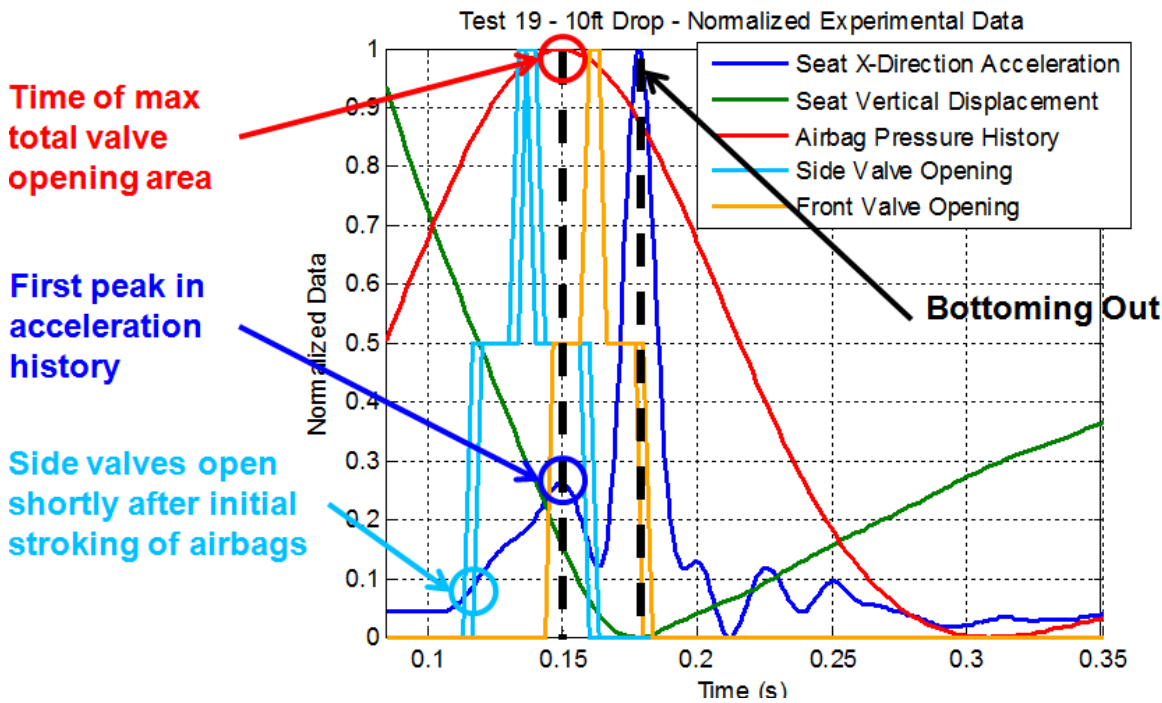


Figure 6-42: Session 1 Test 19 Normalized and Time Synchronized Data Set

Here, all data has been synchronized to lie between a value of 0 and 1, thus allowing for easier comparisons to be made between the data. From this, it can be seen that the side valves open shortly after the airbags begin to stroke. More importantly however, is the fact that the time of maximum total opening area of the pressure relief valves coincides with the observed first peak in acceleration. This suggests that as the airbags stroke and the pressure relief

valves open, the acceleration and corresponding pressure increases until the peak opening area is achieved. At this moment, the effect of the gas vented from the airbags causes the experienced acceleration to decrease. As this occurs, the airbag continues to stroke until either the system comes to rest or the stroke is depleted, causing a bottoming-out event to occur. For this particular case, the latter scenario was experienced, causing a subsequent sharp acceleration spike. Here, the correlation between this spike and a bottoming event was verified using high speed camera footage.

Following this bottoming-out event, the system was found to experience transient pitch dynamics as it bounced off the ground surface. After reaching its maximum bounce height, the system experienced a second impact with the ground, registering two miniature peaks in the acceleration response as various parts of the system came into contact with the ground surface. This entire impacting event is summarized by the dynamically tagged x-direction acceleration response shown below:

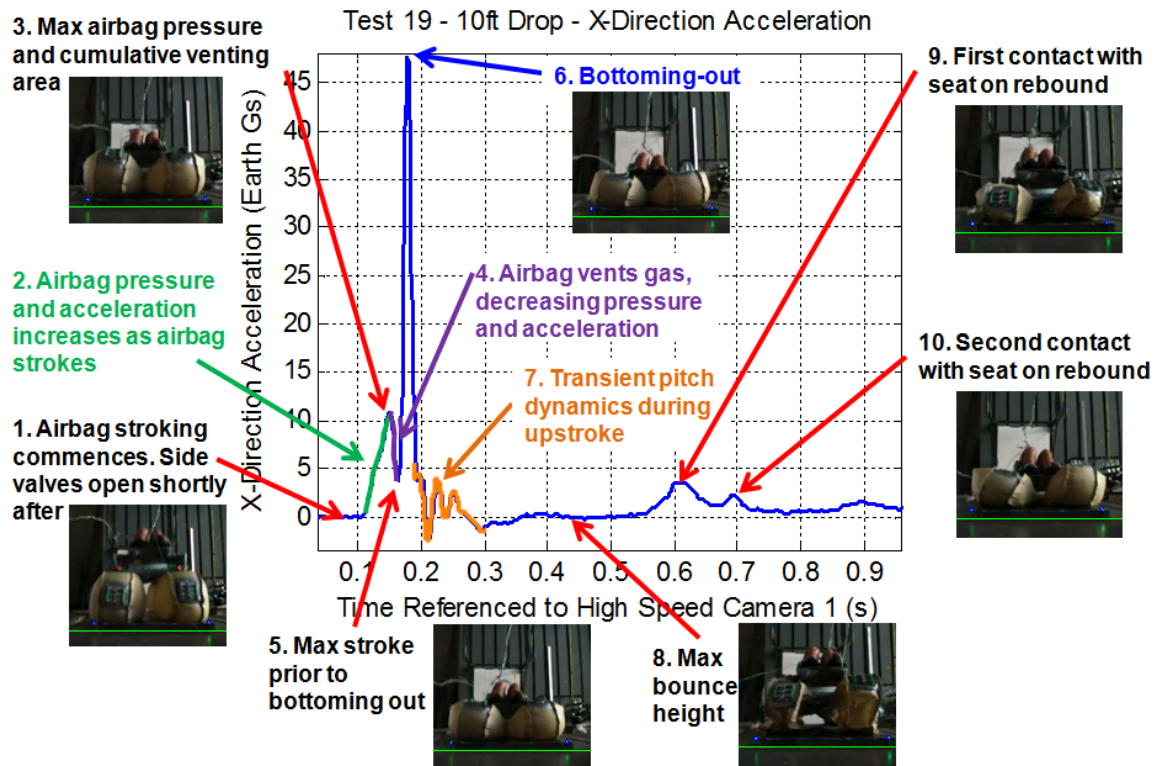


Figure 6-43: Session 1 Test 19 - Dynamically Tagged X-Direction Acceleration Response

Using this newly obtained insight, the entire Test Session 1 data set can be revisited in an attempt to gain additional understanding of the system performance. From this, it was found that the effects of bottoming-out began to become significant from drop heights of 6 feet (with an impact velocity of 5.92m/s) onwards. This can be seen below, in Figure 6-44.

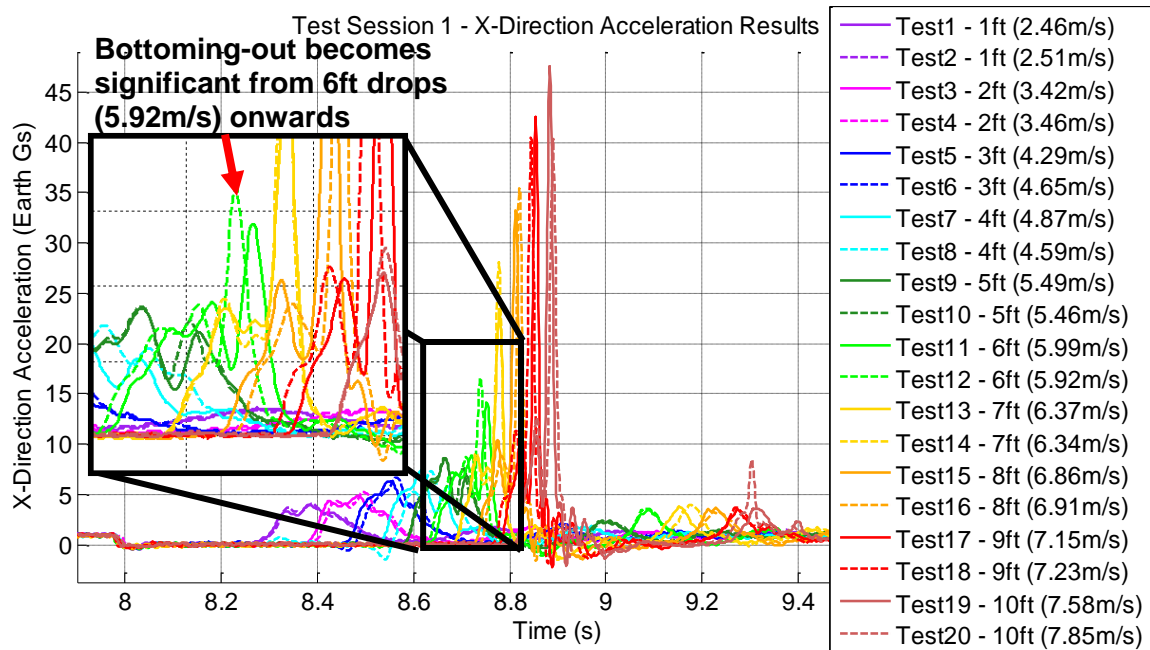


Figure 6-44: Effects of Drop Height on Bottoming-Out of Multi-Airbag System

Of greater significance, however, is the observation that the system dynamics is a superposition of the natural airbag dynamics, and the dynamics of bottoming-out. Specifically, this refers to the natural functions of airbag compression, pressure build-up, and venting characterized by the first peak observed in the acceleration response; and the bottoming-out dynamics characterized by the acceleration spike occurring shortly thereafter. This suggests that if this bottoming-out dynamics can be prevented, the overall system performance can be vastly improved due to the consequent reduction in peak acceleration and corresponding Brinkley Index. This can be seen in Figure 6-45, where the peak acceleration for the 10foot drop case would be 12.6G's, if bottoming-out is prevented. Interestingly, this potential peak acceleration is very close to the 11.8G peak acceleration value predicted by the multi-airbag for the developed system.

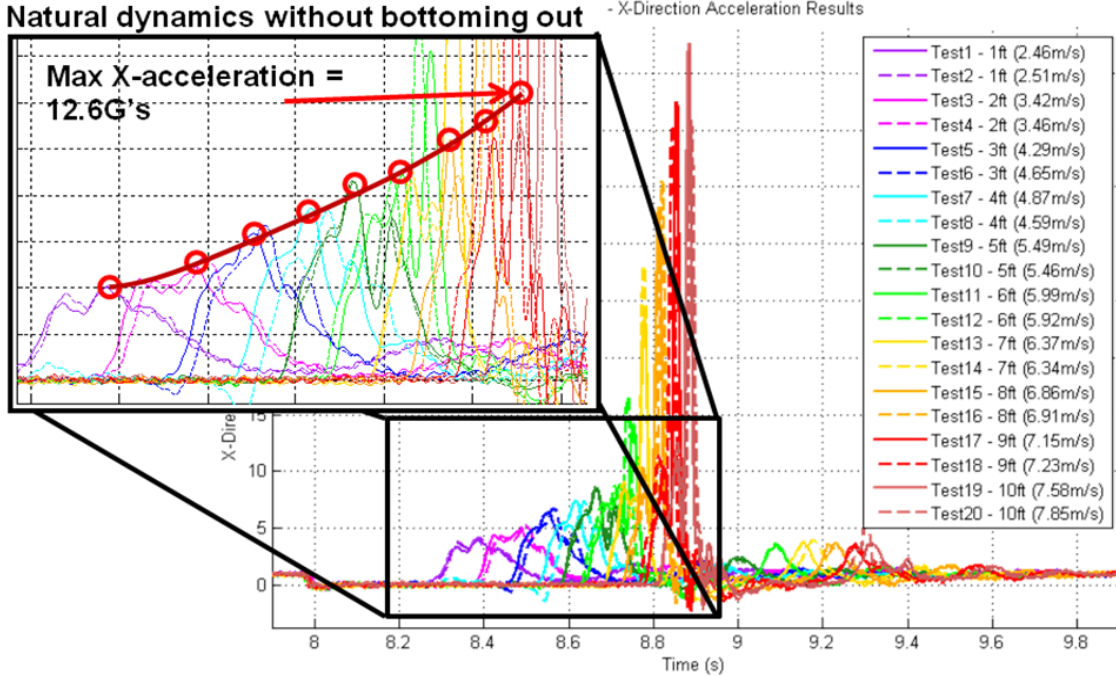


Figure 6-45: Potential System Dynamics without Bottoming-Out

From a practical point of view, this motivates the need to explore the implementation of anti-bottoming airbags within the system, as was used in the original external airbag system for the Orion CEV. It is hypothesized that by adding anti-bottoming airbags, the influence bottoming-out on the overall system dynamics will be largely mitigated.

6.4.3 Test Session 2 Results Analysis

In order to quantify and analyze the multi-airbag system performance during the 30° impact angle drop tests performed as part of the second test session, the same approach as that employed for the first test session was used. In particular, a photogrammetric analysis was first performed to extract the impact velocity for each test, and a subsequent detailed analysis performed in an attempt to explain the preliminary observations made. Figures 6-45 to 6-47 present the acceleration and injury-risk data obtained for all Session 2 drop tests, whilst Table 6.9 summarizes this data. Note here that three drop tests were performed at heights of 3 and 6 feet due to inconsistencies observed in the obtained dataset after the second drop.

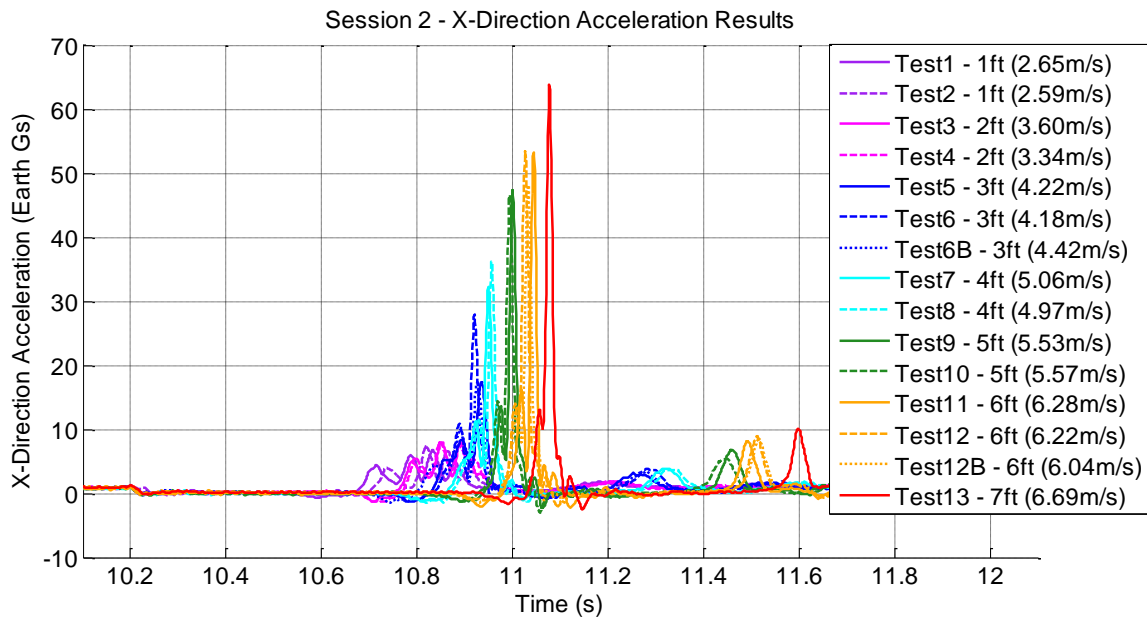


Figure 6-46: Test Session 1 X-Direction Acceleration Results

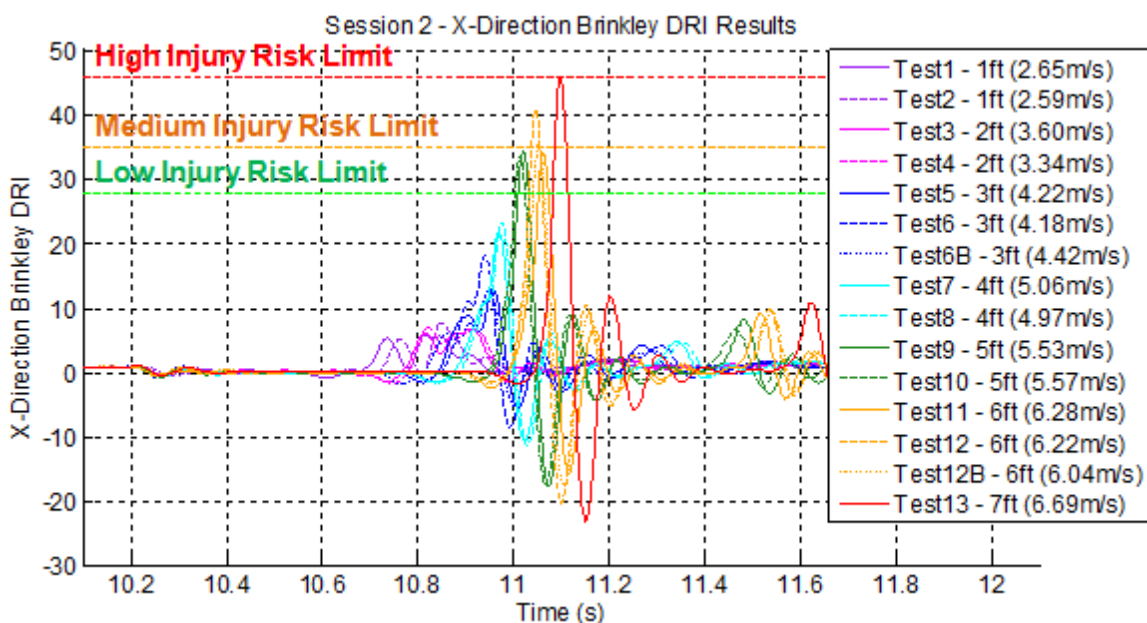


Figure 6-47: Test Session 2 X-Direction Brinkley DRI Results

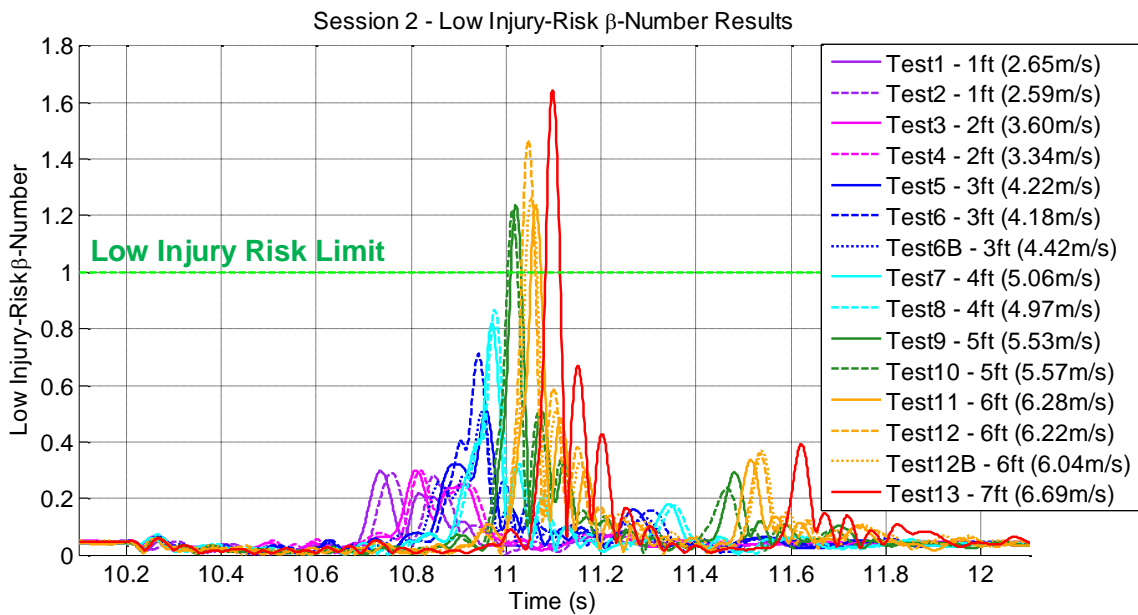


Figure 6-48: Test Session 2 Low Injury-Risk β -Number Results

Table 6.9: Summary of Multi-Airbag System Drop Test Session 1 Results

Test No.	Drop Height (ft)	Impact Velocity (m/s)	Max X-Acceleration (G's)	Max Brinkley DRx	Max β -Number
1	1	2.65	6.714	5.79	0.298
2	1	2.59	7.277	7.75	0.290
3	2	3.6	8.089	6.84	0.300
4	2	3.34	7.986	6.97	0.300
5	3	4.22	17.428	12.91	0.510
6	3	4.18	27.897	18.05	0.711
6B	3	4.42	17.476	13.27	0.504
7	4	5.06	32.353	21.83	0.818
8	4	4.97	36.103	23.22	0.868
9	5	5.53	47.274	34.45	1.237
10	5	5.57	46.522	33.65	1.217
11	6	6.28	53.321	33.95	1.237
12	6	6.22	53.359	40.79	1.466
12B	6	6.04	48.074	35.25	1.263
13	7	6.69	63.754	45.91	1.642

Here, it can be immediately seen that the system does not perform adequately during 30° impact angles, with the low-injury risk criteria being exceeded at drop heights of 5 feet, the medium injury-risk criteria being exceeded at drop heights of 6 feet, and the high injury-risk

criteria being exceeded during the failed drop tests at 7 feet. Considering the fact that all of these failed drops had impact velocities less than the nominal 7.62m/s, this result definitively verifies the original NESC finding that flatter angles are more favorable for land-landings.

As a consequence of this finding, a study was initiated to determine the reasons as to why the system performed so poorly at the 30° impact angle. Here, the same process as that used in the detailed analysis of the Test Session 1 results was employed, whereby all data sources were time synchronized and over-plotted to investigate their interactions. In particular, the worst performing test case was chosen as the baseline for this analysis, being the single drop performed from 7 feet.

To time synchronize the test data, the process summarized in Figure 6-41 was again employed, with a slight modification in the method used to time synchronize the data from both high speed cameras. Because the LEDs located on the simulated floor were no longer in the same horizontal plane due to the inclined impact angle, their timestamps could not be directly compared to each other, as had been done in the Test Session 1 analysis. As a result, a line detection scheme, like that used during the first generation system test results analysis, was implemented. In turn, this allowed for attitude information to be extracted from the High Speed Camera 1 footage, which could then be used to predict the moment of impact of the front edge of the simulated floor. With knowledge of this timestamp, the data extracted from High Speed Camera 2 could be time synchronized with that of High Speed Camera 1, since it is situated such that it views the dynamic motion of the front of the system. Figure 6-49 shows the time-synchronized and normalized data set obtained from this process.

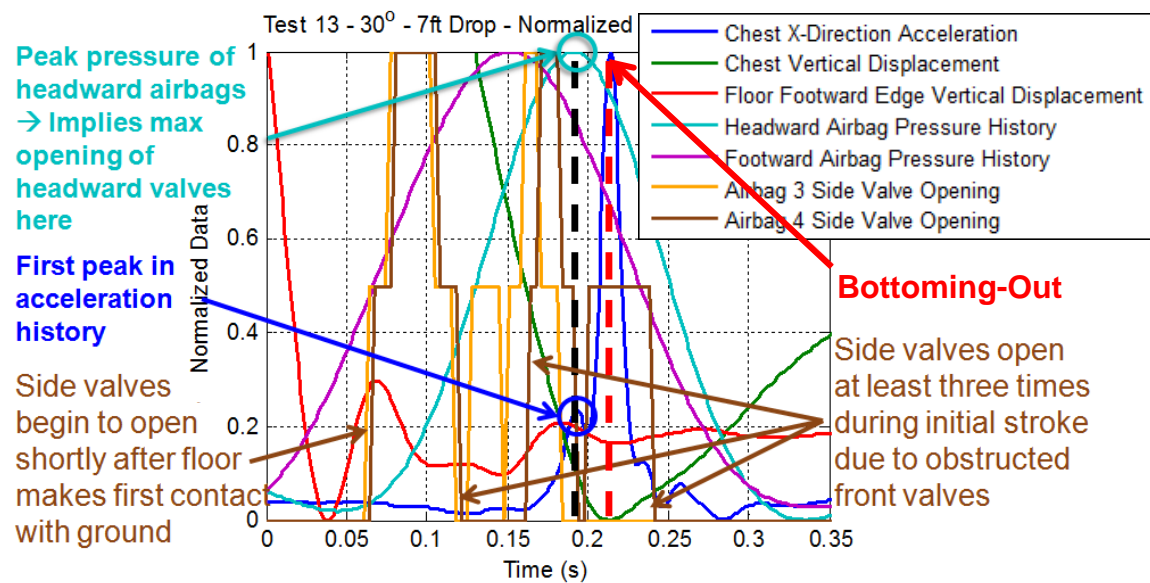


Figure 6-49: Session 2 Test 13 Normalized and Time Synchronized Data Set

From Figure 6-49, several phenomena are seen to be occurring simultaneously; one of which, being that the side valves on Airbags 3 and 4 open at least three times during the impacting event. This was one of the first observations made during data processing, where the high speed camera footage indicated that because the system was pitched forward during impact, the positioning of the front pressure relief valves was such that the crush up of the airbags prevented them from opening. As a result, this caused the generated pressure wave to move back and forth through the airbag, causing the side valves to open every time the wave moved back into their vicinity. Interestingly, the side valves were found to open shortly after initial contact of the simulated floor with the ground surface, as had been observed in the 0° impact case. The effects of this valve obstruction phenomenon are presented in Figure 6-50.

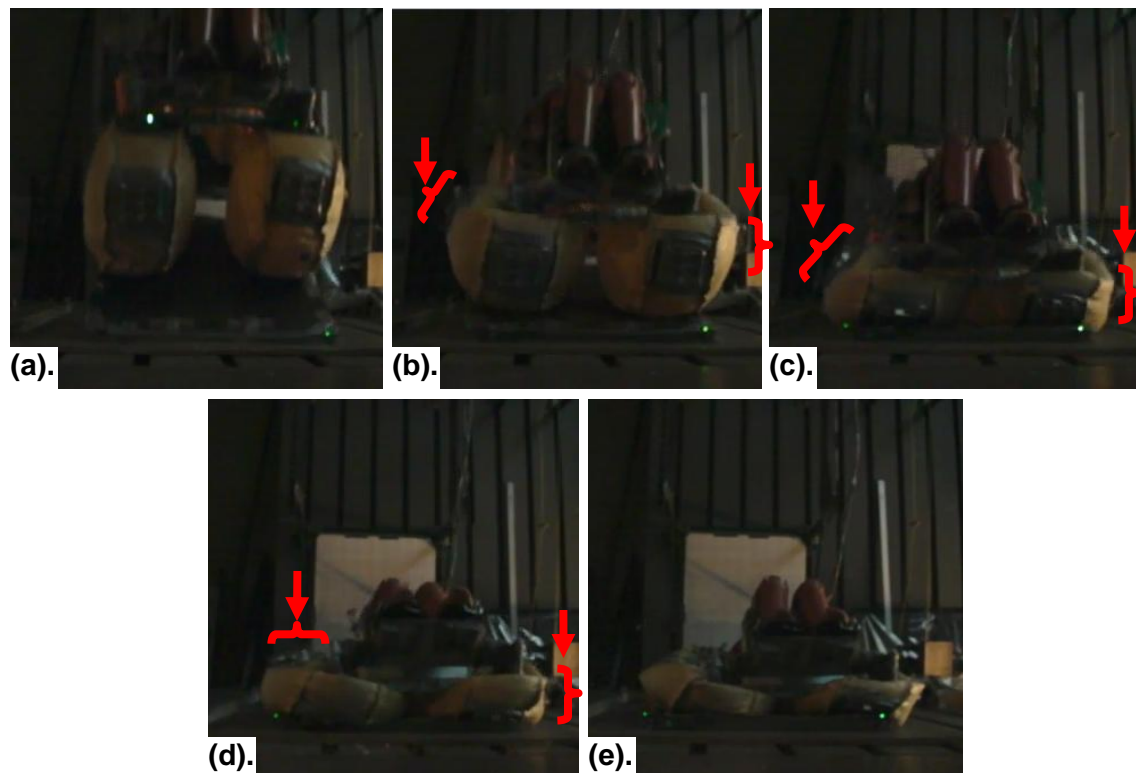


Figure 6-50: Breakdown of Valve Performance and Obstruction during Session 2 –Test 13
 (a). First Contact of System with the Ground Surface (b). First Opening of Foot-ward Airbag Side Valves (c). Second Opening of Foot-ward Airbag Side Valves (d). Third Opening of Foot-ward Airbag Side Valves (e). System Rest with all Valves Closed

In addition, the differential pressure peaks occurring at the airbags located at the head-ward and foot-ward ends of the system can also be observed from Figure 6-49. Here, these are represented respectively by the purple and cyan curves. This time offset can be explained

by the fact that the system impacted the ground surface at an inclined angle, with the foot-ward airbags beginning to stroke before the head-ward airbags. As had been previously performed, the pressure history in the foot-ward airbags (purple curve) was coarsely time synchronized with the footage from High Speed Camera 2 using the extracted valve opening time history (orange and brown curves). Because data from all pressure transducers was acquired by the same data acquisition unit, their output was already time synchronized, thus allowing for the pressure history of the head-ward airbags (cyan curve) to be compared to the already time synchronized accelerometer data (blue curve). Upon performing this comparison, it was found that the timestamp of the peak pressure experienced by the head-ward airbags was the same as the timestamp of the first peak in the acceleration time history, as denoted by the black dotted line in Figure 6-49. This suggests that at this point in time, the valves in the head-ward airbags experienced their peak combined opening area, thus allowing for gas to be vented at a rate high enough to decrease the airbag pressure and resulting acceleration. The fact that the valves on the head-ward airbags were not obstructed in the same manner as those on the foot-ward airbags, and as well as the close vertical alignment between the head-ward airbags and the physical location of the accelerometers, further verifies this observation. This finding hence allows the accelerometer time history to be dynamically tagged, as was earlier performed. The result of this is shown below:

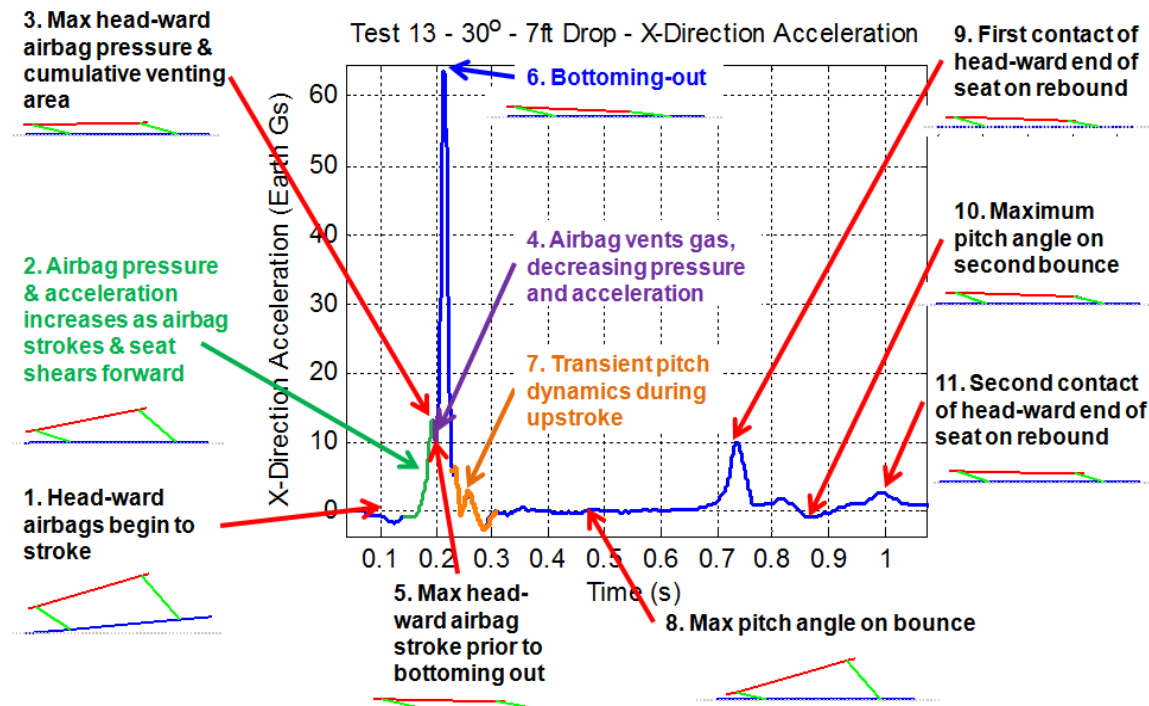


Figure 6-51: Session 2 Test 13 - Dynamically Tagged X-Direction Acceleration Response

From Figure 6-51, it can be seen that shortly after the first acceleration peak, the system experiences a bottoming out event, as observed in the first test session results. Here, the short period of decreasing acceleration between the first and second acceleration spikes indicates that there was significantly less stroke in the airbags prior to bottoming-out, when compared to the 0° impact case. Following this bottoming-out event, the system experiences the previously observed transient pitch dynamics during its rebound, after which it obtains a maximum pitch angle during the peak height of its bounce. In turn, this pitch angle causes the system to experience a second impact at an inclined angle.

Upon comparison of the dynamically tagged acceleration response with the high speed camera footage, it was noticed that all peak acceleration events occurred as a result of the head-ward end of the seat pivoting about the foot-ward airbags. Closer inspection of the video footage captured during this test, indicated that this was a result of the differential stroking of the foot-ward and head-ward airbags, causing the head-ward end of the seat to pivot about the feet and towards the ground as it continued to fall. As the seat pivoted about the foot-ward airbags, it sheared forward relative to the simulated floor, hence removing a significant amount of stroke from the head-ward airbags. This hence explains the short decrease in acceleration between the first and second acceleration peaks observed in Figure 6-51. Furthermore, by the time the head-ward airbags began to stroke, most of the air in the foot-ward airbags had already been depleted, causing this foot-ward end to continue to act as a pivot point for consequent rebounds of the system. These events can be seen in the original frame by frame breakdown of this drop test, presented in Figure 6-33, and again in Figure 6-52, for the convenience of the reader.

Here, the presence of this shearing effect suggests that the three row configuration found in the optimization exercise presented in Section 6.2.1 and summarized in Figure 6-11, may have been more preferable in the design of the airbag configuration. The inclusion of an additional row of airbags between the existing airbags could potentially compensate for the lost stroke in the head-ward airbags due to the forward shearing motion. In turn, this would increase the time over which the acceleration response decreases after the first peak, thereby reducing the magnitude of any subsequent bottoming-out event.

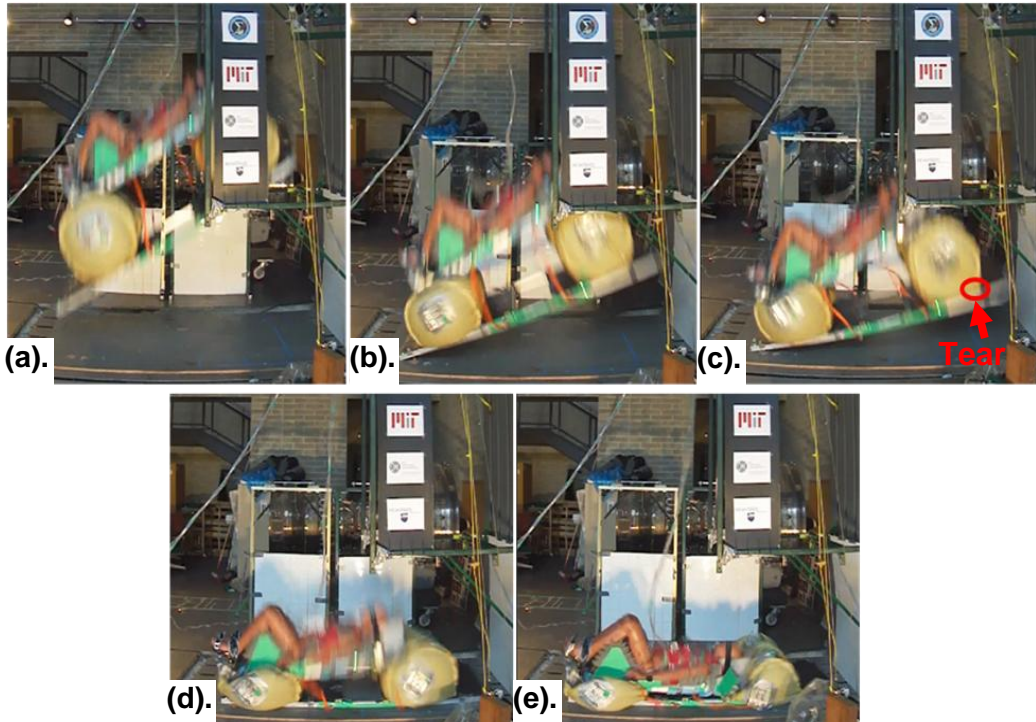


Figure 6-52: Frame by Frame Breakdown of the 7 foot, 30° Impact Angle Drop

(a). System in free-fall (b). Differential Stroking between Foot-ward and Head-ward Airbags as system makes first contact with ground surface (c). Forward Shearing of Seat System relative to Simulated Floor (d). Start of Head-ward Airbag Stroke. Note that a significant amount of stroke from these airbags has been removed due to the forward shearing of the Seat System. Additionally, most of the air in the Foot-ward airbags has been depleted by this point, causing them to act as a pivot point (e). System Rest after multiple impacts of the head-ward end of the seat with the ground surface

6.5 Chapter Summary

Over the course of this chapter, the design, development, and testing of a full-scale multi-airbag drop test article was presented, followed by an analysis of the results obtained from an extensive drop test campaign. Through this effort, the basic feasibility of the personal airbag system was established by experimentally proving that it could meet the low injury-risk Brinkley targets, at nominal landing velocities and at an impact angle of zero degrees. In achieving this, along with the 37 other drop tests performed, the manufacturing, integration, and testing processes which had been developed over the previous two development cycles were validated. This was particularly demonstrated by the consistent performance of the pressure relief valves to design specifications.

Furthermore, a detailed analysis of the test results revealed two key insights. The first of which, was that the dynamic response of the system during impact was a superposition of the natural airbag dynamics, and the dynamics of bottoming-out. By mitigating the effects of bottoming-out, it was found that the resulting peak Brinkley response under nominal landing conditions could be more than halved. This in turn motivates the need to explore the implementation of anti-bottoming airbags into the system.

The second important insight gained from this exercise was related to the reasons as to why inclined impacts resulted in significantly poorer performance compared to impacts at flatter angles. Here, it was found that this was due to a combination of differential stroking between the front and rear airbags, and a consequent forward shearing motion between the seat and the simulated floor. The resultant effect of this was the removal of a significant amount of stroke from the head-ward airbags, and pivoting of the system about the foot-ward airbags causing further impacts of the head-ward end of the system. Moreover, the presence of the observed shearing effect motivates the need to revisit the design of the airbag configuration, where the inclusion of an additional row of airbags may potentially offset the adverse effects of this shearing motion.

Chapter 7

Conclusions

Throughout this thesis, the complete development and testing of three generations of drop test articles, consisting of two full-scale personal airbag systems and a single airbag drop test article, has been presented. In moving through the development of each of these systems, several lessons have been learned and key findings made, culminating in the final design and testing of a multi-airbag system. Through this effort, the concept of airbag-based crew impact attenuation has been proven to be **feasible**. This feasibility is further verified by the fact that all drop tests were performed on land, with the only means of impact attenuation being the airbag system. This contrasts significantly to the more benign nominal Orion landing scenario of water landings attenuated by both crushable structures and strut-based mechanical damping.

Consequently, this finding warrants further study to determine the specific modifications and methods necessary for the practical implementation of this system into the Orion Crew Exploration Vehicle. Since the design of the Orion CEV is largely fixed at this current moment in time, the constraints imposed by the existing cabin design will need to be accounted for in the next evolution of this work. Such constraints include limits on available stroke, crew member positioning constraints relative to the spacecraft controls and viewing ports, and stowage constraints. In order to provide a concise basis for the initiation of this future work, all findings made throughout this initial effort have been compiled and summarized in the following section. Following this, a list of recommendations for future work based on these findings is presented to further support this basis.

7.1 Summary of Findings

In this section, the findings made throughout this thesis are summarized, and organized with respect to the development cycle in which they were obtained. These findings are listed as follows:

7.1.1 Findings from Preliminary Modeling of the Airbag-Based Impact Attenuation Problem

- F-1 The efficiency of the energy transfer from the occupant to the operating medium of the airbags is related to the change in geometry as the airbag compresses
- F-2 The final system energy is dependent on how much air is vented from the airbags during the venting phase
- F-3 Improved impact attenuation occurs when both:
 - The magnitude of the acceleration of the impacting event is minimized; and
 - The frequency content of the acceleration response is weighted away from that of the Brinkley natural frequency in the given direction

7.1.2 Findings from the Development of the Analog-Airbag System

- F-4 The seat frame design and positioning needs to be conducive to allowing maximum stroke in the airbags
- F-5 The most likely failure mode in a personal airbag system is due to local stress concentrations causing the airbags to rupture
- F-6 Two dimensional effects are present in impacting events (even in only the vertical plane), and need to be accounted for
- F-7 The highest risk to injury occurs at the end of the combined first stroke of the system

- F-8 A simulated spacecraft floor is required to properly replicate the impact dynamics of a personal airbag system

7.1.3 Findings from the Single Airbag Impact Dynamics Investigation

- F-9 For a fixed geometry, airbag impact attenuation performance is most sensitive to variations in the venting area
- F-10 Airbag impact attenuation performance is least sensitive to variations in inflation pressure
- F-11 For an airbag design utilizing pressure relief valves, systems with low Brinkley DRI values tend to have smaller geometries. This is because smaller geometries result in higher pressures being maintained over a longer period of time, which in turn allows for the PRVs to remain open for longer and hence more gas to be vented from the airbag (related to F-2)
- F-12 The minimum mass, minimum Brinkley DRI PRV-based airbag design is one with the minimum geometry such that bottoming-out does not occur (ie. minimum volume with adequate stroke)

7.1.4 Findings from the Development of the Multi-Airbag System

- F-13 The final mass and volume of the multi-airbag system equates to a 24% mass saving and a 26% volume saving over the currently baselined six person Orion pallet-based CIAS
- F-14 Under a zero degree impact angle, the personal airbag system concept is feasible for land landings
- F-15 Superior impact attenuation can be achieved with a personal airbag system if bottoming-out is prevented

- F-16 Forward shearing of the seat relative to the spacecraft floor, and differential stroking of airbags contributes to poorer impact attenuation performance of the personal airbag system during landings with oblique impact angles

7.2 Recommendations for Future Work

Based on the previously listed findings of this work, the following recommendations for future work have been formulated:

R-1 Explore options for burst valves (*From F-2 and F-11*)

This is based on the consistent finding that improved impact attenuation performance is dependent on the amount of gas vented through the pressure relief valves. By implementing a burst-type means of venting, where a valve stays open once triggered, more gas can theoretically be released, thereby improving impact attenuation performance. Such a system could be either passively or actively actuated. An alternative concept which also warrants further study is the use of multiple pressure relief valves, each with a different burst pressures set to open in a predefined sequence.

R-2 Revisit choice of geometry for airbag (*From F-2 and F-11*)

This recommendation is based on the fact that the original choice of cylinders as the baseline shape for the airbags was chosen for their ease of manufacturability. In a design space with additional constraints imposed by the existing Orion CEV cabin design, it will be likely that the optimal airbag geometry will be a shape other than a cylinder.

R-3 Explore the effects of weave direction at the airbag seams, and contact surfaces between the airbag and all hard-points (*From F-5*)

This arises from the fact that during the construction of the airbags, the direction of the Vectran weave at the seams and airbag mounting locations was arbitrarily chosen. It is hypothesized that by intentionally choosing a particular weave direction at a given location, the effects of local stress concentrations can be

mitigated, thereby resulting in a stronger and more robust system. Furthermore, performing a detailed characterization to determine the constitutive laws characterizing Vectran strength will aid in this local stress concentration mitigation effort.

- R-4 Explore methods for integrating anti-bottoming airbags into the personal airbag system (*From F-15*)

This recommendation is motivated by consistent observation that bottoming-out had the largest contribution to the acceleration response, and hence the resulting Brinkley Index. By mitigating the effects of this bottoming-out event, it was predicted that the peak Brinkley response could be more than halved. Implementing anti-bottoming airbags acts to mitigate these bottoming-out effects, whilst having a minimum impact on the overall system volume – a particularly beneficial attribute in the context of the constrained cabin environment of the Orion CEV.

- R-5 Explore options for reconfiguration and mass optimization of the seat system and the airbag inflation mechanisms (*F-13*)

This recommendation is related to the original value proposition of the system, whereby mass and volume savings could be achieved via the inherent lightness and reconfigurability of airbag-based systems. One potential area of focus here, is to investigate methods to incorporate a personal airbag system about the existing Orion CEV seat design – one which is already designed to be able to folded and stowed away when desired.

- R-6 Investigate means to address impact attenuation in the lateral (y) direction

This was an area which was not explicitly investigated in this study, but has the potential to become significant in the operational context. Potential means of addressing this issue are by designing the airbag geometry and configuration to accommodate loads in the lateral direction; or by employing a hybrid means whereby airbags are used to attenuate loads in the vertical plane, whilst an alternative means (eg. struts) is used to attenuate out of plane loads.

- R-7 Perform a Failure Modes, Effects, and Criticality Analysis on the system

The intention of this analysis is to identify potential failure modes within the system, and to develop means for mitigating them. This is particularly important for a personal airbag system as its purpose is to perform a time and mission critical function in which there is little margin for error.

In addition to the aforementioned recommendations, an isoperformance-type approach [73] can be utilized to address the land-landing impact attenuation problem within a volume constrained environment, such as that of the Orion CEV cabin. Specifically, the Brinkley Model trends found in Section 3.2.2 and summarized in Finding 3 can be used to determine the injury-risk-optimal deceleration profile for a given amount of available stroke. With this, a range of impact attenuation technologies capable of achieving the established optimal profile can then be directly compared in terms of mass, volume, and other criteria. In doing this, the optimal impact attenuation concept can be selected in a systematic manner. This work has proven that personal airbag systems can indeed achieve low-injury risk deceleration profiles under nominal impact conditions, thereby making it a viable option in the space of impact attenuation technologies to be traded amongst.

It is anticipated that with each of the aforementioned areas of further study addressed, the personal airbag system concept will be steadily matured such that it enables a wider selection of options for impact attenuation in the next generation of crewed space vehicles. In doing so, the elusive goal of capsule-shaped vehicle land-landing with a safe and low mass and volume system may finally be achieved.

Appendix A

Project Team Members

This project was authorized by Mr. Joseph Pellicciotti, Technical Fellow at the Mechanical Systems Branch of the NESC, and funded through the Constellation University Institutes Project (CUIP) under prime award number NCC3989 and subaward number Z634013. To support this development effort, a core and support team was formed. The members of this team are listed as follows:

Team Member	Role	Position	Institute
Core Team			
Olivier L. de Weck	Principle Investigator	Associate Professor	MIT
Sydney Do	Project Lead	Research Assistant	MIT
Project Support			
Todd Billings	Manufacturing Support	Technical Instructor	MIT
Richard Perdichizzi	Facilities Support	Technical Instructor	MIT
David Robertson	Data Acquisition Support	Technical Instructor	MIT
Analog Airbag System Support			
Peter Cheung	Airbag Development	Senior	PSU
Ricardo Robles Jr.	Manufacture & Test Support	Senior	MIT
Jackson Siu	Airbag Development	Senior	PSU
Single Airbag System Support			
Josh Gafford	Development & Test Support	Senior	MIT
Jack Weinstein	Valve Development	Sophomore	MIT
Multi-Airbag System Support			
Alban Cobi	Valve Manufacture	Junior	MIT
Adrian Dobson	Development & Test Support	Senior	MIT
Daniel Goodman	Development & Test Support	Freshman	MIT
Jared Trotter	Airbag Manufacture	Junior	MIT

Appendix B

Model Newton Iteration Function Derivation

In this appendix, the complete derivation of the function used in the Newton step of the single airbag impact model will be presented.

As was described in Section 3.1.3, a general Newton step for a function of pressure can be expressed as:

$$P_{t+\Delta t, n+1} = P_{t+\Delta t, n} - \frac{f(P_{t+\Delta t, n})}{f'(P_{t+\Delta t, n})} \quad (\text{B.1})$$

Where P is the airbag pressure, t is a time coordinate and n is an increment denoting the iteration number. For the purposes of simplifying the notation used in this derivation, let $P_{t+\Delta t, n}$ be denoted by $P_{\text{new}}(n)$ and $P_{t+\Delta t, n+1}$ be denoted by $P_{\text{new}}(n+1)$. Furthermore, let the pressure from the previous time step, that is, P_t , be denoted by P_{old} . Thus, Equation (B.1) becomes:

$$P_{\text{new}}(n+1) = P_{\text{new}}(n) - \frac{f(P_{\text{new}}(n))}{f'(P_{\text{new}}(n))} \quad (\text{B.2})$$

From this, explicit relationships for $f(P_{\text{new}})$ and $f'(P_{\text{new}})$ will now be derived, as follows:

$$F(P_{new})$$

In Equation (3.43), the relationship describing the change in airbag pressure from one timestep to the next was given. This is presented again below, as follows:

$$P_{new} = P_{old} \left(\frac{\rho_{new}}{\rho_{old}} \right)^\gamma = P_{old} \left(\frac{w_{new}}{\rho_{old} V_{new}} \right)^\gamma = P_{old} \left(\frac{w_{old} - dw(P_{new})/dt \times dt}{\rho_{old} V_{new}} \right)^\gamma \quad (\text{B.3})$$

Moreover, the mass flow rate component of this equation for subsonic flow, as derived in Section 3.1.2 is given by:

$$\frac{dw}{dt} = C_D(P_{new}) A_{th} P_{atm} \left(\frac{1}{R_{GAS} T_I} \right)^{\frac{1}{2}} \left(\frac{2\gamma}{\gamma-1} \left(\frac{P_I}{P_{atm}} \right)^{\frac{\gamma-1}{\gamma}} \right)^{\frac{1}{2}} \left(\left(\frac{P_{new}}{P_{atm}} \right)^{\frac{\gamma-1}{\gamma}} - 1 \right)^{\frac{1}{2}} \quad (\text{B.4})$$

Substituting Equation (B.4) into Equation (B.3) yields:

$$P_{new} = P_{old} \left(\frac{I}{\rho_{old} V_{new}} \left\{ \begin{aligned} & \left(w_{old} - dt \times C_D(P_{new}) A_{th} P_{atm} \left(\frac{1}{R_{GAS} T_I} \right)^{0.5} \times \right. \\ & \left. \left(\frac{2\gamma}{\gamma-1} \left(\frac{P_I}{P_{atm}} \right)^{\frac{\gamma-1}{\gamma}} \right)^{0.5} \left(\left(\frac{P_{new}}{P_{atm}} \right)^{\frac{\gamma-1}{\gamma}} - 1 \right)^{0.5} \right) \end{aligned} \right\} \right)^\gamma \quad (\text{B.5})$$

From this, a function in terms of P_{new} can be determined by rearranging Equation (B.5). This function is given as follows:

$$F(P_{new}) = P_{old} \left(\frac{I}{\rho_{old} V_{new}} \left\{ \begin{aligned} & \left(w_{old} - dt \times C_D(P_{new}) A_{th} P_{atm} \left(\frac{1}{R_{GAS} T_I} \right)^{0.5} \times \right. \\ & \left. \left(\frac{2\gamma}{\gamma-1} \left(\frac{P_I}{P_{atm}} \right)^{\frac{\gamma-1}{\gamma}} \right)^{0.5} \left(\left(\frac{P_{new}}{P_{atm}} \right)^{\frac{\gamma-1}{\gamma}} - 1 \right)^{0.5} \right) \end{aligned} \right\} \right)^\gamma - P_{new} \quad (\text{B.6})$$

$$\underline{F'(\mathbf{P}_{new})}$$

Using the chain rule, Equation (B.6) can be differentiated, with the following results obtained:

$$\begin{aligned}
F'(P_{new}) &= \frac{dF(P_{new})}{dP_{new}} \\
&= \gamma(F(P_{new}) + P_{new})^{\gamma-1} \times \\
&\quad \frac{-dtA_{th}P_{atm}}{\rho_{old}V_{new}} \left(\frac{1}{R_{GAS}T_I} \right)^{0.5} \left(\frac{2\gamma}{\gamma-1} \left(\frac{P_I}{P_{atm}} \right)^{\frac{\gamma-1}{\gamma}} \right)^{0.5} \times \\
&\quad \left(C_D'(P_{new}) \left(\left(\frac{P_{new}}{P_{atm}} \right)^{\frac{\gamma-1}{\gamma}} - 1 \right)^{0.5} \right. \\
&\quad \left. + 0.5C_D(P_{new}) \left(\left(\frac{P_{new}}{P_{atm}} \right)^{\frac{\gamma-1}{\gamma}} - 1 \right)^{-0.5} \left(\frac{\gamma-1}{\gamma} \right) \left(\frac{P_{new}}{P_{atm}} \right)^{-\frac{1}{\gamma}} \right)^{-1} \tag{B.7}
\end{aligned}$$

With this, Equations (B.6) and (B.7) can be substituted in to Equation (B.1) and computationally implemented in to an iterative scheme to obtain the pressure and gas mass solution over a given timestep.

Appendix C

Mass Comparison between Crew Impact Attenuation Systems

Presented below is a mass comparison between the baseline Orion Crew Impact Attenuation System, and the second generation personal airbag system. Here, the mass values for the Orion system were provided by the project sponsor.

Orion Crew Impact Attenuation System	
Component	Mass
<i>Crew Seats</i>	
Operators 1 & 2	31.3kg (69lb) each
Operators 3-6	27.4kg (60.5lb) each
<i>System Support Structure</i>	
Pallet Struts (9 total: 4-X, 3-Y, 2-Z)	10.9kg (24lb) each (average)
Miscellaneous components supported by system	100kg (221lb)
Total Mass	493.5kg (1088lb)

Generation 2 Personal Airbag System	
Component	Mass
<i>Crew Seats</i> (6 total)	27.7kg (61lb) each
<i>System Support Structure</i>	
Integrated Airbag (4 per crew member)	4.0kg (8.8lb) each
Inflation System	11.3kg (25lb)
Miscellaneous components supported by system	100kg (221lb)
Total Mass	373kg (823lb)

References

- [1] Johnson, C. J., and Hixson, R. A., 2008, "Orion Vehicle Descent, Landing, and Recovery System Level Trades," AIAA Space 2008 Conference & Exposition, 9-11 September 2008, AIAA 2008-7745, ed.
- [2] NASA HQ, February 2004, "The Vision for Space Exploration," NASA Headquarters, Washington, DC.
- [3] Nevills, A., 2008, "Constellation Photo Gallery," NASA, [Online], URL: http://www.nasa.gov/mission_pages/constellation/multimedia/orion_contract_images.html [Cited: May 28th, 2009].
- [4] Baker, J.D., Eisenman, D.J., Yuchnovicz, D.E., 2007, "Evaluation of Land versus Water Landings for Crew Exploration Vehicle," NASA Document RP-07-29, NASA Johnson Space Center.
- [5] NASA ESMD, 2005, "NASA's Exploration Systems Architecture Study," NASA, NASA-TM-2005-214062.
- [6] Davis, C.E.J., and Jahn, N.P., January 1969, "Qualification Test of Apollo Crew Couch X-X Axis Foot Cyclic Impact Strut Assembly (V36-571711-121)," North American Rockwell Corporation, NA-68-474, Los Angeles, CA.
- [7] de Weck, O.L., 2009, "Personal Airbag System – NASA NESCR Research Project Overview," Presentation to NESCR Orion Alternative Seat Attenuation Systems Team, March 17th 2009, Cambridge, MA.
- [8] Siddiqi A., de Weck O. L., October 2008, "Modeling Methods and Conceptual Design Principles for Reconfigurable Systems," Journal of Mechanical Design, 130(10), 101102) pp. 15.
- [9] NASA, 2006, "NASA Constellation Program Human-Systems Integration Requirements," NASA, CxP 70024.
- [10] Boehm, B. W., May 1988, "A Spiral Model of Software Development and Enhancement," Computer, pp. pp61-72.
- [11] Xenith LLC, 2009, "Xenith X1 Catalog," Xenith LLC, Lowell, MA.

- [12] Xenith LLC, 2010, "Xenith's Images," Xenith LLC, [Online], URL: <http://www.xenith.com/users/xenith/photos/> [Cited: September 28th, 2010].
- [13] Dumitrache, A., June 18th, 2010, "Dainese D-Air Racing Airbag System Explained," Autoevolution.Com, [Online], URL: <http://www.autoevolution.com/news/dainese-d-air-racing-airbag-system-explained-21541.html> [Cited: September 28th, 2010], 2010, SoftNews NET.
- [14] Mugen Denko, 2001, "Hit-Air Airbag System - Shock Buffering Protection System," Hit-Air, [Online], URL: <http://www.eggarka.com/english/system/index.html> [Cited: September 29th, 2010], Mugen Denko.
- [15] Simeonov, P., 2006, "Wearable airbags - emerging technology for fall injury prevention (state of the art and research needs)," International Society for Fall Protection Symposium 2006
- [16] Hull, D., 1987, "Gas-Inflatable, Floating, Portable Seat," United States Patent Application, (4687452) .
- [17] Stawicki, E., 2004, "Seat Integrated Inflatable Neck Support," United States Patent Application, (5330255) .
- [18] Bentley, J., 1980, "Inflatable Seat Cushion and Body Support Assembly," United States Patent Application, (4190286) .
- [19] Skrzycki, C., 2005, "FAA Requires Safer Seats on New Planes (October 19, 2005)," The Seattle Times, [Online], URL: http://seattletimes.nwsource.com/html/traveloutdoors/2002571372_webairseats19.html [Cited: October 6th, 2010].
- [20] Paur, J., 2009, "Airbags Help Airlines Meet New Safety Regs (October 7, 2009)," Wired - Autopia, [Online], URL: <http://www.Wired.com/autopia/2009/10/airbags-help-airlines-meet-new-safety-standards/#more-13764> [Cited: October 6th, 2010].
- [21] AmSafe Aviation, 2008, "Commercial Aviation Airbag Deployed," AmSafe Aviation, [Online], URL: <http://www.amsafe.com/products/document.php?id=189&pid=4&type=business> [Cited: October 6th, 2010].
- [22] Schroth Safety Products, 2007, "Inflatabelts," BAE Systems, Arnsberg, Germany, [Online], URL: <http://english.schroth.com/military/inflatabelts.php> [Cited: October 24th, 2008].
- [23] Dream Cars, 2007, "Honda Accord Sedan Safety - Front Side Airbags with Passenger-Side Occupant Position Detection System (OPDS)," Dream Cars, [Online], URL: http://www.cars.virkson.net/accord%20sedan%202007/safety_honda_accord_sedan.html [Cited: October 24th, 2008].

- [24] Autoevolution, 2008, "Honda Gold Wing Motorcycle Airbag System Explained - Photo Gallery," Autoevolution, SoftNews NET., [Online], URL: <http://www.autoevolution.com/news-g-image/honda-gold-wing-motorcycle-airbag-system-explained/17820.html#image> [Cited: October 6th, 2010].
- [25] BAE Systems, 2009, "CABS - Cockpit Air Bag System," BAE Systems, CABS Brochure, obtained from URL: http://artisan-3d.com/BAEProd/groups/public/documents/bae_publication/bae_pdf_mps_oc_cabs.pdf [Cited: October 24th, 2008].
- [26] Wikipedia, 2008, "Airbag," Wikimedia Foundation, Inc., [Online], URL: <http://en.wikipedia.org/wiki/Airbag> [Cited: October 24th, 2008].
- [27] Jackson, K.E., Boitnott, R.L., Fasanella, E.L., 2004, "A History of Full-Scale Aircraft and Rotorcraft Crash Testing and Simulation at NASA Langley Research Center," NASA Langley Research Center, Hampton, VA.
- [28] F-111.net, 2004, "F-111 Ejection System," F-111.Net, [Online], URL: <http://www.f-111.net/ejection.htm> [Cited: October 6th, 2010].
- [29] Robinson, T., 2010, "Farnborough Airshow - Day 4 Highlights," Aero Society Channel, the Royal Aeronautical Society, [Online], URL: <http://www.aerosocietychannel.com/2010/07/farnborough-airshow-day-4-highlights/> [Cited: October 6th, 2010].
- [30] Rafael, 2005, "REAPS Demonstrates Maximum Crash Protection," Rafael Advanced Defense Systems Ltd., [Online], URL: <http://www.rafael.co.il/marketing/444-1254-en/marketing.aspx> [Cited: October 6th, 2010].
- [31] Wikipedia, 2010, "Basilar Skull Fracture," Wikimedia Foundation Inc., [Online], URL: http://en.wikipedia.org/wiki/Basilar_skull_fracture [Cited: October 6th, 2010].
- [32] McCullough, J., 2008, "Spacecraft Landing Systems History," NASA Internal Slide Package.
- [33] Grayzck, E., 2010, "Luna 9," National Space Science Data Center, NASA, [Online], URL: <http://nssdc.gsfc.nasa.gov/nmc/spacecraftDisplay.do?id=1966-006A> [Cited: October 4th, 2010].
- [34] Cherkasov, I. I., Mikheev, V. V., Smorodinov, M. I., November 1986, "20 Years of Soviet Investigations of Lunar Soils," Soil Mechanics and Foundation Engineering, **23**(6) pp. pp 214-244.
- [35] Sebolt, W., Dachwald, B., Streppel, J., 2007, "Lander Mission to Europa with Solar Electric Propulsion," 7th International Symposium on Launcher Technologies, Barcelona, Spain, 2-5 April 2007.

- [36] Astronautix.com, 2009, "Luna E-6," Astronautix.Com, [Online], URL: <http://www.astronautix.com/craft/lunae6.htm> [Cited: January 6th, 2010], .
- [37] Grayzeck, E., 2010, "Luna 13," National Space Science Data Center, NASA, [Online], URL: <http://nssdc.gsfc.nasa.gov/nmc/spacecraftDisplay.do?id=1966-116A> [Cited: October 4th 2010].
- [38] MacCormack, A., and Wynn, J., 2004, "Mission to Mars," Harvard Business School, Case Study 9-603-083, Cambridge, MA.
- [39] NASA JPL, 1997, "Mars Pathfinder Entry Descent and Landing," NASA Jet Propulsion Laboratory, [Online], URL: <http://marsprogram.jpl.nasa.gov/MPF/mpf/edl/edl1.html> [Cited: October 5th, 2010].
- [40] Malin Space Science Systems, 2005, "Getting Data from the Mars Exploration Rovers: Mars Relay Plans," Malin Space Science Systems, [Online], URL: http://www.msss.com/mars_images/mars_relay/mer_role/index.html [Cited: October 5th, 2010].
- [41] Cadogan, D., Sandy, C., and Grahne, M., 2002, "Development and Evaluation of the Mars Pathfinder Inflatable Airbag Landing System," *Acta Astronautica*, **50**(10) pp. pp. 633-640.
- [42] Lavoie, S., 1997, "Photojournal: Sojourner Rover Near the Dice," NASA Jet Propulsion Laboratory, [Online], URL: <http://photojournal.jpl.nasa.gov/catalog/PIA01122> [Cited: October 5th, 2010].
- [43] Watanabe, S., 2003, "Artist's Concept of Rover on Mars," NASA Jet Propulsion Laboratory, [Online], URL: <http://www.jpl.nasa.gov/missions/mer/images.cfm?id=284> [Cited: October 5th, 2010].
- [44] Stein, J., and Sandy, C., 2003, "Recent Developments in Inflatable Airbag Impact Attenuation Systems for Mars Exploration," AIAA, AIAA 2003-1900, 44th AIAA/ASME/ASCE/AHS Structures, Structural Dynamics, and Materials Conference, 7-10 April 2003, Norfolk, VA.
- [45] Timmers, R.B., Hardy, R.C., Wiley, C.E., 2009, "Modeling and Simulation of the Second-Generation Orion Crew Module Air Bag Landing System," AIAA, AIAA 2009-6593, AIAA Space 2009 Conference & Exposition, 14-17 September 2009, Pasadena, CA.
- [46] Smith, T.R., Sandy, C.R., Ware, J.S., 2007, "Orion CEV Earth Landing Impact Attenuating Airbags - Design Challenges and Application," IEEE, IEEEAC Paper No. 1111, 29th IEEE Aerospace Conference, March 3-10, 2007, Big Sky, Montana.
- [47] CNES, 2008, "ExoMars Lander," CNES, [Online], URL: http://smsc.cnes.fr/EXOMARS/OLD/GP_lander.htm [Cited: August 8th, 2009].

- [48] Aero Sekur, 2008, "ExoMars Lander Testing Video," Aero Sekur, [Online], URL: <http://www.aerosekur.com/Space/docs/2.mpg> [Cited: August 8th, 2009].
- [49] Shayler, D. J., 2009, "Return to Earth," pp. 287-339.
- [50] Siddiqi, A.A., 2000, "Challenge to Apollo: The Soviet Union and the Space Race, 1945-1974," National Aeronautics and Space Administration, Washington D.C., pp. 1011.
- [51] Hall, R., and Shayler, D., 2001, "The rocket men : Vostok & Voskhod, the first Soviet manned spaceflights," Springer; Published in association with Praxis, London ; New York; Chichester England, pp. 326.
- [52] Swenson, L.S., Grimwood, J.M., and Alexander, Charles C., 1966, "This new ocean; a history of Project Mercury," Scientific and Technical Information Division, Office of Technology Utilization, National Aeronautics and Space Administration; for sale by the Supt. of Docs., U.S. Govt. Print. Off., Washington, pp. 681.
- [53] SpaceRef, 2008, "NASA ISS on-Orbit Status 11 January 2008," SpaceRef, [Online], URL: <http://www.spaceref.com/news/viewsr.html?pid=26655> [Cited: August 8th, 2009]. .
- [54] Shayler, D., 2009, "Space rescue : ensuring the safety of manned spaceflight," Springer; Published in association with Praxis, Berlin ; New York; Chichester, UK, pp. 356.
- [55] Shayler, D., 2001, "Gemini : steps to the moon," Springer; Published in association with Praxis Pub., London ; New York; Chichester England, pp. 433.
- [56] Garber, S., and Hahn, M., 2010, "Gemini 12 Splashdown," Great Images in NASA, [Online], URL: <http://grin.hq.nasa.gov/ABSTRACTS/GPN-2000-000994.html> [Cited: October 6th, 2010].
- [57] Woods, D., and Brandt, T., 2009, "Crew Couches," NASA History Office, [Online], URL: http://history.nasa.gov/ap16fj/02system_couches.htm [Cited: October 10th, 2010].
- [58] Woods, W.D., 2008, "How Apollo flew to the Moon," Springer Verlag; published in association with Praxis Publishing, New York; Chichester, U.K., pp. 412.
- [59] Coltman, J.W., Van Ingen, C., and Zimmerman, R.E., 1989, "Aircraft Crash Survival Design GuideVolume II - Aircraft Design Crash Impact Conditions and Human Tolerance," Aviation Applied Technology Directorate, U.S. Army Aviation Research & Technology Activity (AVSCOM), USAAVSCOM TR 89-D-228, Fort Eustis, VA.
- [60] Lawrence, C., Carney, K.S., and Littell, J., 2007, "Astronaut Risk Levels During Crew Module (CM) Land Landing," NASA GRC, NASA-TM-2007-214669, Cleveland, OH.

- [61] Barrows, D.A., Burner, A.W., Berry, F.C., 2008, "Photogrammetric Measurements of CEV Airbag Landing Attenuation Systems," AIAA, AIAA 2008-846, 46th AIAA Aerospace Sciences Meeting and Exhibit, 7-10 January 2008, Reno, Nevada.
- [62] Cooper, M., Sinclair, R., Sanders, J., 2005, "Design and Testing of an Airbag Landing Attenuator System for a Generic Crew Return Vehicle," AIAA, AIAA 2005-1616, 18th AIAA Aerodynamic Decelerator Systems Technology Conference and Seminar.
- [63] Cengal, Y.A., and Turner, R.H., 2005, "Fundamentals of Thermal-Fluid Sciences," McGraw-Hill Companies, Boston, pp. 1111.
- [64] Cole, K.J., and Waye, D.E., 1993, "BAG: A Code for Predicting the Performance of a Gas Bag Impact Attenuation System for the PATHFINDER Lander," Sandia National Laboratories, SAND93-2133, Albuquerque, NM.
- [65] Esgar, J.B., and Morgan, W.C., 1960, "Analytical Study of Soft Landings on Gas-Filled Bags," NASA, NASA Technical Report R-75, Lewis Research Center, Cleveland, Ohio.
- [66] Ames Research Staff, 1953, "NACA Report 1135 - Equations, Tables, and Charts for Compressible Flow," National Advisory Committee for Aeronautics, NACA-TR-1135, Washington D.C.
- [67] Perry, J.A., Jr., October 1949, "Critical Flow Through Sharp-Edged Orifices," Transactions of the American Society of Mechanical Engineers, pp. 757-764.
- [68] Brinkley, J. W., Specker, L. J., and Mosher, S. E., 1990, "Development of Acceleration Exposure Limits for Advanced Escape Systems," Implications of advanced technologies for air and spacecraft escape : papers presented at the Aerospace Medical Symposium held in Munich, Germany, from 24 to 28 April 1989, Anonymous AGARD, Neuilly Sur Seine, France.
- [69] Eiband, M., 1959, "Human Tolerance to Rapidly Applied Accelerations: A Summary of the Literature," National Aeronautics and Space Administration, NASA-TM-5-19-59E, Washington D.C.
- [70] Kumar, K.V., and Norfleet, W.T., 1992, "Issues on Human Acceleration Tolerance After Long-Duration Space Flights," National Aeronautics and Space Administration Lyndon B. Johnson Space Center, NASA-TM-104753, Houston, TX.
- [71] LiquidLatex.com, 2010, "Coating Fabrics and Porous Surfaces with Liquid Latex," LiquidLatex.Com, [Online], URL: <http://www.liquidlatex.com/liquidlatex32.html> [Cited: April 12th, 2010].
- [72] Sarafan, R., 2007, "Coating Fabric with Liquid Latex," Instructables.Com, [Online], URL: <http://www.instructables.com/id/Coating-Fabric-with-Liquid-Latex/> [Cited: April 12th, 2010].

- [73] de Weck, O. L., and Jones, M. B., 2006, "Isoperformance: Analysis and Design of Complex Systems with Desired Outcomes," *Systems Engineering*, **9**(1) pp. 45.